Dear editor,

We submitted the revised version of our manuscript.

We replied to the comments of two Referees (see our detailed answers point by point listed below) and made modifications with respect to the comments.

The changes applied to our manuscript are described in detail below. They are also highlighted in the Marked-up manuscript version with 'track changes' (main text and supplement)

With best regards,

Yang Wang

Reply to Ref. #1

First of all we want to thank this reviewer for the positive assessment of our manuscript and the constructive and helpful suggestions.

General comments
This paper presents long-term (May 2011-November 2014) MAX-DOAS observations of tropospheric aerosols, NO2, SO2 and HCHO in Wuxi, China. Vertical profiles of trace gas concentrations and aerosol extinctions are retrieved using a new inversion algorithm called PriAM. It is based on the Levenberg-Marquardt modified Gauss-Newton numerical procedure and uses the SCIATRAN radiative transfer model as forward model. In the first part of the paper, MAX-DOAS observations and the PriAM algorithm are described and the following issues are investigated: impact of the surface pressure and temperature seasonality regularly observed in Wuxi on O4 VCD and aerosol retrieval, observed differences between VCDs derived using the geometric approximation and the profiling algorithm, impact of the sky conditions on the aerosol and trace gases retrievals and on the agreement between MAX-DOAS and correlative measurements (AERONET, LP-DOAS). In the second part of the paper, MAX-DOAS data are used to characterize the seasonal, diurnal, and weekly variations of NO2, SO2, HCHO and aerosols.
This is a very interesting study of high scientific quality which fits well with the scope of ACP. I recommend its final publication after addressing the following comments.

Author reply:
Many thanks for the positive assessment!

Major comments

-Although clearly structured, the manuscript is difficult to read due to the large number of figures and panels in the manuscript itself (29) and in the supplement (28). The authors should improve the readability of their paper for the final publication in ACP by focusing on the main results only and asking themselves which figures are needed to best illustrate these results.

Author reply:

We minimized the number of figures to only show the necessary figures in the main manuscript. In the revised version there are only 15 figures in the main part of the manuscript and in total fewer subplots in the manuscript and supplement than in the original version. To make the paper more focused on the most important new findings, we moved the original section 2.2.4 into the supplement as new section 3.2 (the main conclusion of the original section 2.2.4 is summarized at the end of section 2.2.2. We also moved the original Fig. 5 into the supplement as new Fig. S10. The original Fig. S11 is removed from the supplement. We made the new Fig. 6 in order to replace the original Figs. 8-12. The key information including the mean differences, standard deviations, R, slopes, intercepts and numbers of observations in the original figures are now all plotted in the new Fig. 6. We made the new Fig. 9 in order to replace the original Figs. 15-19 to only show the key information. In the new supplement the new Figs. S21-24 summarize the key information from the previous Figs. S20-S23. We also moved the original section 3.1 and Fig. 21 and 22 (containing the meteorology data) into the supplement (a yellow arrow is added in Fig.1b of the revised version to show the dominant wind direction). We also removed the original Fig. 4a and only keep Fig. 4b in the revised version (because the information in Fig. 4a is already well presented in Fig. 4b). The original Fig. 7 is removed.
Although the current supplement still contains many figures, we think it is good for the readers who want to learn the details of the study. Thus we paid more effort to shorten the main manuscript.

Specific Comments:

1) Sect. 2.2.3, page 6: One important result is the impact on the seasonal variation of the pressure and temperature profiles on the retrieved AODs and aerosol extinctions. So far most MAXDOAS groups were using US Standard Atmosphere in their aerosol extinction profile retrievals from O4 slant column densities. The authors show in their study that ignoring this systematic seasonal variation in Wuxi can cause a 20-30% bias on the retrieved AODs and near-surface aerosol extinctions, possibly yielding to unrealistic seasonal variations of these quantities. Is such a large effect only specific to the Wuxi region or can we expect similar features in other parts of China, especially the Beijing area where several MAXDOAS instruments are currently in operation?

Author reply:
The variation of O_4 VCD depends on the systematic seasonal variation of temperature and pressure. The seasonal variation of temperature occurs in many locations of the world (especially outside the tropics). However the temporal variation of the pressure is usually more complex and can be very different at different locations. The variation of pressure in Wuxi (and also many other parts of Eastern China) is related to the East Asian Monsoon and shows a systematic seasonal pattern. The monsoon is a general phenomenon in the eastern China. The pressure in the continent is systematically lower and higher than that in the ocean in summer and winter, respectively. Thus a similar seasonal variation of the O4 VCD is expected in general in Eastern China including Beijing. We added this information at the end of section 2.2.3 of the revised manuscript.

2) Sect. 2.2.4, page 6 and Sect. 2.2.5, page 8: The evaluation of the internal consistency of the inversion algorithm and the validation of the retrieval results are performed for favourable measurement conditions, i.e. 'clear-sky with relatively low aerosols (average AOD of about 0.6)'. 'Average AOD of about 0.6' is for me very vague. Is it the daily or hourly average? Looking at Figure 9 showing the scatterplots of the MAX-DOAS versus AERONET AODs, MAXDOAS AOD values much larger than 0.6 (see scatterplot for Spring) are selected while this figure is supposed to

illustrate the agreement between MAXDOAS and AERONET in low aerosols (and clear-sky) conditions. I think a clarification is needed here.

Author reply:
Thanks for pointing out the misleading description. 'Clear-sky with relatively low aerosols' belongs to one category of the sky conditions identified by MAX-DOAS observations. Please see section 2.2.5. To clarify the point, we added a sentence at the end of the first paragraph of section 2.2.5:
"Another point which needs to be clarified is that distinguishing "low aerosols" and "high aerosols" is based on the colour index observed by MAX-DOAS. Thus there is not an explicit AOD value which distinguishes both aerosol categories. The studies of Wang et al., 2015, however, demonstrated that the AODs observed by the Taihu AERONET sun photometer are mostly smaller and larger than 0.6 for the "low aerosols" and "high aerosols", respectively. In addition to the cloud effect, also the effect of high aerosol loads is evaluated (due to the unrealistic assumption of the pdf of the atmospheric state in the OE algorithm for high aerosol loads (see Eq. (1)).."
Note that in the revised version of the manuscript the original section 2.2.4 was moved to the supplement as new section 3.2. In the beginning of section 3.2 in the supplement, we deleted "average AOD of about 0.6", but write "the sky condition is directly identified by MAX-DDOAS observations, see section 2.2.5".

3) Sect. 2.2.5, page 8: MAXDOAS AODs are validated using AERONET data from the Taihu station, which is located at 18 km south west of the MAXDOAS instrument location. Based on the coordinates mentioned on the AERONET website, the sun photometer is located in the south of the Taihu mountains, at the edge the Taihu Lake (west of the lower left corner of the orange rectangle in Figure 1b), which seems to be a much more remote area than the one from where the MAXDOAS instrument is operating (see also figure 1b). The question is therefore how representative is the Taihu station compared to the location of the MAXDOAS instrument? Did the authors consider this point for the interpretation of their comparison results?

Author reply:
Thanks for pointing out this potential source for differences. We added the following discussion to section 2.2.4: "Here it should be noted that AERONET Taihu station is located in a more remote area (from downtown Wuxi) than the MAX-DOAS at Wuxi station. The different locations could contribute to a systematic bias between both data sets. However the long residence time of up to several days (Ahmed et al., 2004) and the relatively homogeneous horizontal distribution of aerosols (implied by the weak dependence of AOD on wind direction, see section 3.4.2) implies that the differences between both measurements should be small."

4) Sect. 2.2.5, pages 8-9: the validation results are discussed only in terms of absolute differences between MAXDOAS and correlative data. It would be useful for the reader to have also an idea about the corresponding relative difference values.

Author reply:
We added the relative differences (compared to the average values) to the manuscript in section 2.2.4 and the conclusions.

5) a) Sect. 2.2.6, pages 9-10: Is it really useful to show the scatterplots of MAXDOAS versus correlative data and histograms of the absolute differences between MAXDOAS and correlative data for all sky conditions, seasons, and trace gas (TG) and aerosol variables (Figs 15-19 and S20-23) ? I think the manuscript could be simplified here. My suggestion for the final publication is to remove all the histograms from the manuscript and to present the linear regression and correlation results in a table. The latter could also be presented in a panel like the ones usually used in MAXDOAS intercomparison campaigns for summarizing the slant column density comparison results (see e.g. Figure 6 in Roscoe et al., Atmos. Meas. Tech., 3, 1629–1646, 2010; the authors would show for each TG or aerosol variable, the correlation coefficient, slope, and intercept values in three different subplots, replacing the x-axis by the sky conditions and the elevation angles (colored circles) by the seasons).

Author reply:
Great thanks for your good suggestions! We followed your suggestions to re-plot the figures. Please see the description in the reply to your "Major comments".

b) Based on these comparison results (Figs 15-19 and S20-23), the authors have developed recommendations for determining under which sky conditions which TG and aerosol data products can be used or not. This filter scheme is presented in Table 3. However, nothing is said on the criteria (e.g. which threshold values on correlation coefficients and/or slopes, etc) used in practice by the authors to develop these recommendations. Maybe a panel summarizing the linear regression results as suggested in comment 5a could also support the discussion here.

Author reply:
It is hard to quantify the cloud effects on the MAX-DOAS results of aerosols and TGs. Here we combine the results shown in Fig. 8 and 9 (in the revised version) to qualitatively discuss the effect of clouds and give our recommendation. We added more discussion of the cloud effects (as shown in the three figures in the end two paragraphs of section 2.2.5) in order to make our selection more clear.

6) Sect. 2.2.7, page 12, lines 12-13: the total error budgets of aerosol retrievals are simply reported as error of TGs related to the errors of aerosols. This is not correct because the relationship between the aerosol extinction profiles and the TG retrievals is not linear, i.e. a 15% difference in the aerosol extinction profile used in the TG retrievals does not lead necessarily to a 15% difference in the retrieved TG profiles. This point should be further investigated and corrected in the revised manuscript.

Author reply:
We agree with the reviewer. But the quantification of the aerosol effects on TG results is difficult because it depends on the aerosol profile, aerosol properties, profiles of TGs and even observation geometries. Many simulation studies need to be done to acquire a more reasonable estimation on the effects. Although the topic is very interesting and new, but it should be done in a separated work in the future. Thus we would only coarsely estimate the relevant errors of TGs using the assumption of linear propagation of the errors of aerosol retrievals. And the following clarification is given in the manuscript: "The estimations of aerosol relevant errors are rough. A further studies need to be done to acquire a more reasonable estimation by considering aerosol properties, profiles of aerosols and TGs and observation geometries."

7) Section 3.2: Interpreting the retrieved profile shapes should be done with caution given the fact that the average DFS is only around 2. This particularly the case for the HCHO profiles which show a secondary maximum around 1km. A possible explanation is of course the transport of longer-lived VOCs to higher altitudes but with a DFS around 2, one should not totally exclude the possibility of a retrieval artifact.

Author reply:
We agree with the reviewer. We added the following clarification in section 3.1 of the revised version: "However it should be noted that VMRs of HCHO at high altitudes are strongly constrained by the a-priori profiles because of the low sensitivity of MAX-DOAS retrievals at these altitudes. More comparisons studies with aircraft measurements need to be done in the future to further quantify the retrieval sensitivities for elevated layers."
In my own opinion, we still have confidence on the extensive vertical distribution of HCHO retrieved by MAX-DOAS because of two reasons: 1) the Fig. S9 in the supplement of the revised version indicates the higher vertical extension can still be partly represented even for using an exponential a-priori profile; 2) the large variation amplitude of HCHO VMRs at the altitude around 1km is retrieved from MAX-DOAS observations. It indicates the sensitivity of MAX-DOAS retrievals to the layers at around 1km is still well. Thus we add the following comment in section 3.1: "Nevertheless we still have confidence on the extensively vertical distribution of HCHO retrieved by MAX-DOAS because of two reasons: 1) the Fig. S9 in the supplement indicates the higher vertical extension can be partly represented even for using an exponential a-priori profile; 2) the large variability of HCHO VMRs at the altitude around 1km is retrieved from MAX-DOAS observations. It indicates the sensitivity of MAX-DOAS retrievals to the elevated layers is still well."

Suggestions for technical corrections:

*Page 1, line 16: 'extinctions' -> 'extinction'

Corrected

*Page 2, line 26: 'ground based' -> 'ground-based'; this should be corrected throughout the manuscript.

Corrected

*Page 3, line 8: 'Clemer' -> 'Clémer'; this should be corrected throughout the manuscript

Corrected

*Page 3, line 22: 'humidity controlled' -> 'humidity-controlled'

Corrected

*Page 3, line 34: 'so called' -> 'so-called'

Corrected

*Page 5, line 26: ‘long term’ -> ‘long-term’

Corrected

*Page 6, line 11: ‘session’ -> ‘section’

Corrected

*Page 12, line 21: ‘budges’ -> ‘budget’ or ‘budgets’

Corrected

*Page 18, line 10: remove ‘.’ after ‘found:’

Corrected

*Page 38, Figure 7: the ‘2’ of ‘NO2’ on the x-axis label of subplot (b) is cut.

Corrected

*Page 39, Figure 9: remove the ‘,’ after ‘Figure 9:’

Corrected

*Supplement, page 8, Figure S2: There is a problem with y-axis labels of subplots (a) and (b).

Corrected

Reply to Ref. #2

First of all we want to thank this reviewer for the positive assessment of our manuscript and the constructive and helpful suggestions.

General comments
This paper presents the temporal variation and vertical distribution characters of the tropospheric aerosol extinction (AE) and trace gases (TGs, including NO2, SO2 and HCHO in this study) derived from relatively long-term (2011-2014) ground-based MAX-DOAS observations in the Wuxi city, located in eastern China. The authors developed a new profile inversion logarithm (PriAM) and applied it to deal with their MAX-DOAS measurement data in this study.
For the retrieval method, the authors find that large, systematic biases of the retrieved AE profiles and thus AOD can be induced if the seasonal variations of temperature and pressure are not considered. They also show that the traditional geometry approximation could lead to larger biases than the profile integration in the retrieval of tropospheric vertical column densities (VCDs) by analyzing the separated processes in the retrieval from their MAX-DOAS measurement data. The authors further analyze the data retrieved from MAX-DOAS measurements and characterize the seasonal, diurnal and weekly variations of NO2, SO2, HCHO and aerosols. One of their results is the finding of a significant annual decreasing of SO2 for both VCD and surface mixing ratio.
The study and its results are interesting, providing important information not only for the development in MAX-DOAS technique, but also for further investigations of urban and regional air pollution issues in eastern China. The manuscript can still be improved before publication if some methods could be described more clearly and some results be presented more concisely. Below are my comments and suggestions in detail.

Author reply:
Many thanks for the positive assessment! In order to present the results more concisely, we minimized the number of figures to only show the necessary figures in the main manuscript. In the revised version there are only 15 figures in the main part of the manuscript and in total fewer subplots in the manuscript and supplement than in the original version. To make the paper more focused on the most important new findings, we moved the original section 2.2.4 into the supplement as new section 3.2 (the main conclusion of the original section 2.2.4 is summarized at the end of section 2.2.2. We also moved the original Fig. 5 into the supplement as new Fig. S10. The original Fig. S11 is removed from the supplement. We made the new Fig. 6 in order to replace the original Figs. 8-12. The key information including the mean differences, standard deviations, R, slopes, intercepts and numbers of observations in the original figures are now all plotted in the new Fig. 6. We made the new Fig. 9 in order to replace the original Figs. 15-19 to only show the key information. In the new supplement the new Figs. S21-24 summarize the key information from the previous Figs. S20-S23. We also moved the original section 3.1 and Fig. 21 and 22 (containing the meteorology data) into the supplement (a yellow arrow is added in Fig.1b of the revised version to show the dominant wind direction). We also removed the original Fig. 4a and only keep Fig. 4b in the revised version (because the information in Fig. 4a is already well presented in Fig. 4b). The original Fig. 7 is removed.
Although the current supplement still contains many figures, we think it is good for the readers who want to learn the details of the study. Thus we paid more effort to shorten the main manuscript.

Specific comments

1) In Sect. 2.3, the authors compare the VCD derived by integrating the retrieved vertical profile (VCD_pro) with the VCD calculated by the so-called geometry approximation (VCD_geo). The relative difference is denoted as

Diff_total (see Eq. (3)). To identify the dominating difference (which they called "error") source, they split the total difference (Diff_total) between VCD_geo and VCD_pro into two parts: one is the difference between VCD_geo and VCD_geo_m, denoted as Diff_inversion (see Eq. (4)), and an-other is the difference between VCD_geo_m and VCD_pro, denoted as Diff_geometry (see Eq. (5)), where VCD_geo_m is calculated by applying the geometric approximation to the modelled dSCD. I would say it is a good idea to make such a trial. But one should be noted that the VCD_pro has been taken as a standard value in the comparison and the retrieved profile is assumed to be true in their evaluation. Are the results shown in Fig. 20 for all the measurements including cloudy and haze-foggy conditions? Since both the VCD_pro and VCD_geo_m are calculated from the retrieved profile, a large bias in the retrieved profile may lead to biases in both Diff_inversion and Diff_geometry as well as their relative contributions.

Author reply:
Thanks for your general support of our approach. Concerning your suggestion, we think the problem pointed out is not that serious: if the retrieved profile is quite different from the true profile, the Diff_inversion will increase, but the Diff_geometry will not be impacted (both VCD_pro and VCD_geo_m are based on the retrieved profile). Thus the increased Diff_inversion can present the large errors of the retrieved profile. We added this information to the end of section 2.3 of the manuscript as follows:
"One point need to be clarified that the discrepancy of retrieved profile from the true profile doesn't impact the approach, although both VCD_{pro} and VCD_{geo}^{m} are as function of the retrieved profile. Because in this case, only $Diff_{inversion}$ will increase, but $Diff_{geometry}$ will not be impacted. The increased $Diff_{inversion}$ present the large errors of the profile inversion."

2) Sect. 3.5.2 can be omitted as some discussions are very speculative and the meaningfulness of results seems to be local. The measurements site of this study were made at a suburban site, located in the industrial area. From Fig 1 and Fig. 23, one can see that the dominating winds come from the NE, which is neither in the direction of Wuxi urban center nor in the direction of the large industrial sources. There is no doubt that pollution plumes from the urban center and the larger industrial sources could affect the measurement site, as shown in Fig. 22. Since the characters of the emission sources from the urban area, including the fractions of pollutants and emission heights, can be rather different from those from the industrial area, the concentrations of trace gases, aerosols and its components as well as their vertical distribution might be different for different plumes. These episode effects can be investigated in-depth explicitly in the future studies considering the focus and length of the paper.

Author reply:
Although this study is local and rough, it still shows several general and important results: 1) the dependence of the measured TG VMRs on the wind direction indicates that the dominating sources of the pollutions are local, but not from the long range transport. Also, strong horizontal gradient appears. Because of the expected similar life time, meteorological conditions and emission sources, the conclusion probably fits to the whole YRD region. 2) The study provides an example on how to use ground-based MAX-DOAS observations to find strong emission sources in an urban-size area. 3) The seasonality of the wind dependence of the trace gases, especially for HCHO, indicates the different sources in different seasons. Because of these reasons, we prefer to keep this section. Further explicit studies could be done in the future to further investigate these findings. We added this statement to the end of section 3.4.2 of the revised manuscript.

Technical issues:

P1, L15-16: Change “spatial distribution” to “vertical distribution” and remove “using vertical profiles”. The measurements were made only at one station and might not be used to characterize the (3-D or 2-D) spatial distribution.

Corrected

P1, L28: Change “from the aerosol results” to “for the aerosol results”.

Corrected

P1, L30 – P2, L2: The sentences here need to be rewritten. The phrase “are found” or “is found” occurs so many times here. Better to use them only for the most important findings. The result on wind direction dependency can be skipped as it is only locally meaningful with little information for general chemistry and transport.

We rewrote the paragraph based on the suggestion. We prefer to keep the results about the wind direction dependency (see our reply to the second specific comment).

P2, L8-9: Add “respectively” after “nitrate and sulfate”. Remove “and methane” as methane also belongs to VOCs.

Corrected

P2, L18: Actually, photochemistry of precursor gases was not discussed in the paper of Huang et al. (2014).

We corrected the sentence to “Recent studies found that in megacities in different regions of China most of aerosol particles are from secondary sources, e.g. formed through photochemistry of precursor gases, during haze pollution events (Crippa et al., 2014 and Huang et al., 2014).” Huang et al, 2014 characterized the percentages of different compositions in total aerosols.

P2, L23: Change “Since about 15 years” to “Since about 15 years ago”.

Corrected

P3, L10: The “stability” and “flexibility” issues can be explained a little bit, taking the OE and look-up table methods as example

We add the explanation as “Here good stability means that an inversion approach is robust with respect to the effects of measurement noise. Good flexibility means that it can well retrieve diverse profile shapes.”

P4, L9-12: Use “Section” or “Sect.”, and the same for other places in the manuscript.

Corrected

P4, L13: Change “discussed” to “summarized”.

Corrected

P5, L13-17: I would suggest to rewrite this paragraph as “The PriAM algorithm was originally introduced by Wang et al. (2013a and b). Below we summarize the basic concept of the PriAM algorithm and its implementation settings for this study, while details can be found in Sect. 2 of the supplement. Like for other algorithms, a two-step inversion procedure is used in PriAM. In the first step, tropospheric vertical profiles (in the layer from the ground to the altitude of 4 km) of aerosol extinction are retrieved from the O4 dSCDs. Afterwards, the profiles of NO2, SO2 and HCHO volume mixing ratios (VMRs) are retrieved from the respective dSCDs in each MAX-DOAS elevation angle sequence”.

We rewrote the part based on the suggestion.

P5, L24: “Fig. 7” appears earlier than “Fig. 3”.

We agree with your suggestion to correct the order. However, as described above, we already removed the Fig. 7 in the revised manuscript.

P5, L29: To do (simulate) what with RTM?

We correct it as “the RTM simulations of weighting functions are done at 370 nm”.

P5, L32: For the single scattering albedo, a fixed value of 0.9 is used, or it is allowed to change between 0.85 and 0.95 in the retrievals?

A fixed value is used. To be clear, we corrected the sentence as “The fixed single scattering albedo of 0.9 and asymmetry factor (Henyey and Greenstein, 1941) of 0.72 are chosen according to average inversion results from the Taihu AERONET station from 2011 to 2013 (the data in 2014 is unavailable).”

P6, L18: Fig. S10 should be relabeled as Fig. S8 (its position should also be moved to the front in the Supplement).

We followed this suggestion. We put the Fig. S16 before Fig. S17 in the revised version.

P7, L24: Change “shown” to “as shown”.

Corrected

P8, L16: How are clear sky conditions classified, by AERONET data or by MAX-DOAS data?

The sky condition is identified by MAX-DDOAS observations as described in section 2.2.5 in the revised version.

P9, L24-25: It makes me confusing that the retrieval is based on a “forward model”. Do you mean a “radiation transfer” model or you still have a “backward” model?

We changed “forward model” to “RTM”. Because the SCIATRAN RTM used in this study is a forward model. Both of “RTM” and forward model represent the same thing in this study.

P11, L12-13: I would suggest moving Figs. 16-19 to the Supplement.

Please see the reply to your general comment. We use the new Fig.9 in the revised version to replace the original Fig. 16-19.

P12, L10: Change “45 k” to “45 K”.

Corrected

P14, L5-13: Sect. 3.1 can be skipped.

We moved section 3.1 and Fig. 21 and 22 in the revised version into the supplement. We added a yellow arrow to show the dominant wind direction in Fig. 1b.

P15, L1-2: This sentence can be rewritten, e.g., as “The observed seasonal variations of the different species are related to various processes: the seasonal variations of source emissions, chemical formation and destruction, dry and wet deposition, and atmospheric transport”.

We correct it based on the suggestion as “The observed seasonal variations of the different species are related to various processes: the seasonal variation of source emissions, chemical (trans-) formation and destruction, dry and wet deposition, and atmospheric transport (Wang et al., 2010; Lin et al., 2011)”.

P15, L10-12: It is difficult to understand that there is no seasonal variation for NOx while the SO2 emissions vary by about 20%. Note that the boiler for domestic heating could also make a contribution to the NOx emissions.

Because the contribution of boilers to NOx is only about 5%, but to SO_2 is about 20% based on the study of Huang et al., 2011. We agree that we can’t totally ignore the effect of seasonal use of domestic heating on the seasonality of NOx. But its effect on NOx is much weaker than SO_2. Thus we modified the test as “It is assumed that about 94% of total NOx emission in the Wuxi region is emitted from the power plants, industrial fuel combustions and vehicles (Huang et al., 2011), which emit similar amounts in different seasons. The contribution of boilers for the seasonal use of domestic heating to NOx is only about 5% (Huang et al., 2011). Thus the seasonal variation of the MAX-DOAS results cannot be explained by the variation of the NOx emissions. However, the SO_2 emissions might vary by about 20% due to the significant contribution of boilers (Huang et al., 2011).”

P17, L33 - P18, L3: Similar to the seasonal variation (P15, L1-2), the diurnal variation can be affected by various factors. The explanation here seems to be very speculative and can be skipped.

We agree on your opinion. Thus we skip the speculative explanation and rewrite it as “Their diurnal variations can be affected by various factors, e.g. the diurnal variation of the emission sources, as well as secondary formation, deposition and dispersion.”

P18, L16: The title of Sect. 3.5.1 can be omitted since Sect. 3.5.2 has been suggested to be skipped.

Because we decide to keep the section 3.4.2 in the revised manuscript (section 3.5.2 in the original version), the title of section 3.4.1 (3.5.1 in the original version) needs to be kept.

P18, L17-19: I would suggest to skip over the sentences “Huang et al. (2014) : : :: : : The aerosol in Wuxi close to Shanghai is expected to have similar properties”. There are many kinds of properties for aerosols. It is not clear what properties of aerosols are referred to here. The statement that the aerosols in Wuxi have similar properties with those in Shanghai is very speculative.

We agree that there are many kinds of properties for aerosols. Thus we specified the statement as “The aerosols in Wuxi (which is close to Shanghai) are expected to be similarly dominated by secondary aerosol”. We prefer to keep it because the previous study motivated our study here. Because the distance between Wuxi and Shanghai is 130km. And the life time of aerosols in the boundary layer is up to several days. The aerosols can be mixed well in the region including Wuxi and Shanghai through a transport of 1-2 days. Thus the dominant aerosol sources can be expected to be similar.

P19, L18-21: Too speculative.

We think it is reasonable to say that the wind dependence of HCHO indicates the anthropogenic sources of HCHO. Because the natural sources are rather homogenously spread around the measurement site, but the factories which emit VOCs are located in specific areas.

P20, L2: Change “3 km” to “4 km”.

Corrected

P21, L18-24: This paragraph can be omitted.

Because we decide to keep section 3.4.2 (see the reply to the second specific comment), the relevant paragraph is needed in the conclusion.

P22-30: Use indented lines for each reference.

Corrected

P31, Table 1: The format of this table looks not good and needs to be rearranged. Try to avoid using the same items in both column and row. For instance, use species for each column, and for the row use Cross section, Fitting interval, Polynomial degree, Intensity, and so on.

We modified the table based on the suggestion.

P34, L9: Change “mean maps of” to “maps of mean”.

Corrected

P37, Fig. 5; P39, Fig. 8; P44, Fig. 15: Better to reduce the absolute maximum/minimum values in Y-Axis appropriately so that the differences can be seen more clearly.

We re-plotted the figures as Fig. 6 and 9 in the revised version.

P39-41: Figs. 9-12 can be merged into one figure, with 4 columns for different seasons.

We merged the Figs. 9-12 into one figure (as Fig. 6 in the revised version).

P41-42, Fig. 13: It might be difficult to understand the top panels (colored) of this figure if one had not read the manuscript carefully. It can be more helpful if some words like “primary sky” and “secondary sky” are added, e.g., to the legend, in the figure.

We modified Fig. 13 (Fig. 7 in the revised version) based on the suggestions.

P45-46: It is suggested to move Figs. 16-19 to the Supplement.

We replace Figs. 16-19 by the new Fig. 9 in the revised version (see general comments above).

P48-49, Figs. 21-22: These two figures can be omitted or be moved to the Supplement. Since the seasonal variability of wind directions is not so high, you may consider making a wind rose diagram averaged for all the experiment period and adding it to Fig. 1.

We modified them based on your suggestion.

P58, Fig. 27: The positions of the characters in X-Axis need to be adjusted.

Corrected

P59-60, Fig. 28: This figure can be omitted or be moved to the Supplement.

Because we decide to keep section 3.4.2 (see the reply to the second specific comment), the relevant figure (Fig. 15 in the revised version) is needed to show.

Supp.-P1, L31: With what do NO2 and O4 dSCDS show a systematic increase or decrease?

With the increase of SZA. We correct the sentence.

Supp.-P3, L12: The dSCDs shown here read not as large as two times of the mean RMS.

We corrected the text: They are assumed as two times of the mean RMS.

Supp.-P6, L16: Fig. S9 should be renumbered as its position be moved the place after Fig. S23. Change “the for elevation angles” to “the elevation angles”.

We correct it as “the AODs for elevation angles of” in the revised version.

Supp.-P7, Fig. S1; P8, Fig. S2; Fig. 10, Fig. S5: Both RAA and SAA are used. Please check if they refer to the same variable.

We change all “RAA” as “SAA”. Because the instrument is pointed to the north, the SAA is the same as RAA.

Supp.-P12, Fig. S8: I did not find a place in the main manuscript as well as in the Supplement that this figure is referred to.

We corrected the manuscript. Fig. S8 (Fig. S17 in the revised version) is cited in section 2.2.3.

Supp.-P15, Fig. S10: This figure should be moved to the front.

We moved it to the front.

Supp.-P19, L3: Change “ds” to “DoF”?

Corrected

Supp.-P7-37: Please try to let the main body figure and its caption to be in the same page.

We followed the suggestion.

Supp.-P39: Use indented lines for each reference.

Corrected

Marked-up manuscript version:

Ground-based MAX-DOAS observations of tropospheric aerosols, NO_2, SO_2 and HCHO in Wuxi, China, from 2011 to 2014

Yang~~.~~ Wang[1], Johannes~~.~~ Lampel[1,2], Pin~~. H.~~hua Xie[3,4,5], Steffen~~.~~ Beirle[1], Ang~~.~~ Li[3], De~~. X~~xia Wu[3], and Thomas~~.~~ Wagner[1]

[1] Max Planck Institute for Chemistry, Mainz, ~~55128,~~ Germany

[2] Institute ~~Institute~~ of Environmental Physics, University of Heidelberg, Heidelberg, ~~69120,~~ Germany

[3] Anhui Institute of Optics and Fine Mechanics, Key laboratory of Environmental Optics and Technology, Chinese Academy of Sciences, Hefei, ~~230031,~~ China

[4] CAS Center for Excellence in Urban Atmospheric Environment, Institute of Urban Environment, Chinese Academy of Sciences, Xiamen, ~~361021,~~ China

[5] School of Environmental Science and Optoelectronic Technology, University of Science and Technology of China, Hefei, ~~230026,~~ China

Correspondence to: Yang~~.~~ Wang (y.wang@mpic.de); Pin~~.~~ ~~H.~~hua Xie (phxie@aiofm.ac.cn)

Abstract.

We characterize the temporal variation and ~~spatial~~ vertical distribution of nitrogen dioxide (NO_2), sulphur dioxide (SO_2), formaldehyde (HCHO) and aerosol extinction~~s using vertical profiles derived from~~based on long-term Multi Axis - Differential Optical Absorption Spectroscopy (MAX-DOAS) observations from May 2011 to November 2014 in Wuxi, China. A new inversion algorithm (PriAM) is implemented to retrieve profiles of the trace gases (TGs) and aerosol extinction (AE) from the UV spectra of scattered sunlight recorded by the MAX-DOAS instrument. We investigated two important aspects of the retrieval process. We found that the systematic seasonal variation of temperature and pressure (which is regularly observed in Wuxi) can lead to a systematic bias of the retrieved aerosol profiles (e.g. ~~up~~ up to 20% for the AOD) if it is not explicitly considered. In this study we take this effect for the first time into account. We also investigated in detail the reason for the differences of tropospheric VCDs derived from either the geometric approximation or by the integration of the retrieved profiles, which were reported by earlier studies. We found that these differences are almost entirely caused by the limitations of the geometric approximation (especially for high aerosol loads). The results retrieved from the MAX-DOAS observations are compared with independent techniques not only under cloud free sky

conditions, but also under various cloud scenarios. ~~-~~Under most cloudy conditions (except fog and optically thick clouds), the trace gas results still show good agreements. In contrast, ~~from~~ for the aerosol results, only near-surface AEs could be still well retrieved under cloudy situations.

After a quality controlling procedure, the MAX-DOAS data are used to characterize the seasonal, diurnal, and weekly variations of NO_2, SO_2, HCHO and aerosols. A regular seasonality of the three trace gases is found, but not for aerosols. Similar annual variations of the profiles of the trace gases ~~are found~~appear in different years~~, especially for the trace gases.~~. Only NO_2 ~~has~~shows a significant seasonality of ~~Similar~~ the diurnal variations~~ are found for SO_2, HCHO and aerosols in different seasons, but not for NO_2. Similar annual variations of the profiles are found in different years, especially for the trace gases.~~Considerable amplitudes of weekly cycles occur for NO_2 and SO_2, but not for HCHO and aerosols. The TGs and aerosols ~~have~~show ~~G~~good correlations, ~~between the TGs and aerosols are found,~~ especially for HCHO in winter. ~~Much m~~More pronounced ~~S~~significant wind direction dependencies, especially for the near-surface concentrations, are found for ~~of~~ the trace gases, ~~especially for the near-surface concentrations,~~ than~~are found, but only a weak dependence is found~~ for the aerosols, which ~~properties, especially the AOD. Our findings It imply~~ implies that the local emissions from ~~the~~ nearby industrial areas (including traffic emissions) dominate the ~~amount of~~ local ~~pollutants~~ pollution while long distance transport might also considerably contribute to the local aerosol levels.

1 Introduction

Nitrogen dioxide (NO_2), sulphur dioxide (SO_2), and formaldehyde (HCHO) are important atmospheric constituents which play crucial roles in tropospheric chemistry (Seinfeld and Pandis, 1998). NO_2 is involved in many chemical cycles such as the formation of tropospheric ozone. NO_2 and SO_2 can be converted to nitrate and ~~sulfates~~sulphate, respectively, through the reaction with the OH radical. HCHO is formed mainly from the oxidation of volatile organic compounds (VOCs)~~ and methane~~. Primary emissions of HCHO could be also important, especially in industrial regions (Chen et al., 2014). Due to the short life time of HCHO, it can be used as a measure of the level of the local VOC amount. The VOCs can then be eventually oxidized to form organic aerosols. NO_2, SO_2 and VOCs (marked by HCHO) are essential precursors of aerosols. During the industrialization and urbanization, anthropogenic emissions from traffic, heating, industry, and biomass burning have significantly increased the concentrations of these gases in the boundary layer in urban areas (Environmental Protection Agency, 1998; Seinfeld and Pandis, 1998). Nowadays, strong haze pollution events occur frequently around megacities and urban agglomerations, especially in newly industrializing countries like China, and have a significant impact on human health (Fu et al., 2014a). Recent studies found that in megacities in different regions of China most of aerosol particles are from ~~formed~~ secondary sources, e.g. formed through ~~through~~ photochemistry of precursor gases, during haze pollution events (Crippa et al., 2014 and Huang et al., 2014). Understanding the temporal variation and spatial distribution of the trace gases (TGs) and aerosols through long-term observations is thus helpful to identify the dominating pollution sources, distinguish the contribution of transport and local emission as well as the relation between aerosols and their precursors. To

accomplish this, one Multi Axis - Differential Optical Absorption Spectroscopy (MAX-DOAS) instrument was operated from 2011 to 2014 in Wuxi (China).

Since about 15 years ago, the MAX-DOAS technique has drawn lots of attention because of the potential to retrieve the vertical distribution of TGs and aerosols in the troposphere from the scattered sunlight recorded at multiple elevation angles (Hönninger and Platt, 2002; ~~Hönninger et al., 2004;~~ Bobrowski et al., 2003; Van Roozendael et al., 2003; Hönninger et al., 2004; Wagner et al., 2004~~; Van Roozendael et al., 2003~~ and Wittrock et al., 2004) using relatively simple and cheap ground-based instrumentation. Ground~~-~~-based measurements of TG profiles are complementary to global satellite observations and allow for inter-comparisons and validation exercises (Irie et al., 2008; Roscoe et al., 2010; Ma et al., 2013; Kanaya et al., 2014; Vlemmix et al., 2015a). Using different inversion approaches, the column densities, vertical profiles and near-surface concentrations of the TGs and aerosols can be derived and provide additional information compared to in-situ monitoring or satellite observations.

The tropospheric vertical column density (VCD) of TGs is either derived by the geometric approximation (e.g. Brinksma et al., 2008) or by integration of the retrieved concentration profiles (Vlemmix et al., 2015b). The near-surface concentration can be derived using simplified rapid methods (Sinreich et al., 2013 and Wang et al., 2014b) or directly from the derived profile. The existing profile inversion schemes developed by different groups can be subdivided into two groups: the 'full profile inversion' based on optimal estimation (OE) theory (Rodgers, 2000; Frieß et al., 2006, 2011; Wittrock et al., 2006; Irie et al., 2008, 2011; Clémer et al., 2010; Yilmaz, 2012; ~~Clemer et al., 2010; Irie et al., 2008, 2011;~~ Hartl and Wenig, 2013 and Wang et al., 2013a and b) and the ~~so~~ so-called parameterization approach using look-up tables (Li et al., 2010, 2012; Vlemmix et al., 2010, 2011; Wagner et al., 2011). In comparison with the look-up table methods, the OE-based inversion algorithms are in principle easily applied to different species, different measurement locations and instruments, but they require radiative transfer simulations during the inversion and can therefore be computationally expensive for large datasets. ~~Clemer~~Clémer et al. (2010), Frieß et al. (2011), Kanaya et al. (2014), Hendrick et al. (2014), Wang et al. (2014a) applied their OE approaches to long-term MAX-DOAS observations in different locations of the world. The stability ~~or~~ and flexibility of the inversion algorithms depends on the choice of the inversion approach, the iteration scheme and the a-priori constraints (Vlemmix et al., 2015b). Here ~~G~~good stability means that an inversion approach is ~~well~~ robust ~~to constrain~~with respect to the effects of measurement noise. Good flexibility means that it can well ~~realize~~retrieve diverse profile shapes. Designing an approach balancing stability and flexibility is quite important for long-term observations because of the occurrences of various atmospheric scenarios caused by natural variability and human activities.

In this study, we use the Levenberg-Marquardt modified Gauss-Newton numerical procedure (Yilmaz, 2012) with some modifications to optimally balance stability and flexibility, which will be referred to in the following as "**Pr**ofile **i**nversion algorithm of aerosol extinction and trace gas concentration developed by **A**nhui Institute of optics and fine mechanics, Chinese academy of sciences (AIOFM, CAS) in cooperation with **M**ax Planck Institute for Chemistry (MPIC)" (PriAM) (Wang et al., 2013a and b). The PriAM algorithm joined the intercomparison exercise of aerosol vertical profiles retrieved from MAX-DOAS observations, between five inversion algorithms during the Cabauw Intercomparison Campaign of

Nitrogen Dioxide measuring Instruments (CINDI) in summer 2009 (Frieß et al., 2016). The intercomparison displayed good agreements of the aerosol extinction (AE) profiles, AODs and near-surface AEs retrieved by the PriAM algorithm with those by other algorithms and with a collocated ceilometer instrument, a sun photometer and a humidity-controlled nephelometer. In this work the PriAM is applied to the long-term MAX-DOAS observations in Wuxi, China. The retrieved results of NO_2, SO_2 and HCHO and aerosols are verified by comparisons with several independent data sets for a period longer than one year.

Under cloudy skies the retrieval algorithm could be subject to large errors because of the increased complexity of the atmospheric light paths inside clouds (e.g. Erle et al., 1995; Wagner et al., 1998, 2002, 2004; Winterrath et al., 1999), which are usually not considered in the forward model. Previous studies usually either ignore the effects of clouds or simply discard cloud-contaminated measurements. However, depending on location and season, a large fraction of measurements might be affected by clouds, e.g. about 80% of all MAX-DOAS measurements in Wuxi (Wang et al., 2015). We investigate the effect of clouds on the different MAX-DOAS retrieval results of aerosols and TGs, especially the near-surface concentrations by comparisons with results from independent techniques under various cloud scenarios. Information on different cloud scenarios is directly derived from the MAX-DOAS observations and can thus be assigned to each MAX-DOAS result without temporal interpolation. Tropospheric TG VCDs are also important for satellite validation. So far, most studies used the so-called geometric approximation to derive TG VCDs from MAX-DOAS measurements. However, considerable systematic discrepancies of tropospheric TG VCDs derived by the geometric approximation and by integration of the TG profiles are already reported in Hendrick et al. (2015), but which of the two values is closer to reality remains unclear. It is essential to answer this question in order to use a trustworthy method to determine the tropospheric TG VCDs. In this study we show evidence that the dominant error is associated with the geometric approximation, thus the TG VCDs by integration of the profiles are used for further studies here. After the series of verification exercises, the MAX-DOAS results are used to characterize temporal variations and vertical distributions of aerosols and TGs in Wuxi. The relation between aerosols and TGs are also discussed.

The paper is organized as follows: in section 2 the observations and different steps of the data analysis are described and results are verified. Moreover, the cloud effect on the retrievals and the errors of the geometric approximation are discussed. In section 3 we characterize seasonal variations and inter-annual trends, diurnal variations, weekly cycles and wind dependencies of the aerosols and TGs. The relation between aerosols and TGs are also discussed. In section 4 the results are ~~discussed~~ summarized and conclusions are given.

2 MAX-DOAS measurements

2.1 MAX-DOAS in Wuxi ~~station~~

A MAX-DOAS instrument developed by AIOFM shown in Fig. 1a is located on the roof of a 11-story building in Wuxi City (Fig. 1b), China (31.57 °N, 120.31 °E, 50 m a.s.l.) at the transition between the urban and suburban area. The suburban area with lots of farmlands is located in the east, and Taihu Lake is located in the north. The heavily industrialised area and the urban centre (living and business area) are in southwest and northwest direction of the MAX-DOAS station, respectively. Wuxi city belongs to the Yangtze River delta industrial zone and is located about 130 km north-west of Shanghai (Fig. 1c). Wuxi is an important industrial city and has about six million inhabitants. Because of the high population density and high industrial activity, relatively high abundances of NO_2, SO_2 and VOCs are found (Fu, et al, 2013). Fig. 1d displays the mean distributions of NO_2 (Boersma et al., 2011), HCHO (de Smedt et al., 2010) and SO_2 (Theys et al., 2015) as derived from the Ozone Monitoring instrument (OMI) (Levelt et al., 2006 b). In north-west direction of Wuxi city the large industrial zone of North China plain is located, which has even higher pollution loads. The dominant wind is from the northeast and no significant seasonality is observed (see Fig. S2 in the supplement). The meteorological conditions including, temperature, relative humility and wind field are introduced in section 1 of the supplement.

The MAX-DOAS instrument was operated by the Wuxi CAS Photonics Co. Ltd from May 2011 to ~~Dec~~December 2014. The instrument was pointed to the north and automatically recorded spectra of UV scattered sunlight at sequences consisting of five elevation angles (5 °, 10 °, 20 °, 30 ° and 90 °). One elevation sequence scan took about 12 min depending on the received radiance. More details of the instrument can be found in Wang et al. (2015). During the whole observation period, the instrument stopped twice: 15 December 2012 to 29 February 2013 and 16 July to 12 August 2013.

2.2 Retrievals of the tropospheric profiles of aerosol extinctions, NO_2, SO_2 and HCHO volume mixing ratios.

2.2.1 Retrieval of slant column densities

The slant column densities (SCDs) of the oxygen dimer (O_4), NO_2, SO_2 and HCHO are retrieved from scattered sunlight spectra measured by the MAX-DOAS instrument using the DOAS technique (Platt and Stutz, 2008) implemented by the WINDOAS software (Fayt and van Roozendael, 2009). SCD represents the TG concentrations integrated along the effective atmospheric light path. The TG cross sections, wavelength ranges and additional properties of the DOAS ~~analysis~~ analyses are provided in Table 1. Figure~~.~~ 2 shows typical DOAS fit examples. We skip data for ~~a~~ solar zenith angle (SZAs) larger than 75 ° because of stronger absorptions of stratospheric species and low signal to noise ratio. We also skip the data with large root mean square (RMS) of the residuals and large relative intensity offset (RIO). All thresholds of the quantities used for filtering the results and the percentages of screened data of the total number of observations are listed in Table 2. Detailed discussions of the DOAS fit parameters for each species can be found in section ~~1~~ 2 of the supplement.

2.2.2 The PriAM algorithm

Tropospheric vertical profiles (in the layer from the ground to ~~the~~an altitude of 4 km) of aerosol extinctions and trace gas~~es~~ volume mixing ratios are retrieved from the SCDs by a use of the PriAM algorithm, which~~In the first step of the retrieval, tropospheric vertical profiles (in the layer from the ground to the altitude of 4 km) of aerosol extinction are retrieved from the O_4 dSCDs. Afterwards, the profiles of NO_2, SO_2 and HCHO volume mixing ratios (VMRs) are retrieved from the respective dSCDs in each MAX-DOAS elevation angle sequence by using the PriAM algorithm, which is described in Wang et al., 2013a and b, both in Chinese language. We summarize the basic concept of the PriAM algorithm and its implementation settings for this study below, while details can be found in the section 2 of the supplement.~~ was originally introduced by Wang et al. (2013a and b). Below we summarize the basic concept of the PriAM algorithm and its ~~implementation~~specific settings for this study, while details can be found in section 3 of the supplement. Like for other algorithms, a two-step inversion procedure is used in PriAM. In the first step, profiles of aerosol extinctions are retrieved from the O_4 dSCDs. Afterwards, profiles of NO_2, SO_2 and HCHO volume mixing ratios (VMRs) are retrieved from the respective dSCDs in each MAX-DOAS elevation ~~angle~~ sequence. ~~In PriAM t~~The retrieval problem is solved by the Levenberg-Marquardt modified Gauss-Newton numerical iteration procedure (Rodgers, 2000). Considering the frequent variation of aerosols and the TGs, very little is known about the expected profiles. Thus a set of fixed a-priori profiles is used for each species. A smoothed box-shaped a-priori AE profile (Boltzmann distribution) (Yilmaz, 2012), exponential a-priori profiles of NO_2 and SO_2 (similar to Yilmaz, 2012 and Hendrick et al., 2014), and a Boltzmann distribution a-priori HCHO profile (based on the MAX-DOAS and aircraft measurements in Milano during summer of 2003 reported in Wagner et al., 2011) are used ~~by the PriAM algorithm~~in this study and denoted by the ~~grey~~ black curves in Fig. S~~7~~8 in the supplement~~,~~ ~~respectively~~. Besides these standard a-priori profiles, we tested the effect of changing the profile shapes and absolute values on the fit results. The description of these sensitivity tests is ~~provided~~ given in section ~~2~~3.1 of the supplement. We conclude that the standard a-priori profiles are ~~an optimum choice~~well suited for the application to the long~~-~~-term MAX-DOAS measurements in Wuxi. We also find that improper a-priori profiles can strongly impact the aerosol profile retrievals, but only slightly impact the TG results.

PriAM uses the radiative transfer model (RTM) SCIATRAN version 2.2 (Rozanov et al., 2005). Based on the wavelength intervals of the DOAS fits, the RTM simulations are done at 370 nm for the retrieval of aerosols and NO_2, at 339 nm for HCHO and at 313 nm for SO_2. The surface height and surface albedo are set as 50 m a.s.l. and 0.05, respectively. The fixed single scattering albedo of ~~(~~0.9~~±0.05)~~ and asymmetry factor (Henyey and Greenstein, 1941) ~~(~~of 0.72~~±0.03)~~ are chosen according to average inversion results from the Taihu AERONET station (see section 2.2.4) from 2011 to 2013 (the data in 2014 is unavailable). The retrieved aerosol extinction at 370 nm is converted to those around 313 nm for the SO_2 and 339 nm for the HCHO retrieval using Ångström exponents derived also from the Taihu AERONET data sets.

In addition, here it should be noted that~~,~~ the Levenberg-Marquardt modified Gauss-Newton procedure is based on the assumption that the probability distribution function (pdf) of the atmospheric state (x~~x~~) can be described by a Gaussian pdf (P) around the a-priori state (x_a ~~xa~~) (Rodgers, 2000):

$$-2\ln P(x) = (x - x_a)^T S_a^{-1}(x - x_a) + c \quad (1)$$

Here c~~c~~ is a constant value and S_a is the covariance matrix of the a-priori. Thus the solution can not reach the true state when the pdf of the atmospheric state (x~~x~~) is skew or asymmetric (Rodgers, 2000). In this study the retrieval of the AE for extremely high aerosol loads (e.g. fog and haze) belongs to cases, which probably do not fulfil this assumption. In such cases the AE is underestimated by the inversion (see ~~session~~ section 2.2.~~6~~5).

The mean averaging kernels (AKs) for retrievals of AEs and the NO_2 VMRs for favourable measurement conditions, namely cloud-free sky with relatively low aerosols (the sky condition is directly identified by MAX-DDOAS observations as described in section 2.2.5), are shown in Fig. 5. AKs for SO_2 and HCHO are similar to NO_2. They indicate that the inversions are sensitive to the layers from the surface up to 1.5 km. The degrees of freedom (DoF) are about 1.5 for aerosols (similar to Frieß et al., 2006), 2 for NO_2 and 2.3 for SO_2 and HCHO. The detailed discussion of the performance of the profile retrievals ~~are~~is given in the section 3.2 of the supplement by comparing the measured and modelled dSCDs for different elevation angles, and comparing profiles, averaging kernels (AKs) and retrieval errors in different seasons. In general ~~well~~a consistent performance of the retrievals is found for different elevation angles and seasons.

2.2.3 Correcting the effect of the variation of ambient temperature and pressure

In previous studies (~~Clemer~~Cl émer et al., 2010; Hendrick et al., 2014; Wang et al. 2014a) usually fixed temperature and pressure (TP) profiles are used (e.g. obtained from the US standard summer atmosphere for the measurements in China). However for locations with a significant and systematic annual variation of TP, as in this study, this simplification can affect the retrieved AODs and AE profiles (and thus also the TG profiles) systematically, yielding virtual seasonal variations. The time series of TP near the surface from the weather station nearby the MAX-DOAS instrument are shown in Fig. 3 for the year 2012 (similar patterns are found for other years, see Fig. ~~S10~~ S16 ~~of~~ in the supplement). A regular annual variation of surface TP is obvious with amplitudes between winter and summer of about 20 K and 30 hPa, respectively. The O_4 VCDs derived from the fitted curves of surface TP (the method is described in the section 3.3 of the supplement) is also shown in Fig. 3. The O_4 VCD in summer is systematically lower than in winter by about 15% of the yearly mean O_4 VCD. Ignoring this systematic seasonal variation can cause a 20-30% bias of the AOD and near-surface aerosol extinction (see ~~details in section 3~~ Fig. S17 ~~of~~of the supplement~~supplement~~). The error of the aerosol retrieval can further nonlinearly impact the TG profile retrievals. To account for this effect, the seasonal variation of TP and the O_4 VCD is parameterized and explicitly considered in the forward model during the MAX-DOAS retrievals by the PriAM algorithm. Figure 4 shows the AODs retrieved by PriAM using either explicit TP information or the TP profiles from the US summer standard atmosphere. The

consistency of the AODs retrieved based on the explicit TP data with the simultaneous Taihu AERONET level 1.5 AOD data sets (see section 2.2.~~5~~4) is better than -for TP profiles from the US standard summer atmosphere.

The systematic variation of TP could be also considerable in many other locations of the world. The seasonal variation of temperature occurs in many locations, especially outside the tropics. However the temporal variation of the pressure is usually more complex and can be very different at different locations. The variation of pressure in Wuxi (and also many other parts of Eastern China) is related to the East Asian Monsoon and shows a systematic seasonal pattern. The monsoon is a general phenomenon in the eastern China. The pressure in the continent is systematically lower and higher than that in the ocean in summer and winter, respectively. Thus a similar seasonal variation of the O_4 VCD is expected in general in Eastern China.

~~**2.2.4 Evaluation of the internal consistency of the inversion algorithm**~~

~~In this section the retrieval quality is evaluated for favourable measurement conditions, namely cloud-free sky with relatively low aerosols (average AOD of about 0.6), and the performance of the retrievals in different seasons is discussed.~~

~~Comparing the measured TG-dSCDs to the modelled dSCDs (the results of the forward model corresponding to the retrieved AE and TG profiles) is a direct way to evaluate how close to the real profile the retrieved profile is. Ideally, the differences between measured and modelled dSCDs are minimized by the inversion. However because of measurement errors, deviations of the forward model from reality (e.g. for cloudy skies, shown in section 2.2.6) and the not always realistic assumption of the Gauss-Newton Algorithm in Eq. (1) (especially under the condition with strong aerosol load, also shown in section 2.2.6), the derived profiles might strongly deviate from the real profiles. Figure 5 shows the mean differences (and standard deviations denoted by error bars) between the measured and modelled dSCDs for the four species during the whole measurement period. Almost symmetrical Gaussian-shape histograms of the absolute differences for the different elevation angles are found and shown in Fig. S11 of the supplement. For the aerosol retrieval, a larger negative difference of the O_4 dSCD of 2.9×10^{41} molecules^2 cm^{-5} is found for 5 °elevation angle, indicating an underestimation of the aerosol extinction in the layer close to the surface; however the magnitude of the underestimation is only about 2% based on the mean O_4 dSCD of about 1.6×10^{43} molecules^2 cm^{-5} for 5 °elevation angle. For the TG retrievals, in general the differences for high elevation angles are slightly larger than those for low elevation angles. This finding probably indicates the higher sensitivity of the inversion algorithm to lower altitudes. This is also indicated by the averaging kernels in Fig. 6b. Even so, the mean deviations of the dSCDs for the 30 ° elevation angle are only 0.28×10^{15} molecules cm^{-2} for NO_2 (mean dSCD of 2.6×10^{16} molecules cm^{-2}), 0.07×10^{15} molecules cm^{-2} for SO_2 (mean dSCD of 3.3×10^{16} molecules cm^{-2}) and 0.65×10^{15} molecules cm^{-2} for HCHO (mean dSCD of 1.6×10^{16} molecules cm^{-2}).~~

~~The mean averaging kernels (AKs) for retrievals of AE and the NO_2 VMR are shown in Fig. 6. AKs for SO_2 and HCHO are similar to NO_2 (see Fig. S14c and S15c of the supplement). They indicate that the inversions are sensitive to the layers from~~

~~the surface up to 1.5 km. The degrees of freedom (DoF) are about 1.5 for aerosols (similar to Frieß et al., 2006), 2 for NO_2 and 2.3 for SO_2 and HCHO. AKs are generally similar for different seasons (see Fig. S12d–S15d of the supplement), indicating the consistent response of the measurements to the true atmospheric state. The slight seasonality is probably related to the variation of the SZA. The same reason probably causes the weak diurnal variation of the DoF of the inversions shown in Fig. S16 of the supplement. The totally averaged~~during ~~and seasonally averaged retrieved profiles are shown in Fig. 7 together with the corresponding a priori profiles. The retrieved profiles below 1.5 km are quite different from the a priori profiles, indicating that the measurements contain sufficient information for the altitude below 1.5 km. The mean contributions of the noise and the smoothing error (this error originates from the limited resolution of the inversion) of the retrievals are shown in Fig. S12b – S15b of the supplement. The total (absolute) retrieval errors have a maximum around 1 km and decrease towards the surface. The relative errors are minimal close to the surface (10% for AE, NO_2 and SO_2, and 30% for HCHO). Most of the errors originate from the smoothing error, which largely contributes to the total error at high altitudes.~~

2.2.~~5~~ 4 Comparisons with independent data sets under clear skies

To validate the results from MAX-DOAS observations, the column densities and averaged concentrations in the lowest layer from 0 to 200m are compared to independent measurements:

(a) AODs at 380 nm (level 1.5) from the sun photometer at the AERONET (Holben et al., 1998 and 2001) Taihu station. The data is downloaded from the website of http://aeronet.gsfc.nasa.gov/. The AERONET sun photometer is located 18 km south west of the MAX-DOAS instrument. AERONET data in the period from May 2011 to October 2013 is included in the study. In the level 1.5 data, a cloud screening scheme is used to filter most of the cloud contaminated data (Smirnov et al., 2000). Here it should be ~~clarified~~noted that AERONET Taihu station is locate~~s~~d in a more remote area (from ~~the~~ downtown Wuxi) than the MAX-DOAS at Wuxi station. The different locations could contribute to a systematic bias ~~on the comparison activities~~between both data sets. However the long residence time of up to several days (Ahmed et al., 2004) and the relatively homogeneous horizontal distribution of aerosols (implied by the weak dependence of AOD on wind direction, see section 3.4.2) impl~~y~~ies that the differences between ~~two~~both measurements ~~are comparable~~should be small.

(b) Visibilities near the ground from a forward-scattering visibility meter (Manufacturer: Anhui Landun Photoelectron Co. Ltd. Model: DNQ2 forward-scattering visibility meter) (Wang et al., 2015), which is located at the same site as the MAX-DOAS instrument. The data from May 2011 to December 2013 is available.

(c) NO_2 and SO_2 VMRs (no HCHO data are available) near the ground from a long path DOAS (LP-DOAS) instrument (Qin et al., 2006) located at the same site as the MAX-DOAS instrument. The LP-DOAS is directed to the East with a total light path length of about 2km. The data from May 2011 to April 2012 is available

MAX-DOAS results are compared to the available independent measurements within 15 minute time difference.

In this section only the data recorded during clear sky conditions with low aerosol load (the sky condition is identified by MAX-DOAS observations as described in section 2.2.5) are compared ~~to the MAX-DOAS results~~ (comparisons for different cloud conditions are shown in the section 2.2.5~~6~~). For the comparisons of AODs, near-surface AEs, NO_2 and SO_2 VMRs ~~between the MAX-DOAS and the independent techniques~~, the averaged absolute differences, standard deviations, correlation coefficients (R) (Pearson's product moment correlation coefficient is applied in this paper) and the slopes and intercepts derived from the linear regressions are shown in Fig. 6 for different seasons. The histograms of the absolute differences in different seasons are ~~also~~ shown in Fig. S18 in the supplement.

For the comparisons of AODs between ~~Almost symmetrical Gaussian-shape histograms of the absolute difference of the AODs~~ from the MAX-DOAS and the AERONET sun photometer, almost symmetrical Gaussian-shape histograms of the absolute difference ~~of the AODs~~ are found for different seasons except summer (see Fig. S18a in the supplement).~~for different seasons except summer are found and shown in Fig. S17a of the supplement. The averaged absolute differences and standard deviations (indicated by the error bars) of the AODs are shown in Fig. 8a.~~ The mean differences of AODs are smaller than 0.16 (about 20% of the average value). ~~The AODs from MAX-DOAS and AERONET show~~The correlation coefficients are ~~(Pearson's product moment correlation coefficient is applied in this paper)~~ within 0.56 to 0.91 (see Fig ~~9~~6). The highest ~~coefficient~~ R of 0.91 is found in summer, probably related to the wider range of AODs covered, but in that season also the largest absolute difference of -0.16 is found probably due to the stronger aerosol load than in other seasons. Underestimation of high aerosol amounts by MAX-DOAS will be discussed in ~~session~~ section 2.2.5~~6~~. ~~In spring, there are several points (mostly in May of 2011 and 2012) above the 1:1 line. For this finding we have currently no explanation.~~

Several previous studies applied a correction factor to measured O_4 dSCDs to improve the consistency between the AODs derived from MAX-DOAS and those from AERONET (e.g. Wagner et al., 2009; ~~Clemer~~Clémer et al., 2010 and Frieß et al., 2016). ~~And so~~ So far there is no credible explanation for this correction factor. In this study we don't apply any correction factor, because we achieve reasonable consistency between MAX-DOAS and AERONET results without the application of a correction factor.

The averaged AEs in the lowest layer derived from the MAX-DOAS are compared with those from the visibility meter. Here it has to be noted that both instruments do not probe exactly the same air masses: the visibility meter is sensitive to air masses at the measurement location while the MAX-DOAS is sensitive to the air masses along the line of sight for up to several kilometres away from the instrument and up to a few hundred meters above the ground. Fig~~.~~ure ~~S17b~~ S18b ~~of~~in the supplement shows almost symmetrical Gaussian-shape histograms of the absolute differences of the AEs between the two techniques. The mean differences are < 0.18 km^{-1} (about 33% of the average value) as shown in Fig. ~~8b~~6. The highest ~~correlation coefficient~~R of 0.74 is found in summer (see Fig. 6) probably related to the wider range of values and the stronger vertical convection, which causes a higher boundary layer and possibly a smoother vertical distribution of aerosols than in other seasons ~~(see Fig. 10)~~. In spring, the worst correlation is found ~~and~~ which might be related to the occurrence of long-distance transport of dust with elevated aerosol layers (see section 3.~~2~~1).

The VMRs of NO_2 and SO_2 in the lowest layer derived from MAX-DOAS are compared with the values from LP-DOAS measurements for the individual seasons. Like for the AE, it has to be noted that both instruments do not probe exactly the same air masses; as the LP-DOAS yields the mean TG concentration for the light path defined by the set-up of instrument and reflector. In general the mean absolute differences are smaller than 5 ppb (about 50% of the average value) for NO_2 and 6 ppb (about 60 % of the average value) for SO_2 (see ~~see~~ Fig. ~~8c~~6). Almost symmetrical Gaussian-shape histograms of the absolute differences are also found for NO_2 and SO_2 in different seasons (Fig. ~~S17c~~ S18c and d ~~of~~ in the supplement). The ~~correlation coefficients~~ range of R is from 0.4 to 0.7 for NO_2 ~~(see Fig. 11)~~ and from 0.7 to 0.8 for SO_2 ~~(see Fig. 12)~~ in all seasons (see Fig. 6). The higher ~~correlation coefficients~~R for SO_2 than for NO_2 ~~are~~ is probably related to the longer lifetime and thus more homogeneous vertical and horizontal distribution of SO_2 compared to NO_2, especially in the layer from 0 to 200m. The worst correlation of NO_2, especially in the afternoon (see Fig. ~~S18~~ S19 ~~of~~ in the supplement) is found in summer probably because of the low NO_2 VMR near the surface, the small value range and the steep vertical gradient in the layer from 0 to 200m (see below). The generally positive absolute differences of NO_2 and SO_2 shown in Fig. ~~8c and d~~6 could be attributed to strong gradients in the layer from 0 to 200m as e.g. found from tower measurements in Beijing, Meng et al. (2008): they concluded that the largest values of the NO_2 and SO_2 concentrations are not directly located at the surface, but at an altitude of about 100 meters, especially in summer. However, it should be noted that the vertical gradients around Wuxi might be different from those in Beijing and thus also other reasons might contribute to the observed differences.

2.2.~~6~~ 5 Evaluations of retrievals under cloudy and strong aerosol conditions.

The retrieval of AEs by PriAM from O_4 absorptions is based on a ~~forward model~~RTM, which does not include the effects of clouds. In principle it should be possible to also include cloud effects in the ~~forward model~~RTM (at least for horizontally homogenous clouds), but in the current version of our retrieval this is not yet accomplished. In this section, we investigate how strongly different types of clouds affect the MAX-DOAS retrieval results of aerosols and TGs. For that purpose we compare the MAX-DOAS results with independent data sets for different cloud types. For the characterization of the cloud conditions we use the cloud classification scheme described in Wang et al., 2015 (based on the concept of Wagner et al., 2014) to classify the sky conditions from the MAX-DOAS observations, i.e. radiance, colour index and O_4 absorption. The scheme differentiates between eight primary sky conditions (varying between clear skies with low aerosol load to continuous cloud cover) and two secondary sky conditions of fog and optically thick clouds. In this study we condense the eight primary sky conditions to five primary conditions by merging two types of cloud holes and two types of continuous clouds and ignoring the rare condition of "extremely high midday CI" (Wang et al., 2015). The remaining five primary conditions are clear sky with low aerosol loads ("low aerosols"), clear sky with high aerosol loads ("high aerosol"), "cloud holes", "broken clouds", and "continuous clouds". Each MAX-DOAS measurement scan is assigned to one of the five primary sky conditions. In addition, they can be assigned to the two secondary sky conditions of "fog" and "optically thick clouds". Here it should be clarified that the "fog" sky condition does not exactly belong to the meteorology definition, but represents a sky

condition derived from MAX-DOAS observations with a low visibility. Another point which needs to be clarified is that distinguishing "low aerosols" and "high aerosols" is based on the colour index observed by MAX-DOAS~~, but not on the exact aerosol properties~~. Thus there is not an explicit ~~boundary of~~ AOD value which distinguishes ~~between them~~both aerosol categories. The studies of Wang et al., 2015, however, demonstrated that the AODs observed by the ~~nearby~~Taihu AERONET sun photometer are mostly smaller and larger than 0.6 for the "low aerosols" and "high aerosols", respectively. In addition to the cloud effect, also the effect of high aerosol loads is evaluated (due to the unrealistic assumption of the pdf of the atmospheric state in the OE algorithm for high aerosol loads (see Eq. (1)).

Firstly measured and modelled dSCDs (results of the forward model) are compared under various sky conditions. In Fig. ~~13~~ 7 (grey columns), the histograms of the differences between the measured and modelled dSCDs are shown for the four species (note Figure~~.~~ ~~13~~ 7 represents the differences for all non-zenith elevation angles). The histograms are symmetric and the maximum probabilities occur around zero for all four species. ~~I~~i.e., overall, there is no indication for a significant systematic retrieval bias. In the same figure, the relative frequencies for the different sky conditions are shown in different colours. In general, for cloudy sky conditions, especially for continuous clouds and optically thick clouds, larger discrepancies are found compared to cloud free sky conditions. The effect of clouds on the inversion is stronger for aerosols than for TGs. For the aerosol inversion, more negative differences are found for "fog", which indicates that the strong extinction in "fog" is not well represented by the forward model (The phenomenon is also found in Fig. ~~15~~ 9 and discussed below). To skip those inverted profiles, which probably differ largely from the real profiles, we only keep the profiles, for which the differences between measured and modelled dSCDs are smaller than 2×10^{42} molecules^2 cm^{-5} for the O_4 dSCDs (90.6% of the total observations) and 5×10^{15} molecules cm^{-2} for NO_2 (89.8%), SO_2 (90.4%), and HCHO dSCDs (97.9%) for each elevation angle in one elevation sequence.

After this screening of potentially bad profiles, the mean profiles of AEs and TG mixing ratios as well as the corresponding total averaging kernels (which ~~mean~~represent the sum of the averaging kernels at ~~each~~the individual altitudes) are shown in Fig. ~~14~~ 8 for~~-~~ different sky conditions. While the total averaging kernels differ only slightly, the resulting profiles are quite different for different sky conditions. There are two interesting findings for the retrieved profiles: first, for all cloudy scenarios (incl. fog), the maximum AE is not found at the surface, but at higher altitudes, as observed also by Nasse et al., (2015). This can be explained by the fact that clouds act as a diffusing screen. The effect on MAX-DOAS observations is that the light paths, especially for low elevation angles, become longer than for cloud-free conditions. Consequently, also increased O_4 absorptions are measured for such conditions. A similar effect can also be caused by elevated aerosol layers. Since the forward model does not explicitly include clouds, usually elevated 'cloud-induced' aerosol layers are derived in the profile inversion under cloudy conditions. The diffusing screen effect depends on the cloud optical thickness. The most pronounced cloud-induced elevated aerosol layers are retrieved for optically thick clouds.

Interestingly, also for measurements under "fog" conditions, elevated aerosol layers are obtained from the MAX-DOAS inversion. This is at first sight surprising, but can be explained by two aspects: first, for most measurements classified as "fog", still a weak systematic dependence of the O_4 dSCDs on elevation angles is found, indicating that during most "fog"

events the visibility is still not close to zero. Second, for most of the measurements classified as "fog" also the presence of clouds (including thick and broken clouds) was detected (Wang et al., 2015). This finding indicates that, for most observations classified as "fog", increased aerosol scattering close to the surface occurred indeed, but at higher altitudes, even larger extinction was present. We also found a general larger value of the cost function under cloudy conditions (consistent with Fig. ~~13~~7) and a systematic variation of the TG VCDs and near-surface VMRs for the different cloud scenarios. Besides measurement errors, these variations are probably also due to different photolysis rates and atmospheric dynamics (see Fig. ~~S19~~ S20 in the supplement).

In the following we compare the results from MAX-DOAS and other techniques under different sky conditions. Since the frequencies of different cloud conditions depend on season (Wang et al., 2015) and also the agreement~~s~~ between MAX-DOAS and other techniques ~~were~~ was found to be different for different seasons (see section 2.2.4~~5~~), the comparisons are done for individual seasons. In Fig~~s~~. ~~15 to 19~~9 the comparison results ~~for~~ in ~~autumn~~autumn are shown (similar conclusion are found for other seasons and the relevant figures are shown in Fig. ~~S20~~ S21 – ~~S23~~ S24 ~~of~~ in the supplement). Based on the comparisons of the retrieved profiles ~~for~~ under different sky conditions (Fig. ~~14~~8) and the comparison results with independent data sets (Fig~~s~~. ~~15 – 19~~9), we have developed recommendations, under which sky conditions which data product might be still useful or should better not be used. These recommendations, as summarized in Table 3, should not be seen as generally binding, but rather as a general indication of the usefulness of a given observation, and might change for improved inversion algorithms in the future.

In general we find that the aerosol results are more strongly affected by the presence of clouds than the trace gas results. This is especially true for the retrieved AOD. ~~The obviously larger~~Especially large mean difference and worse correlation are found under "continuous clouds" for AOD (Fig. 9)~~.~~, ~~A~~and also the cloud effects on the retrieved AE profiles are significant (Fig. 8a). ~~-~~Thus we recommend that retrieved AOD and AE profiles (except close to the surface) should not be used for all cloudy conditions. However, AE close to the surface can still well be retrieved under most cloudy conditions~~(~~, except for "thick clouds" ~~or~~ and~~"fog",~~ especially for "fog", because~~)~~ ~~the~~a significant increase of the mean difference and decrease of the linear correlation are found for "fog" (Fig. 9). ~~-~~ The TG results are less affected by clouds. No significant effects of clouds on the profiles of TGs are found in Fig 8c, e and g. ~~And o~~Only larger mean differences and worse linear correlations of the surface mixing ratios are found for "thick clouds" and "fog" (Fig. 9). Thus not only surface mixing ratios, but also TG profiles and tropospheric VCDs can still be well retrieved for most cloudy situations (except for thick clouds and fog). The MAX-DOAS data used in Section 3 are filtered by the recommendations listed in Table 3.

~~The~~A significant increase of the mean differences and change of the slopes are found for both ~~of~~ aerosols and TGs under "high aerosol" conditions in Fig. 9. The~~i~~s phenomenon ~~could~~probably indicates that the profile retrievals show lower accuracies than~~can not run as well as~~ under "low aerosol" conditions because of the constraint of the a-priori profiles and the assumption of Eq. (1). Meanwhile the systematic overestimation of the modelled O_4 dSCDs compared to the measured O_4 dSCDs as shown in Fig. 7 under "high aerosol" conditions also imply the ~~un well~~degraded performance. In addition, the typically stronger inhomogeneity of the horizontal and vertical distributions of aerosols and TGs in heavy aerosol pollution

events ~~could~~probably also contribute to the increased ~~of~~ discrepancies because ~~of~~ different air masses are observed by MAX-DOAS and the other techniques. ~~-~~Further studies on the evaluation and improvement of profile retrievals of MAX-DOAS under heavy aerosol pollution conditions need to be ~~done~~carried out in the future. In this study, we decide to keep the MAX-DOAS results under "high aerosol" condition in the following analysis ~~to avoid artificial effects~~because in spite of their lower accuracy they still provide important information.

2.2.~~7~~ 6 Error budgets

For the MAX-DOAS results, we derive the error estimates from different sources. Firstly we estimate the error budgets for the near surface values and column densities of the TGs and aerosols, which are summarized in Table 4. The following error sources are considered:

(a) Smoothing and noise errors (fitting error of DOAS fits) on the near-surface values and column densities are derived from the averaged error of profiles from the retrievals (shown in Fig. ~~S12b~~ S11b - S1~~5~~4b in~~of~~ the supplement), and amount on average to 10% and 6% for aerosols, 12% and 17% for NO_2, 19% and 25% for SO_2 and 50% and 50% for HCHO, respectively.

(b) Algorithm errors related to an imperfect minimum of the cost function, namely the discrepancy between the measured and modelled dSCDs. Based on the fact that measurements for 5 ° and 30 ° elevation angles are sensitive to the low and high air layers, respectively, we estimate the algorithm errors on the near-surface values and the column densities using the averaged relative differences between measured and modelled dSCDs for 5 °and 30 ° elevation angle, respectively. These errors on the near-surface values and the column densities are on average estimated at 4% and 8% for aerosols, 3% and 11% for NO_2, 4% and 10% for SO_2, 4% and 11% for HCHO, respectively.

(c) Cross section errors of O_4 (aerosols), NO_2, SO_2, and HCHO are 5%, 3%, 5% and 9%, respectively according to Thalman and Volkamer (2013), Vandaele et al. (1998), Bogumil et al. (2003) and Meller and Moortgat (2000).

(d) The errors related to the temperature dependence of the cross sections are estimated in the following way. We firstly calculate the amplitude changes of the cross sections per kelvin using two cross sections at two temperatures from the same data sets. Then the amplitude changes per kelvin are multiplied by the variation magnitude of the ambient temperature (45 ~~k~~ K during the whole measurement period, see Fig. 3). The corresponding systematic error of O_4 (aerosols), NO_2, SO_2 and HCHO are estimated to up to 10%, 2%, 3% and 6%, respectively.

(e) The errors of TGs related to the errors of aerosols are estimated at 16% for VCDs and 15% for near-surface VMRs for the three TGs according to the total error budgets of aerosol retrievals. The estimations of aerosol relevant errors are rough. A further studies need to be done to acquire a more reasonable estimation by considering aerosol properties, profiles of aerosols and TGs and observation geometries.

The total error budgets on the TGs and aerosols are given by combining all the above error sources in the bottom row of Table 4. In general the sum of the smoothing and noise error is the dominant error source in the total error budget.

The error budgets of the profiles also consist of the five (four for aerosol profiles) error sources. The error (a) depends on the height, has much larger (relative) error at high altitudes and is already shown in Fig. ~~S12b~~ S11b - ~~S15b~~ S14b ~~of~~ in the supplement. The error (b) can not be realistically estimated because of the difficulty of assigning discrepancies between measured and modelled dSCDs to each altitude of profiles. The error (c) and (d) have the identical number at all the altitudes and are same as the estimations for the near surface values and column densities above. The error (e) of TG profiles can be estimated as the total error budgets of aerosol profiles. However because of error (b) is unknown, the error (e) can not be quantified at the moment.

~~2.3 Comparisons between geometrical VCD and VCD from profile inversion~~

~~The geometric approximation (e.g. Brinksma et al., 2008) is often used to convert the dSCD for an elevation angle of α ($dSCD_{\alpha}$) to the tropospheric VCD_{geo}:~~

$$VCD_{geo} = \frac{dSCD_{\alpha}}{\frac{1}{sin(\alpha)} - 1} \quad (2)$$

~~The elevation angles between about 30 ° and 20 ° are usually used for the application of the geometric approximation (e.g., Ma et al., 2013 and Shaiganfar et al., 2011). The tropospheric VCD (VCD_{pro}) can also be derived by the vertical integration of the retrieved profiles. The relative differences ($Diff_{total}$) between VCD_{pro} and VCD_{geo} for NO_2, SO_2 and HCHO are calculated by Eq. (3):~~

$$Diff_{total} = \frac{VCD_{geo} - VCD_{pro}}{VCD_{pro}} \quad (3)$$

~~In Fig. 20, the average relative differences for elevation angles of 30 ° and 20 ° are shown as function of the relative azimuth angle (RAA), i.e. the difference between the azimuth angles of the sun and the viewing direction of the telescope. In general, the discrepancy is larger for an elevation angle of 30 ° than for 20 °. In addition, also an increase of the difference with increasing relative azimuth angle is found. Both findings have different magnitudes for the different TGs. The observed dependencies could be attributed to two reasons: first, the validity of the geometric approximation is limited, especially if the last scattering event occurs in the TG layer of interest. The respective probability depends on the layer height, wavelength, aerosol load and viewing geometry. A second reason for the observed differences is the uncertainty of the profile inversion. Some studies already reported systematic errors of the geometrical approximation:~~

~~1) Ma et al. (2013) showed that the systematic error of the NO_2 VCDs calculated by the geometrical approximation for an elevation angle of 30 °is about 20% on average, which is quite similar with the value in Fig. 20b. Also, the error is larger for larger elevation angles and larger RAA, which is also consistent with the results shown in Fig. 20a and b.~~

~~2) The simulation studies for an elevation angle of 22 ° in Shaiganfar et al. (2011) show that the error of the geometrical approximation depends on the layer height of the TGs and aerosols. They found that a higher layer of TGs leads to a larger negative error. This finding is consistent with the results shown in Fig 20e, where the largest biases are found for HCHO, which has a higher layer than NO_2 and SO_2 (see Fig. 7)~~

~~To identify the dominating error source, we split the total difference ($Diff_{total}$) between VCD_{geo} and VCD_{pro} into two parts: The first part is the difference between VCD_{geo} and VCD_{geo}^{m}. Here VCD_{geo}^{m} is calculated by applying the geometric approximation to the modelled dSCD (from the forward model of the profile inversion) for the same elevation angle. This difference describes the error from the profile inversion and is referred to as $Diff_{inversion}$:~~

~~$$Diff_{inversion} = \frac{VCD_{geo} - VCD_{geo}^{m}}{VCD_{pro}} \quad (4)$$~~

~~The second part is the difference ($Diff_{geometry}$) between VCD_{geo}^{m} and VCD_{pro}:~~

~~$$Diff_{geometry} = \frac{VCD_{geo}^{m} - VCD_{pro}}{VCD_{pro}} \quad (5)$$~~

~~$Diff_{geometry}$ describes the error due to the limitations of the geometric approximation. $Diff_{inversion}$ and $Diff_{geometry}$ are also shown in Fig. 20 with red and blue colours, respectively. It is found that $Diff_{inversion}$ is mostly smaller than 4% for the 30 ° elevation angle of and smaller than 2% for the 20 ° elevation angle. Moreover, the variation of $Diff_{total}$ along RAA is similar with $Diff_{geometry}$. Both findings clearly indicate that the error due to the limitation of the geometric approximation is the dominating error contributing to $Diff_{total}$. Moreover the systematic errors of the geometric approximation become significant when the aerosol load is large (see the section 4 of the supplement). Thus in the following, we integrate the retrieved profiles to extract the respective tropospheric VCD.~~

2.3 Comparisons between the geometrical VCD and the VCD derived from the profile inversion

The geometric approximation (e.g. Brinksma et al., 2008) is often used to convert the dSCD for an elevation angle of α ($dSCD_{\alpha}$) to the tropospheric VCD_{geo} as Eq. (2):

$$VCD_{geo} = \frac{dSCD_{\alpha}}{\frac{1}{sin(\alpha)} - 1} \quad (2)$$

~~The e~~Elevation angles between about ~~3~~20 ° and ~~2~~30 ° are usually used for the application of the geometric approximation (e.g., ~~Ma et al., 2013 and~~ Shaiganfar et al., 2011 and Ma et al., 2013). The tropospheric VCD (VCD_{pro}) can also be derived by the vertical integration of the retrieved profiles. The relative differences ($Diff_{total}$) between VCD_{pro} and VCD_{geo} for NO_2, SO_2 and HCHO are calculated by Eq. (3):

$$Diff_{total} = \frac{VCD_{geo} - VCD_{pro}}{VCD_{pro}} \quad (3)$$

In Fig. ~~20~~10, the average relative differences for elevation angles of ~~3~~20 ° and ~~2~~30 ° are shown as function of the relative azimuth angle (RAA), i.e. the difference between the azimuth angles of the sun and the viewing direction of the telescope. In general, the discrepancy is larger for an elevation angle of 30 ° than for 20 °. In addition, also an increase of the difference with increasing relative azimuth angle is found. Both findings have different magnitudes for the different TGs. The observed dependencies could be attributed to two reasons: first, the validity of the geometric approximation is limited, especially if the last scattering event occurs in the TG layer of interest. The respective probability depends on the layer height, wavelength,

aerosol load and viewing geometry. A second reason for the observed differences is the uncertainty of the profile inversion. Some studies already reported systematic errors of the geometrical approximation:

3)1) Ma et al. (2013) showed that the systematic error of the NO_2 VCDs calculated by the geometrical approximation for an elevation angle of 30 ° is about 20% on average, which is quite similar with the values shown in Fig. 1020b. Also, the error is larger for larger elevation angles and larger RAA, which is also consistent with the results shown in Fig. 2010a and b.

4)2) The simulation studies for an elevation angle of 22 ° in Shaiganfar et al. (2011) show that the error of the geometrical approximation depends on the layer height of the TGs and aerosols. They found that a higher layer of TGs leads to a larger negative error. This finding is consistent with the results shown in Fig 2010e, where the largest biases are found for HCHO, which has a higher layer height than NO_2 and SO_2 (see Fig. 137)

To identify the dominatingdominant error source, we split the total difference ($Diff_{total}$) between $\mathrm{VCD_{geo}}$ and VCD_{pro} into two parts: The first part is the difference between $\mathrm{VCD_{geo}}$ and VCD_{geo}^{m}. Here VCD_{geo}^{m} is calculated by applying the geometric approximation to the modelled dSCD (from the forward model of the profile inversion) for the same elevation angle. This difference describes the error from the profile inversion and is referred to as $Diff_{\mathrm{inversion}}$:

$$Diff_{\mathrm{inversion}} = \frac{\mathrm{VCD_{geo}} - \mathrm{VCD_{geo}^{m}}}{\mathrm{VCD_{pro}}} \quad (4)$$

The second part is the difference ($Diff_{geometry}$) between VCD_{geo}^{m} and VCD_{pro}:

$$Diff_{geometry} = \frac{VCD_{geo}^{m} - VCD_{pro}}{VCD_{pro}} \quad (5)$$

$Diff_{geometry}$ describes the error due to the limitations of the geometric approximation. $Diff_{inversion}$ and $Diff_{geometry}$ are also shown in Fig. 2010 with red and blue colours, respectively. It is found that $Diff_{inversion}$ is mostly smaller than 4% for the 30 ° elevation angle of and smaller than 2% for the 20 ° elevation angle. Moreover, the variation of $Diff_{total}$ along RAA is similar with $Diff_{geometry}$. Both findings clearly indicate that the error due to the limitation of the geometric approximation is the dominant dominating error contributing to $Diff_{total}$. Moreover the systematic errors of the geometric approximation become significant when the aerosol load is large (see the section 44 of the supplement). Thus in the following, we integrate the retrieved profiles to extract the respective tropospheric VCD. One point need to be clarified that the discrepancy of retrieved profile from the reality doesn't impact the approach, although both VCD_{pro} and VCD_{geo}^{m} are as function of the retrieved profile. Because in this case, only $Diff_{inversion}$ will increase, but $Diff_{geometry}$ will not be impacted. The increased $Diff_{inversion}$ present the large errors of the profile inversion.

3 Results and discussion

In this section, MAX-DOAS results of column densities, near-surface concentrations and vertical profiles of aerosols and TGs are shown and discussed for a) seasonal variations and inter-annual trends, b) diurnal variations, c) weekly cycles as well as wind dependencies.

~~3.1 Meteorological conditions~~

~~The ground-based weather station near the MAX-DOAS instrument records the ambient temperature, wind speed and direction, and relative humidity during the whole observation period. Fig 21 shows their seasonally mean diurnal variations. A large seasonal difference occurs only for the ambient temperature, but not for the wind speed and relative humidity. Similar diurnal variations for the three meteorology parameters are found for the different seasons. The ambient temperature and the relative humidity reach the maximum and minimum values around noon, respectively. The wind speed has the maximum value around 16:00 LT. The wind directions recorded by the same weather station are shown by the wind roses for the individual seasons in Fig. 22, indicating that the dominant wind is from the northeast in all seasons. In spring and summer the non-dominant wind directions occur more frequently than in winter and autumn.~~

3.~~2~~ 1 Seasonal variations and inter-annual trends of daytime NO_2, SO_2, HCHO and aerosols

The time series of monthly averaged (after daily averaging) TG VCDs and near-surface VMRs as well as AODs and near-surface AEs (all the data are filtered by the recommended scheme in Table 3) derived from MAX-DOAS observations are presented in Fig. ~~23~~11. Also shown are AODs and AEs obtained from AERONET and visibility meter, respectively.

Similar annual variations are found for TG VCDs and near-surface VMRs. The seasonal cycles of NO_2 and SO_2 show minimum values (NO_2 and SO_2 VCD of 9-17 $\times 10^{15}$ and 12-23 $\times 10^{15}$ molecules cm^{-2}, respectively; NO_2 and SO_2 VMR of 5-11 and 4-11 ppb, respectively) in summer and maximum values (NO_2 and SO_2 VCD of 27-35 $\times 10^{15}$ and 33-54 $\times 10^{15}$ molecules cm^{-2}, respectively; NO_2 and SO_2 VMR of 12-16 ppb and 14-18 ppb) in winter. These characteristics are already well-known over urban areas in the eastern China region (Richter et al., 2005~~,~~; Qi et al., 2012; Ma et al., 2013; Hendrick et al., 2014~~, Qi et al., 2012~~ and Wang et al., 2014a). In contrast, HCHO shows an ~~adverse seasonality~~opposite seasonality compared to NO_2 and SO_2. The HCHO VCD and near-surface VMR are 16-20 $\times 10^{15}$ molecules cm^{-2} and 4-6 ppb in summer, respectively, 7-10 $\times 10^{15}$ molecules cm^{-2} and 2-4 ppb in winter, respectively. A similar seasonality of HCHO in the eastern China region was already reported by De Smedt et al.~~, -~~(2010 and 2015).

For AOD and AE no pronounced seasonal cycle is found. The MAX-DOAS results mostly reveal similar levels like the other two techniques. Note that the data in 2014 is not available from both the AERONET Taihu station and the visibility meter. The AOD is typically larger than 0.7 and the AE typically larger than 0.5 km^{-1}. Note that the extremely low values in July

and August of 2013 are unrepresentative because of low statistics caused by the temporal shutdown of the instrument (see Fig. ~~23c~~11c).

The observed seasonal variations of the different species are related to various processes: the seasonal variation~~s~~ of source emissions, chemical (trans-) formation and destruction, dry and wet deposition, and atmospheric transport~~The observed seasonal variations of the different species are related to three factors: the seasonal variation of emissions (or chemistry formation mechanism), removal mechanisms, and atmospheric transports~~ (Wang et al., 2010; Lin et al., 2011). Different from the column densities, the near-surface concentrations of all species can be systematically affected by the seasonality of the boundary layer (BL) height (Baars et al., 2008). The compression effect of the lower BL height in winter than in summer systematically increases the near-surface concentrations.

The details for the different species are discussed as follows:

1) NO_2 and SO_2

NO_2 (rapidly formed from NO_x after its emission) and SO_2 originate mostly from direct emissions. It is assumed that about 94% of total NO_x emission in the Wuxi region is emitted from the power plants, industrial fuel combustions and vehicles (Huang et al., 2011), which emit similar amounts in different seasons. The contribution of boilers for the seasonal use of domestic heating to NOx is only about 5% (Huang et al., 2011). Thus the seasonal variation of the MAX-DOAS results cannot be explained by the variation of the NO_x emissions. However, the SO_2 emissions might vary by about 20% due to the significant contribution of ~~seasonal use of~~ boilers ~~for domestic heating~~ (Huang et al., 2011). Because of the short lifetime of NO_x under urban pollution (~~about some~~usually a few hours, e.g. Beirle et al., 2011 and Liu et al., 2015), most NO_x should ~~be~~ originate from local emissions (Liu et al., 2015), and NO_x~~x~~ long-range transport could be negligible in Wuxi. It needs to be noted that because of the longer life time of NO_x~~x~~ in winter (Schaub et al., 2015) than in summer, transport of NO_2 from a nearby pollution area in winter might play a role on the seasonality of NO_2. Due to the large range of SO_2 residence time (from less than one hour to 2 weeks and longer in winter than in summer, e.g. von Glasow et al., 2009; Lee et al., 2011; Beirle et al., 2014), transport from the highly polluted regions in the east and north likely play a role, especially in winter. Here it is interesting to note that indications for long range transport of SO_2 are also found in the elevated SO_2 profiles in winter as shown in Fig ~~25b~~13b. Because of the strong seasonal variation of the SO_2 emissions due to domestic heating in the North (Wang et al., 2014a), long range transport from these regions could strongly impact the SO_2 amount in Wuxi in winter, thus contributing to the seasonality. In conclusion, the seasonality of NO_2 can be mostly attributed to the removal mechanisms due to the OH radical, which has a minimum in winter and maximum in summer (Stavrakou et al., 2013). The same removal mechanism could be partly responsible for SO_2 seasonality (Lee et al., 2011). Additional heterogeneous reactions (Oppenheimer et al., 1998) might also play a role. Since we find a high correlation between the NO_2 and SO_2 VCDs and near surface VMRs (see Fig. ~~S24~~ S26 ~~of~~in the supplement), we conclude that also for SO_2 the seasonality of the removal mechanism is the most important factor controlling the seasonality of the SO_2 VCDs and near-surface VMRs.

2) HCHO

HCHO originates mainly from the oxidation degradation of many VOCs by the OH radical. But because the OH radical also plays a role in the removal mechanism of HCHO, the seasonal variation of the OH radical level contributes to the seasonality of HCHO in a complex way. Apart from the ubiquitous background levels of HCHO from the methane oxidation, emissions of non-methane VOCs (NMVOCs) (including HCHO) from biogenic sources, biomass burning and anthropogenic sources control local HCHO concentrations. Therefore, in addition to the seasonality of OH, also the seasonal variations of the VOC emissions should be important factors for the HCHO seasonality. Firstly stronger biogenic emissions are expected in the growing period, namely from spring to autumn. Based on a study in Beijing (Xie et al., 2008) a relative contribution of biogenic emissions to the total VOC levels is estimated at about 13%. Secondly, biomass burning events frequently occur in May and June (Cheng et al., 2014) in the Wuxi region. Thirdly anthropogenic emissions contribute a lot to the VOCs amounts. However the dominating sources, such as non-combustion industrial processes and vehicles (Huang et al., 2011), do not show an obvious seasonality. Thus, their effect on the HCHO seasonality can be probably ignored. Fourth, biogenic primary emissions of HCHO could be another factor contributing to the HCHO seasonality due to its significant differences between in summer and winter (Chen et al., 2014).

3) Aerosols

The local aerosol sources, including primary aerosol emissions and secondary aerosol formations, and transport of aerosols can in principle both contribute to the local aerosol amount. The contribution of transported aerosols has an obvious seasonality: In May and June, the transport from biomass burning might contribute to up to 37% of the $PM_{2.5}$ amount based on a case study in summer 2011 (Cheng et al., 2014). In spring and autumn dust storms from Mongolia can reach Wuxi (Liu et al., 2012; Fu et al., 2014b and Li et al., 2014). The polluted air from the eastern area (for example, Shanghai) and northern area (for example Jing–Jin–Ji region) (Jiang et al., 2015) could also move to Wuxi under appropriate meteorological conditions (Liu et al., 2012). Haze events frequently occur in autumn and winter (Fu et al., 2014a).

The inter-annual trends of TGs and aerosols are presented in Fig. ~~24~~12. Because of missing observations in some months and inner-annual variations of abundances of the species, only data in May to November are used. SO_2 shows a clear decreasing trend from 2011 to 2014. However NO_2, HCHO and aerosols almost maintain constant amounts.

The monthly mean profiles of NO_2, SO_2 and HCHO (under clear and cloudy sky conditions except thick clouds and fog) and aerosols (only under clear sky conditions) (screened by the scheme in Table 3) are presented in Fig. ~~25~~13. The monthly mean TG profiles under clear sky conditions (see Fig. ~~S25~~ S27 ~~of~~ in the supplement) are almost identical to those under various sky conditions except fog and thick clouds ~~in Fig. 25~~. During all seasons, NO_2 shows an exponentially decreasing profile (see Fig. ~~25a~~13a). On average the NO_2 VMR at 0.5 km is about half of the near-surface VMR and it rapidly decreases above 0.5km to about 2 ppb at 1.5 km. Aircraft measurements of NO_x in October 2007 in the Yangtze River Delta region by Geng et al. (2009) presented similar vertical profiles. The profile shape of NO_2 can be mostly attributed to its near-surface emission sources and short life time.

The SO_2 layer is found at a higher altitude compared to NO_2 (see Fig. 13~~25~~b). A more box-like shape up to the altitude of about 0.7km to 1km is found in autumn and winter when the SO_2 load is large and also long-range transport might

effectively contribute to the SO_2 amounts in Wuxi. In contrast, for the rather small SO_2 loads in summer, an exponential profile shape is found. Similar profile shapes are also obtained from aircraft measurements during September to October of 2007 over Wuxi (Xue et al., 2009). One interesting finding is the lofted SO_2 layer at around 0.7 km in February and March 2012, which is probably related to long distance transport from a heavily polluted region. This interpretation is supported by the dominating wind direction (coming from the nearby polluted area around Shanghai) in March 2012 (see Fig. ~~S26~~ S28 of the supplement) compared to other years.

In all seasons, the HCHO profile shape consists of three parts (see Fig. ~~25c~~13c): a decrease from the surface to about 0.3 km, an almost constant value from about 0.3 km to about 1.1 km, and a steep decrease above. The high values at the surface are probably caused by primary emissions and rapid formation from particular VOCs near the surface. Transport of longer lived VOCs to higher altitudes and subsequent destruction probably contributes to the increased values at up to about 1 km. While other measurements of tropospheric profiles of HCHO are not available around Wuxi, it is still reasonable to compare our results with the aircraft measurements of HCHO over Bresso near Milano during summer of 2003 (Junkermann, 2009; Wagner et al., 2011) because both of the measurements took place in polluted urban regions. They found a layer height with high HCHO concentration values of up to 1km and the highest values were found normally close to the ground. This feature is consistent with our results in Wuxi. However it should be noted that VMRs of HCHO at high altitudes ~~could~~are strongly ~~be~~ constrained by the a-priori profiles because of the low sensitivity of MAX-DOAS retrievals at these altitudes. More comparisons studies with aircraft measurements need to be done in the future to ~~verify the retrievals~~further quantify the retrieval sensitivities for elevated layers. Nevertheless we still have confidence on the extensively vertical distribution of HCHO retrieved by MAX-DOAS because of two reasons: 1) the Fig. S9 in the supplement indicates the higher vertical extension can be partly represented even for using an exponential a-priori profile; 2) the large variability of HCHO VMRs at the altitude around 1km is retrieved from MAX-DOAS observations. It indicates the sensitivity of MAX-DOAS retrievals to the elevated layers is still well.

Figure~~.~~ ~~25d~~ 13d shows the aerosol profiles representing a box-like shape near the surface and an exponential decrease above 0.5 to 1 km. The box-like part in winter is systematically lower than in other seasons probably due to the lower BL in winter. Baars et al. (2008) reported such a seasonal dependence of the top height of the BL obtained by lidar observations in Germany over a one-year period. A similar seasonal dependence of the BL can be expected in Wuxi. From May to October the highest aerosol extinction is found at an elevated altitude of up to 0.7km, especially in 2014. This feature could indicate long distance transports of aerosols, probably from biomass burning events.

3.~~3~~ 2 Diurnal variations of NO_2, SO_2, HCHO and aerosols

Figure~~.~~ ~~26~~ 14 shows the seasonally averaged diurnal variations of TG VCDs and near-surface VMRs as well as AODs and near-surface AEs from 2011 to 2014. The morning and afternoon averaged profiles of aerosols and TGs are also shown in

winter and summer, respectively, in Fig. ~~S27~~ S29 ~~of~~ in the supplement. The diurnal variations can probably be attributed to the complex interaction of the primary and secondary sources, depositions and atmospheric transport processes in the BL. The diurnal variation of the BL height (Baars et al., 2008) can systematically affect the diurnal patterns of near-surface VMRs and AEs, but has almost no impact on the TG VCDs and AOD.

As seen in Fig. ~~26a~~14a, the seasonality of the diurnal variation of the NO_2 VCDs is quite similar to the MAX-DOAS observations in Beijing (Ma et al., 2013). They conclude that the phenomenon is probably caused by the complex interplay of the emission, chemistry and transport, with generally higher emission rates and a longer NO_2 lifetime in winter. In Fig. ~~26b~~14b, the SO_2 VCD shows almost constant values during the whole day in summer (with a slight decrease in the afternoon). In winter high values persist until 13:00 LT and then rapidly decrease. In autumn and spring the highest values occur around noon. The SO_2 variation mostly happens in the layer below 0.5 km (see Fig. ~~S27~~ S29 ~~of~~ in the supplement). The variation features are different from the observations in Beijing (Wang et al., 2014a), probably caused by different sources, transport and life time at the two locations. In Fig. ~~26c~~ 14c it is shown that the HCHO VCDs increase rapidly after sunrise with a faster increase in summer. HCHO has a stronger variation at the layer from 0.5km to 1km. This diurnal pattern is probably mainly related to the photochemical formation of HCHO and the VOCs emitted by vehicles and biogenic emissions (Kesselmeier and Staudt, 1999). In Fig. ~~26d~~ 14d similar relative diurnal variations of AODs and AE are found for the different seasons. Their diurnal variations can be affected by various factors, e.g. ~~source~~the diurnal variation of the emission sources, as well as secondary formation, ~~and~~ deposition and dispersion. ~~The decrease of AOD from sunrise to around 9:00 LT might be caused by the decrease of the relative humidity after sunrise as shown in Fig. 21c. The increase of AOD from about 9:00 LT to noon might be caused by the photochemical formation of second aerosol particles. The decrease of AOD in the afternoon might indicate a reduced formation reaction rate.~~

3.~~4~~ 3 Weekly cycles of NO_2, SO_2, HCHO and aerosol extinction

In urban areas, anthropogenic sources often control the amounts of pollutants. Because human activities are usually strongest during the working days, weekly cycles of NO_2, SO_2, HCHO and aerosols can provide information on the contributions from natural and anthropogenic sources (Beirle et al., 2003 and Ma et al., 2013). As shown in Fig. ~~27~~S30 in the supplement, weekly cycles are found for NO_2 and SO_2. The relative differences of the VCDs and near-surface VMRs between the average working day level (from Monday to Friday) and the value on Sunday are 11% and 18% for NO_2, 13% and 11% for SO_2, respectively. For HCHO smaller weekly cycles (7% of VCD and 12% of near-surface VMR) are found.~~:~~ ~~In~~ In contrast, no clear weekend reduction is found for aerosols. The negligible weekly cycle of aerosols is probably caused by the rather long life time of aerosols and the effect of long-range transport, e.g. from biomass burning and dust. Figure~~.~~ ~~S28~~ S31 of the supplement shows that the diurnal variations of the three TGs are almost the same on different days of a week indicating similar sources during the working days and weekends.

3.~~5~~ 4 Source analysis of the pollutants

3.~~5~~4.1 Relation between the precursors and aerosols

Huang et al. (2014) showed that secondary aerosols including organic and inorganic aerosols (nitrates and sulfates) contribute to about 74% of the $PM_{2.5}$ mass collected during high pollution events in January 2013 at the urban site of Shanghai. The aerosols in Wuxi (which is close to Shanghai) ~~is~~ are expected to be similarly dominated by secondary aerosol ~~as in Shanghai.have similar properties.~~ NO_x ~~(NO_2 and NO)~~ and SO_2 are the precursors of secondary inorganic aerosols through their conversion into nitrates and sulfates, respectively. HCHO can be used as a proxy for the local amount of VOCs, which are precursors of secondary organic aerosols (Claeys et al., 2004). To ~~characterize~~identify the domina~~t~~ent precursor~~s~~, ~~W~~we ~~have~~ investigated the relationship between aerosols and their precursors through a correlation study as in Lu et al. (2010), Veefkind et al. (2011) and Wang et al. (2014a). Table 5 lists the correlation coefficients between the TG VCDs and AODs as well as the TG VMRs and AEs near the surface. The correlations of near-surface values are always higher than those of the column densities. This finding could be probably explained by the effect of long-range transport, which typically occurs at elevated layers. For long-range transport, ~~primary aerosols might be dominating, e.g. dust, and~~ the effect of different atmospheric lifetimes is especially large probably leading to weaker correlations between the aerosol and its precursors. In contrast, close to the surface, local emissions dominate the concentrations of TG and aerosols and the effect of different lifetimes is negligible.

In general, correlations in spring are the worst probably due to the transport of dust and biomass burning aerosols. The correlations between aerosols and HCHO are higher in winter than in summer. This finding may be explained by the fact that anthropogenic emissions dominate the (primary and secondary) sources of HCHO and aerosols simultaneously in winter. Meanwhile the correlations between aerosols and HCHO are higher than those between aerosols and NO_2 or SO_2 in winter and autumn. This finding can be possible explained by the fact that both HCHO and aerosols are dominated by secondary sources, while NO_2 and SO_2 are mostly from primary emissions in this region.

3.~~5~~4.2 Wind dependence of the pollutants

The MAX-DOAS station is located on the boundary of the urban and suburban areas as shown in Fig. 1b. Several iron factories, cement factories, and petroleum industries are operated in the south-west industrial area. The industrial activities and vehicle operations in the industrial area lead to significant emissions of NO_2, SO_2, VOCs as well as aerosols (Huang et al., 2011). In the urban centre area, traffic, construction sites and other anthropogenic emissions emit significant amounts of NO_2, VOCs as well as particles. Some factories, such as an oil refinery, are located in the north-west of the urban centre, emitting pollutants including SO_2 and VOCs. In addition, one power plant located at about 50km in the north and the Suzhou city in the south-east direction of the MAX-DOAS station might contribute to the observed pollutants in Wuxi depending on the meteorological condition.

We analysed the distributions of column densities and near-surface values of the TGs and aerosols for different wind directions in Fig. ~~28~~15. In principle, the near surface pollutants are expected to be dominated by nearby emission sources, while the column densities can be additionally affected by transport of pollutants from remote sources. Long-range transport can weaken the dependence of the column densities on the wind direction because of the complex trajectories the air masses might have followed. For all four species, the highest values are observed for south-westerly winds, especially for the near-surface pollutants. This finding implies that the industrial area emits large amounts of NO_x, SO_2, VOCs and aerosols. Fig. ~~28c~~ 15c shows that the HCHO southwest peak is only present in winter. This finding is probably caused by the fact that in winter anthropogenic sources (of precursors and direct HCHO emissions) dominate the HCHO amounts, while in other seasons natural sources dominate the HCHO amounts. Another peak of NO_2 and SO_2 is found in the northwest, obviously in winter, indicating considerable emissions in the urban centre. Fig ~~28d~~ 15d shows a weaker dependence of AODs on the wind direction than the VCDs of the TGs, which probably indicates the stronger contribution of long-range transport to the local aerosol levels compared to the TGs. In addition for daily averaged wind speed of smaller than 1 m/s, the averaged TGs VCDs and near-surface VMRs are higher than those for larger wind speeds (shown in Fig. ~~29a~~ S32a and b~~and b~~), indicating that dispersion of local emissions is more important than the transport from distant sources. For aerosols, a wind speed dependency is only observed for near-surface AEs, but not for AODs (see Fig. S~~29c~~32c), indicating the higher importance of transport for aerosols than for TGs.

Although this study is local and rough, it still shows several general and important results: 1) the dependence of the measured TG VMRs on the wind direction indicates that the dominating sources of the pollutions are local, but not from the long range transport. Also, strong horizontal gradient appears. Because of the expected similar life time, meteorological conditions and emission sources, the conclusion could fit to the whole YRD region. 2) The study provides an example on how to use ground-based MAX-DOAS observations to find strong emission sources in an urban-size area. 3) The seasonality of the wind dependence of the trace gases, especially for HCHO, indicates the different sources in different seasons.

4 Conclusions

The long-term characteristics of the spatial and temporal variation of NO_2, SO_2, HCHO and aerosols in Wuxi (part of the Yangtze River delta region) are characterized by automatic MAX-DOAS observations from May 2011 to Dec 2014. The PriAM OE-based algorithm was applied to the MAX-DOAS observations to acquire vertical profiles, VCDs (AODs) and near-surface VMRs (AEs) of TGs (aerosols) in the layer from the surface to an altitude of about ~~3~~ 4 km.

The AODs and near-surface AEs and the VMRs of NO_2 and SO_2 from MAX-DOAS are compared with coincident data sets (for one year) obtained by a sun photometer at the AERONET Taihu station, a nearby visibility meter and a LP-DOAS, respectively. In general good agreement was found: ~~Under~~ under clear sky conditions, correlation coefficients of 0.56–0.91 for AODs, 0.31–0.71 for AEs, 0.42–0.64 for NO_2 VMRs and 0.68–0.81 for SO_2 VMRs as well as the low systematic bias of

-0.16−0.029 (<20%) for AODs, 0.05−0.19 ~~-~~km^{-1} (<33%) for AEs, -2.23−5.11 ppb (<50%) for NO_2 VMRs and 1.8−6.1 ppb (<60%) for SO_2 VMRs are found in different seasons.

Further comparisons were performed for different cloud conditions identified by the MAX-DOAS cloud classification scheme ~~(Wagner et al., 2014 and Wang et al., 2015)~~. For most cloud conditions (except optically thick clouds and fog) similar agreement as for clear sky conditions is found for the results of near-surface TG VMRs and AEs. However, the AOD results are more strongly affected by clouds and we recommend to only ~~retrieve~~retrieving near-surface AEs for cloudy observations. In the presence of fog and optically thick clouds, no meaningful profile inversions for TGs and aerosols are possible. Thus for further interpretations, we considered TG results and near-surface AEs for clear and cloudy sky conditions (except fog and optically thick clouds), but AOD only for clear sky conditions.

In this study we also investigated two important aspects of the MAX-DOAS data analysis: For the first time the effect of the seasonality of temperature and pressure on the MAX-DOAS retrievals of aerosols was investigated. Such an effect is especially important for the measurements in Wuxi, because strong and systematic variations of temperature and pressure are regularly found. Accordingly the O_4 VCD changes systematically with seasons, which was in our study for the first time explicitly taken into account for the aerosol profile retrieval. It was shown that without this correction, deviations of the AOD of up to 20% can occur.

Moreover, we systematically compared trace gas VCDs derived either by the so-called geometric approximation with those derived by integration of the derived vertical profiles. Such discrepancies were reported in previous studies. We could show that the difference between both methods can be clearly assigned to limitations of the geometric approximation. This error becomes especially significant when the aerosol load is strong, which is the situation in most industrialised regions. Thus we conclude that in general the integration of the retrieved profiles is the more exact way to extract the tropospheric TG VCDs, and we used this method in this study.

A prominent seasonality of all TGs is found in agreement with many previous studies based on satellite and ground-based observations. NO_2 and SO_2 have maxima and minima in winter and summer, respectively, while HCHO has an ~~adverse seasonality~~opposite seasonality. No pronounced seasonality of aerosols is found. From 2011 to 2014, only SO_2 shows a clear decreasing trend, while NO_2, HCHO and aerosol levels stay almost constant.

Different profile shapes are found for the different species: for NO_2 exponentially decreasing profiles with a scale height of about 0.6km are observed in different seasons. SO_2 profiles extend to slightly higher altitudes than NO_2, probably due to the longer lifetime of SO_2. Especially in winter often elevated layers of enhanced SO_2 are found between about 0.7km and 1km (especially in early 2012), probably indicating the importance of long range transport of SO_2. HCHO reaches up to even higher altitudes (up to > 1 km) than NO_2 and SO_2, probably indicating the effect of the secondary formation from VOCs. However, typically the largest HCHO VMRs are still found near the surface (like for NO_2 and SO_2). The aerosol profiles typically show constant values close to the surface (below about 0.5km), but decrease exponentially above that layer. Especially in winter often elevated layers (between 0.5km and 0.7km) are observed.

Different diurnal variations are found for the different species: For the NO_2 VCDs, depending on season, a decrease or increase is found during the day. For the NO_2 VMRs and SO_2 VCDs and VMRs, typically a slight decrease during the day is observed. The diurnal variations of HCHO and aerosols are more complex and show a pronounced maximum around noon in summer indicating photochemical production. Systematic weekly cycles occur for NO_2 and SO_2 with the maximum values on Thursday or Friday and minimum values on Sunday indicating a large contribution of anthropogenic emissions. In contrast, the amplitudes of the weekly cycles for HCHO and aerosols are rather small.

We performed correlation analyses between the different TG results versus the aerosol results for individual seasons. For all TGs and seasons positive correlations (correlation coefficient between 0.12 and 0.65) were found with the highest correlations in winter. In general the highest correlation is found for HCHO in winter probably indicating a similar secondary formation process for both species. In general, higher correlations are found for the near-surface products (VMRs versus AE) compared to the column products (VCDs versus AOD).

We found a clear wind direction dependence of TG and aerosols results, especially for the near-surface concentrations. The dependencies indicate that the largest sources of the observed pollutants in Wuxi are anthropogenic emissions from the nearby industrial area (including traffic emissions). In addition the obvious lower TG results for ~~a~~ high wind speed than for ~~a~~ low wind speed indicate that the dispersion of local emissions is more important than the transport from distant sources. Interestingly, for HCHO, a considerable dependence on the wind direction is only observed in winter probably indicating significant VOC emissions from natural sources in the growing seasons.

The data sets of the TGs and aerosols are also valuable to validate tropospheric products from satellite observations and chemical transport models. This study is in progress.

Acknowledgements: We thank the Wuxi CAS Photonics Co. Ltd for their contributions to operate the observations of the MAX-DOAS instrument, the long path DOAS instrument, the visibility meter and the weather station in Wuxi. We thank the Institute of Remote Sensing / Institute of Environmental Physics, University of Bremen, Bremen, Germany for their freely accessible radiative transfer model SCIATRAN. We thank Belgian Institute for Space Aeronomy (BIRA-IASB), Brussels, Belgium for their freely accessible WINDOAS software and generating the mean map of SO_2 and HCHO tropospheric VCDs derived from OMI observations over eastern China. We thank Goddard Space Flight Center, NASA for their freely accessible archive of AERONET data. We thank Prof. Ma Ronghua in Nanjing Institute of Geography & Limnology Chinese Academy of Sciences for his effort to operate the Taihu AERONET station. We thank Royal Netherlands Meteorological Institute for their freely accessible archive of OMI tropospheric NO_2 data. We thank Trissevgeni Stavrakou in BIRA-IASB, Hang Su and Ya~~ng~~fang Cheng in MPIC for their help to interpret the correlations between aerosols and the trace gases. This work was supported by Max Planck Society-Chinese Academy of Sciences Joint Doctoral Promotion Programme, and National Natural Science Foundation of China (Grant No.: 41275038 and 41530644) and Monitoring and Assessment of Regional air quality in China using space Observations, Project Of Long-term sino-european co-Operation (MarcoPolo), FP7 (Grant No: 606953).

References

Aliwell, S. R., Van Roozendael, M., Johnston, P. V., Richter, A., Wagner, T., Arlander, D. W., Burrows, J. P., Fish, D. J., Jones, R. L., Tørnkvist, K. K., Lambert, J.-C., Pfeilsticker, K., and Pundt, I.: Analysis for BrO in zenith-sky spectra: An intercomparison exercise for analysis improvement, J. Geophys. Res., 107, D140, doi:10.1029/2001JD000329, 2002.

Ahmed, A.A., Mohamed, A., Ali, A.E., Barakat, A., El-Hady, M.A. and El-Hussein, A.: Seasonal variations of aerosol residence time in the lower atmospheric boundary layer, Journal of environmental radioactivity, 77(3), 275-283, 2004.

Baars, H., Ansmann, A., Engelmann, R., and Althausen, D.: Continuous monitoring of the boundary-layer top with lidar, Atmos. Chem. Phys., 8, 7281-7296, doi:10.5194/acp-8-7281-2008, 2008.

Beirle, S., Platt, U., Wenig, M., and Wagner, T.: Weekly cycle of NO_2 by GOME measurements: a signature of anthropogenic sources, Atmos. Chem. Phys., 3, 2225–2232, doi: 10.5194/acp-3-2225-2003, 2003.

Beirle, S., Boersma, K. F., Platt, U., Lawrence, M. G., and Wagner, T.: Megacity emissions and lifetimes of nitrogen oxides probed from space, Science, 333, 1737–1739, 2011.

Beirle, S., Hörmann, C., Penning de Vries, M., Dörner, S., Kern, C., and Wagner, T.: Estimating the volcanic emission rate and atmospheric lifetime of SO2 from space: a case study for Kīlauea volcano, Hawai`i, Atmos. Chem. Phys., 14, 8309-8322, doi:10.5194/acp-14-8309-2014, 2014.

Bobrowski, N., Honninger, G., Galle, B. and Platt, U.: Detection of bromine monoxide in a volcanic plume, Nature, 423, 273–276, 2003.

Boersma, K. F., Eskes, H. J., Veefkind, J. P., Brinksma, E. J., van der A, R. J., Sneep, M., van den Oord, G. H. J., Levelt, P. F., Stammes, P., Gleason, J. F. and Bucsela, E. J.: Near-real time retrieval of tropospheric NO2 from OMI, Atmos. Chem. Phys., 7, 2103–2118, 2007.

Boersma, K.F., H.J. Eskes, R. J. Dirksen, R. J. van der A, J. P. Veefkind, P. Stammes, V. Huijnen, Q. L. Kleipool, M. Sneep, J. Claas, J. Leitao, A. Richter, Y. Zhou, and D. Brunner, An improved retrieval of tropospheric NO2 columns from the Ozone Monitoring Instrument, Atmos. Meas. Tech. , 4, 1905-1928, 2011.

Bogumil, K., Orphal, J., Homann, T., Voigt, S., Spietz, P., Fleischmann, O. C., Vogel, A., Hart-mann, M., Kromminga, H., Bovensmann, H., Frerick, J., and Burrows, J. P.: Measurements of molecular absorption spectra with the SCIAMACHY pre-flight model: instrument characterization and reference data for atmospheric remote-sensing in the 230–2380 nm region, J. Photoch. Photobio. A, 157, 167–184, 2003.

Brinksma, E. J., Pinardi, G., Volten, H., Braak, R., Richter, A., Schönhardt, A., van Roozendael, M., Fayt, C., Hermans, C., Dirksen, R. J., Vlemmix, T., Berkhout, A. J. C., Swart, D. P. J., Oetjen, H., Wittrock, F., Wagner, T., Ibrahim, O. W., de Leeuw, G., Moerman, M., Curier, R. L., Celarier, E. A., Cede, A., Knap, W. H., Veefkind, J. P., Eskes, H. J., Allaart, M., Rothe, R., Piters, A. J. M., and Levelt, P. F.: The 2005 and 2006 DANDELIONS NO_2 and aerosol intercomparison campaigns, J. Geophys. Res., 113, D16S46, 2008.

Chen, W. T., Shao, M., Lu, S. H., Wang, M., Zeng, L. M., Yuan, B., and Liu, Y.: Understanding primary and secondary sources of ambient carbonyl compounds in Beijing using the PMF model, Atmos. Chem. Phys., 14, 3047-3062, doi:10.5194/acp-14-3047-2014, 2014.

Cheng, Z., Wang, S., Fu, X., Watson, J. G., Jiang, J., Fu, Q., Chen, C., Xu, B., Yu, J., Chow, J. C., and Hao, J.: Impact of biomass burning on haze pollution in the Yangtze River delta, China: a case study in summer 2011, Atmos. Chem. Phys., 14, 4573-4585, doi:10.5194/acp-14-4573-2014, 2014.

Claeys, M., Graham, B., Vas, G., Wang, W., Vermeylen, R., Pashyn-ska, V., Cafmeyer, J., Guyon, P., Andreae, M. O., Artaxo, P., and Maenhaut, W.: Formation of secondary organic aerosols through photooxidation of isoprene, Science, 303, 1173–1176, 2004.

Clémer, K., Van Roozendael, M., Fayt, C., Hendrick, F., Hermans, C., Pinardi, G., Sperr, R., Wang, P., and De Maziere, M.: Multiple wavelength retrieval of tropospheric aerosol optical properties from MAXDOAS measurements in Beijing, Atmos. Meas. Tech., 3, 863–878, 2010.

Crippa, M., Ciarelli, G., Piazzalunga, A., Schwikowski, M., Abbaszade, G., Schnelle-Kreis, J., Zimmermann, R., An, Z., Szidat, S., Baltensperger, U., El Haddad, I., and Prevot, A. S.: High secondary aerosol contribution to particulate pollution during haze events in China, Nature, 514, 218–222, 2014.

De Smedt, I., Stavrakou, T., Müller, J. F., van der A, R. J., and Van Roozendael, M.: Trend detection in satellite observations of formaldehyde tropospheric columns, Geophys. Res. Lett., 37(18), L18808, doi:10.1029/2010GL044245, 2010.

De Smedt, I., Stavrakou, T., Hendrick, F., Danckaert, T., Vlemmix, T., Pinardi, G., Theys, N., Lerot, C., Gielen, C., Vigouroux, C., Hermans, C., Fayt, C., Veefkind, P., Müller, J.-F., and Van Roozendael, M.: Diurnal, seasonal and long-term variations of global formaldehyde columns inferred from combined OMI and GOME-2 observations, Atmos. Chem. Phys., 15, 12519-12545, doi:10.5194/acp-15-12519-2015, 2015.

Environmental Protection Agency: National air quality and emissions trends report 1998, Rep. EPA 454/R-00-003, 1998.

Erle F., Pfeilsticker K., Platt U, On the influence of tropospheric clouds on zenith scattered light measurements of stratospheric species, Geophys. Res. Lett., 22, 2725-2728, 1995.

Fayt, C. and van Roozendael, M.: WinDOAS 2.1 Software User Manual, IASB/BIRA (http://www.oma.be/GOME/GOMEBrO/WinDOAS-SUM-210b.pdf), 2009.

Frieß, U., Monks, P. S., Remedios, J. J., Rozanov A., Sinreich R., Wagner T., and Platt, U.: MAX-DOAS O_4 measurements: A new technique to derive information on atmospheric aerosols: 2. Modeling studies, J. Geophys. Res., 111, D14203, 2006, doi:10.1029/2005JD006618.

Frieß U, Sihler H, Sander R. The vertical distribution of BrO and aerosols in the Arctic: Measurements by active and passive differential optical absorption spectroscopy, J. Geophys. Res., 116, D00R04, 2011.

Frieß, U., Klein Baltink, H., Beirle, S., Clèmer, K., Hendrick, F., Henzing, B., Irie, H., de Leeuw, G., Li, A., Moerman, M. M., van Roozendael, M., Shaiganfar, R., Wagner, T., Wang, Y., Xie, P., Yilmaz, S., and Zieger, P.: Intercomparison of aerosol extinction profiles retrieved from MAX-DOAS measurements, Atmos. Meas. Tech. Discuss., doi:10.5194/amt-2015-358, 2016.

Fu, X., Wang, S., Zhao, B., Xing, J., Cheng, Z., Liu, H., and Hao, J.: Emission inventory of primary pollutants and chemical speciation in 2010 for the Yangtze River Delta region, China, Atmos. Environ., 70, 39–50, doi:10.1016/j.atmosenv.2012.12.034, 2013.

Fu, G. Q., Xu, W. Y., Yang, R. F., Li, J. B., and Zhao, C. S.: The distribution and trends of fog and haze in the North China Plain over the past 30 years, Atmos. Chem. Phys., 14, 11949-11958, doi:10.5194/acp-14-11949-2014, 2014a.

Fu, X., Wang, S. X., Cheng, Z., Xing, J., Zhao, B., Wang, J. D., and Hao, J. M.: Source, transport and impacts of a heavy dust event in the Yangtze River Delta, China, in 2011, Atmos. Chem. Phys., 14, 1239-1254, doi:10.5194/acp-14-1239-2014, 2014b.

Geng, F., Zhang, Q., Tie, X., Huang, M., Ma, X., Deng, Z., Yu, Q., Quan, J., Zhao, C.: Aircraft measurements of O3, NOx, CO, VOCs, and SO2 in the Yangtze River Delta region. Atmospheric Environment, 43(3), 584-593, 2009.

Hartl, A. and Wenig, M. O.: Regularisation model study for the least-squares retrieval of aerosol extinction time series from UV/VIS MAX-DOAS observations for a ground layer profile parameterisation, Atmos. Meas. Tech., 6, 1959-1980, doi:10.5194/amt-6-1959-2013, 2013.

Hendrick, F., Müller, J.-F., Clémer, K., Wang, P., De Mazière, M., Fayt, C., Gielen, C., Hermans, C., Ma, J. Z., Pinardi, G., Stavrakou, T., Vlemmix, T., and Van Roozendael, M.: Four years of ground-based MAX-DOAS observations of HONO and NO2 in the Beijing area, Atmos. Chem. Phys., 14, 765-781, doi:10.5194/acp-14-765-2014, 2014.

Hendrick, F., Gielen, C., Lerot, C., Stavrakou, T., De Smedt, I., Fayt, C., Hermans, C., Müller, J. F., Pinardi, G., Volkamer, R., Wang, P., and Van Roozendael, M.: Retrieval of CHOCHO from MAX-DOAS measurements in the Beijing area, 7th DOAS workshop 2015, Brussels, Belgium, 7 July 2015.

Henyey, L. G. and Greenstein J. L.: Diffuse radiation in the galaxy, Astrophysical Journal, 93, 70-83, 1941.

Ho, K. F., Lee, S. C., Louie, P. K. K., and Zou, S. C.: Seasonal variation of carbonyl compound concentrations in urban area of Hong Kong, Atmos. Environ., 36, 1259–1265, 2002.

Holben, B. N., Eck, T. F., Slutsker, I., Tanre, D., Buis, J. P., Set-zer, A., Vermote, E., Reagan, J. A., Kaufman, Y., Nakajima, T., Lavenu, F., Jankowiak, I., and Smirnov, A.: AERONET – A federated instrument network and data archive for aerosol characterization, Remote Sens. Environ., 66, 1–16, 1998.

Holben, B. N., Tanre, D., Smirnov, A., Eck, T. F., Slutsker, I., Abuhassan, N., Newcomb, W. W., Schafer, J., Chatenet, B., Lav-enue, F., Kaufman, Y. J., Van de Castle, J., Setzer, A., Markham, B., Clark, D., Frouin, R., Halthore, R., Karnieli, A., O'Neill, N. T., Pietras, C., Pinker, R. T., Voss, K., and Zibordi, Z.: An emerging ground-based aerosol climatology: Aerosol optical depth from AERONET, J. Geophys. Res., 106, 12067–12097, 2001

Hönninger, G. and Platt, U.: Observations of BrO and its vertical distribution during surface ozone depletion at Alert, Atmos. Environ., 36, 2481–2489, 2002.

Hönninger, G., Friedeburg, C. von and Plat, U., Multi axis differential optical absorption spectroscopy (MAX-DOAS), Atmos. Chem. Phys., 4, 231–254, 2004

Huang, C., Chen, C. H., Li, L., Cheng, Z., Wang, H. L., Huang, H. Y., Streets, D. G., Wang, Y. J., Zhang, G. F., and Chen, Y. R.: Emission inventory of anthropogenic air pollutants and VOC species in the Yangtze River Delta region, China, Atmos. Chem. Phys., 11, 4105-4120, doi:10.5194/acp-11-4105-2011, 2011.

Huang, R.-J., Zhang, Y., Bozzetti, C., Ho, K.-F., Cao, J., Han, Y., Dällenbach, K. R., Slowik, J. G., Platt, S. M., Canonaco, F., Zotter, P., Wolf, R., Pieber, S. M., Bruns, E. A., Crippa, M., Ciarelli, G., Piazzalunga, A., Schwikowski, M.,

Abbaszade, G., Schnelle-Kreis, J., Zimmermann, R., An, Z., Szidat, S., Baltensperger, U., Haddad, I. E., and Prévôt, A. S. H.: High secondary aerosol contribution to particulate pollution during haze events in China, Nature, 514, 218–222, 2014.

Irie, H., Kanaya, Y., Akimoto, H., Iwabuchi, H., Shimizu, A., and Aoki, K.: First retrieval of tropospheric aerosol profiles using MAX-DOAS and comparison with lidar and sky radiometer measurements, Atmos. Chem. Phys., 8, 341–350, 2008.

Irie, H., Takashima, H., Kanaya, Y., Boersma, K. F., Gast, L., Wittrock, F., Brunner, D., Zhou, Y., and Van Roozendael, M.: Eight-component retrievals from ground-based MAX-DOAS observations, Atmos. Meas. Tech., 4, 1027–1044, 2011.

Jiang, C., Wang, H., Zhao, T., Li, T., and Che, H.: Modeling study of PM2.5 pollutant transport across cities in China's Jing–Jin–Ji region during a severe haze episode in December 2013, Atmos. Chem. Phys., 15, 5803-5814, doi:10.5194/acp-15-5803-2015, 2015.

Junkermann, W.: On the distribution of formaldehyde in the western Po-Valley, Italy, during FORMAT 2002/2003, Atmos. Chem. Phys., 9, 9187–9196, doi:10.5194/acp-9-9187-2009, 2009.

Kanaya, Y., Irie, H., Takashima, H., Iwabuchi, H., Akimoto, H., Sudo, K., Gu, M., Chong, J., Kim, Y. J., Lee, H., Li, A., Si, F., Xu, J., Xie, P.-H., Liu, W.-Q., Dzhola, A., Postylyakov, O., Ivanov, V., Grechko, E., Terpugova, S., and Panchenko, M.: Long-term MAX-DOAS network observations of NO2 in Russia and Asia (MADRAS) during the period 2007–2012: instrumentation, elucidation of climatology, and comparisons with OMI satellite observations and global model simulations, Atmos. Chem. Phys., 14, 7909-7927, doi:10.5194/acp-14-7909-2014, 2014.

Kesselmeier, J. and Staudt, M.: Biogenic volatile organic compounds (VOC): an overview on emission, physiology and ecology. J. Atmos. Chemistry 33, 23-88, 1999.

Kraus, S.: DOASIS, A Framework Design for DOAS, PhD-thesis, University of lMannheim,http://hci.iwr.uni-heidelberg.de/publications/dip/2006/Kraus_PhD2006.pdf, 2006.

Lee, C., Martin, R. V., van Donkelaar, A., Lee, H., Dicker-son, R. R., Hains, J. C., Krotkov, N., Richter, A., Vinnikov, K., and Schwab, J. J.: SO_2 emissions and lifetimes: Estimates from inverse modeling using in situ and global, space–based (SCIAMACHY and OMI) observations, J. Geophys. Res., 116, D06304, doi:10.1029/2010JD014758, 2011.

Levelt, P. F., Hilsenrath, E., Lepppelmeier, G. W., van den Oord, G. H. J., Bhartia, P. K., Taminnen, J., de Haan, J. F. and Veefkind, J. P.: Science objectives of the Ozone Monitoring Instrument, IEEE Trans. Geosci. Remote Sens., 44, 1199, 2006a.

Levelt, P. F., van den Oord, G. H. J., Dobber, M. R., Malkki, A., Visser, H., de Vries, J., Stammes, P., Lundell, J. and Saari, H.: The Ozone Monitoring Instrument, IEEE Trans. Geosci. Remote Sens., 44, 1093, 2006b.

Li X., Brauers, T. and Hofzumahaus, A.: MAX-DOAS measurements of NO2, HCHO and CHOCHO at a rural site in Southern China. Atmos. Chem. Phys. Discuss., 12, 3983-4029, 2012.

Li X., Brauers, T., Shao, M., Garland, R. M., Wagner, T., Deutschmann, T., and Wahner, A.: MAX-DOAS measurements in southern China: retrieval of aerosol extinctions and validation using ground-based in-situ data. Atmos. Chem. Phys., 10, 2079–2089, 2010.

Li, G. L., Zhou, M., Chen, C. H., Wang, H. L., Wang, Q., Lou, S. R., .Qiao, L. P., Tang, X. B., Li, L., Huang H. Y., Chen M., H., Huang C., and Zhang, G. F.: Characteristics of particulate matters and its chemical compositions during the dust episodes in Shanghai in spring, 2011, Environmental Science, 35(5), 1644-1653, 2014

Lin, W., Xu, X., Ge, B., and Liu, X.: Gaseous pollutants in Beijing urban area during the heating period 2007–2008: variability, sources, meteorological, and chemical impacts, Atmos. Chem. Phys., 11, 8157–8170, doi:10.5194/acp-11-8157-2011, 2011.

Liu, F., Beirle, S., Zhang, Q., Dörner, S., He, K. B., and Wagner, T.: NO_x lifetimes and emissions of hotspots in polluted background estimated by satellite observations, Atmos. Chem. Phys. Discuss., 15, 24179-24215, doi:10.5194/acpd-15-24179-2015, 2015.

Liu, J., Zheng, Y., Li, Z., Flynn, C., and Cribb, M.: Seasonal variations of aerosol optical properties, vertical distribution and associated radiative effects in the Yangtze Delta region of China. Journal of Geophysical Research: Atmospheres (1984–2012), 117(D16), 2012.

Lu, Z., Streets, D. G., Zhang, Q., Wang, S., Carmichael, G. R., Cheng, Y. F., Wei, C., Chin, M., Diehl, T., and Tan, Q.: Sulfur dioxide emissions in China and sulfur trends in East Asia since 2000, Atmos. Chem. Phys., 10, 6311–6331, doi:10.5194/acp-10-6311-2010, 2010.

Ma, J. Z., Beirle, S., Jin, J. L., Shaiganfar, R., Yan, P., and Wagner, T.: Tropospheric NO2 vertical column densities over Beijing: results of the first three years of ground-based MAX-DOAS measurements (2008–2011) and satellite validation, Atmos. Chem. Phys., 13, 1547-1567, doi:10.5194/acp-13-1547-2013, 2013.

Meller, R. and Moortgat, G. K.: Temperature dependence of the ab-sorption cross sections of formaldehyde between 223 and 323 K in the wavelength range 225–375 nm, J. Geophys. Res., 105, 7089–7101, 2000

Meng, Z. Y., Ding, G. A., Xu, X. B., Xu, X. D., Yu, H. Q., and Wang, S. F.: Vertical distributions of SO2 and NO2 in the lower atmosphere in Beijing urban areas, China. Science of the Total Environment, 390(2), 456-465, 2008.

Nasse, J. M., Zielcke, J., Frieß, U., Lampel, J., König-Langlo, G. and Platt, U.: Inference of cloud altitude and optical properties from MAX-DOAS measurements, EGU General Assembly 2015, Wien, 12 April 2015 - 17 April 2015, hdl:10013/epic.45412, http://hdl.handle.net/10013/epic.45412.

Oppenheimer, C., Francis, P., and Stix, J.: Depletion rates of sulfur dioxide in tropospheric volcanic plumes, Geophys. Res. Lett., 25, 2671–2674, doi:10.1029/98GL01988, 1998.

Pinardi, G., Van Roozendael, M., Abuhassan, N., Adams, C., Cede, A., Clémer, K., Fayt, C., Frieß, U., Gil, M., Herman, J., Hermans, C., Hendrick, F., Irie, H., Merlaud, A., Navarro Comas, M., Peters, E., Piters, A. J. M., Puentedura, O., Richter, A., Schönhardt, A., Shaiganfar, R., Spinei, E., Strong, K., Takashima, H., Vrekoussis, M., Wagner, T., Wittrock, F., and Yilmaz, S.: MAX-DOAS formaldehyde slant column measurements during CINDI: intercomparison and analysis improvement, Atmos. Meas. Tech., 6, 167-185, doi:10.5194/amt-6-167-2013, 2013.

Platt, U. and Stutz, J.: Differential Optical Absorption Spectroscopy. Springer, Heidelberg, Berlin, 229-375, 2008.

Qi, H., Lin, W., Xu, X., Yu, X., and Ma, Q.: Significant downward trend of SO2 observed from 2005 to 2010 at a background station in the Yangtze Delta region, China. Science China Chemistry, 55(7), 1451-1458, 2012.

Qin, M., Xie, P. H., Liu, W. Q., Li, A., Dou, K., Fang, W., Liu, J. G. Zhang, W. J.: Observation of atmospheric nitrous acid with DOAS in Beijing, China, Journal of Environmental Sciences, 18, 69-75, 2006.

Richter, A., Burrows, J. P., Nüß, H., Granier, C., and Niemeier, U.: Increase in tropospheric nitrogen dioxide over China observed from space. Nature, 437(7055), 129-132, 2005

Rodgers, C. D.: Inverse methods for atmospheric sounding, theory and practice, Series on Atmospheric, Oceanic and Planetary Physics, World Scientific, 2000.

Roscoe, H. K., Van Roozendael, M., Fayt, C., du Piesanie, A., Abuhassan, N., Adams, C., Akrami, M., Cede, A., Chong, J., Clémer, K., Friess, U., Gil Ojeda, M., Goutail, F., Graves, R., Griesfeller, A., Grossmann, K., Hemerijckx, G., Hendrick, F., Herman, J., Hermans, C., Irie, H., Johnston, P. V., Kanaya, Y., Kreher, K., Leigh, R., Merlaud, A., Mount, G. H., Navarro, M., Oetjen, H., Pazmino, A., Perez-Camacho, M., Peters, E., Pinardi, G., Puentedura, O., Richter, A., Schönhardt, A., Shaiganfar, R., Spinei, E., Strong, K., Takashima, H., Vlemmix, T., Vrekoussis, M., Wagner, T., Wittrock, F., Yela, M., Yilmaz, S., Boersma, F., Hains, J., Kroon, M., Piters, A., and Kim, Y. J.: Intercomparison of slant column measurements of NO2 and O4 by MAX-DOAS and zenith-sky UV and visible spectrometers, Atmos. Meas. Tech., 3, 1629-1646, doi:10.5194/amt-3-1629-2010, 2010.

Rozanov, A., Rozanov, V., Buchwitz, M., Kokhanovsky, A., and Burrows, J.: SCIATRAN 2.0 - A new radiative transfer model for geophysical applications in the 175-2400 nm spectral region, in: Atmospheric Remote Sensing: Earth's Surface, Troposphere, Stratosphere and Mesosphere - I, edited by Burrows, J. and Eichmann, K., vol. 36 of ADVANCES IN SPACE RESEARCH, 1015-1019, 2005.

Schaub, D., Brunner, D., Boersma, K. F., Keller, J., Folini, D., Buchmann, B., Berresheim, H., and Staehelin, J.: SCIAMACHY tropospheric NO2 over Switzerland: estimates of NOx lifetimes and impact of the complex Alpine topography on the retrieval, Atmos. Chem. Phys., 7, 5971-5987, doi: 10.5194/acp-7-5971-2007, 2007.

Seinfeld, J. H. and Pandis, S. N.: Atmospheric Chemistry and Physics — From Air Pollution to Climate Change. John Wiley, New York, 1998.

Shaiganfar, R., Beirle, S., Sharma, M., Chauhan, A., Singh, R. P., and Wagner, T.: Estimation of NO_x emissions from Delhi using Car MAX-DOAS observations and comparison with OMI satellite data, Atmos. Chem. Phys., 11, 10871-10887, doi:10.5194/acp-11-10871-2011, 2011.

Sinreich, R., Merten, A., Molina, L., and Volkamer, R.: Parameterizing radiative transfer to convert MAX-DOAS dSCDs into near-surface box averaged mixing ratios and vertical profiles, Atmos. Meas. Tech., 6, 1521-1532, 2013.

Smirnov, A., Holben, B. N., Eck, T. F., Dubovik, O. and Slutsker, I.: Cloud-Screening and Quality Control Algorithms for the AERONET Database, Remote Sensing of Environment, 73, 337, 2000.

Stavrakou, T., Müller, J.-F., Boersma, K. F., van der A, R. J., Kurokawa, J., Ohara, T., and Zhang, Q.: Key chemical NOx sink uncertainties and how they influence top-down emissions of nitrogen oxides, Atmos. Chem. Phys., 13, 9057–9082, doi:10.5194/acp-13-9057-2013, 2013.

Theys, N., De Smedt, I., Gent, J., Danckaert, T., Wang, T., Hendrick, F., Stavrakou, T., Bauduin, S., Clarisse, L., Li, C., Krotkov, N., Yu, H., Brenot, H., and Van Roozendael, M.: Sulfur dioxide vertical column DOAS retrievals from the Ozone Monitoring Instrument: Global observations and comparison to ground‐based and satellite data. Journal of Geophysical Research: Atmospheres, 120(6), 2470-2491, 2015.

Vandaele, A. C., Hermans, C., Simon, P. C., Carleer, M., Colin, R., Fally, S., Mérienne, M.-F., Jenouvrier, A., and Coquart, B.: Measurements of the NO2 absorption cross section from 42000 cm^{-1} to 10000 cm^{-1} (238–1000 nm) at 220 K and 294 K, J. Quant. Spectrosc. Ra., 59, 171–184, 1998.

Van Roozendael, M., Fayt, C., Post, P., Hermans, C., Lambert, J.-C.: Retrieval of BrO and NO2 from UV-Visible Observations, in: Sounding the troposphere from space: a new Era for Atmospheric Chemistry. The TROPOSAT Final Report. Peter Borrell, Patricia M. Borrell, John P. Burrows and Ulrich Platt (editors), Springer, 155-166, 2003

Veefkind, J. P., Boersma, K. F., Wang, J., Kurosu, T. P., Krotkov, N., Chance, K., and Levelt, P. F.: Global satellite analysis of the relation between aerosols and short-lived trace gases, Atmos. Chem. Phys., 11, 1255–1267, doi:10.5194/acp-11-1255-2011, 2011.

Vlemmix, T., Eskes, H. J., Piters, A. J. M., Schaap, M., Sauter, F. J., Kelder, H., and Levelt, P. F.: MAX-DOAS tropospheric nitrogen dioxide column measurements compared with the Lotos-Euros air quality model, Atmos. Chem. Phys., 15, 1313-1330, doi:10.5194/acp-15-1313-2015, 2015a.

Vlemmix, T., Hendrick, F., Pinardi, G., De Smedt, I., Fayt, C., Hermans, C., Piters, A., Wang, P., Levelt, P., and Van Roozendael, M.: MAX-DOAS observations of aerosols, formaldehyde and nitrogen dioxide in the Beijing area: comparison of two profile retrieval approaches, Atmos. Meas. Tech., 8, 941-963, doi:10.5194/amt-8-941-2015, 2015b.

Vlemmix, T., Piters, A. J. M., Berkhout, A. J. C., Gast, L. F. L., Wang, P., and Levelt, P. F.: Ability of the MAX-DOAS method to derive profile information for NO2: can the boundary layer and free troposphere be separated?, Atmos. Meas. Tech., 4, 2659–2684, 2011

Vlemmix, T., Piters, A. J. M., Stammes, P., Wang, P., and Levelt, P. F.: Retrieval of tropospheric NO_2 using the MAX-DOAS method combined with relative intensity measurements for aerosol correction, Atmos. Meas. Tech., 3, 1287–1305, 2010.

Von Glasow, R., Bobrowski, N., and Kern, C.: The effects of volcanic eruptions on atmospheric chemistry, Chem. Geol., 263, 131–142, doi:10.1016/j.chemgeo.2008.08.020, 2009.

Wagner, T., Erie, F., Marquard, L., Otten, C., Pfeilsticker, K., Senne, T., Stutz, J. and Platt, U.: Cloudy sky optical paths as derived from differential optical absorption spectroscopy observations, J. Geophys. Res., 103, 25307, 1998.

Wagner, T., Friedeburg, C. von, Wenig M., Otten, C. and Platt, U.: UV/vis observations of atmospheric O4 absorptions using direct moon light and zenith scattered sunlight under clear and cloudy sky conditions, J. Geophys. Res., 107, D204424, 2002.

Wagner, T., B. Dix, C. von Friedeburg, Frieß, U., Sanghavi, S., Sinreich, R. and Platt, U.: MAX-DOAS O_4 measurements: A new technique to derive information on atmospheric aerosols—Principles and information content, J. Geophys. Res., 109, D22205, 2004.

Wagner, T., Beirle, S., and Deutschmann, T.: Three-dimensional simulation of the Ring effect in observations of scattered sun light using Monte Carlo radiative transfer models, Atmos. Meas. Tech., 2, 113-124, 2009.

Wagner, T., Beirle, S., Brauers, T., Deutschmann, T., Frieß, U., Hak, C., Halla, J. D., Heue, K. P., Junkermann, W., Li, X., Platt, U. and Pundt-Gruber, I.: Inversion of tropospheric profiles of aerosol extinction and HCHO and NO_2 mixing ratios from MAX-DOAS observations in Milano during the summer of 2003 and comparison with independent data sets, Atmos. Meas. Tech. Discuss, 4, 3891–3964, 2011.

Wagner, T., Beirle, S., Dörner, S., Friess, U., Remmers, J. and Shaiganfar, R.: Cloud detection and classification based on MAX-DOAS observations, Atmos. Meas. Tech., 7, 1289-1320, 2014

Wang, T., Nie, W., Gao, J., Xue, L. K., Gao, X. M., Wang, X. F., Qiu, J., Poon, C. N., Meinardi, S., Blake, D., Wang, S. L., Ding, A. J., Chai, F. H., Zhang, Q. Z., and Wang, W. X.: Air quality during the 2008 Beijing Olympics: secondary pollutants and regional impact, Atmos. Chem. Phys., 10, 7603-7615, doi:10.5194/acp-10-7603-2010, 2010.

Wang, T., Hendrick, F., Wang, P., Tang, G., Clémer, K., Yu, H., Fayt, C., Hermans, C., Gielen, C., Müller, J.-F., Pinardi, G., Theys, N., Brenot, H., and Van Roozendael, M.: Evaluation of tropospheric SO_2 retrieved from MAX-DOAS measurements in Xianghe, China, Atmos. Chem. Phys., 14, 11149-11164, doi:10.5194/acp-14-11149-2014, 2014a.

Wang, Y., Li, A., Xie, P. H., Chen, H., Xu, J., Wu, F. C., G., L. J., and Q., L. W.: Retrieving vertical profile of aerosol extinction by multi-axis differential optical absorption spectroscopy, Acta Phys. Sin., 16, doi: 10.7498/aps.62.180705, http://wulixb.iphy.ac.cn/EN/abstract/abstract54703.shtml#, 2013a.

Wang, Y., Li, A., Xie, P. H., Chen, H., Mou, F. S., Xu, J., Wu, F. C., Zeng, Y., Liu, J. G. and Liu, W. Q.: Measuring tropospheric vertical distribution and vertical column density of NO2 by multi-axis differential optical absorption spectroscopy, Acta Phys. Sin., 16, DOI:10.7498/aps.62.200705, http://wulixb.iphy.ac.cn/EN/abstract/abstract56201.shtml, 2013b.

Wang, Y., Li, A., Xie, P. H., Wagner, T., Chen, H., Liu, W. Q., and Liu, J. G.: A rapid method to derive horizontal distributions of trace gases and aerosols near the surface using multi-axis differential optical absorption spectroscopy, Atmos. Meas. Tech., 7, 1663-1680, doi:10.5194/amt-7-1663-2014, 2014b.

Wang, Y., Penning de Vries, M., Xie, P. H., Beirle, S., Dörner, S., Remmers, J., Li, A., and Wagner, T.: Cloud and aerosol classification for 2.5 years of MAX-DOAS observations in Wuxi (China) and comparison to independent data sets, Atmos. Meas. Tech., 8, 5133-5156, doi:10.5194/amt-8-5133-2015, 2015.

Winterrath, T., Koruso, T. P., Richter, A. and Burrows, J. P.: Enhanced O_3 and NO_2 in thunderstorm clouds: convection or production, *Geophys. Res. Lett.*, 26, 1291, 1999.

Wittrock, F., Oetjen, H., Richter, A., Fietkau, S., Medeke, T., Rozanov, A., and Burrows, J. P.: MAX-DOAS measurements of atmospheric trace gases in Ny-Alesund – Radiative transfer studies and their application, Atmos. Chem. Phys., 4, 955–966, 2004.

Wittrock, F.: The Retrieval of Oxygenated Volatile Organic Compounds by Remote Sensing Techniques. Ph.D., University of Bremen, Bremen, Germany, 2006, Available at: http://www.doas-bremen.de/paper/diss_wittrock_06.pdf (last accessed December 2015).

Xie, X., Shao, M., Liu, Y., Lu, S., Chang, C. C., and Chen, Z. M.: Estimate of initial isoprene contribution to ozone formation potential in Beijing, China. Atmospheric Environment, 42(24), 6000-6010, 2008.

Xue, L., Ding, A., Gao, J., Wang, T., Wang, W., Wang, X., Lei, H., Jin, D., and Qi, Y.: Aircraft measurements of the vertical distribution of sulfur dioxide and aerosol scattering coefficient in China. Atmospheric Environment, 44(2), 278-282, 2010.

Yilmaz, S.: Retrieval of Atmospheric Aerosol and Trace Gas Vertical Profiles using Multi-Axis Differential Optical Absorption Spectroscopy, PhD thesis, University of Heidelberg, Germany, 2012.

Thalman, R. M. and Volkamer, R.: Temperature Dependent Absorption Cross-Sections of O2-O2 collision pairs between 340 and 630 nm and at atmospherically relevant pressure, Phys. Chem. Chem. Phys., 15, 15371–15381, doi:10.1039/c3cp50968k, 2013

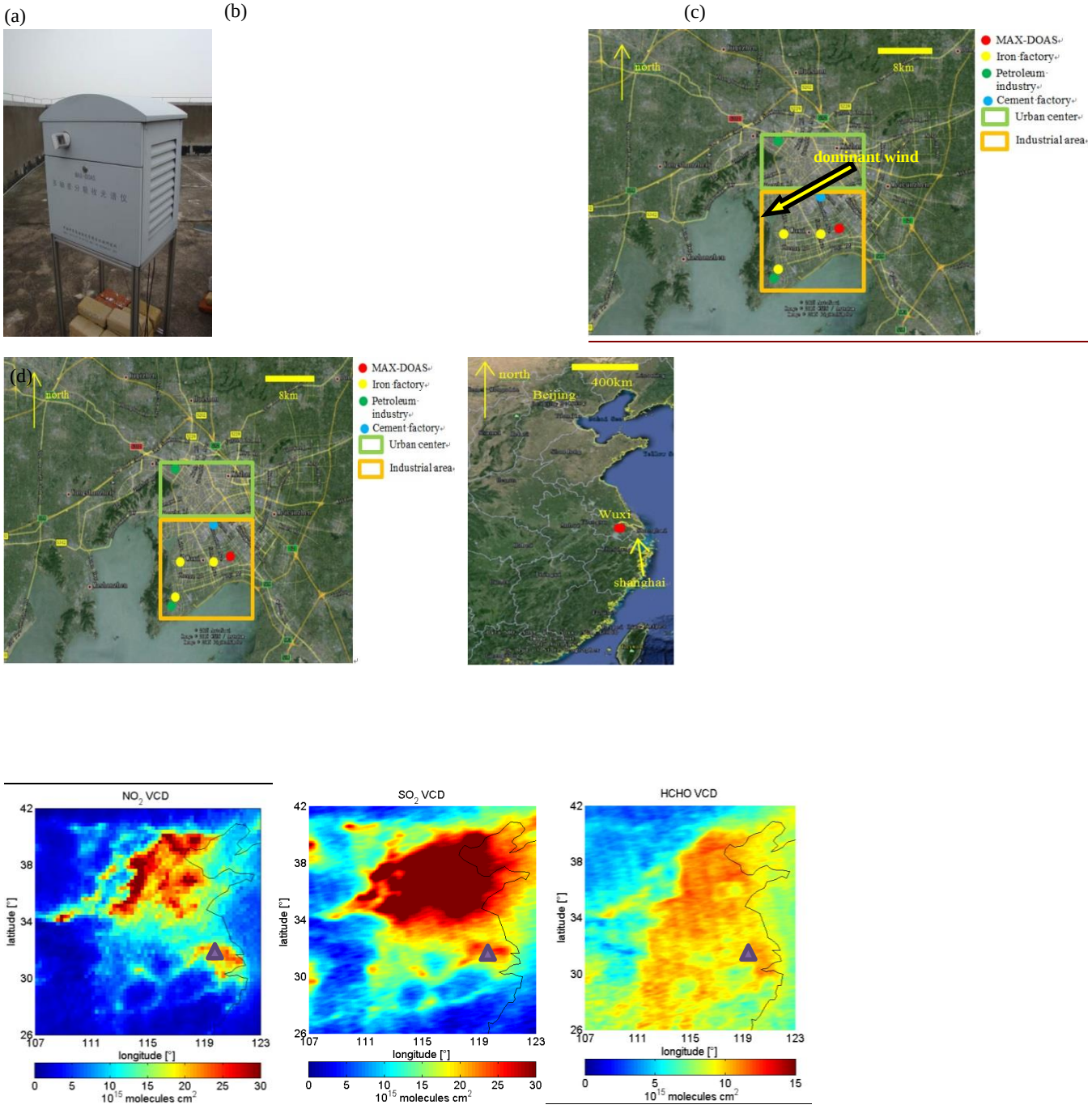

Figure ~~1~~ 1: The MAX-DOAS instrument (a) (also the long path DOAS and the visibility meter) is operated at the location marked by the red dot in subfigure (b) in Wuxi city (c). In subfigure (b), the dots with different colours indicate the positions of different types of emission sources; the green and orange blocks indicate the urban centre and industrial area, respectively; the yellow

arrow ~~points out~~represents the ~~direction of~~ dominant wind direction (northeast wind).~~.~~ The ~~mean~~ maps of mean tropospheric VCDs of NO_2 (from DOMINO version 2), SO_2 (from BIRA, Theys et al., 2015) and HCHO (from BIRA, I. De Smedt et al., 2015) derived from OMI observations over eastern China in the period from 2011 to 2014 are shown in subfigure (d), in which the triangle flag indicates the location of Wuxi.

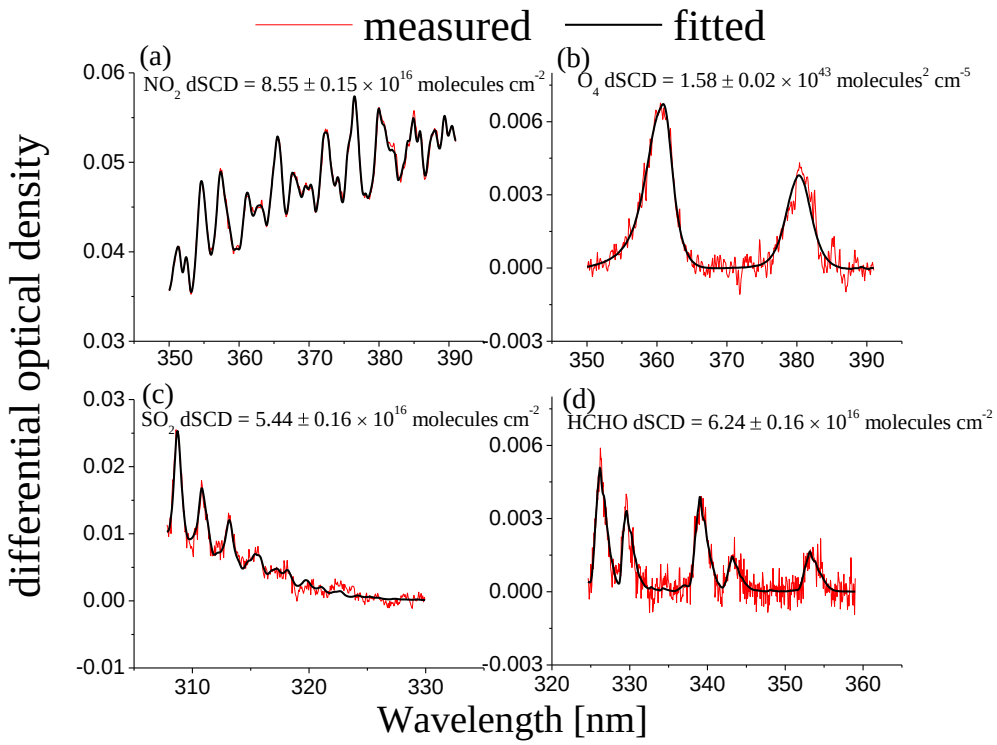

Figure 2: Examples of typical DOAS fits of NO_2 (a), O_4 (b) and SO_2 (c) at 11:37 on 1 December 2011 as well as HCHO (d) at 11:34 on 12 July 2012. The fitted dSCDs of NO_2, O_4, SO_2 and HCHO are given in the corresponding subfigures. The black and red curves indicate the fitted absorption structures and the derived absorption structures from the measured spectra, respectively.

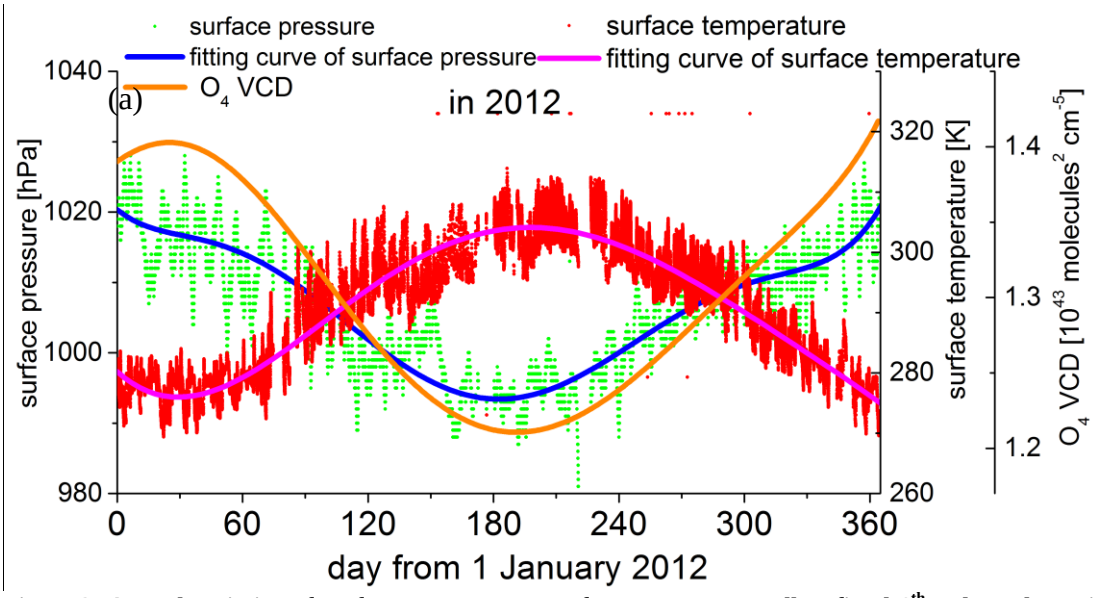

Figure 3: Annual variation of surface temperature, surface pressure as well as fitted 6th order polynomials in 2012. Also the O_4 VCDs calculated based on the fitted curves of the measured annual variations of surface temperature and pressure in 2012 is shown (similar results are found for other years).

(b)

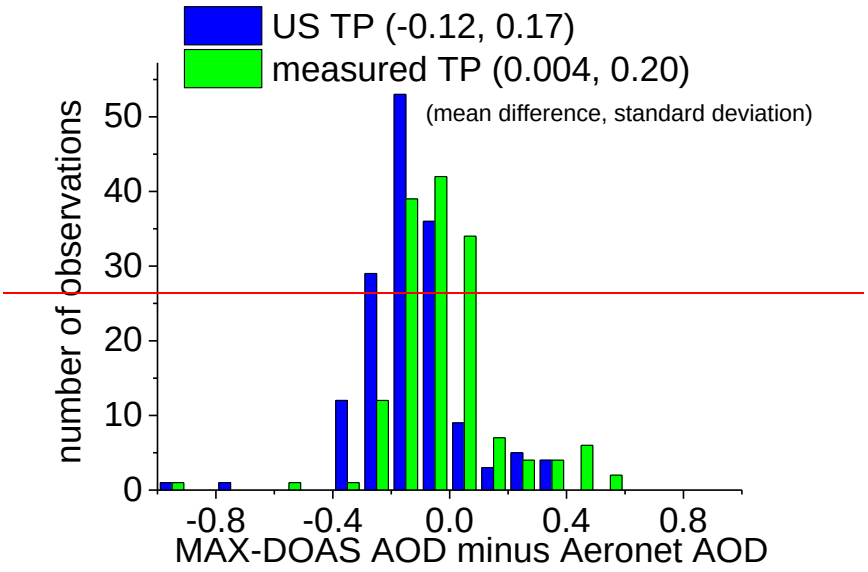

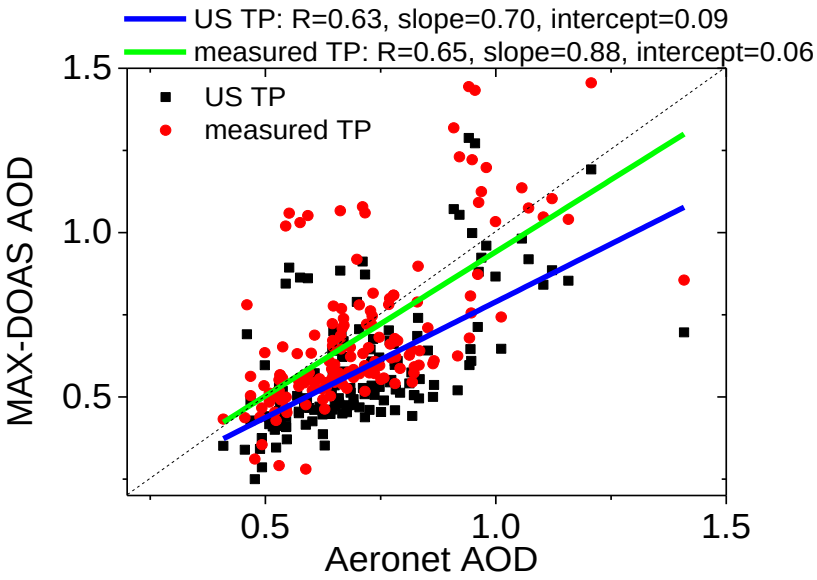

Figure 4: ~~**Dependence of retrieved AOD on temperature and pressure (TP)for clear sky conditions. (a): Frequency distribution of the differences of the AODs derived from MAX-DOAS and AERONET for January 2012. The MAX-DOAS results from the retrieval using either the US standard summer TP profiles or the explicit TP from local measurements are indicated by blue and green colours, respectively. The mean difference and standard deviation are shown in brackets. (b):**~~ ~~**The**~~ **AODs retrieved from MAX-DOAS observations (using either the US standard summer TP profile or the explicit TP from measurements)** ~~**are**~~ **plotted against those from the Taihu AERONET station for clear sky conditions. The results of the linear regressions are shown on top of the diagram.**

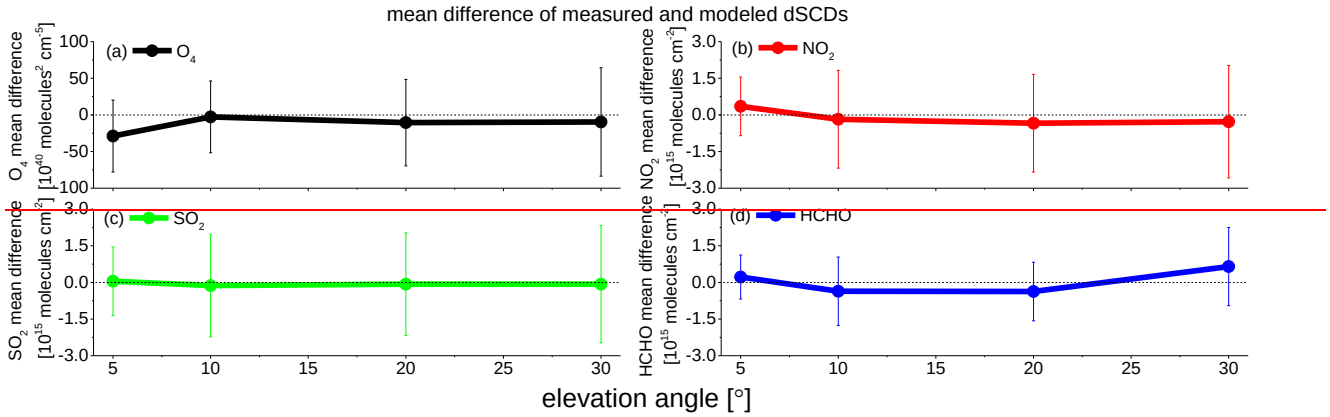

~~**Figure 5: Mean differences and the standard deviations (error bars) between the measured and modelled dSCDs of O_4 (a), NO_2 (b), SO_2 (c) and HCHO (d) for clear sky conditions with low aerosols plotted against the elevation angles of MAX-DOAS measurements.**~~

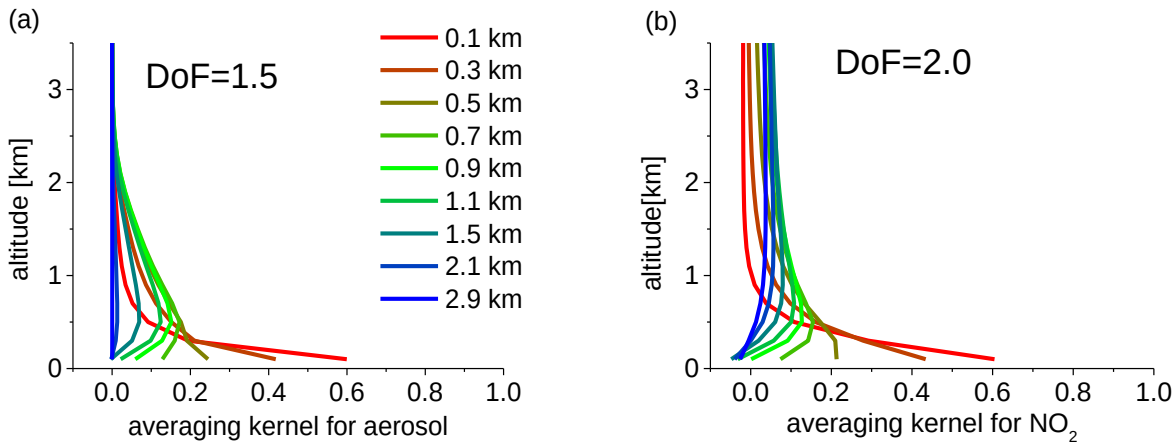

Figure ~~6~~5: Totally averaged averaging kernels of aerosol (a) and NO_2 (b) retrievals for all the MAX-DOAS measurements for clear sky conditions with low aerosols. DoF is the degree of freedom related to the averaging kernel.

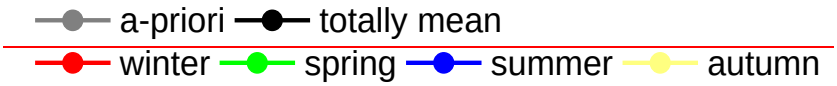

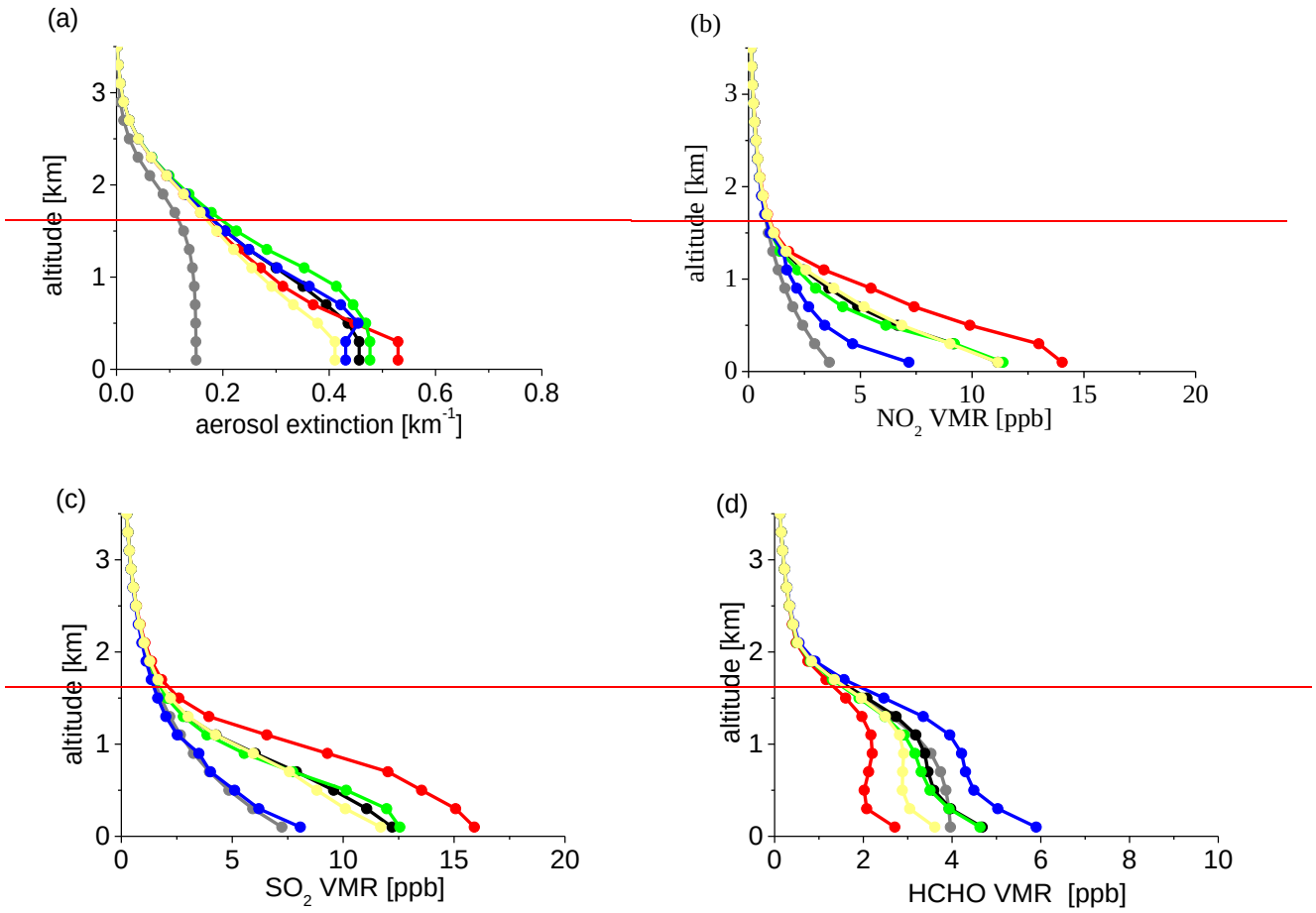

~~**Figure 7: Average profiles derived for different seasons for clear sky conditions with low aerosols: (a) aerosol extinction, (b) NO_2 VMR, (c) SO_2 VMR and (d) HCHO VMR. Also shown are the respective a-priori profiles.**~~

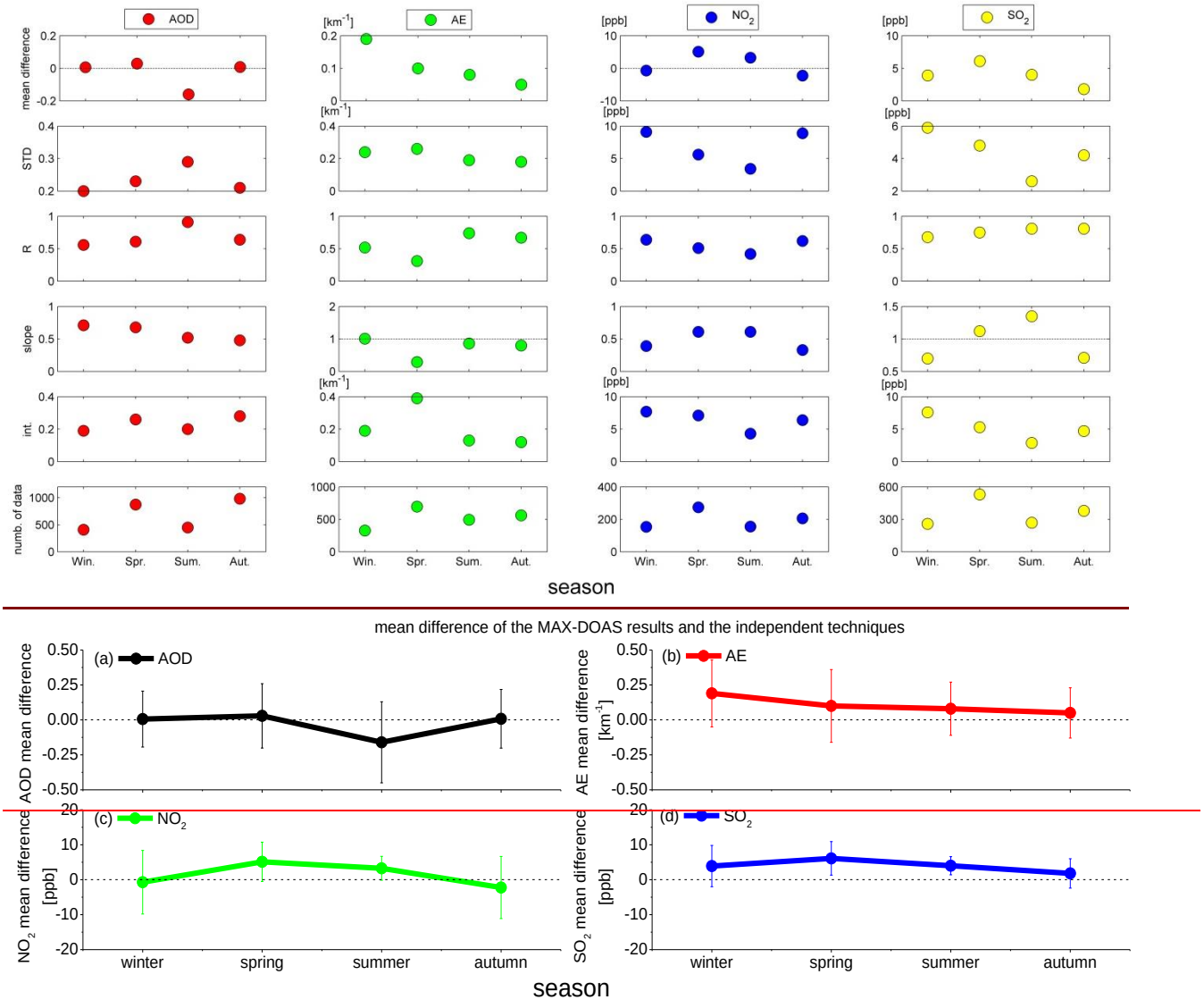

Figure 6~~8~~: ~~Seasonally mean~~ Mean absolute differences ~~and~~, standard deviations as well as correlation coefficients (R), slopes and intercepts derived from linear regressions of the ~~comparisons of~~ AODs, near-surface AEs, NO_2 and SO_2 VMRs ~~(shown as the error bar)~~ between MAX-DOAS ~~results~~ and independent techniques for different seasons for clear sky conditions with low aerosols. ~~N~~The corresponding umbers of data ~~in each comparison~~ are shown in the bottom panel. Different colours denote AOD ~~(a)~~ (compared with the Taihu AERONET level 1.5 data sets), AE ~~(b)~~ (compared with the nearby visibility meter) and NO_2 ~~(c)~~ and SO_2 ~~(d)~~ (compared with the nearby long path DOAS instrument).

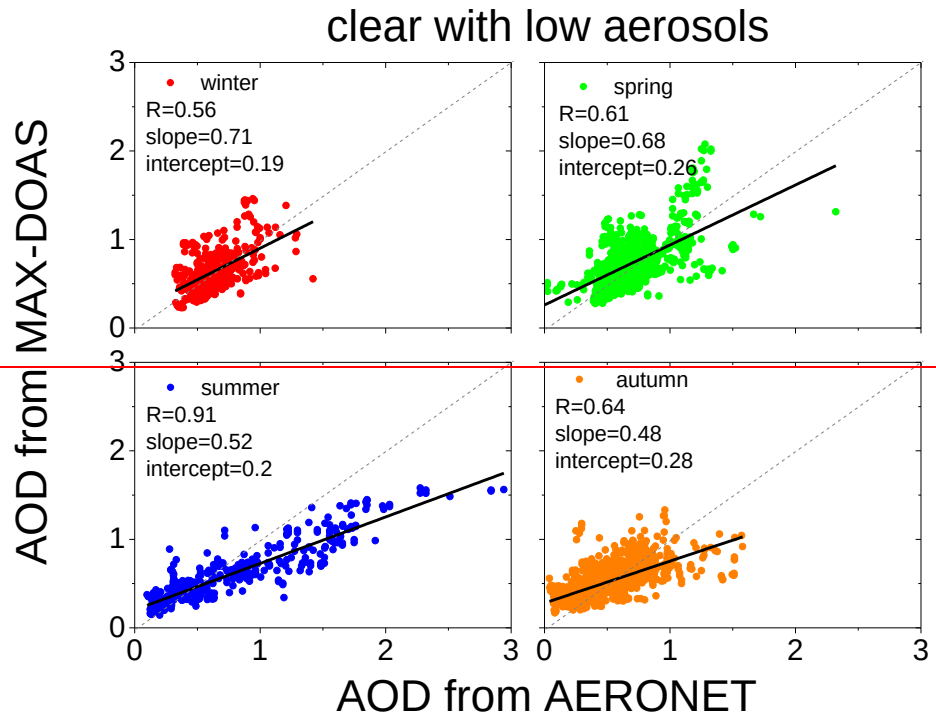

~~Figure 9:, Scatter plots of the AODs derived from MAX-DOAS versus those from the Taihu AERONET station (level 1.5) in different seasons for clear sky conditions with low aerosols. Results of the linear regression are shown in the individual subfigures.~~

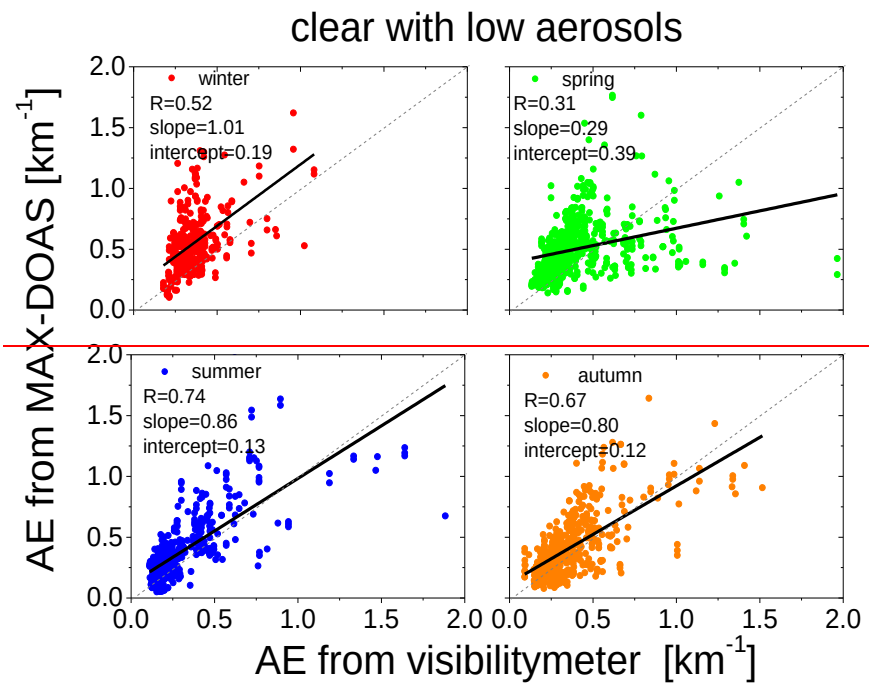

Figure 10: Same as Fig. 9 but for the comparison of the near surface aerosol extinction derived from MAX-DOAS and the visibility meter

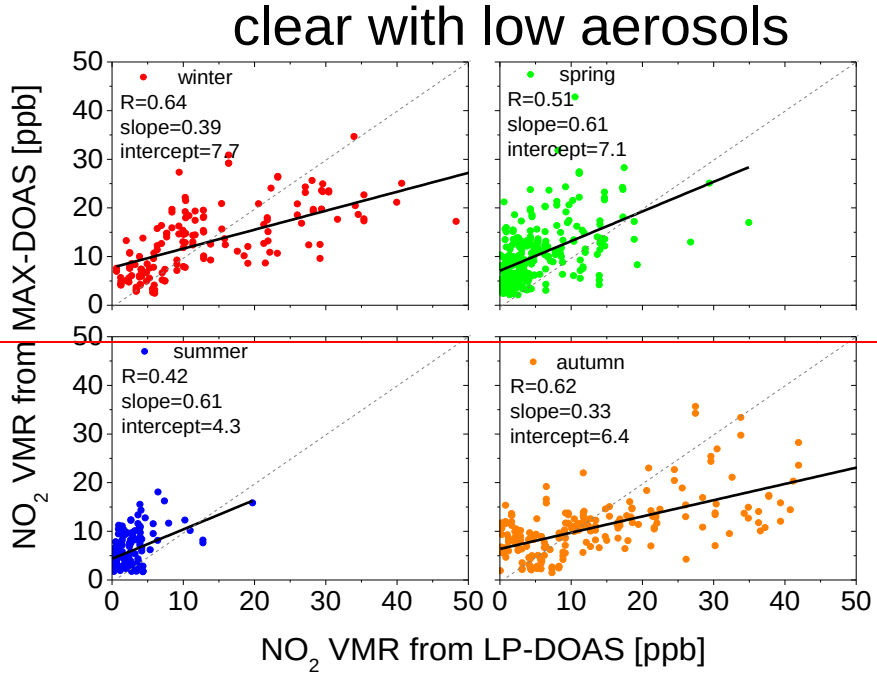

Figure 11: Same as Fig. 9 but for comparison of the near surface NO_2 mixing ratios derived from MAX-DOAS and LP-DOAS.

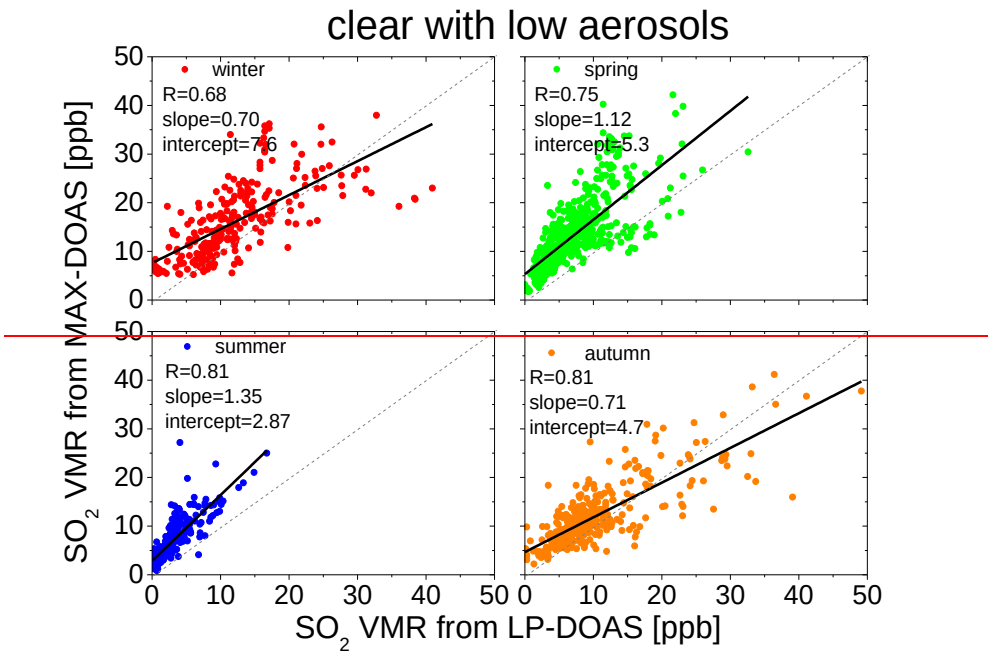

~~Figure 12: Same as Fig. 9 but for comparison of the near surface SO_2 mixing ratios derived from MAX-DOAS and LP-DOAS.~~

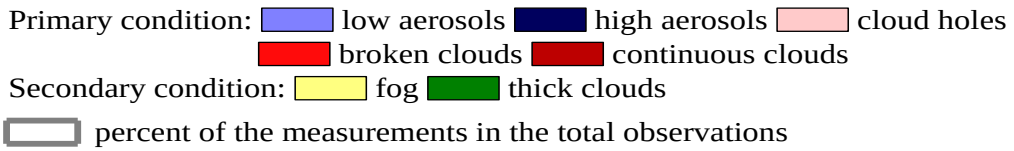

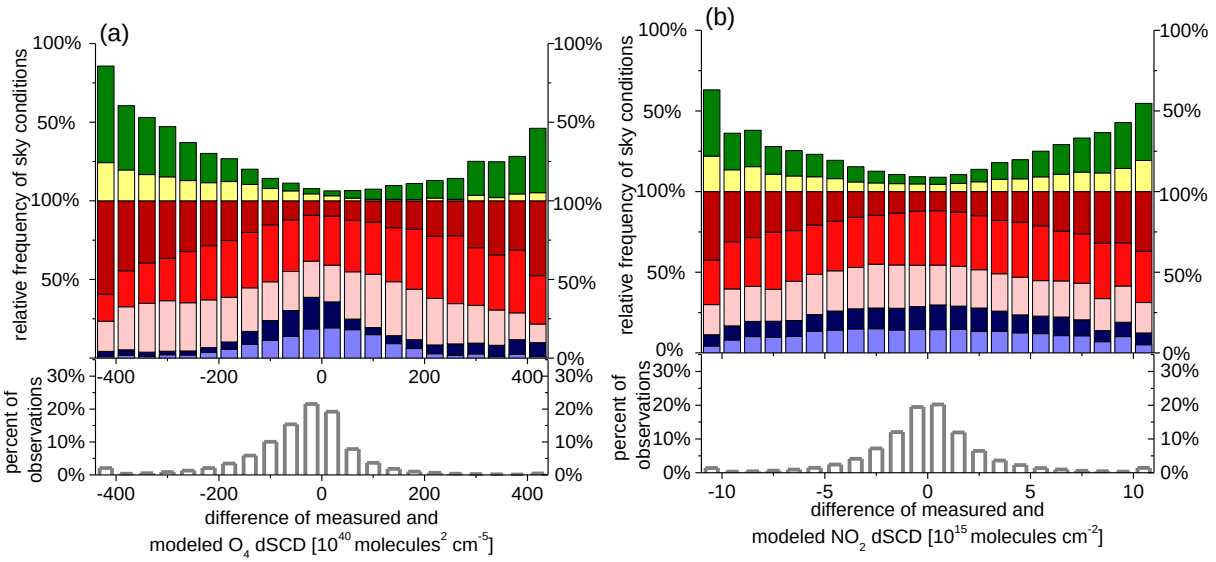

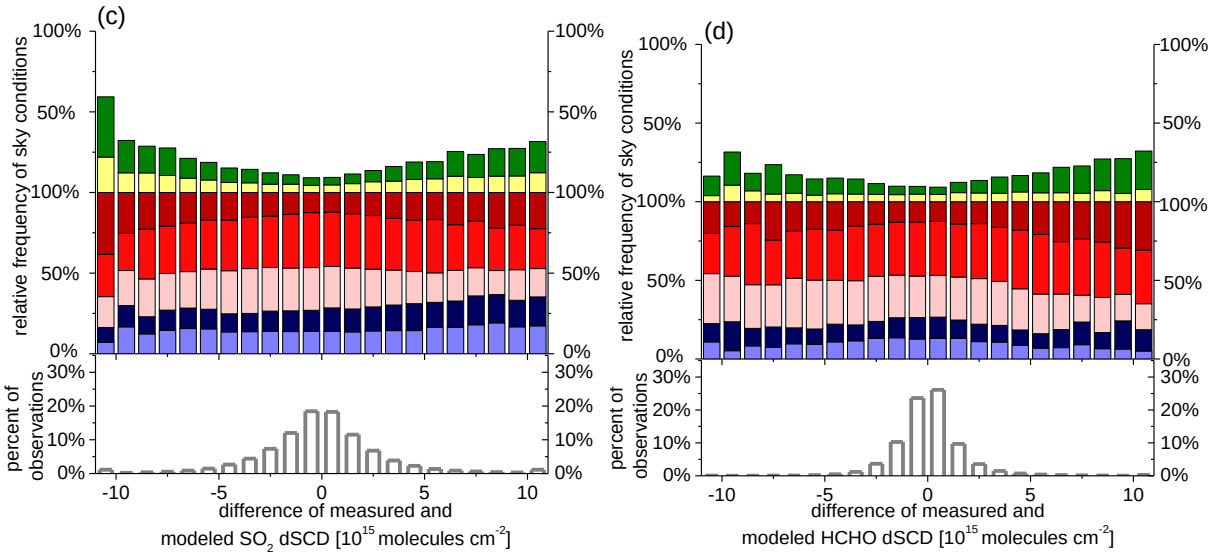

Figure ~~137~~: Histograms of the differences between the measured and modelled dSCDs of O_4 (a), NO_2 (b), SO_2 (c) and HCHO (d) for all elevation angles. The colour bars show the relative frequencies of the different sky conditions for each bin (top). The grey hollow bars (bottom) represent the relative frequencies of the number of measurements compared to the total number of observations.

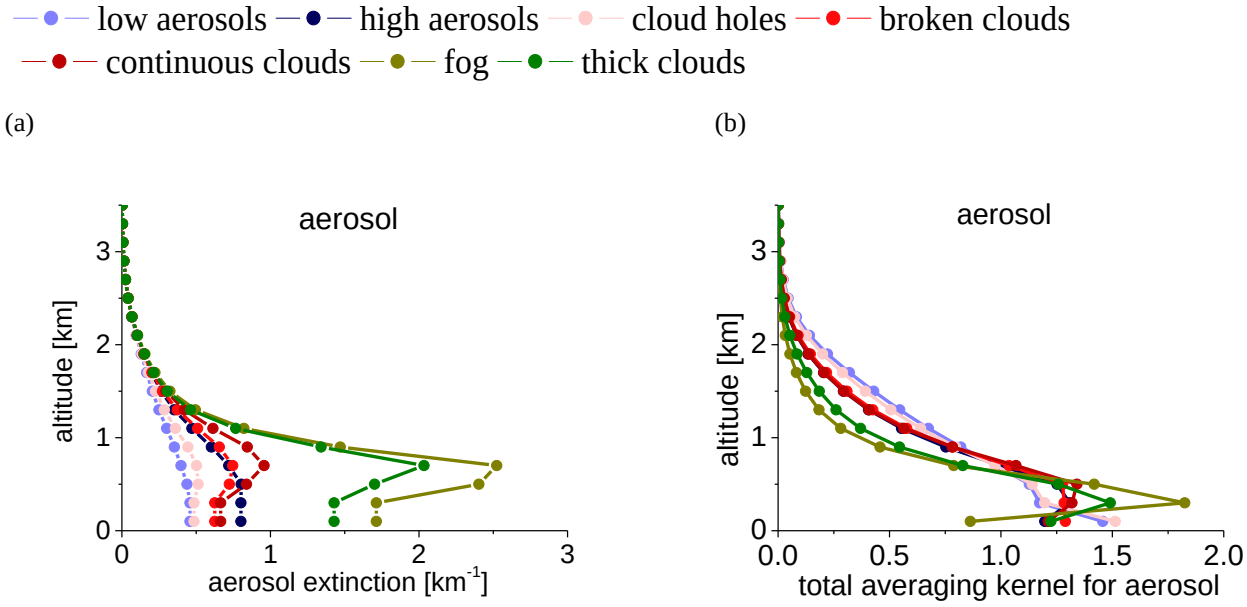

(c)

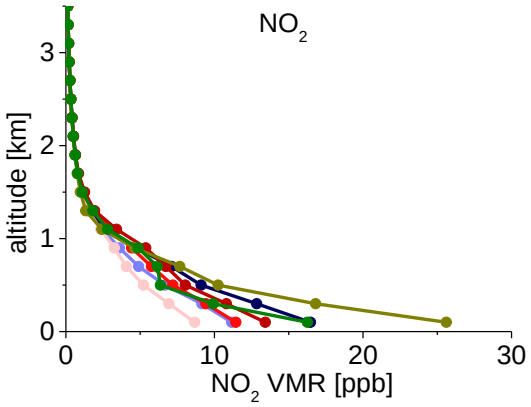
NO2
altitude [km]
NO2 VMR [ppb]
0
1
2
3
0
10
20
30

(d)

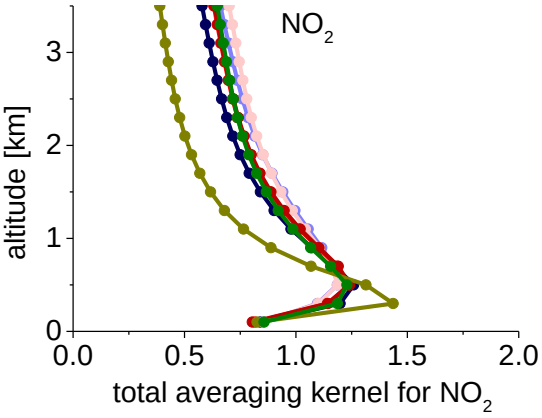
NO2
altitude [km]
total averaging kernel for NO2
0
1
2
3
0.0
0.5
1.0
1.5
2.0

(e)

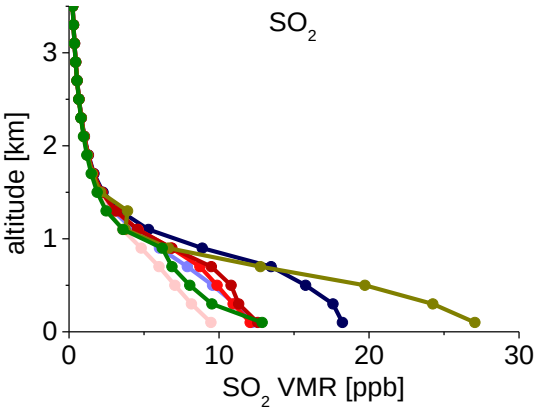
SO2
altitude [km]
SO2 VMR [ppb]
0
1
2
3
0
10
20
30

(f)

(g)

(h)

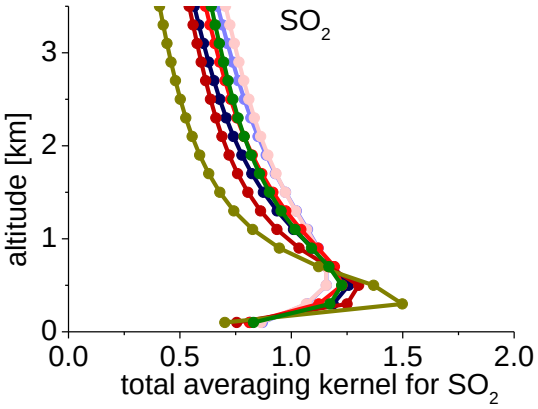
SO2
altitude [km]
total averaging kernel for SO2
0
1
2
3
0.0
0.5
1.0
1.5
2.0

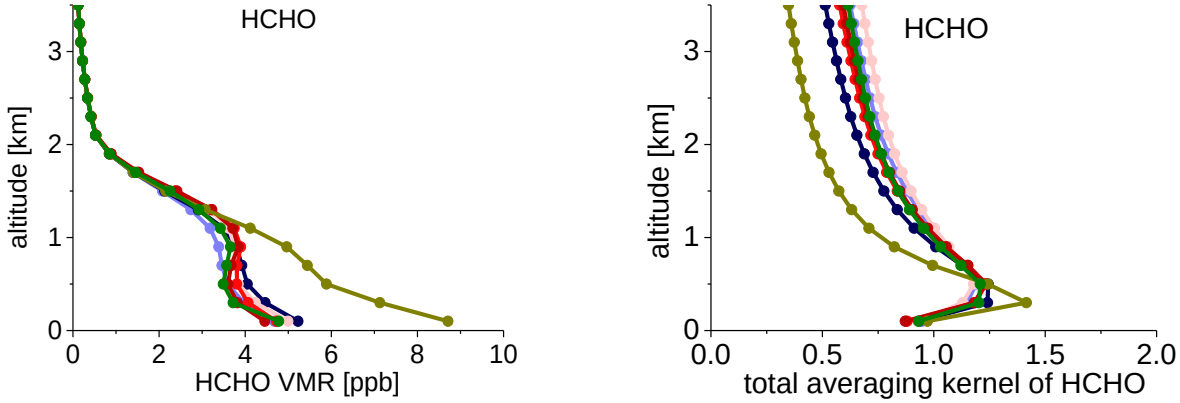

Figure ~~14~~8: Mean profiles of aerosol extinctions (a), NO_2 VMRs (c), SO_2 VMRs (e) and HCHO VMRs (g) from all MAX-DOAS observations under individual sky conditions; the subfigures (b), (d), (f), (h) show the total averaging kernels of the four species under individual sky conditions.

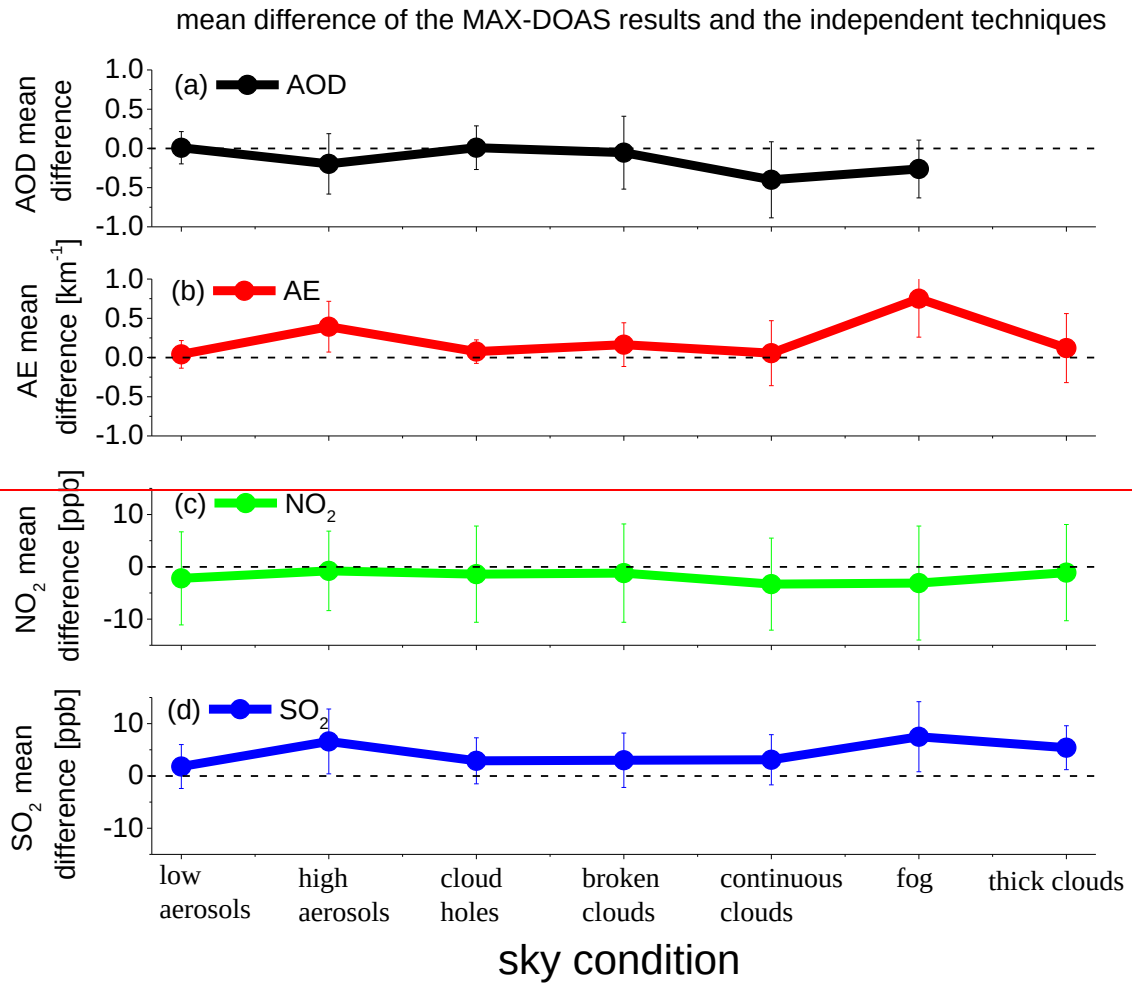
mean difference of the MAX-DOAS results and the independent techniques
AOD mean difference
(a) AOD
1.0
0.5
0.0
-0.5
-1.0
AE mean difference [km-1]
(b) AE
1.0
0.5
0.0
-0.5
-1.0
NO2 mean difference [ppb]
(c) NO2
10
0
-10
SO2 mean difference [ppb]
(d) SO2
10
0
-10
low aerosols
high aerosols
cloud holes
broken clouds
continuous clouds
fog
thick clouds
sky condition

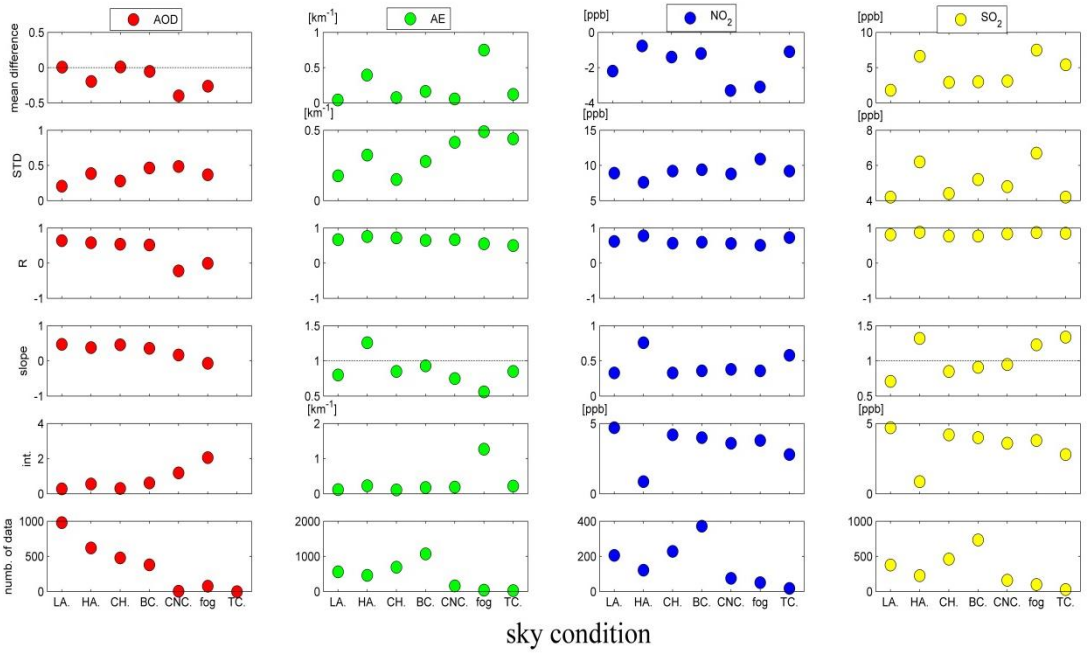

Figure ~~15~~9: ~~m~~Mean absolute differences, standard deviations as well as correlation coefficients (R), slopes and intercepts derived from linear regressions of the ~~comparisons of~~ AODs, near-surface AEs, NO_2 and SO_2 VMRs between MAX-DOAS and independent techniques for different seasons for different sky conditions. ~~N~~The corresponding umbers of data ~~in each comparison~~ are shown in the bottom panel. Different colours denote AOD (compared with the Taihu AERONET level 1.5 data sets), AE (compared with the nearby visibility meter) and NO_2 and SO_2 (compared with the nearby long path DOAS instrument).~~Mean differences and the standard deviation (shown as the error bar) between MAX-DOAS results and independent techniques for different sky conditions. Different colours denote the values of AOD (compared with Taihu AERONET level 1.5 data sets), AE (compared with the visibility meter located nearby) and NO_2 and SO_2 (compared with the close long path DOAS instrument).~~

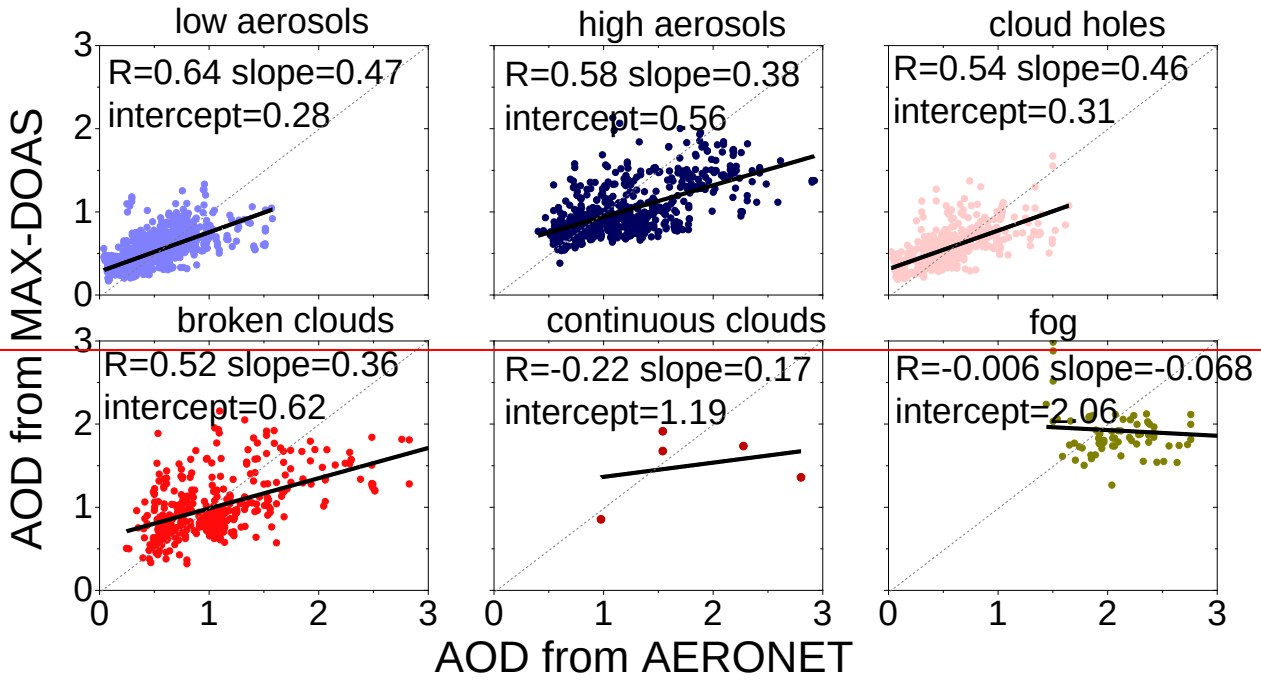

Figure 16: AODs derived from MAX-DOAS measurements in autumn are plotted against those from AERONET for different sky conditions. The linear regression parameters are shown in each subfigure. Note that no AERONET level 1.5 AOD data is available for thick clouds conditions because of the AERONET cloud screening scheme.

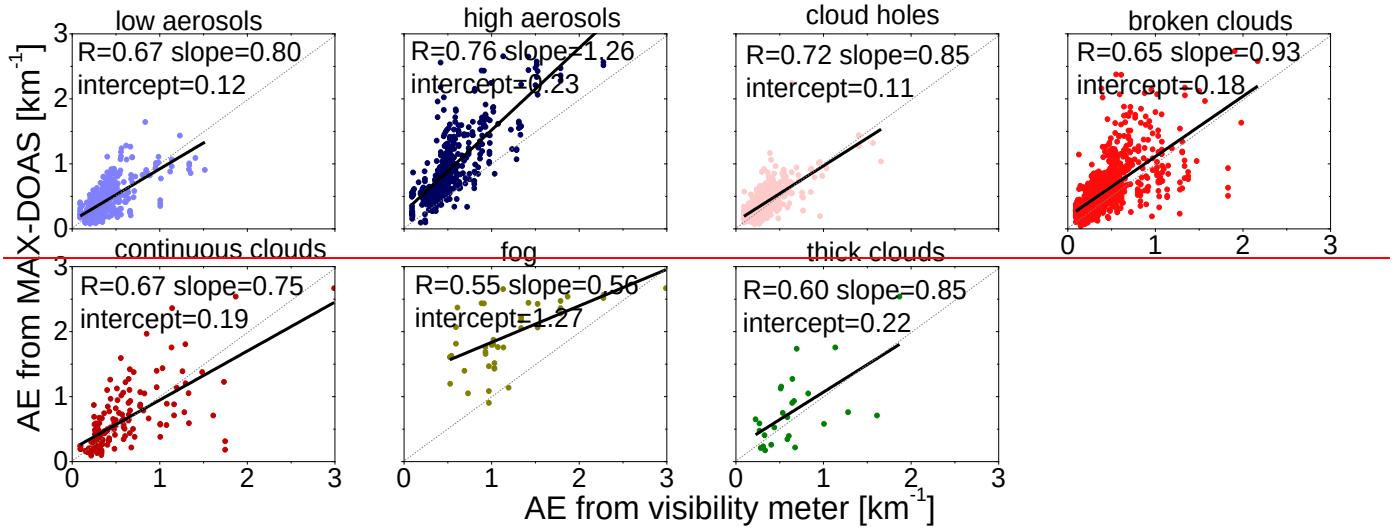

Figure 17: Same as Fig. 16 but for the comparisons of near surface aerosol extinctions with the visibility meter.

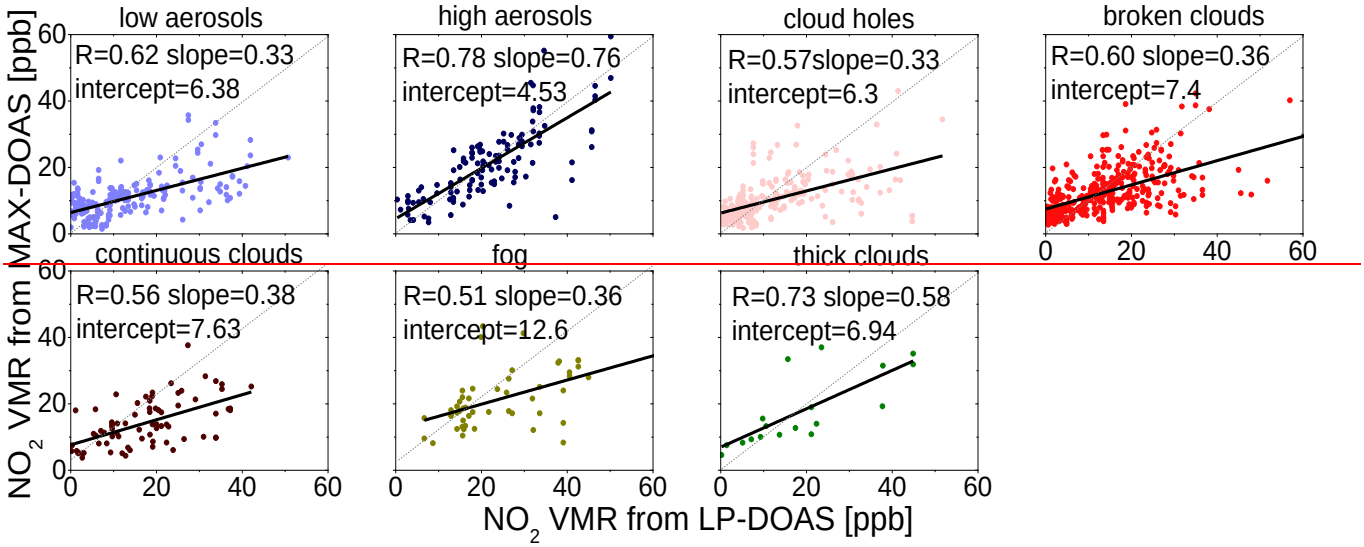

Figure 18: Same as Fig. 16 but for the comparisons of near surface NO_2 VMRs with the LP-DOAS.

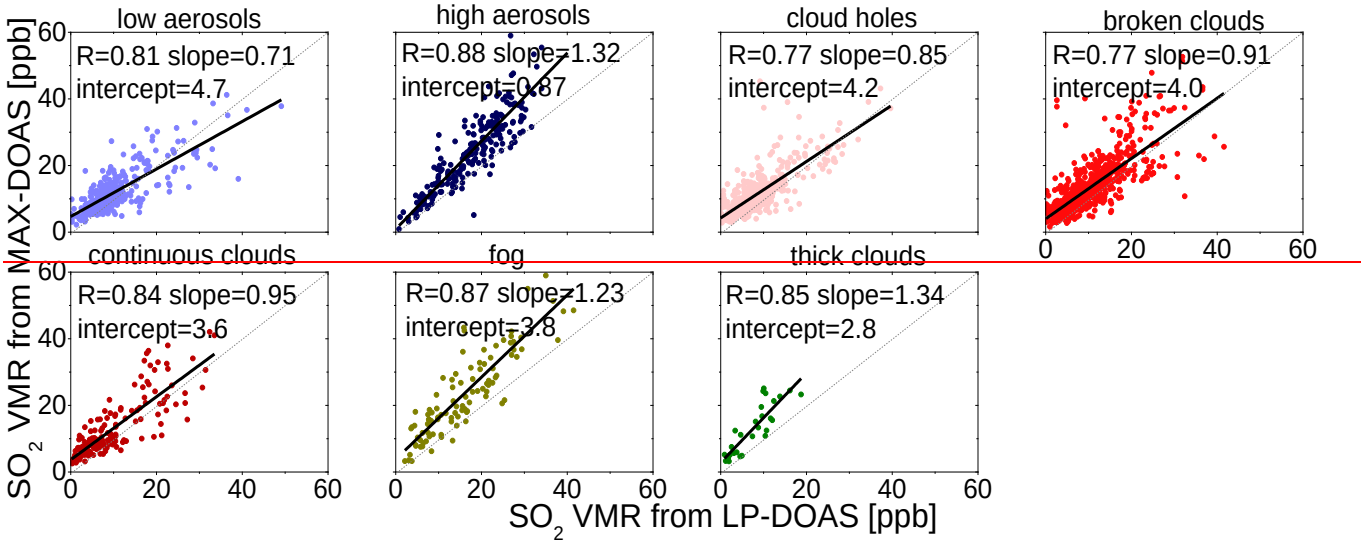

Figure 19: Same as Fig. 16 but for the comparisons of near surface SO_2 VMRs with the LP-DOAS.

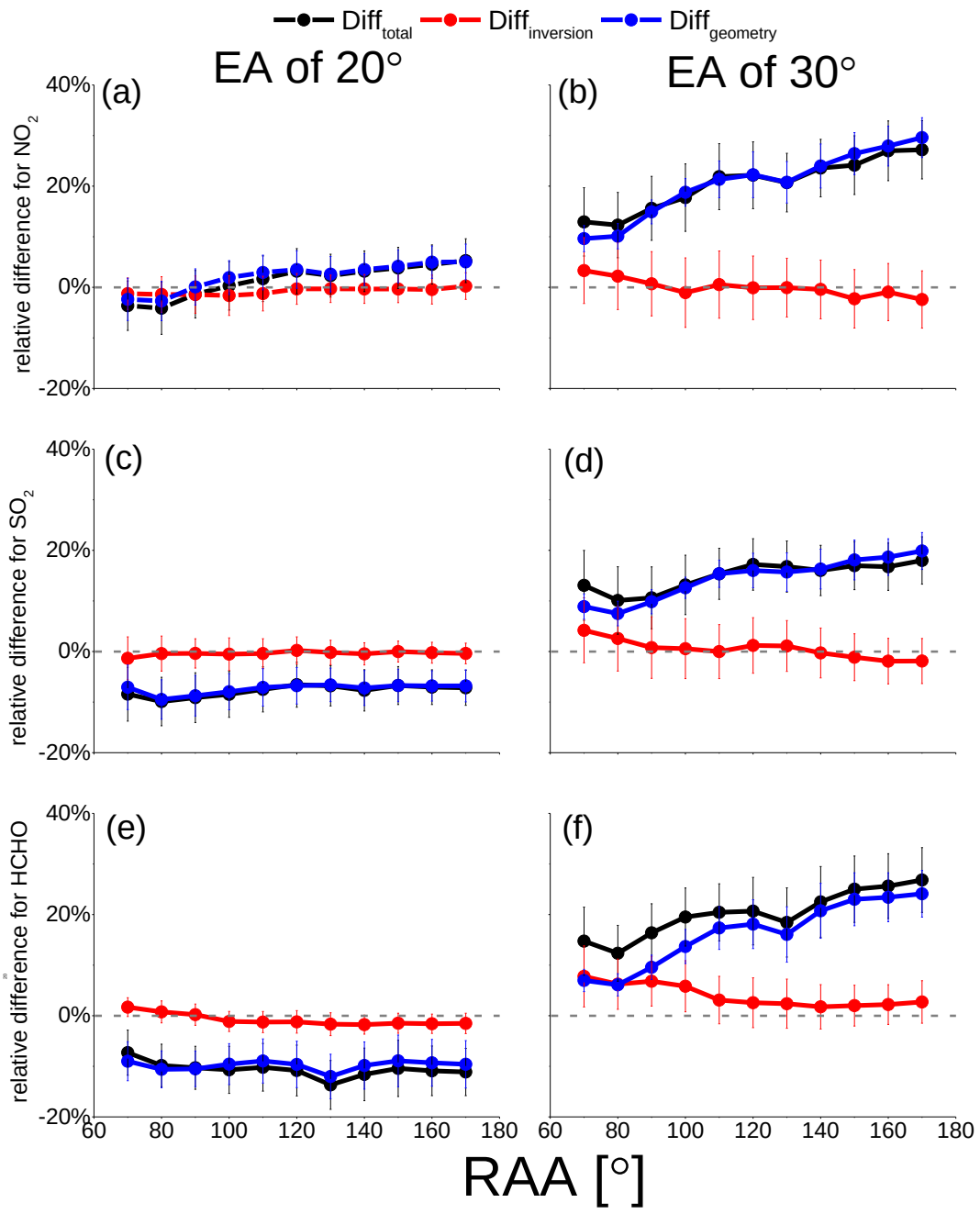

Figure ~~20~~10: Relative differences of the tropospheric NO_2 (top row), SO_2 (middle row) and HCHO (bottom row) VCDs derived by the geometric approximation and from the profile inversion ($Diff_{total}$, black dots) as function of the relative azimuth angle for elevation angles of 20 °(left) and 30 °(right). Also the differences caused by the errors of the profile retrieval ($Diff_{inversion}$, red dots) and of the geometric approximation ($Diff_{geometry}$, blue dots) are shown (see text).

~~(b)~~

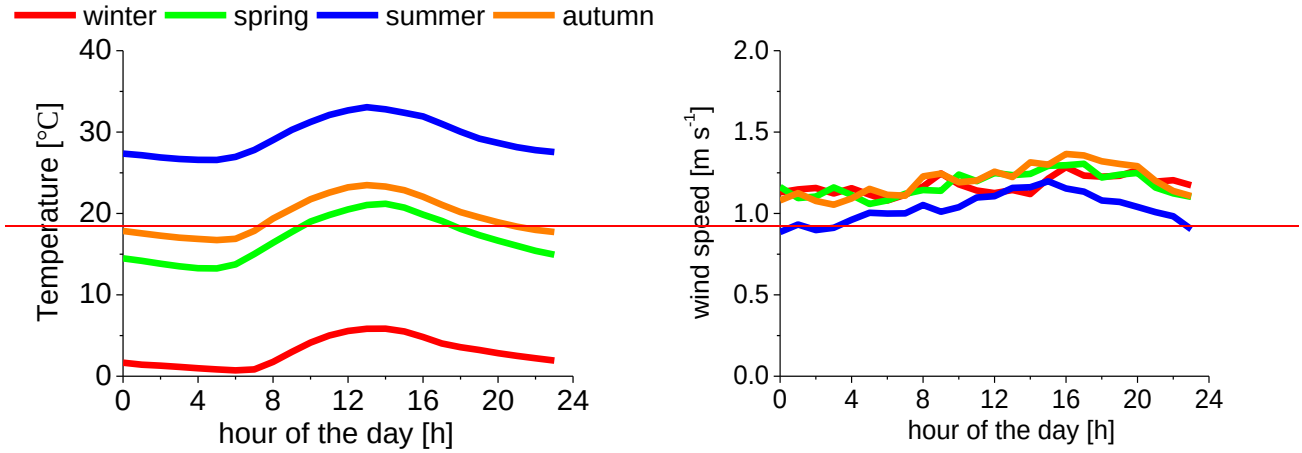

~~(c)~~

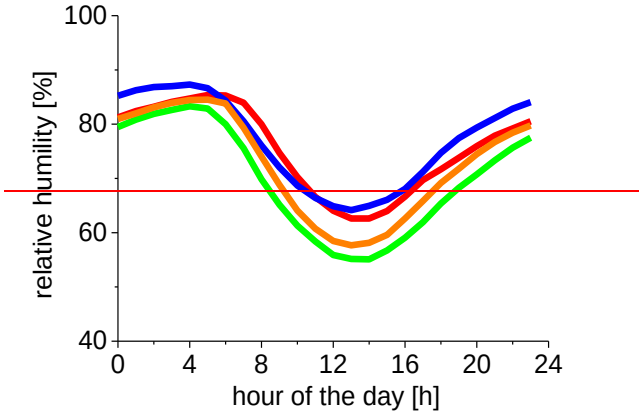

~~Figure 21: Seasonally mean diurnal variations (2011 to 2014) of ambient temperature (a), wind speed (b) and relative humidity (c) obtained from the observations of the weather station nearby the MAX-DOAS instrument.~~

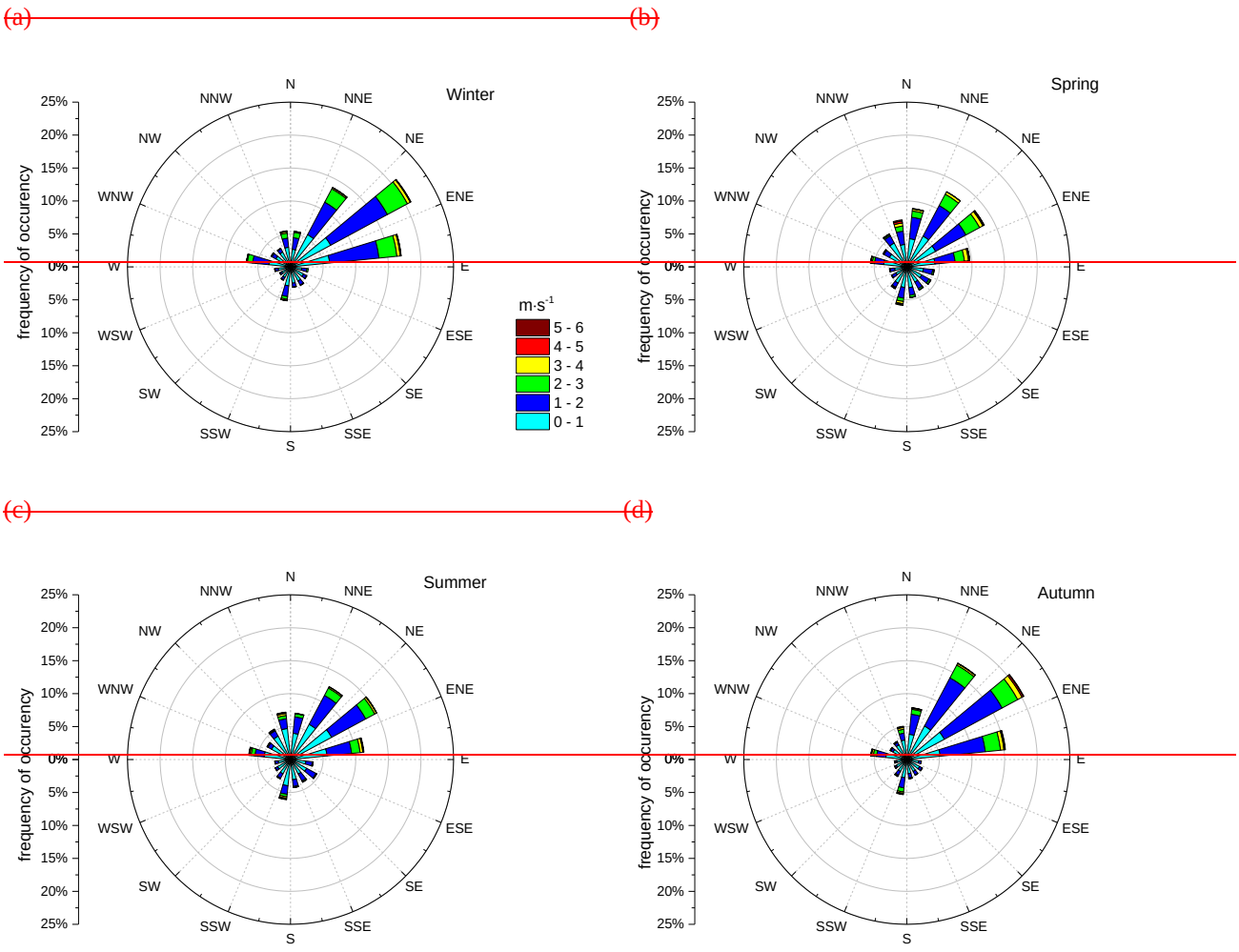

~~Figure 22: Wind rose diagrams based on all hourly averaged observations of the weather station for winter (a), spring (b), summer (c) and autumn (d) from 2011 to 2014.~~

(a)

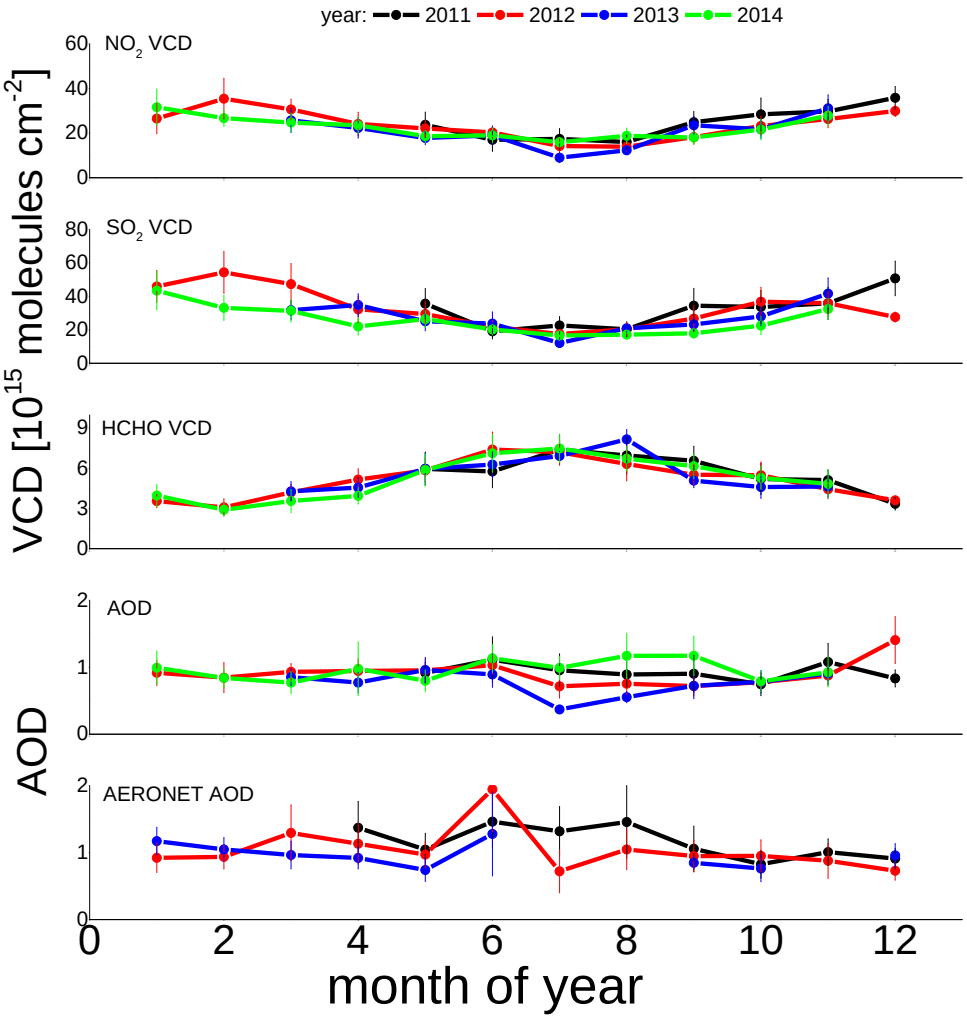
year: 2011 2012 2013 2014
NO2 VCD
SO2 VCD
HCHO VCD
AOD
AERONET AOD
VCD [10^15 molecules cm^-2]
AOD
month of year

(b)

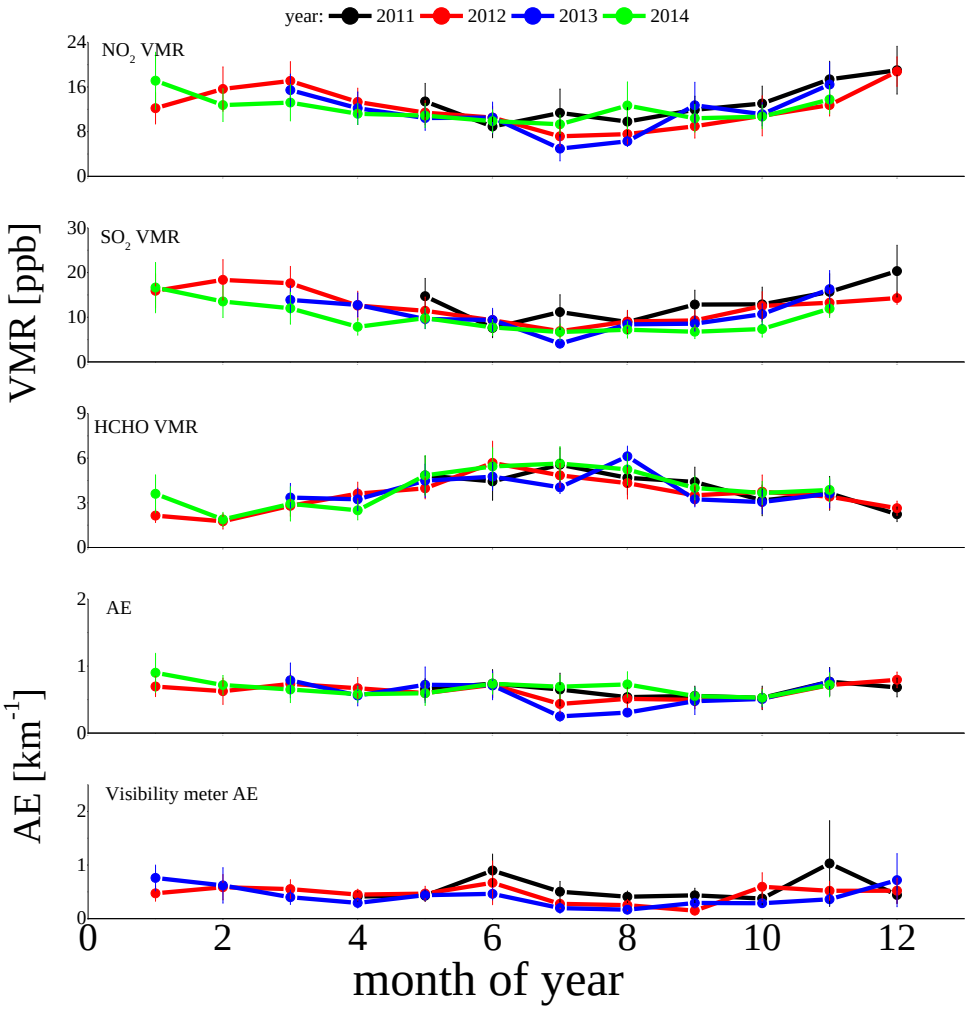
year: 2011 2012 2013 2014
NO2 VMR
SO2 VMR
HCHO VMR
AE
Visibility meter AE
VMR [ppb]
AE [km-1]
month of year

5

(c)

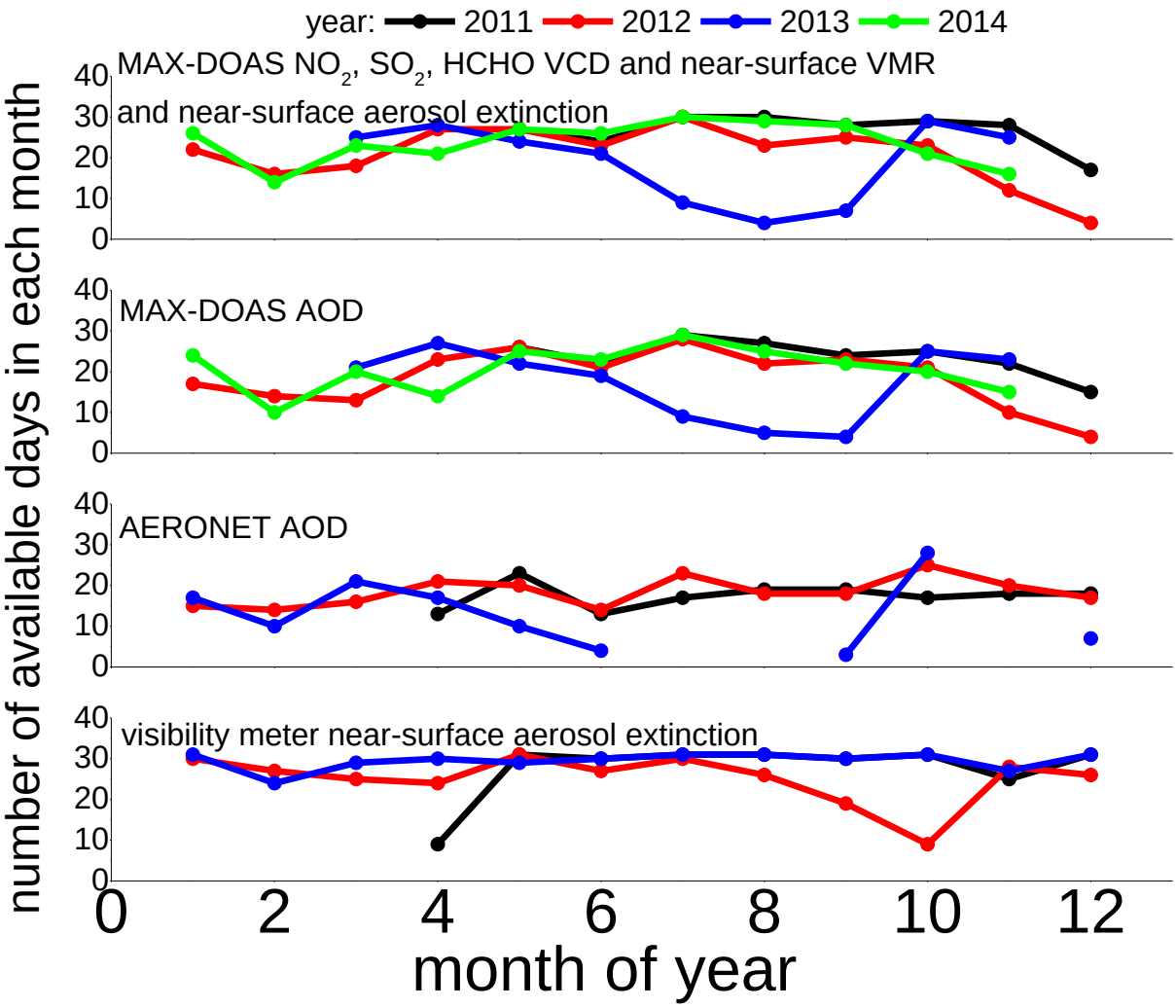

Figure ~~23~~11: Seasonal cycle of monthly mean MAX-DOAS results: VCD and AOD (a), and near-surface VMR of NO_2, SO_2 and HCHO and AE (b) for May 2011 to November 2014. The error bars represent the standard deviations. In addition to the MAX-DOAS data also AOD and AE from AERONET and visibility meter are shown, respectively. The numbers of available days in each month for MAX-DOAS measurements, AERONET and visibility meter are shown in subfigure (c). The different numbers of available AOD and trace gas data derived from MAX-DOAS are caused by the filter scheme (see Table 3).

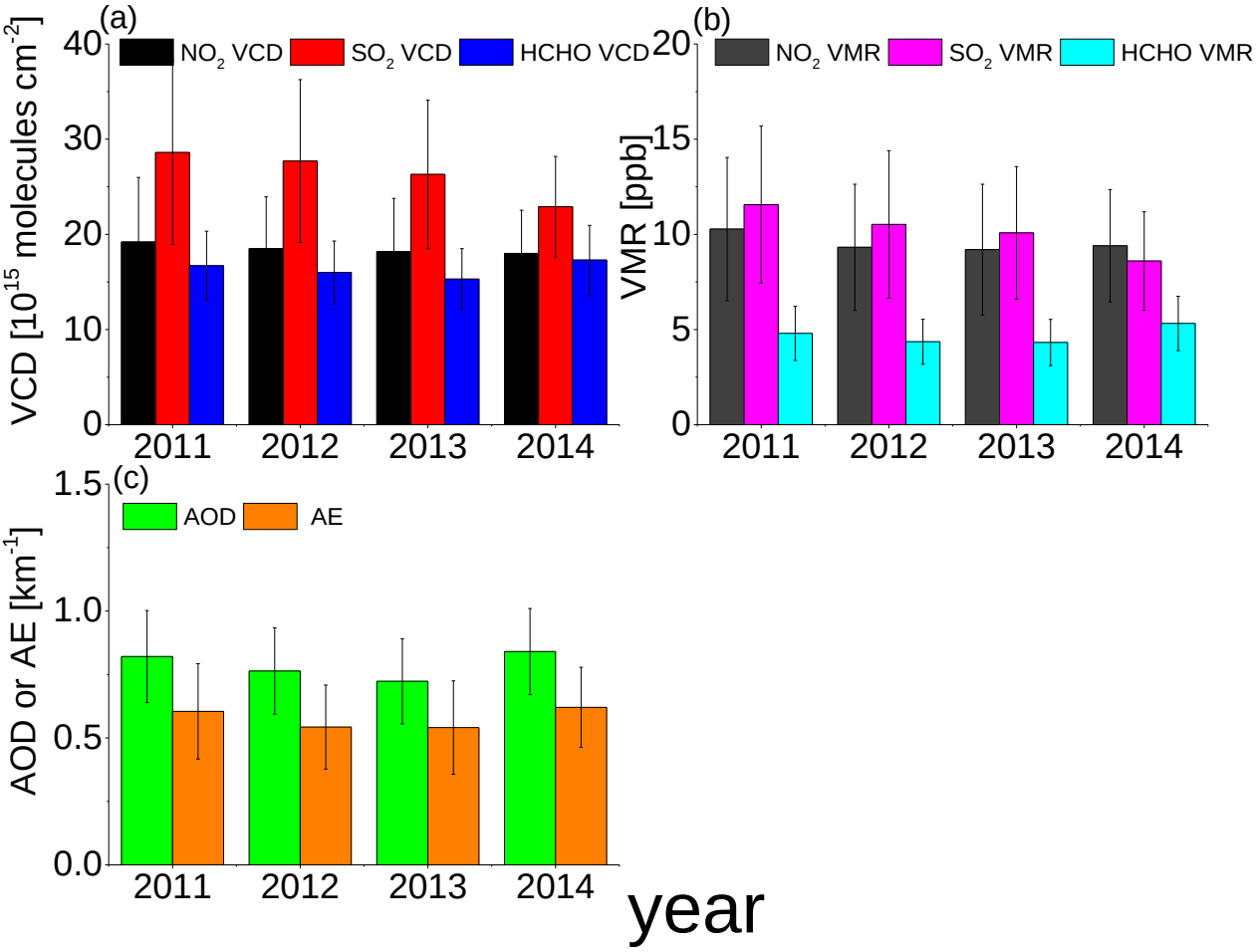

Figure ~~24~~12: Mean (May to November) VCDs (a) and near surface VMRs (b) of NO_2, SO_2, HCHO as well as AODs and near surface aerosol extinctions (c) for each year.

(a)

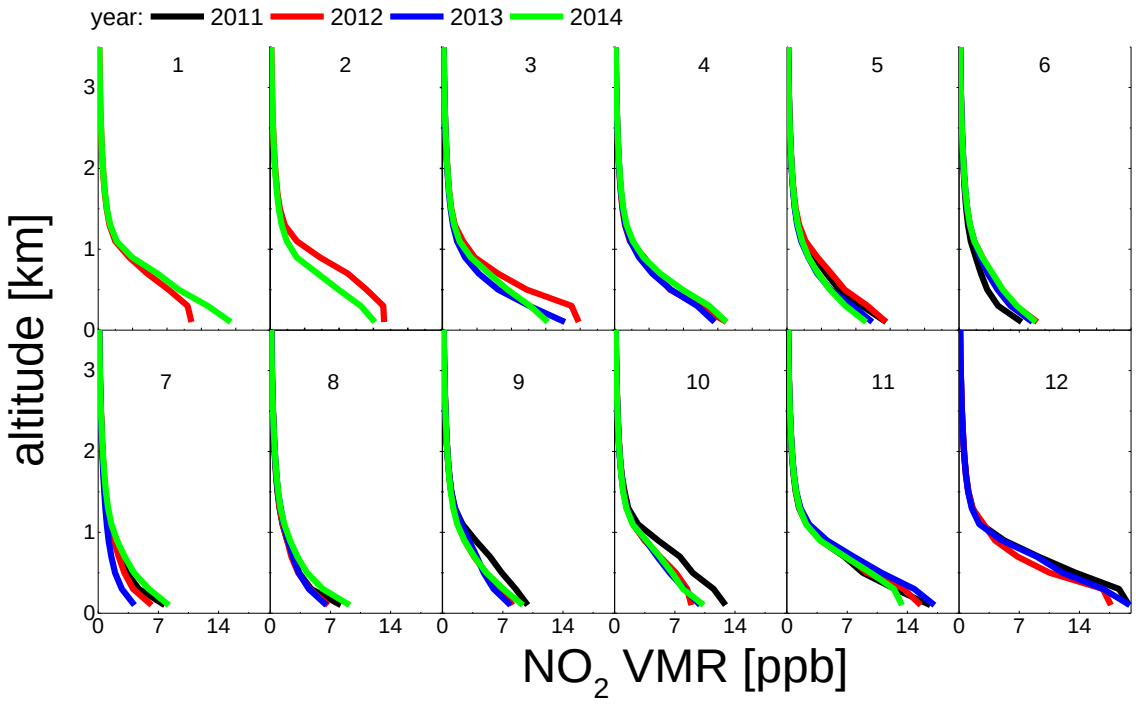
year: 2011 2012 2013 2014
1
2
3
4
5
6
7
8
9
10
11
12
altitude [km]
0
1
2
3
0
7
14
NO2 VMR [ppb]

(b)

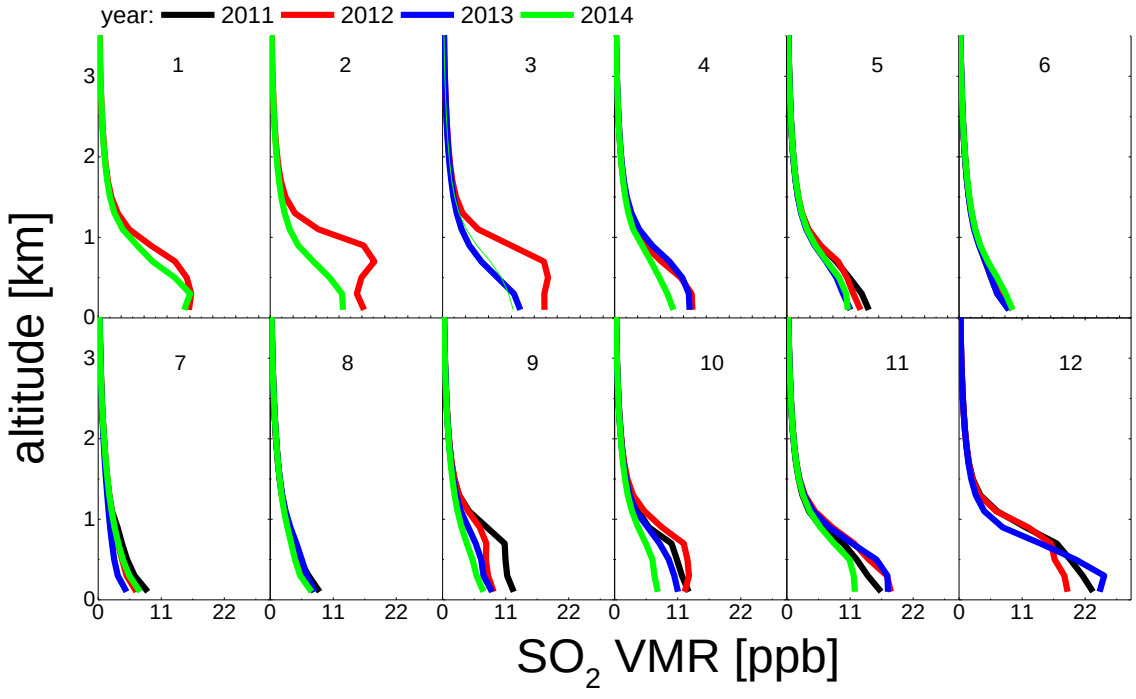
year: 2011 2012 2013 2014
1
2
3
4
5
6
7
8
9
10
11
12
altitude [km]
0
1
2
3
0
11
22
SO2 VMR [ppb]

5

(c)

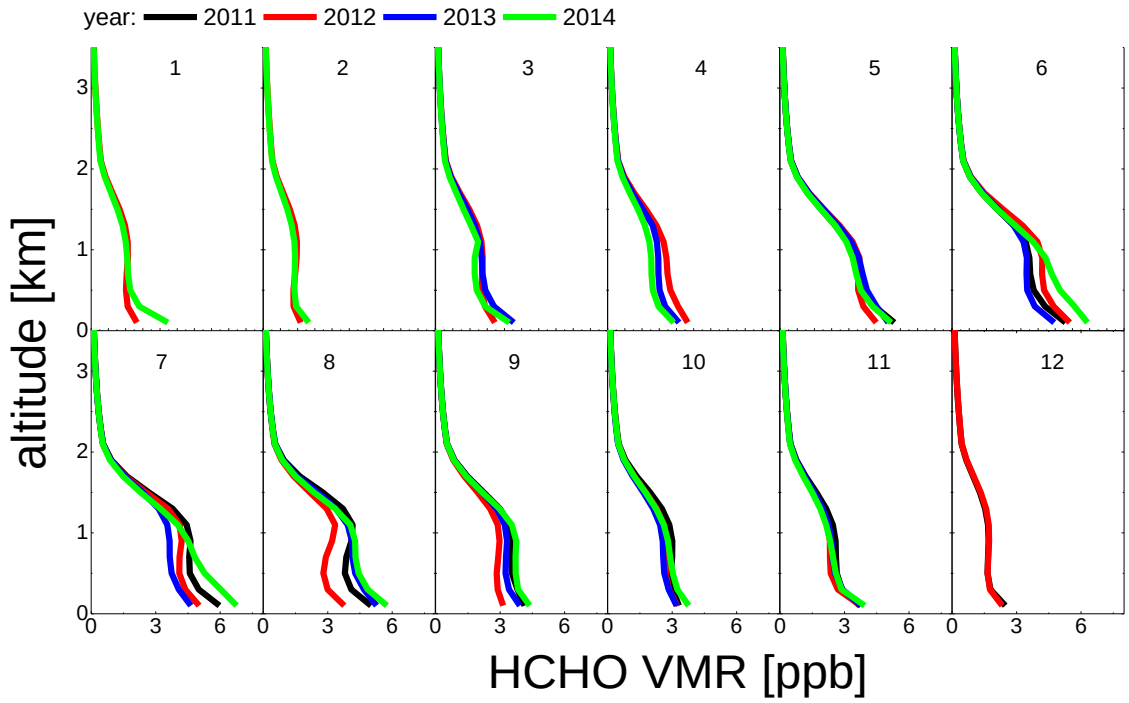
year: 2011 2012 2013 2014
1
2
3
4
5
6
7
8
9
10
11
12
altitude [km]
HCHO VMR [ppb]

(d)

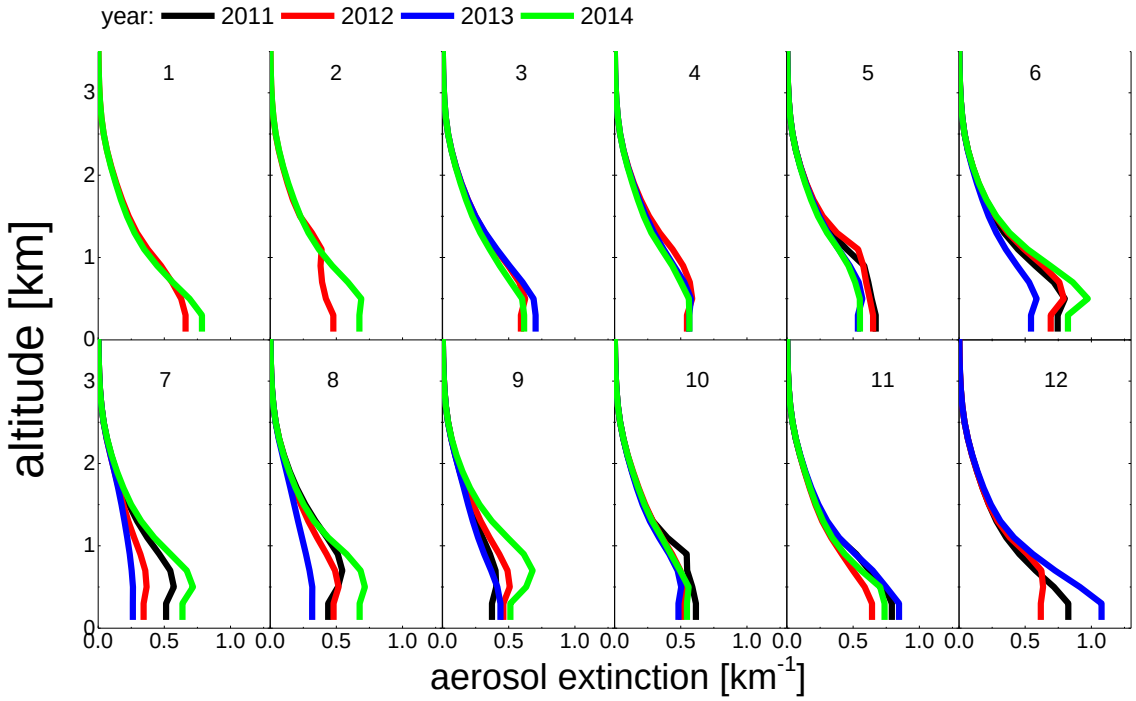
year: 2011 2012 2013 2014
1
2
3
4
5
6
7
8
9
10
11
12
altitude [km]
aerosol extinction [km-1]

5

Figure ~~25~~13: Monthly mean profiles of NO_2 (a), SO_2 (b), HCHO (c) VMRs (under clear and cloudy sky conditions except thick clouds and fog) and aerosol extinction (under clear sky conditions) (d) for the period from May 2011 to November 2014.

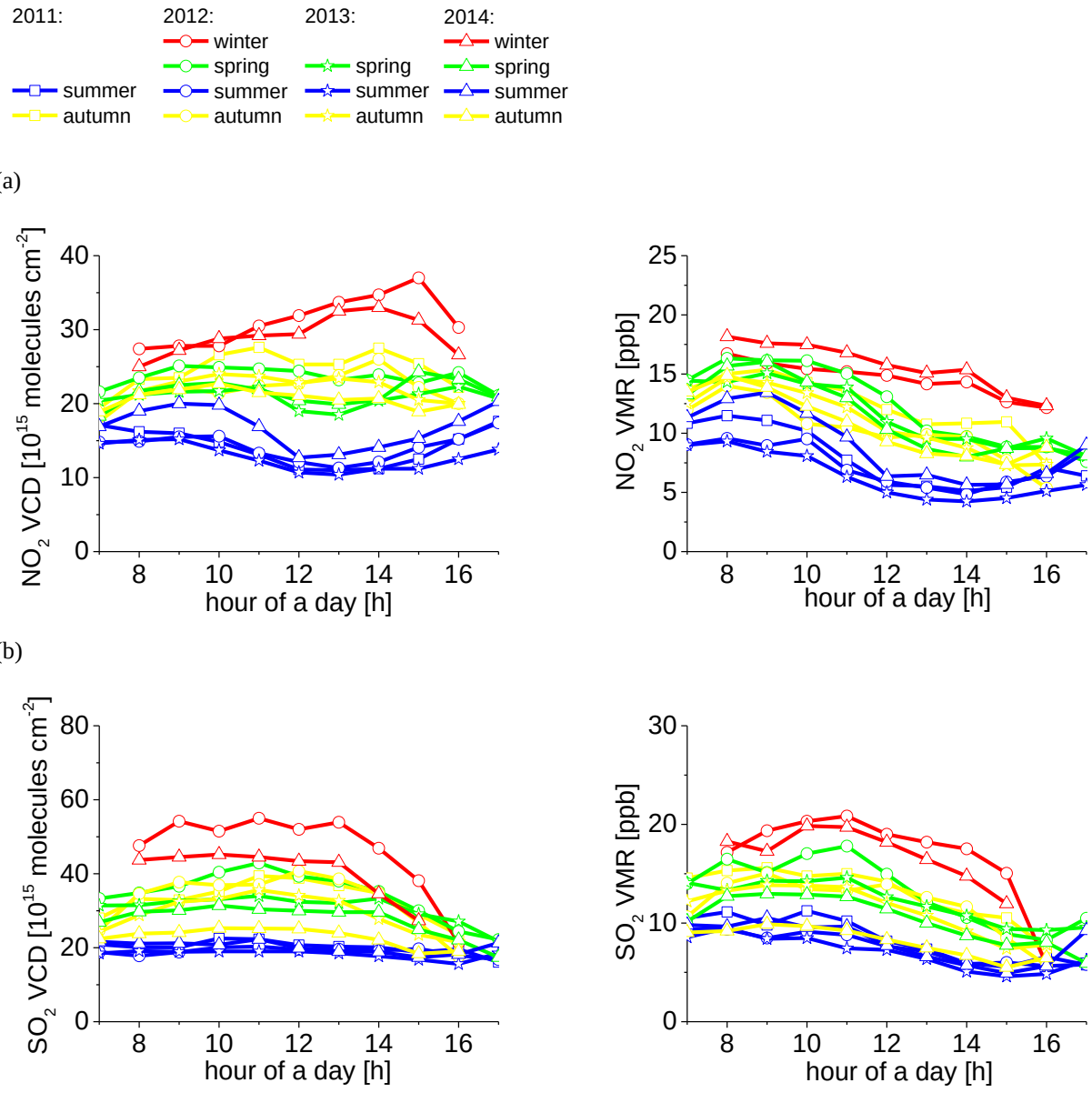

(c)

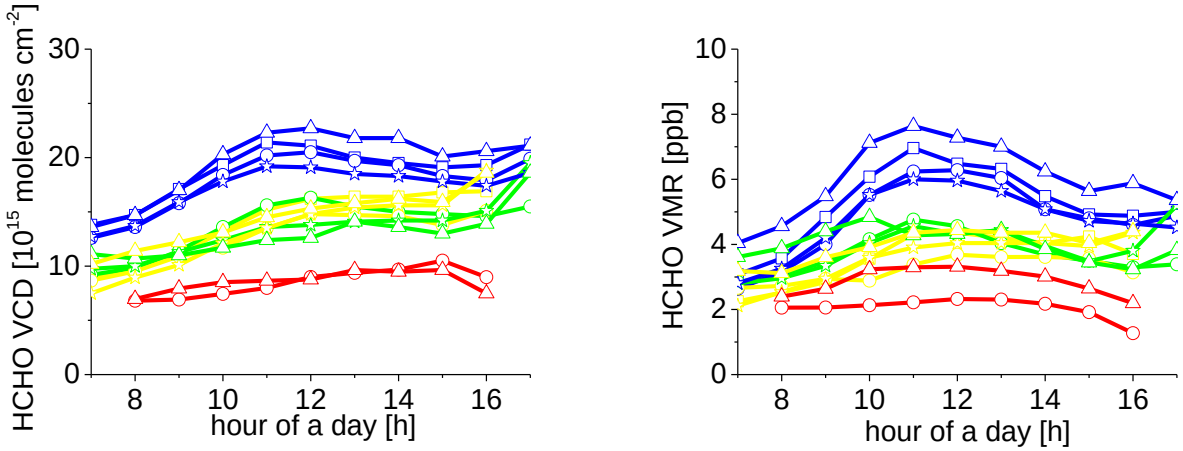

(d)

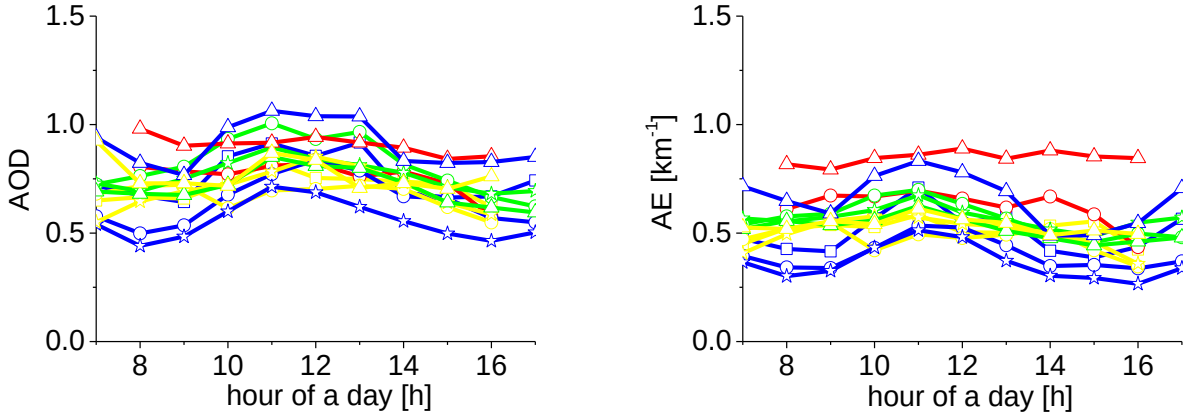

Figure ~~26~~14: Seasonally averaged diurnal variations of TG VCDs and AOD (left) and near surface values (right) of NO_2 (a), SO_2 (b), HCHO (c) and aerosols (d) from 2011 to 2014.

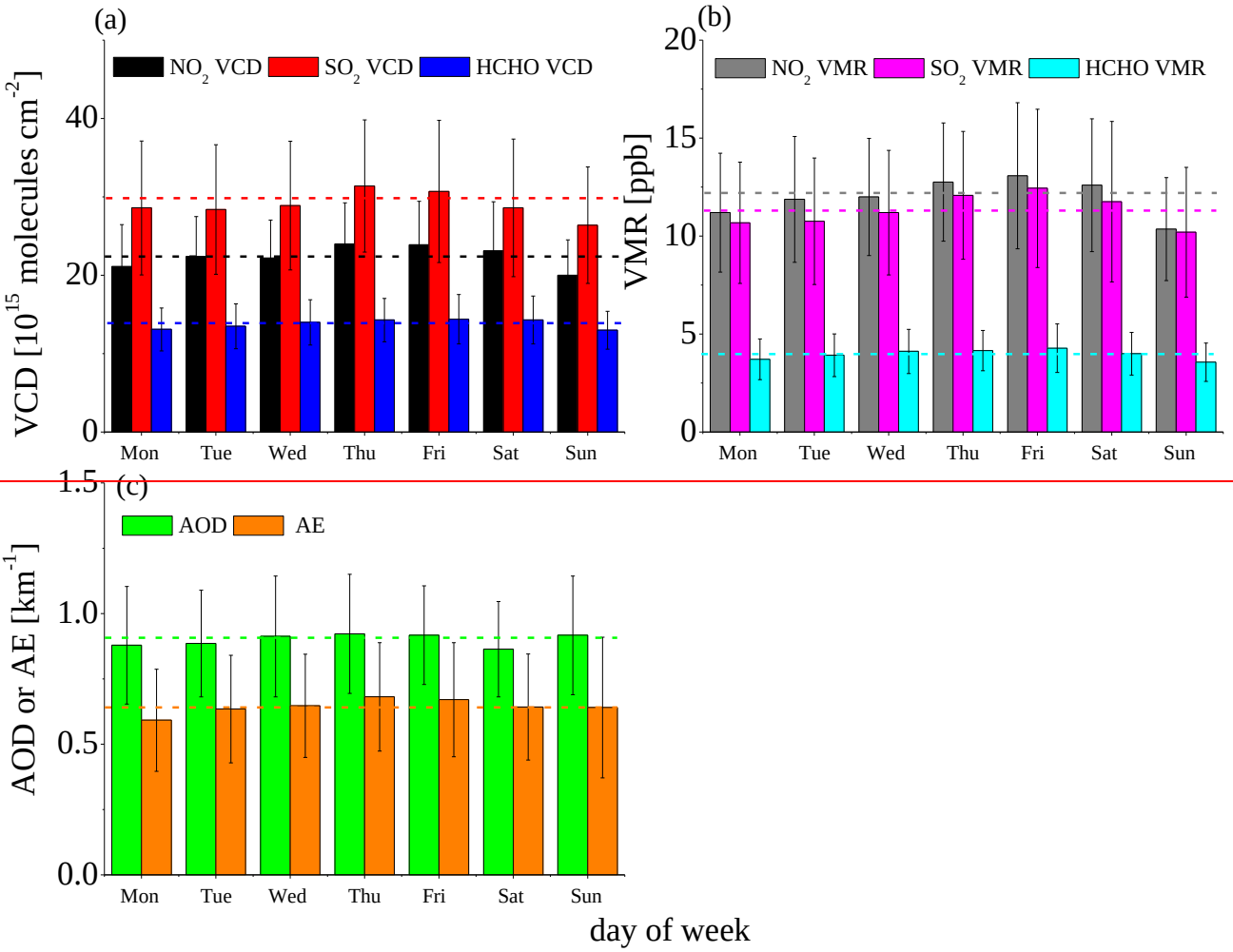

~~**Figure 27: Mean weekly cycles of VCDs (a) and near-surface VMRs (b) of NO_2, SO_2 and HCHO as well as the AODs and near-surface AEs (c) for all MAX-DOAS observations from 2011 to 2014. The dashed lines denote the mean values during the working days from Monday to Friday (same colours as for the daily averages).**~~

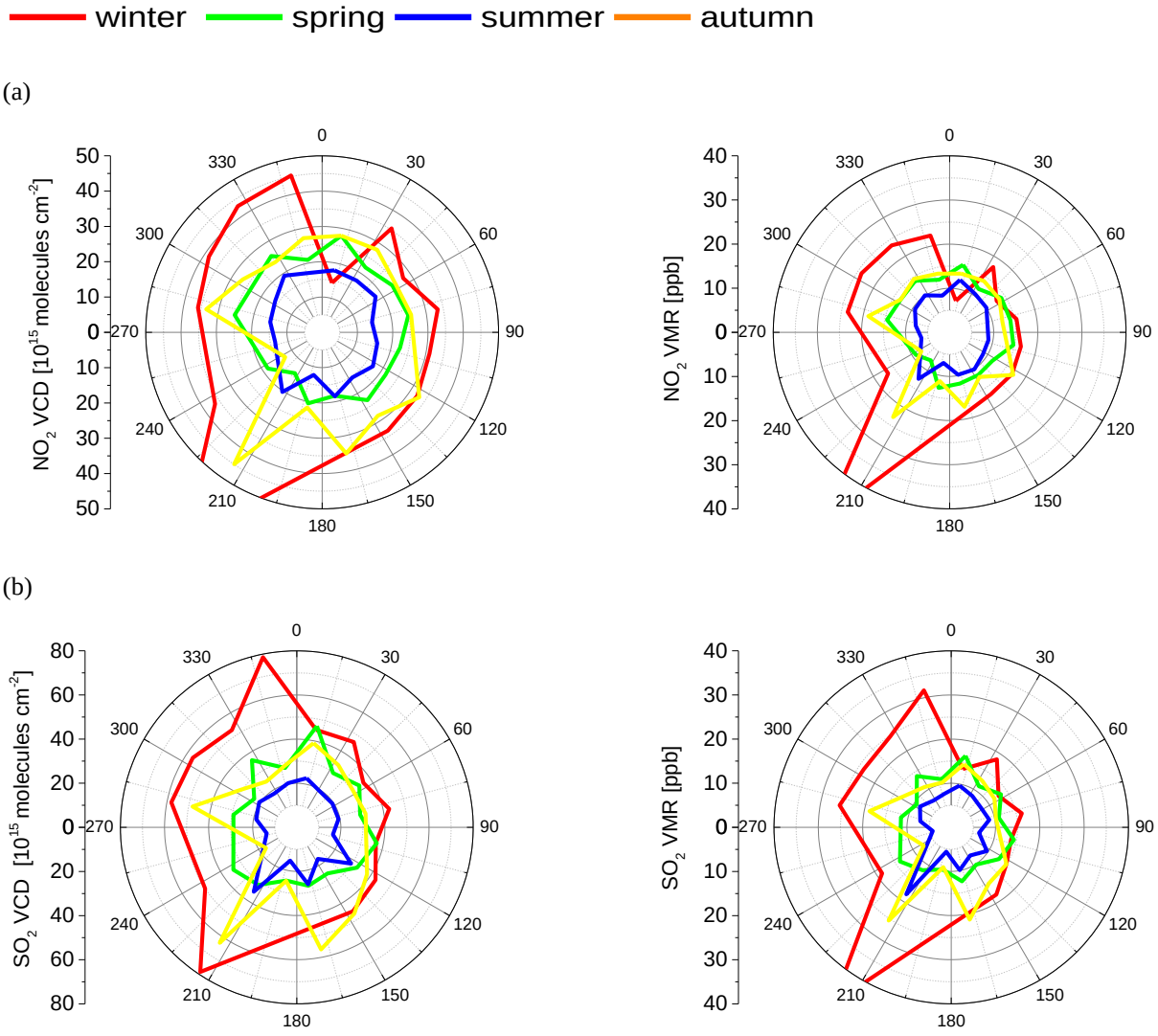
winter
spring
summer
autumn
(a)
NO2 VCD [10^15 molecules cm^-2]
NO2 VMR [ppb]
(b)
SO2 VCD [10^15 molecules cm^-2]
SO2 VMR [ppb]
0
30
60
90
120
150
180
210
240
270
300
330

(c)

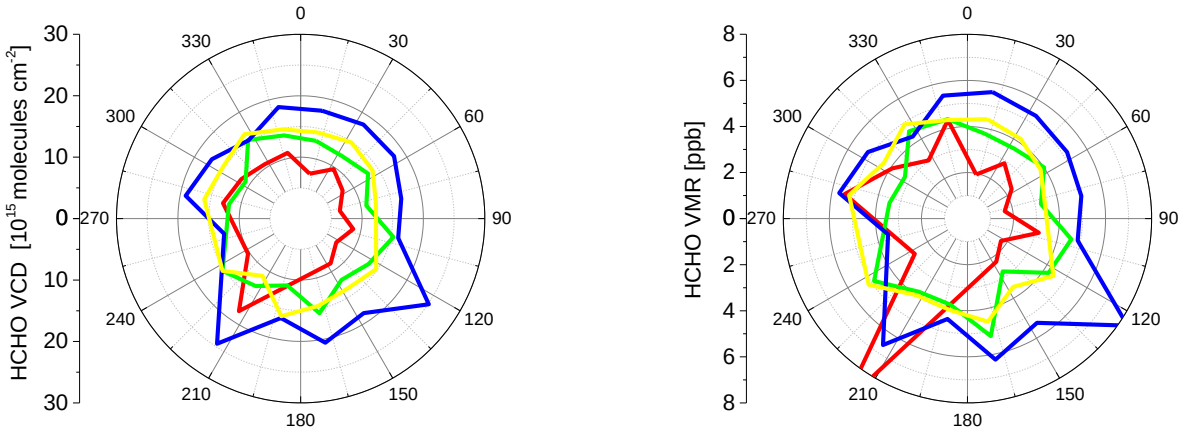

(d)

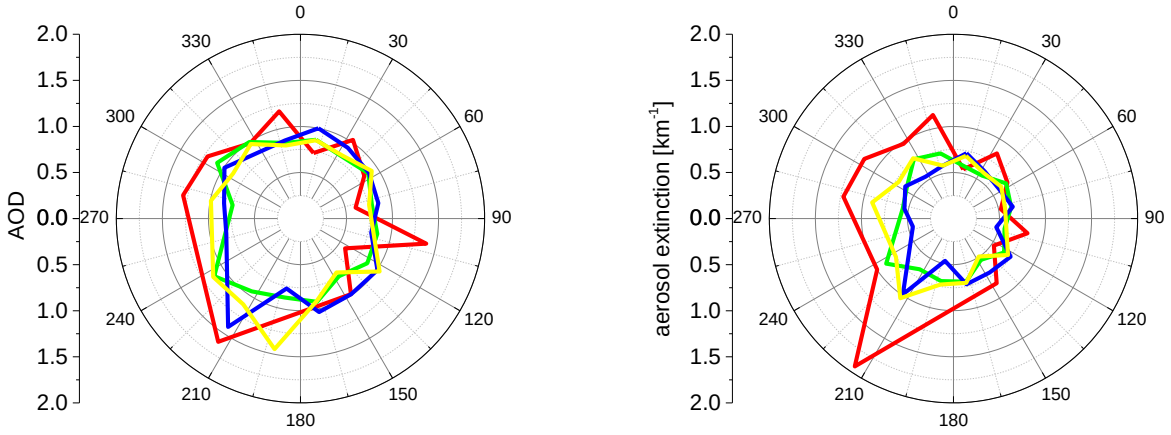

Figure ~~28~~15: Dependencies of VCDs and AODs (left) and near-surface VMRs and AEs (right) of NO_2 (a), SO_2 (b), HCHO (c) and aerosols (d) on wind directions for individual seasons (different colours).

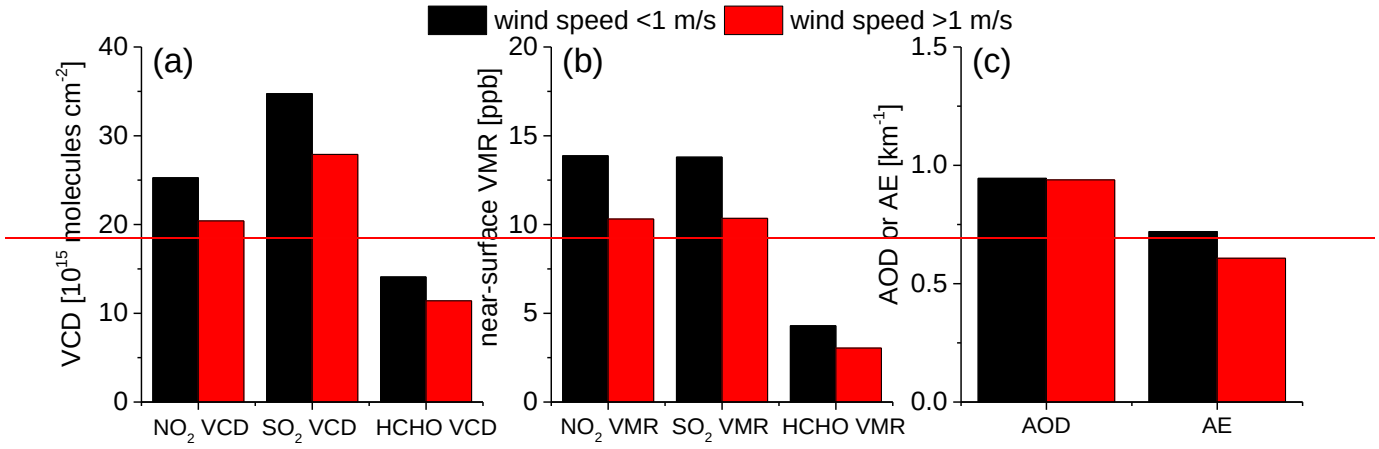

Figure 29: Comparisons of VCDs (a) and near-surface VMRs (b) of NO_2, SO_2 and HCHO, as well as AODs and near-surface AEs for different wind speeds (smaller than 1m/s or larger than 1m/s).

Table 1 Settings used for the O_4, NO_2, SO_2 and HCHO DOAS analyses

Parameter	~~Data s~~Sources	~~Fitting interval~~species			
		O_4	NO_2	SO_2	HCHO
~~Wavelength range~~Fitting interval		351-390nm	351-390nm	307.8-330nm	324.6-359nm
~~NO_2~~ ~~O_3~~ ~~O_4~~ ~~SO_2~~ Cross section~~HCHO~~	NO_2: Vandaele et al. (1998), 220 K, 294 K	×	×	× (only 294 K)	× (only 294 K), I_0-corrected* (10^{17} molecules/cm^2)
	O_3: Bogumil et al., (2003), 223 K and 243 K	×(only 223 K)	×(only 223 K)	×	× (only 223 K) I_0-corrected* (10^{18} molecules/cm^2)
	O_4: Thalman and Volkamer (2013), 293 K	×	×	×	×
				×	×
	SO_2: Bogumil et al. (2003), 293 K HCHO: Meller and Moortgat (2000), 293 K	×	×	×	×
Ring ~~Ring~~	Two Ring spectra calculated with DOASIS (Kraus, 2006; Wagner et al., 2009)	×	×	×	×
Polynomial degree		3	3	5	5
Intensity offset		constant	constant	constant	constant

* solar I_0 correction, Aliwell et al., 2002

5

Table 2 Different filters and corresponding thresholds applied to the retrieved SCDs. Also the corresponding fractions of screened data are shown. (SZA: solar zenith angle; RIO: relative intensity offset; RMS: root mean square of the spectral residual)

O4 and NO_2		SO_2		HCHO	
filter	percentage	filter	percentage	filter	percentage
SZA < 75°	6.2%	SZA < 75°	5.8%	SZA < 75°	6.1%
RIO < 0.01	5.6%	RIO < 0.01	1.1%	RIO < 0.01	7.1%
RMS < 0.003	0.3%	RMS < 0.01	0.2%	RMS < 0.003	0.2%

Table 3 Filter scheme of aerosol and trace gas results derived from MAX-DOAS observations. Filled circles (●): use of measurement is recommended; Open circles (○): use of measurement is not recommended.

	AOD	Aerosol extinction near surface	Profile of aerosol extinction	VCD	VMR near surface	Profile of VMRs
Low aerosols	●	●	●	●	●	●
High aerosols	●	●	●	●	●	●
Cloud holes	○	●	○	●	●	●
Broken clouds	○	●	○	●	●	●
Continuous clouds	○	●	○	●	●	●
fog	○	○	○	○	○	○
Thick clouds	○	○	○	○	○	○

Table 4 Averaged error budget (in %) of the retrieved TG VCDs and AOD, and near-surface (0–200 m) TG VMRs and AE. The total uncertainty is calculated by adding the different error terms in Gaussian error propagation.

	0-200 m				VCD or AOD			
	AE	NO_2	SO_2	HCHO	AOD	NO_2	SO_2	HCHO
Smoothing and noise error	10	12	19	50	6	17	25	50
Algorithm error	4	3	4	4	8	11	10	11
Cross section error	5	3	5	9	5	3	5	9
Related to temperature dependence of cross section	10	2	3	6	10	2	3	6
Related to the aerosol retrieval (only for trace gases)	-	16	16	16	-	15	15	15
Total	16	21	26	54	15	25	31	54

Table 5 Correlation coefficients between hourly averaged trace gas VCDs and AODs (for clear sky conditions) as well as between VMRs and aerosol extinction near the surface (for clear and cloudy conditions except thick clouds and fog). The numbers of the data ~~point~~ used for the ~~analysis~~ analyses are given for each season.

	winter		spring		summer		autumn	
	column	surface	column	surface	column	surface	column	surface
Number of observations	375	525	1339	1739	1308	1830	1142	1676
NO_2	0.51	0.69	0.37	0.58	0.48	0.63	0.44	0.65
SO_2	0.52	0.69	0.45	0.62	0.45	0.62	0.44	0.66
HCHO	0.77	0.81	0.51	0.62	0.35	0.62	0.57	0.69

Supplement for "Ground-based MAX-DOAS observations of tropospheric aerosols, NO_2, SO_2 and HCHO in Wuxi, China, from 2011 to 2014"

Y~~.~~ang Wang[1], Johannes~~.~~ Lampel[1,2], Pinhua Xie ~~P. H. Xie~~[3,4,5], Steffen~~.~~ Beirle[1], Ang~~.~~ Li[3], De~~.~~ xia~~X~~ Wu[3], and T~~.~~homas Wagner[1]

[1] Max Planck Institute for Chemistry, Mainz, ~~55128,~~ Germany
[2] Institute of Environmental Physics, University of Heidelberg, Heidelberg, ~~69120,~~ Germany
[3] Anhui Institute of Optics and Fine Mechanics, Key laboratory of Environmental Optics and Technology, Chinese Academy of Sciences, Hefei, ~~230031,~~ China
[4] CAS Center for Excellence in Urban Atmospheric Environment, Institute of Urban Environment, Chinese Academy of Sciences, Xiamen, ~~361021,~~ China
[5] School of Environmental Science and Optoelectronic Technology, University of Science and Technology of China, Hefei, ~~230026,~~ China

Correspondence to: Y~~ang~~ Wang (y.wang@mpic.de); P~~.H.~~inhua Xie (phxie@aiofm.ac.cn)

1 Meteorological conditions

The ground-based weather station near the MAX-DOAS instrument records the ambient temperature, wind speed and direction, and relative humidity during the whole observation period. Figure S1 shows their seasonally mean diurnal variations. A large seasonal difference occurs only for the ambient temperature, but not for the wind speed and relative humidity. Similar diurnal variations for the three meteorology parameters are found for the different seasons. The ambient temperature and the relative humidity reach the maximum and minimum values around noon, respectively. The wind speed has the maximum value around 16:00 LT. The wind directions recorded by the same weather station are shown by the wind roses for the individual seasons in Fig. S2, indicating that the dominant wind is from the northeast in all seasons. In spring and summer the non-dominant wind directions occur more frequently than in winter and autumn.

~~1~~ 2 DOAS analysis and data screening

In the DOAS analysis, the slant column densities (SCDs) of the trace gases (TGs) are retrieved from the off-axis spectra using a zenith measurement from the same elevation sequence as the Fraunhofer reference spectrum (FRS). As the latter also contains (usually small) absorptions features, the resulting SCD actually represents the differences between the SCDs of the measured spectrum and the FRS. This difference is usually referred to as the differential SCD (dSCD). The use of a FRS from the same elevation sequence can minimise any effects caused by changes of the properties of the instrument (relevant for long term analyses) and the stratospheric absorptions (relevant for measurements at high solar zenith angle (SZA)). The effect of rotational Raman scattering is considered by including a Ring spectrum (Shefov 1959; Grainger and Ring, 1962; Solomon et al., 1987; Chance and Spurr, 1997; ~~Solomon et al., 1987;~~ Wagner et al., 2009) computed by the DOASIS

software (Kraus, 2006, using a routine from Bussemer 1993). To account for the different wavelength dependencies of the filling-in in clear and cloudy skies, an additional Ring spectrum as described in Wagner et al. (2009) is also included.

For the retrieval of O_4 and NO_2, the wavelength range of 351 to 390 nm is selected, covering two O_4 absorption bands and several NO_2 absorption bands. A 3rd order polynomial is used. Besides the NO_2 cross section at the temperature of 294 K, another cross section at 220 K is also included in the fit to account for the temperature dependence of the NO_2 absorptions. The detailed DOAS settings for the retrieval are listed in Table 1 of the main manuscript. In Fig. ~~S1a~~ S3a and b, the O_4 and NO_2 dSCDs from all measurements are plotted against SZA. NO_2 and O_4 dSCDs show an obvious systematic increase or decrease with ~~the increase of~~increasing SZA, respectively, for SZA larger than 75 °. For NO_2 this behaviour can be explained by the larger differences of the stratospheric light paths between the measurement and the FRS for large SZA. The opposite dependencies in the morning and evening (indicated by the different solar azimuth angles) are due to the decrease or increase of the stratospheric light path with time in the morning and evening, respectively. The O_4 behaviour might be related to the interference of the so called intensity offset (see below) and the O_4 absorption. But this hypothesis is still not clearly confirmed.

A quite large relative intensity offset (RIO) is found for measurements at large SZAs as indicated in Fig. ~~S1c~~S3c, which implies a possible interference of the offset corrections and the derived TG dSCDs (see also Coburn et al., 2011). Thus we skip the data for the SZA larger than 75 ° to avoid the interference with the stratospheric contributions and RIO on the retrieved tropospheric dSCDs.

SO_2 dSCDs are retrieved in the wavelength interval from 307.8 nm to 330 nm including O_3, SO_2, HCHO cross sections and Ring spectra shown in Table 1 of the main manuscript. Wang et. al (2014) performed sensitivity studies to find the optimum wavelength interval which minimizes both random and systematic uncertainties on the SO_2 retrieval. They found that the wavelength range of 305 to 317.8 nm provides the lowest fitting errors. Below 305 nm, interference with the strong ozone absorption can affect the SO_2 retrieval. At small wavelengths also the signal to noise ratio decreases. Considering the rather low sensitivity of the miniature spectrometer in the UV range used in our study compared to scientific grade spectrometer used in the study of Wang et. al (2014), here we limit the lower wavelength range to 307.8 nm. We also changed the upper wavelength range to 330 nm to minimise the possible interference with other species. The SO_2, O_3 and Ring dSCDs as well as the intensity offset are plotted against SZAs in Fig. ~~S2~~S4. At large SZAs strong changes of all quantities are found indicating the possible interference of the stratospheric ozone absorptions and the intensity offset on the SO_2 retrieval. To avoid these interferences, we screen the SO_2 dSCD data for SZA larger than 75 °.

HCHO dSCDs are retrieved in the wavelength interval from 324.6 to 359 nm including O_3, O_4, SO_2, HCHO cross sections and Ring spectra shown in Table 1 of the main manuscript. Pinardi et. al (2013) found that the interferences between BrO, Ring spectrum and HCHO can strongly affect the retrieved HCHO dSCDs and they recommended the wavelength range of 336.5 to 359 nm, to minimise the uncertainties of the HCHO retrieval. In the wavelength range below 336.5 nm, the ozone absorption interferes with the HCHO retrieval, like for SO_2. However this conclusion is only appropriate for the retrieval with the daily noon zenith spectrum as the FRS. In this study, the sequential FRS is used. Because BrO is mostly located in

the stratosphere, the difference of the BrO absorptions between the measurement and the FRS is negligible (the differential optical depth of the BrO absorption is typical only 1×10^{-4}) and much lower than using a daily noon FRS (typical 6×10^{-4}). Considering that the BrO absorption signal is too weak to impact the HCHO retrieval, the BrO cross section is not included in the HCHO DOAS fit in this study. Tropospheric BrO is not expected to be found due to large NO_2 concentrations (e.g. Holla et al 2015). Moreover similar to the BrO interference, the effective stratospheric ozone absorption is also much smaller if a sequential FRS is used compared to a daily noon FRS. Thus the wavelength interval can be extended to a shorter wavelength to cover more and stronger absorption bands of HCHO. Moreover a wider wavelength range usually makes the fit more stable, but at shorter wavelengths the interference of the ozone absorption is also stronger. To find the optimal retrieval wavelength interval, the examples of the HCHO retrieval in three different wavelength ranges of 310 to 359 nm, 324.6 to 359 nm and 336.5 to 359 nm are shown in Fig. ~~S3~~S5. The measured structure from the DOAS fit in the wavelength range 310 to 359 nm indicates the strong interference of the ozone absorption. In addition, the HCHO dSCDs and the fitting errors in the three wavelength ranges on two days with low and high HCHO load are shown in Fig. ~~S4~~S6. We find that the HCHO dSCDs in the wavelength range of 324.6 to 359 nm are consistent with those in 336.5 to 359 nm, which is recommended by Pinardi~~,~~ et. al (2013). And both of them are quite different from the values in the wavelength range of 310 to 359 nm, especially on the day with the low HCHO load. The reverse "U" diurnal variation of the HCHO dSCDs in the wavelength range of 310 to 359 nm is an indication for the strong interference of the stratospheric ozone absorption. Moreover the wavelength range of 324.6 to 359 nm has much smaller fitting errors than the wavelength range of 336.5 to 359 nm. Thus we conclude that in general the wavelength range of 324.6 to 359 nm is the optimal wavelength range in which the ozone interference is weak and the fitting error is small. To avoid remaining interferences of the HCHO results with the stratospheric ozone absorption and intensity offset we exclude the HCHO dSCD for SZA > 75 °(see~~.~~ Fig. ~~S5~~S7). After applying these filters, the mean RMS of the residual is 6×10^{-4} for NO_2, O_4 and HCHO, and 1.3×10^{-3} for SO_2. The detection limit of the dSCDs (assumed ~~to~~ as two times of the mean RMS) is 3×10^{15} molecules cm^{-2} for NO_2, 5×10^{41} molecules^2 cm^{-5} for O_4, 5×10^{15} molecules cm^{-2} for SO_2, 5×10^{15} molecules cm^{-2} for HCHO. Only 0.7%, 0.4%, 3.3%, 6.6% of the filtered measurements have results below the respective detection limits for NO_2, O_4, SO_2 and HCHO, respectively.

~~2~~ 3 PriAM inversion algorithm

The profile inversion is based on the fact that the vertical distribution of the light paths depends on the elevation angle of the observation. The vertical trace gas profiles are assumed to be constant for the duration of the elevation angle sequence and also in horizontal dimensions. If the light paths are well-known, vertical trace gas profiles can be derived from a set of dSCDs for the different elevation angles. Besides the observation geometry and sun position, scattering on air molecules (Rayleigh scattering), aerosols and cloud particles (often referred to as Mie scattering) determine the atmospheric light paths.

Opposed to the well-known Rayleigh scattering, scattering on aerosols and cloud particles depends on their respective optical properties, which are diverse and depend on a size, shape and composition. Vertical profiles of AEs can be retrieved from a set of O_4 dSCDs for individual elevation sequences using the well-known vertical profile of the O_4 concentration, which is proportional to the square of the concentration of molecular oxygen and thus only depends on temperature and pressure (Hönninger et al., 2004; Wagner et al., 2004; Frieß et al., 2006). Like for other algorithms, a two-step inversion procedure is ~~also~~ used in the PriAM algorithm: in the first step the aerosol extinction (AE) profiles and in the second step the profiles of the trace gas VMRs are retrieved. In PriAM we applied the Levenberg-Marquardt modified Gauss-Newton procedure (Rodgers, 2000) to solve the ill-posed inversion problem for AEs (Frieß, et al., 2006 and Yilmaz, 2012) through the numerical iteration:

$$x_{i+1} = x_i + \left((1+\gamma_i)S_a^{-1} + K_i^T S_\varepsilon^{-1} K_i\right)^{-1} (K_i^T S_\varepsilon^{-1}(y - F(x_i)) - S_a^{-1}(x_i - x_a)) \quad \text{(s1)}$$

with x_{i+1} and x_i the solutions of atmospheric state at the i and i+1 step. x_a is the a-priori profile and y the measurement vector. γ_i is the Levenberg-Marquardt factor, which is multiplied or divided by two to make the minimization of the cost function faster and more stable than for the normal Gauss-Newton algorithm. S_a is the covariance of the error of the a-priori profile and S_ε is the covariance of the errors of the measurements. K_i and $F(x_i)$, which are calculated for each iteration step, are the weighting function and the forward model value at the state of x_i, respectively.

The set of O_4 dSCDs for the m non-zenith elevation angles in each scan (in this study 5°, 10°, 20° and 30°) is the measurement vector to retrieve the AE (σ) in n atmospheric layers. In this study 20 atmospheric layers from the surface to 4 km with height intervals of 0.2 km are used (the same layers are used for the retrievals of the trace gas profiles). Considering the frequent variation of aerosols, very little is known about the expected AE profile. Thus a fixed smoothed box-shaped a-priori AE profile (Boltzmann distribution) is used, as introduced by Yilmaz (2012):

$$\sigma(z) = \frac{\sigma(0)}{1+\exp\left(\frac{z-\frac{\tau}{\sigma(0)}}{0.3}\right)} \quad \text{(s2)}$$

Here $\sigma(z)$ and $\sigma(0)$ denote the extinction coefficient at the altitude z (km) and at the surface, respectively. τ is the optical depth. In this study, $\sigma(0)$ and τ are 0.15 km^{-1} and 0.3, respectively. The covariance matrix S_a is constructed as follows:

$$S_{a\,ik} = \sigma_{a_i}^2 \times e^{-\frac{|z_i - z_k|}{\eta}} \quad \text{(s3)}$$

With σ_{a_i} the a-priori AE at the atmospheric layer i. z_i and z_k are the heights of the atmospheric layer i and k, respectively. The smoothing factor η is 0.5 km. The covariance matrix of the measurement uncertainties S_ε contains diagonal elements representing the square of the fitting errors of the O_4 dSCDs and off-diagonal elements of zero.

In most previous studies, the optimal linear inverse method (Rodgers, 2000; Frieß, 2011) is used to retrieve the vertical profiles of the trace gas VMRs. In PriAM, we use the Gauss-Newton numerical procedure as in Eeq. (s1) because the use of the safe state of AEs and trace gas VMRs (see below) converts the linear problem into a nonlinear one.

Similar to the retrieval of the AE profiles, the diagonal element of S_ε is the square of the fitting errors of the respective trace gas dSCDs and the off-diagonal elements are zero. The elements of S_a are calculated from Eeq. (s3) but the σ_{a_i} are replaced by the a-priori VMR of the respective trace gas (ρ_{a_i}). One fixed a-priori profile of the VMRs for each trace gas is used. The a-priori profiles of NO_2 and SO_2 are described as an exponential function (similar to Yilmaz, 2012 and Hendrick et al 2014):

$$\rho(z) = \rho(0) \times e^{-\frac{z}{H}} \quad \text{(s4)}$$

Here $\rho(z)$ and $\rho(0)$ are the VMR of the trace gases at altitude z (km) and near the surface, respectively. H is the scaling height (in this study fixed to 1km). The ground VMR $\rho(0)$ is set to 4 ppb for NO_2 and 8 ppb for SO_2.

MAX-DOAS and aircraft measurements in Milano during summer of 2003 indicated that the layer of high HCHO concentration often extends to 1 km or even higher altitudes (Wagner et al., 2011, Junkermann, 2009). Thus for HCHO the same a-priori profile (Boltzmann distribution) as for the AE is used. The surface mixing ratio $\rho(0)$ is set to 4ppb and the VCD to 1.7×10^{16} molecules/cm^2.

During the profile inversion for aerosols and trace gases, negative values can occur, which are physically invalid. To avoid them, the original atmospheric state vector x is transformed to its corresponding 'safe state' x' (Yilmaz, 2012):

$$x' = \ln(x) \quad \text{(s5)}$$

After finishing the calculation of x', x' is transformed back to the original format

$$x = e^{x'} \quad \text{(s6)}$$

In this way it is ensured that x is always positive.

The averaging kernel (AK) is an important quantity to characterize the vertical resolution of the measurement and the sensitivity of the retrieved state $\hat{x}$ to the true state as a function of altitude. The trace of the ~~averaging kernel~~AK matrix yields the degree of freedom (DoF) of the signal, which represents the number of independent pieces of information that can be retrieved. The error of the retrieved state S consists of the smoothing error S_s (due to the limited vertical resolution of the retrieval) and the retrieval noise S_m (due to measurement errors).

~~2~~3.1 Influence of the choice of the a-priori profiles on the retrieved profiles

We investigate the impact of the choice of the a-priori profiles on the retrieved profiles, VCD (AOD) and near-surface VMR (AE) (from the ground to 200 meters) for two months (July 2011 and February 2012) by either varying the VCD (AOD) by 0.5 or 2, or changing the profile shape by replacing the Boltzmann distribution with the exponential distribution (for aerosols and HCHO) or the other way around (for NO_2 and SO_2) (see Fig. ~~S6~~ S8~~in the supplement~~). We compared the respective differences of the measured dSCDs and modeled dSCDs (results of the forward model) and the retrieved profiles (see Fig. ~~S7~~S9), VCDs (AODs) and the near-surface VMRs (AEs) (see Table S1). We found a stronger influence of the a-priori profile for aerosols than for the trace gases. By changing the a-priori profiles, the maximum change of the retrieved VCDs and AODs is on average about 10% and 20%, respectively. The retrieved near-surface VMRs and AEs change by around 2%

and 10%, respectively. For both aerosols and trace gases, typically the smallest differences between the measured and ~~modeled~~modelled dSCDs are found for the standard a-priori profiles (see Fig. ~~S7~~S9) indicating that the standard a-priori profiles are the preferred assumptions.

3.2 Evaluation of the internal consistency of the inversion algorithm

The retrieval quality is evaluated for favourable measurement conditions, namely cloud-free sky with relatively low aerosols (the sky condition is directly identified by MAX-DDOAS observations as described in section 2.2.5 in the main manuscript), and the performance of the retrievals in different seasons is discussed.

Comparing the measured TG dSCDs to the modelled dSCDs (the results of the forward model corresponding to the retrieved AE and TG profiles) is a direct way to evaluate how close to the real profile the retrieved profile is. Ideally, the differences between measured and modelled dSCDs are minimized by the inversion. However because of measurement errors, deviations of the forward model from reality (e.g. for cloudy skies, shown in section 2.2.5 in the main manuscript) and the not always realistic assumption of the Gauss-Newton Algorithm in Eq. (1) in the main manuscript (especially under the condition with strong aerosol load, also shown in section 2.2.5 in the main manuscript), the derived profiles might strongly deviate from the real profiles. The mean differences (and standard deviations denoted by error bars) between the measured and modelled dSCDs for the four species are plotted against the elevation angles during the whole measurement period in Fig. S10. For the aerosol retrieval, a larger negative difference of the O_4 dSCD of 2.9×10^{41} molecules^2 cm^{-5} is found for 5 °elevation angle, indicating an underestimation of the aerosol extinction in the layer close to the surface; however the magnitude of the underestimation is only about 2% based on the mean O_4 dSCD of about 1.6×10^{43} molecules^2 cm^{-5} for 5 °elevation angle. For the TG retrievals, in general the differences for high elevation angles are slightly larger than those for low elevation angles. This finding probably indicates the higher sensitivity of the inversion algorithm to lower altitudes. This is also indicated by the AKs in Figs. S12c, S13c and S14c. Even so, the mean deviations of the dSCDs for the 30 ° elevation angle are only -0.28 $\times10^{15}$ molecules cm^{-2} for NO_2 (mean dSCD of 2.6×10^{16} molecules cm^{-2}), -0.07 $\times$ 10^{15} molecules cm^{-2} for SO_2 (mean dSCD of 3.3×10^{16} molecules cm^{-2}) and 0.65×10^{15} molecules cm^{-2} for HCHO (mean dSCD of 1.6×10^{16} molecules cm^{-2}).

The mean AKs for retrievals of AE, NO_2, SO_2 and HCHO are shown in Figs. S11c - S14c, respectively. They indicate that the inversions are sensitive to the layers from the surface up to 1.5 km. The degrees of freedom (DoF) are about 1.5 for aerosols (similar to Frieß et al., 2006), 2 for NO_2 and 2.3 for SO_2 and HCHO. The total AKs in different seasons are shown in Figs. S11d - S14d for the four species, respectively. The generally similar total AKs in different seasons indicate the consistent response of the measurements to the true atmospheric state. The slight seasonality is probably related to the variation of the SZA. The same reason probably causes the weak diurnal variation of the DoF of the inversions as shown in Fig. S15. The averaged profiles retrieved from the measurements during the whole period and in different seasons are shown in Figs. S11a - S14a for the four species together with the corresponding a-priori profiles. The retrieved profiles below 1.5 km are quite different from the a-priori profiles, indicating that the measurements contain sufficient information for the

altitude below 1.5 km. The mean contributions of the noise and the smoothing error (this error originates from the limited resolution of the inversion) of the retrievals are shown in Fig. S13b - S16b. The total (absolute) retrieval errors have a maximum around 1 km and decrease towards the surface. The relative errors are minimal close to the surface (10% for AE, NO_2 and SO_2, and 30% for HCHO). Most of the errors originate from the smoothing error, which largely contributes to the total error at high altitudes.

~~3~~ 3.3 Deriving O_4 VCDs from the measured surface temperature and pressure

To derive O_4 VCDs from the measured surface temperature and pressure (TP), we first fit 6th order polynomials to the seasonal variations of surface TP (see Fig. 3 in the main manuscript). Second, we calculate height profiles of the temperature assuming a lapse rate of 0.645K / 100m:

$$T_{i+1} = \begin{cases} T_i - 0.645 \times \frac{z_{i+1} - z_i}{0.1} & (0 < z < 12km) \\ T(z = 12km) & (z > 12km) \end{cases} \quad \text{(s7)}$$

Here T_i (in unit of kelvin, K) and z_i indicate the temperature and height of the atmospheric layer i, respectively. Above 12 km the temperature is kept constant to represent the temperature inversion around the tropopause. Here it should be noted that this simplification has only negligible influence on the derived O_4 VCD, because most of the O_4 is present at lower altitudes. For the same reason, the TP profiles are only calculated up to an altitude of 20 km.

Based on the calculated temperature profile and the surface pressure we calculate the corresponding pressure profile:

$$D_i = 28.9 \times 10^{-3} \times {}^{P_i}/_{(T_i \times R)} \quad \text{(s8)}$$

$$P_{i+1} = P_i - (g \times 100 \times D_i) \quad \text{(s9)}$$

Here D (in units of kg/m^3) and P (in unit of hPa) indicate the air density and pressure, respectively. R is the ideal gas constant (8.31 J/mol K), and g is the gravitational constant (9.8 N/kg). Because the O_4 concentration is proportional to the square of the oxygen concentration (which represents 21% of the air density), the profile and VCD of O_4 can be calculated from the assumed air density profile. Fig. 3 in the main manuscript shows the seasonal variation of the O_4 VCD calculated from the measured surface TP in 2012. The O_4 VCD in summer is systematically lower than in winter (by about 2×10^{42} molecules^2 cm^{-5}, which is about 15% of the annually mean O_4 VCD).

~~4~~ 4 Dependencies of the errors of the VCD derived by the geometric approximation and the profile inversion on the aerosol load

In Fig ~~S9~~S25, $Diff_{total}$, $Diff_{\text{inversion}}$ and $Diff_{geometry}$ for the different TGs are plotted against the AODs for elevation angles of 20 °and 30 °(for a range of the ~~RAA~~ SAA between 100 °to 110). We found linear relations of $Diff_{geometry}$ against

AOD for the three species, especially for 20 ° elevation angle. The weaker dependence of $Diff_{geometry}$ on AODs for an elevation angle of 30 ° is due to the lower sensitivity of MAX-DOAS observations on aerosols than for an elevation angle of 20 °. Correlation coefficients of the linear regressions of $Diff_{geometry}$ and AODs are largest for HCHO due to its higher layer height compared to the other species. The same reason causes the better correlation for SO_2 than for NO_2. For relatively large AODs, the relation of $Diff_{total}$ and AOD follows a linear relation of $Diff_{geometry}$ and AODs, but for low AODs, $Diff_{\mathrm{inversion}}$ contributes most to $Diff_{total}$. $Diff_{\mathrm{inversion}}$ is mostly between ±20% and is randomly distributed around zero. Thus $Diff_{\mathrm{inversion}}$ can not be the reason for the systematic bias between the VCD_{geo} and the VCD_{pro}.

Figures

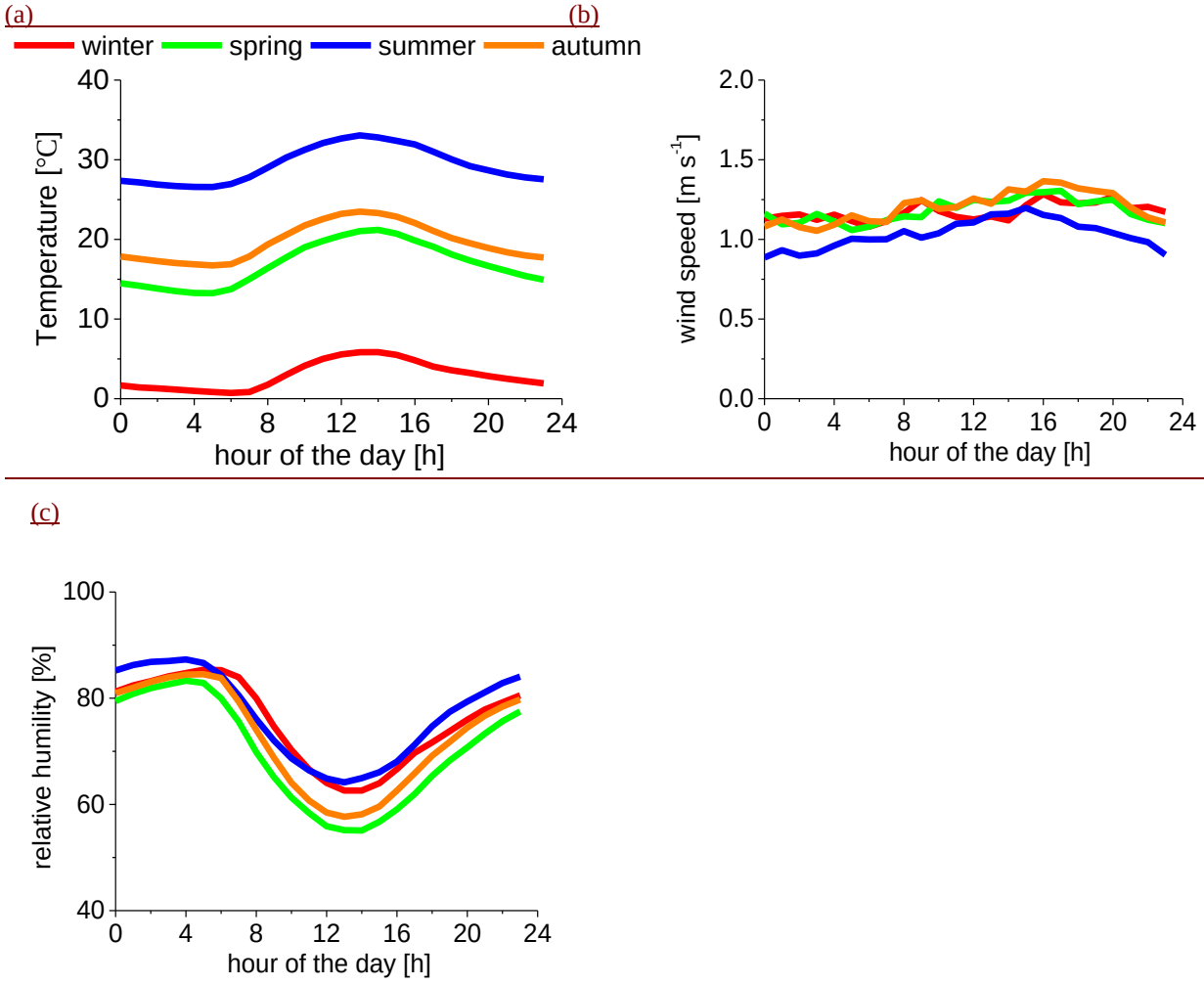

Figure S1: Seasonally mean diurnal variations (2011 to 2014) of ambient temperature (a), wind speed (b) and relative humidity (c) obtained from the observations of the weather station nearby the MAX-DOAS instrument.

(a) (b)

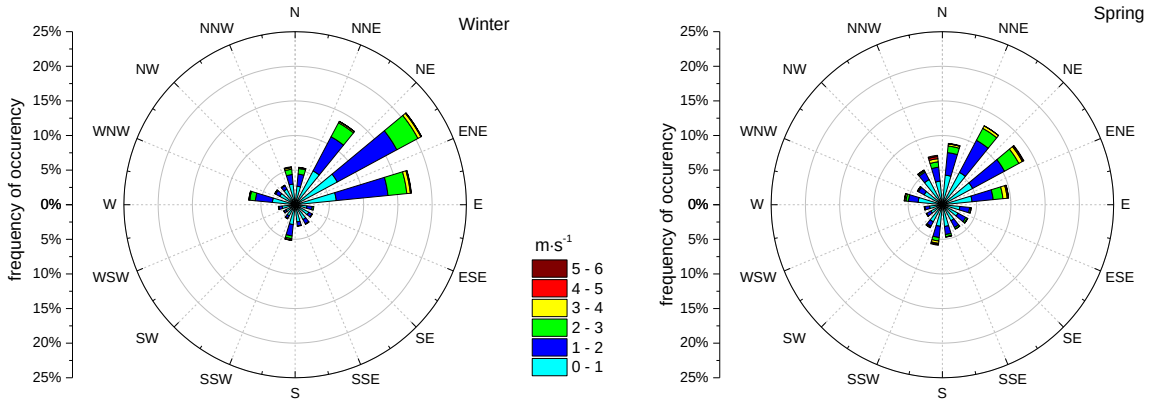

(c) (d)

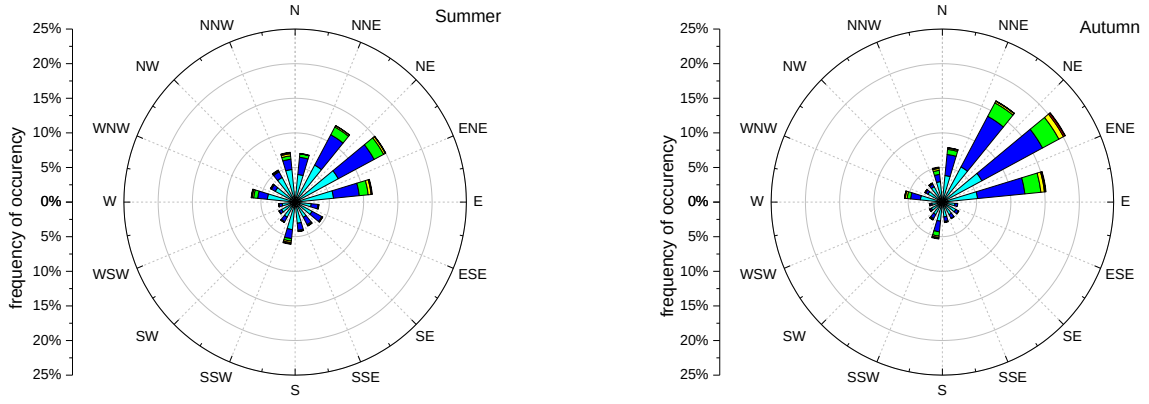

Figure S2: Wind rose diagrams based on all hourly averaged observations of the weather station for winter (a), spring (b), summer (c) and autumn (d) from 2011 to 2014.

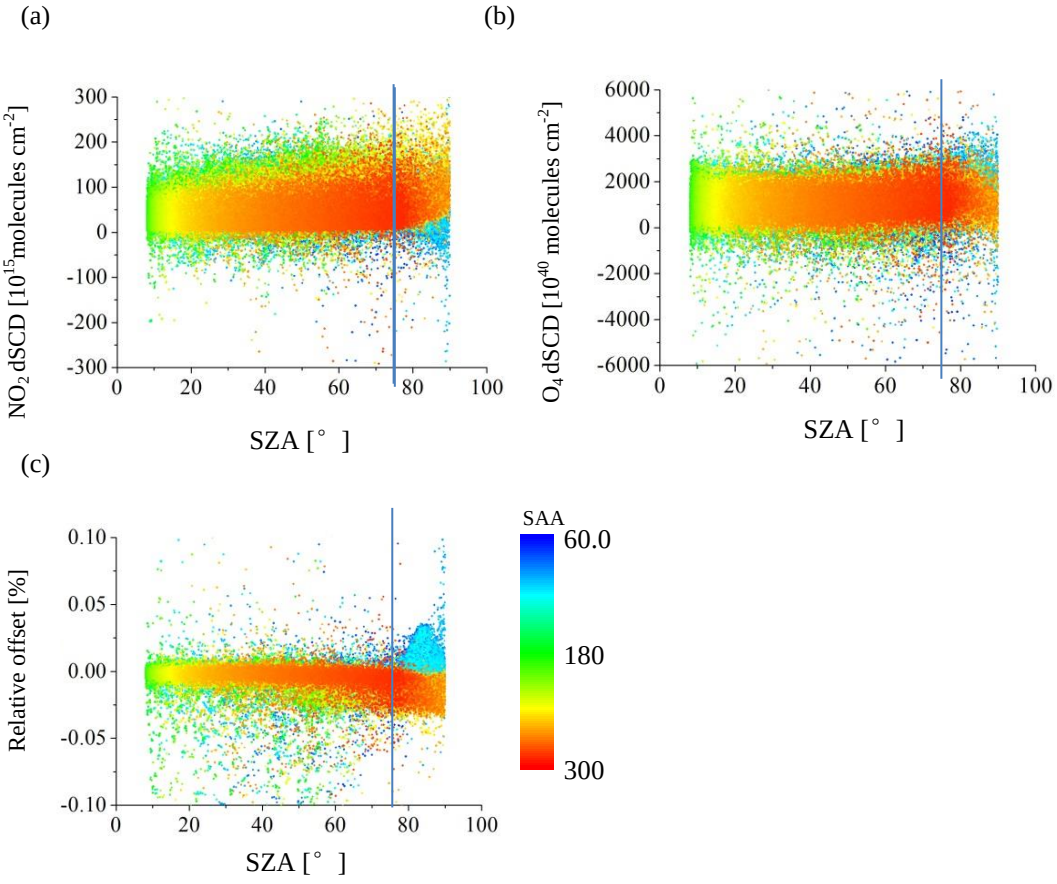

Figure ~~S1~~S3: SZA dependence of the NO_2 dSCDs (a), O_4 dSCDs (b) and relative intensity offset (c) derived from the NO_2 DOAS fits for all measured spectra during the whole observation period. The blue vertical lines indicate a SZA of 75°. The colours indicate the solar azimuth angle (SAA) with north as zero. Small (large) ~~RAA~~ SAA indicate measurements in the morning (evening).

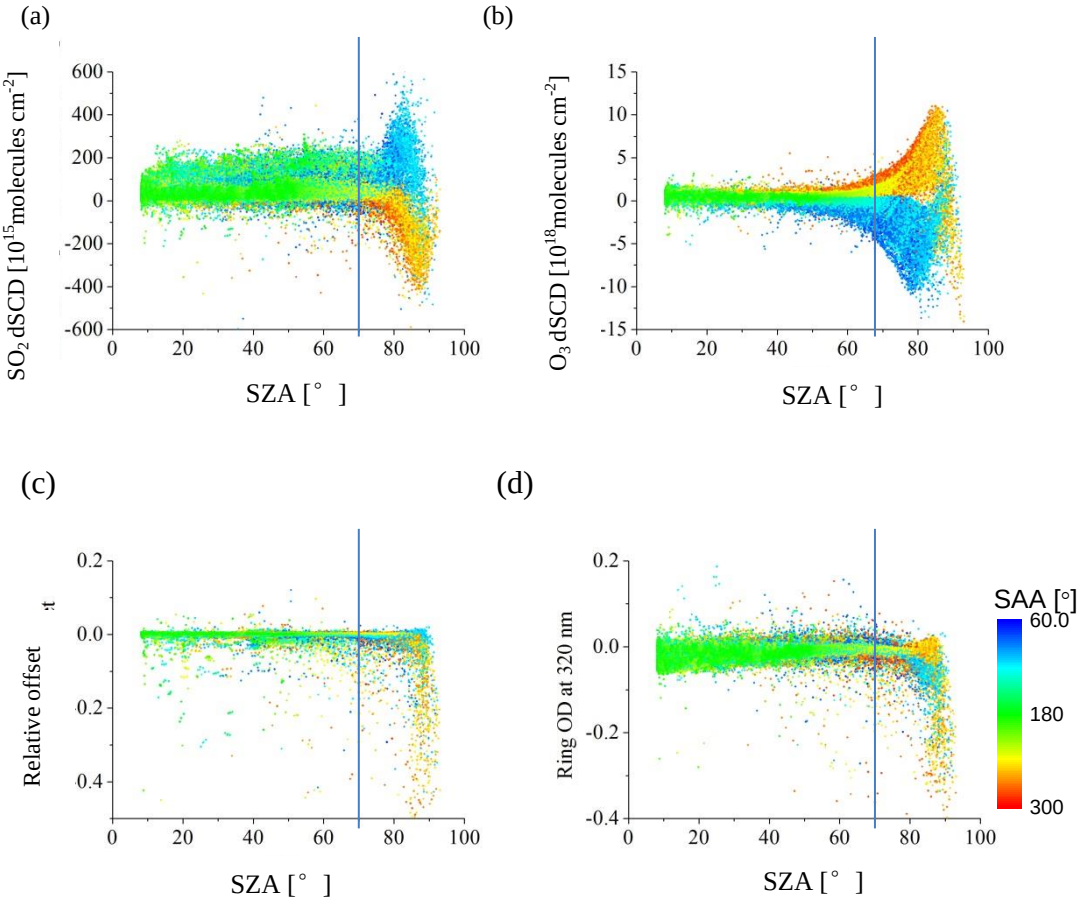

Figure S2S4: SZA dependence of the SO_2 dSCDs (a), O_3 dSCDs (b), relative intensity offset (c) and Ring optical depth (d) derived from the SO_2 DOAS fits for all measured spectra during the whole observation period. The blue lines indicate a SZA of 75 °. The

colours indicate the solar azimuth angle (SAA) with north as zero. Small (large) ~~RAA~~ SAA indicate measurements in the morning (evening).

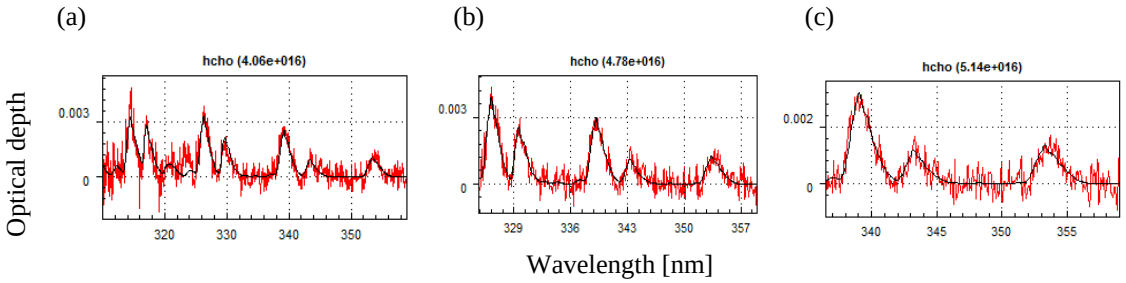

Figure ~~S3~~S5: Examples of DOAS fits of HCHO in the wavelength ranges of 310 to 359 nm (a), 324.6 to 359 nm (b) and 336.5 to 359 nm (c). The black curve and red curve are the fitted and measured HCHO absorption structures, respectively.

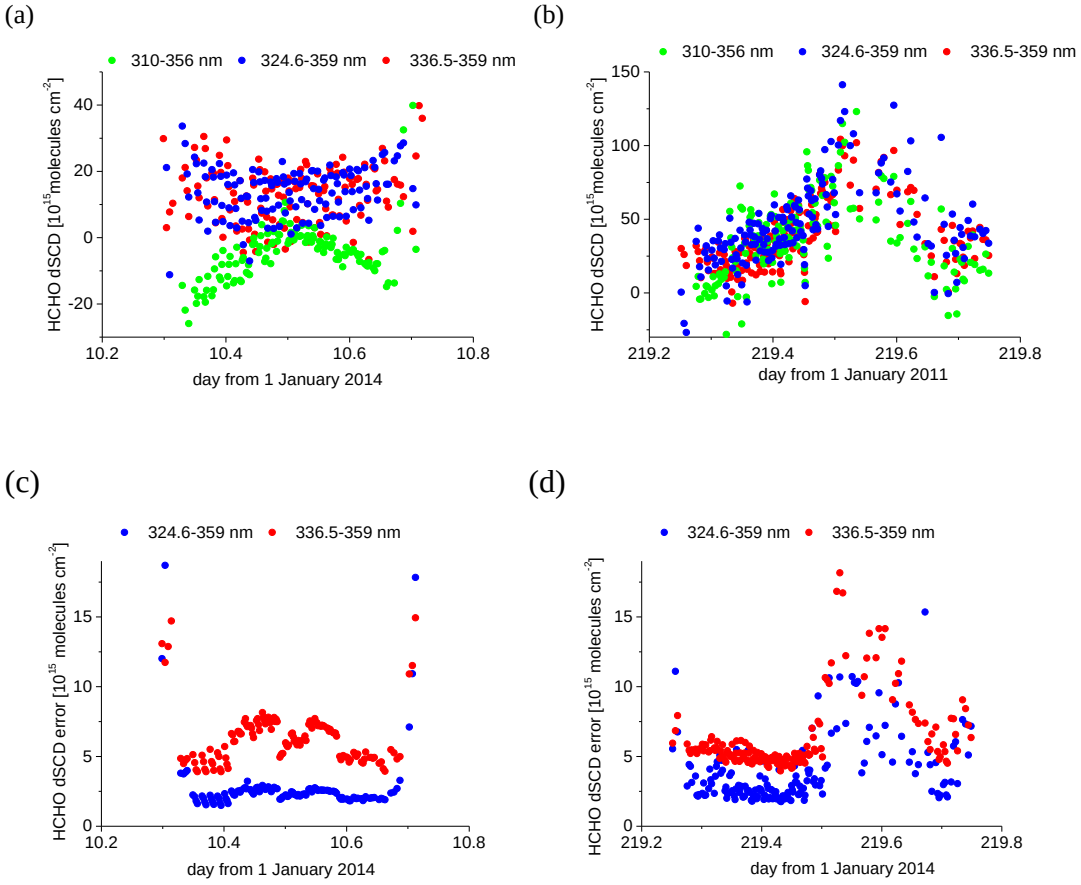

Figure ~~S4~~S6: HCHO dSCDs derived from the DOAS fits in the three wavelength ranges on 10 January (a) and 7 August 2014 (b) as well as the fit errors in the wavelength ranges of 324.6-359 nm and 336.5-359 nm on the both days in (c) and (d).

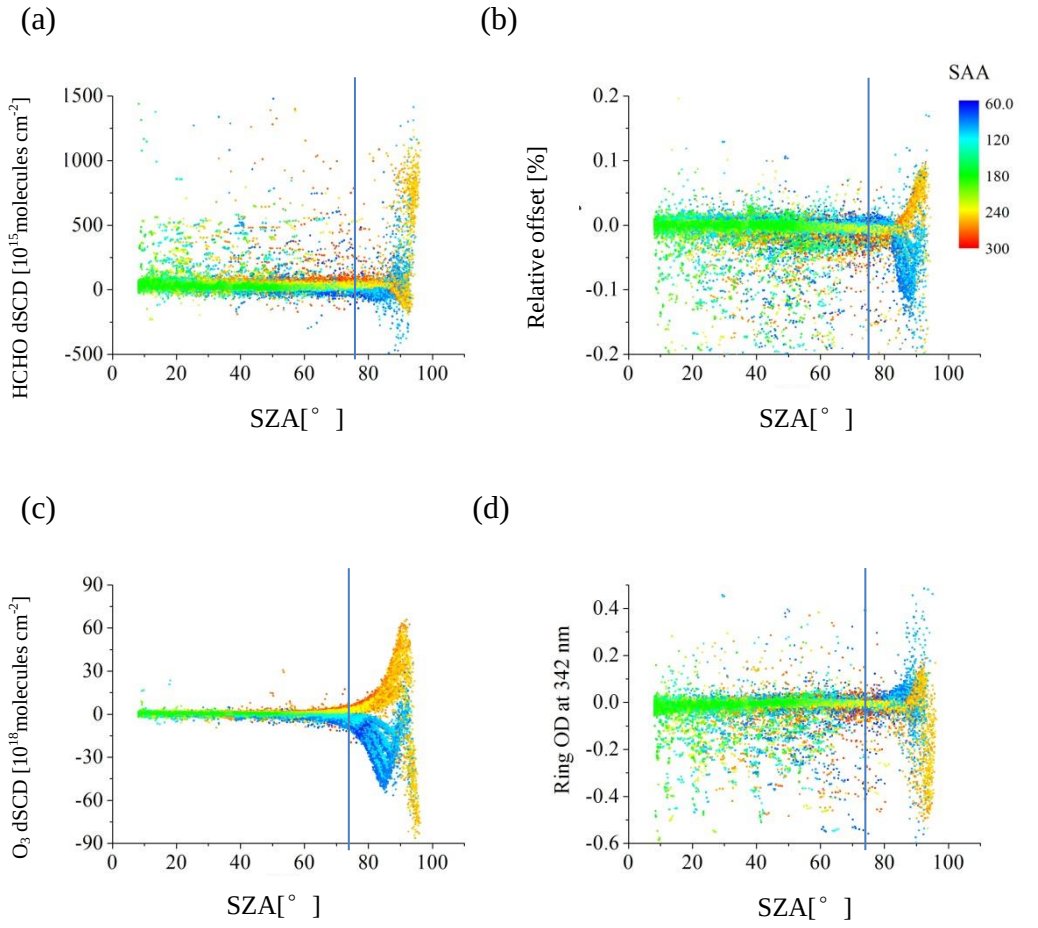

Figure S5S7: SZA dependence of the HCHO dSCDs (a), relative intensity offset (b), O_3 dSCDs (c), and Ring optical depths (d) derived from the HCHO DOAS fits of all measured spectra during the whole observation period. The blue lines flag the position of SZA of 75 °. The blue lines indicate a SZA of 75 °. The colours indicate the solar azimuth angle (SAA) with north as zero. Small (large) RAA SAA indicate measurements in the morning (evening).

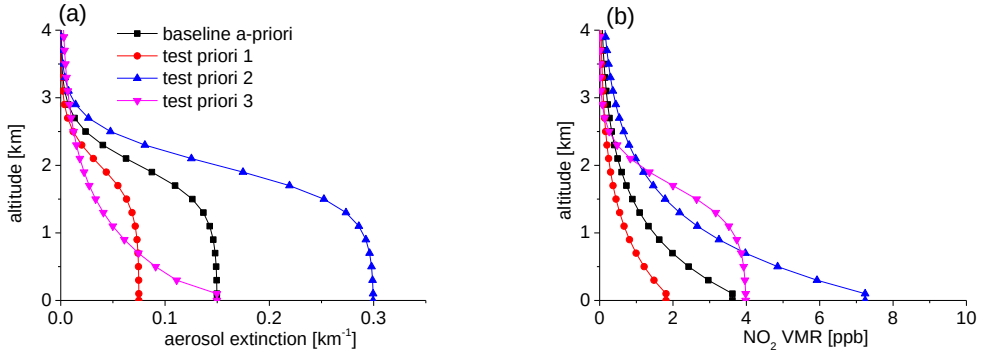

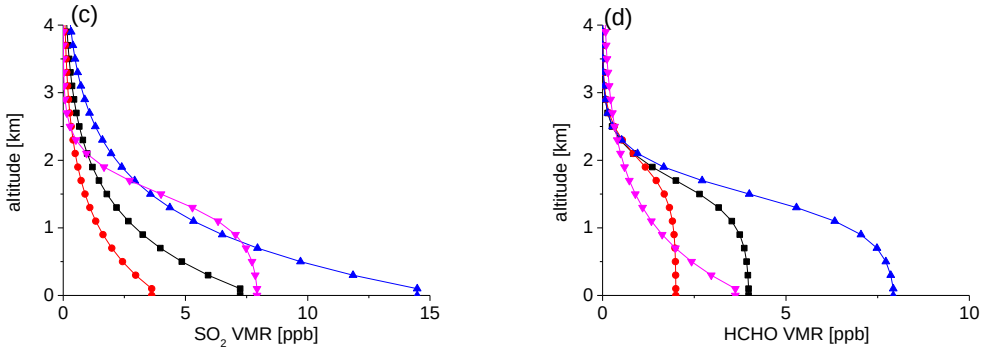

Figure ~~S6~~S8: Four a-priori profiles for aerosol extinction (a), NO_2 VMRs (b), SO_2 VMRs (c) and HCHO VMRs (d) used for the sensitivity tests of the MAX-DOAS profile retrievals. The baseline a-priori profile is used for the standard retrieval of the whole measurements.

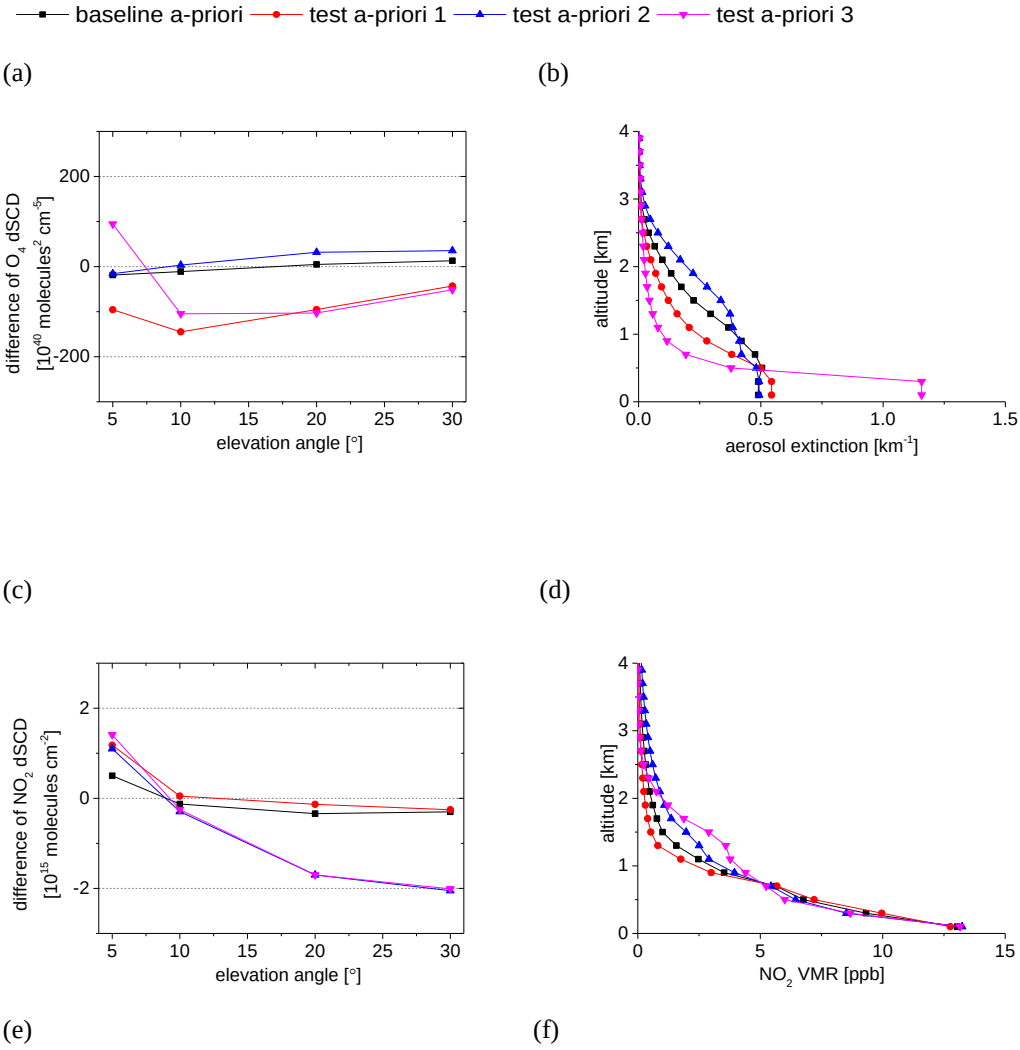

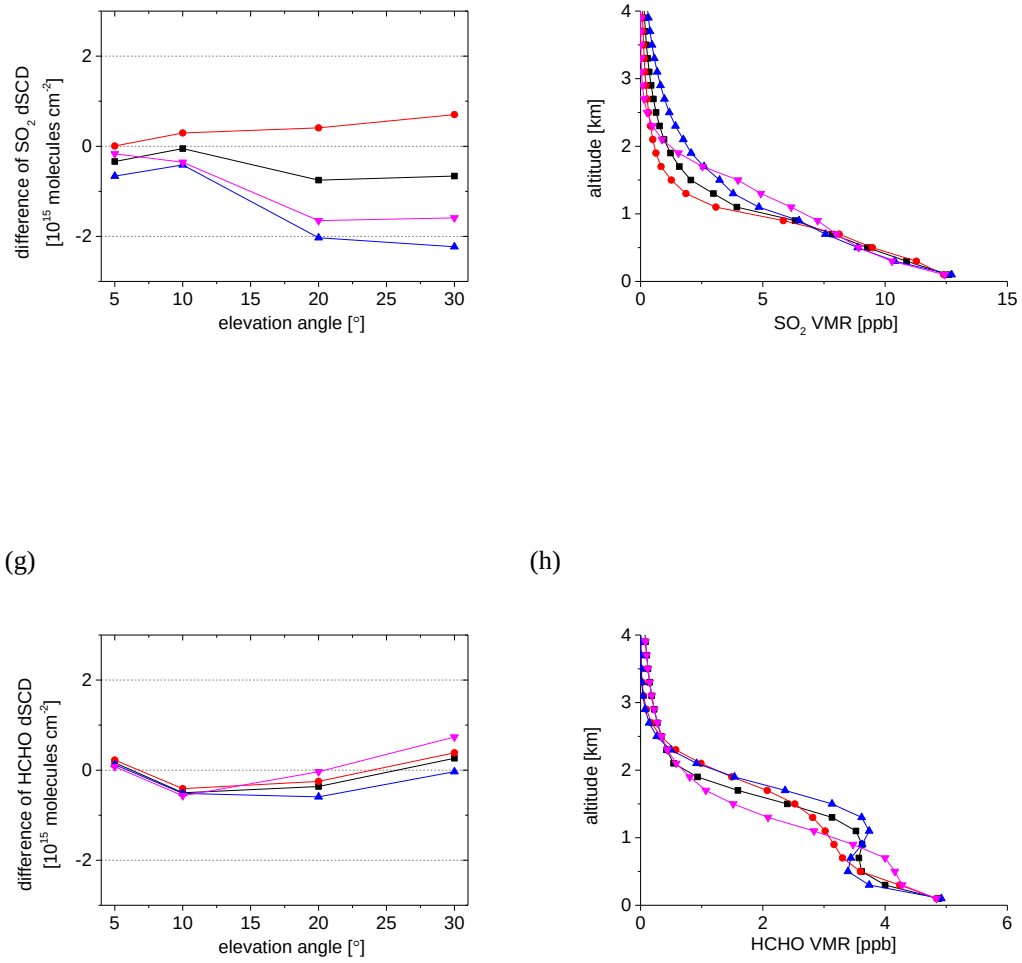

Figure ~~S7~~S9: Left: c~~E~~levation angle dependencies of the differences between measured and modelled dSCDs of O_4, NO_2, SO_2 and HCHO for the different a-priori profiles shown in Fig. ~~S6~~S8. Right: the average profiles of AE, NO_2 VMR, SO_2 VMR and HCHO VMR derived for the different a-priori profiles. The results are obtained for measurements in July 2011 and February 2012.

pressure temperature

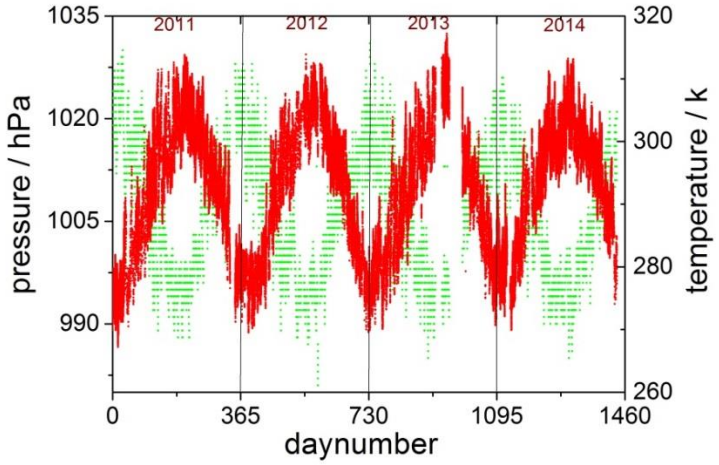

Figure S10: Time series of near-surface temperature and pressure obtained from the ground-based weather station near the MAX-DOAS instrument from 2011 to 2014.

(a) **(b)**

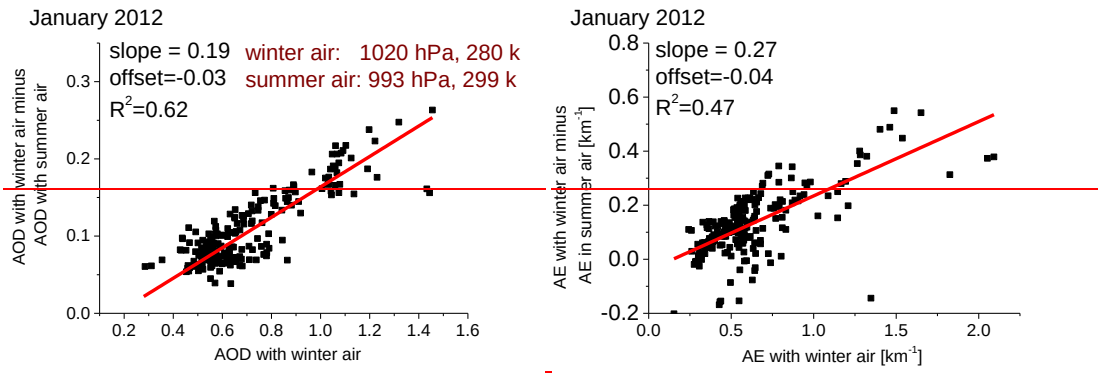

Figure S8: Dependence of the difference of the AOD (left) and AE (right) for January 2011 retrieved using TP profiles for either winter or summer versus the AOD and AE (retrieved using TP profiles for winter). TP profiles for winter are calculated assuming a surface pressure of 1020 hPa and surface temperature of 280 K; those for summer are calculated assuming a surface pressure of 993 hPa and surface temperature of 299 K. The retrievals based on the wrong (summer) TP profiles underestimate the AODs and near-surface AEs by about 20% and 27%, respectively.

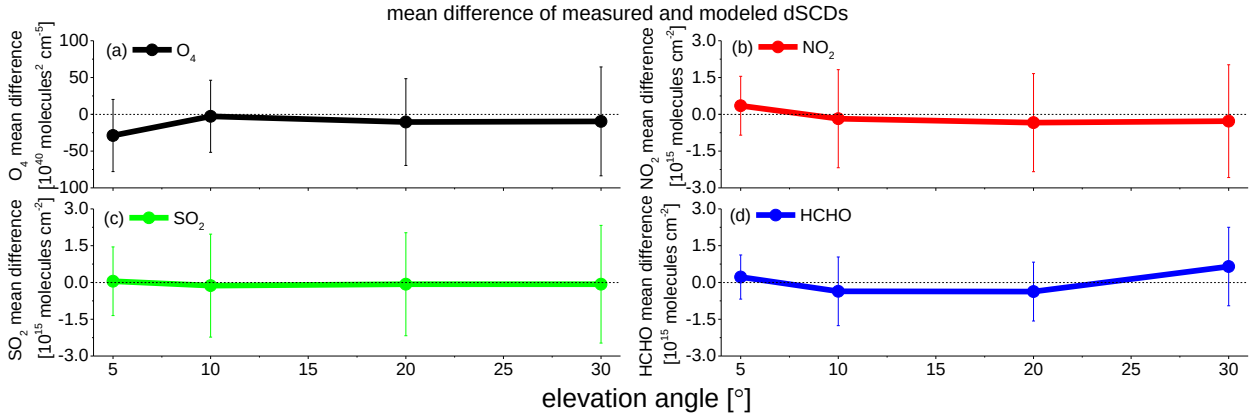

Figure S10: Mean differences and the standard deviations (error bars) between the measured and modelled dSCDs of O_4 (a), NO_2 (b), SO_2 (c) and HCHO (d) for clear sky conditions with low aerosols plotted against the elevation angles of MAX-DOAS measurements.

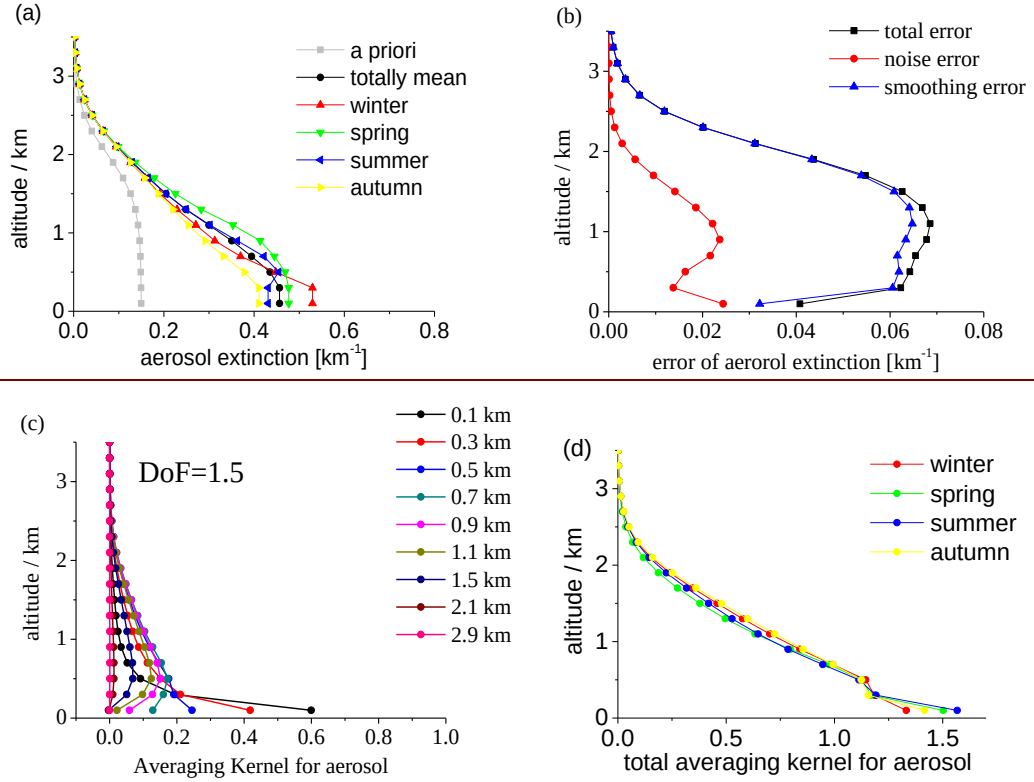

Figure S11: (a) Mean AE profiles for the different seasons derived from observations under clear sky conditions with low aerosols. Also shown is the a-priori profile; (b) total, noise and smoothing errors of the averaged aerosol extinction profile; (c) the corresponding mean averaging kernels for the different height layers (DoF is the degree of freedom); (d) the total averaging kernel for the different seasons.

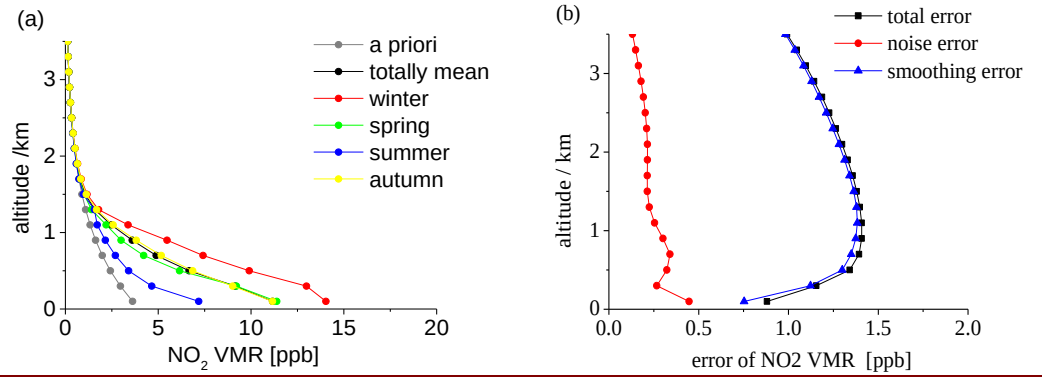

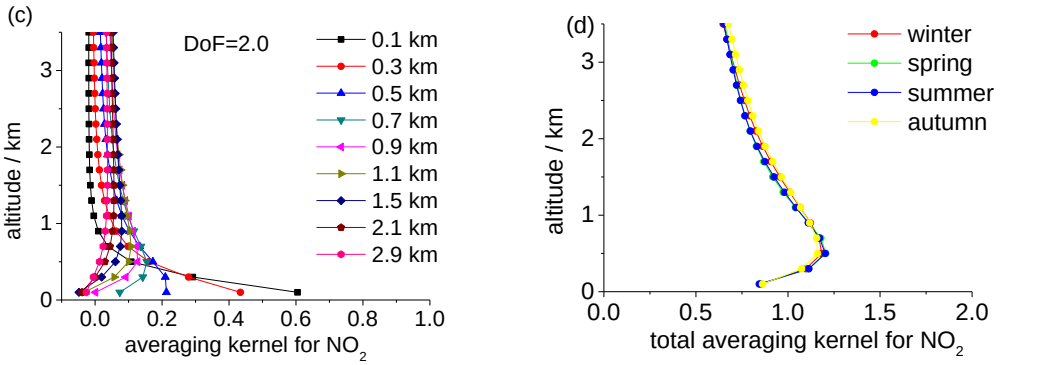

Figure S12: Same as Fig. S11, but for the NO_2 retrieval.

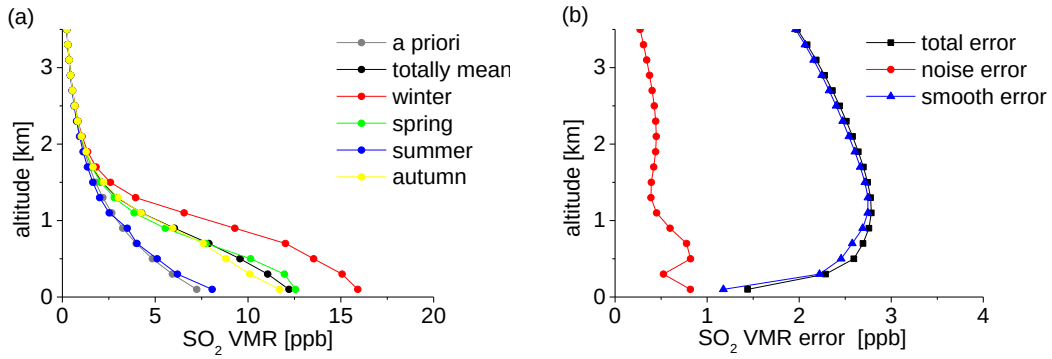

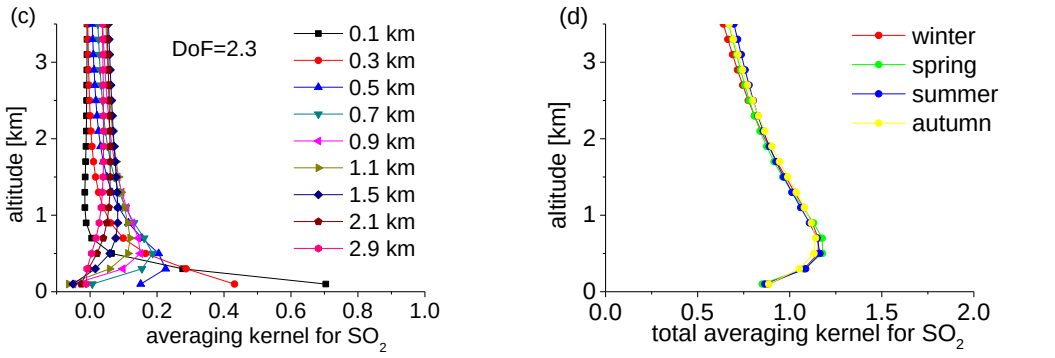

Figure S13: Same as Fig. S11, but for the SO_2 retrieval.

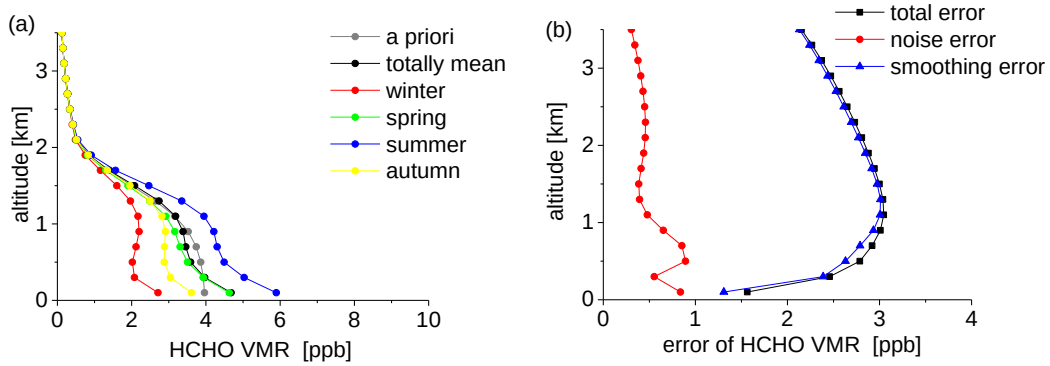

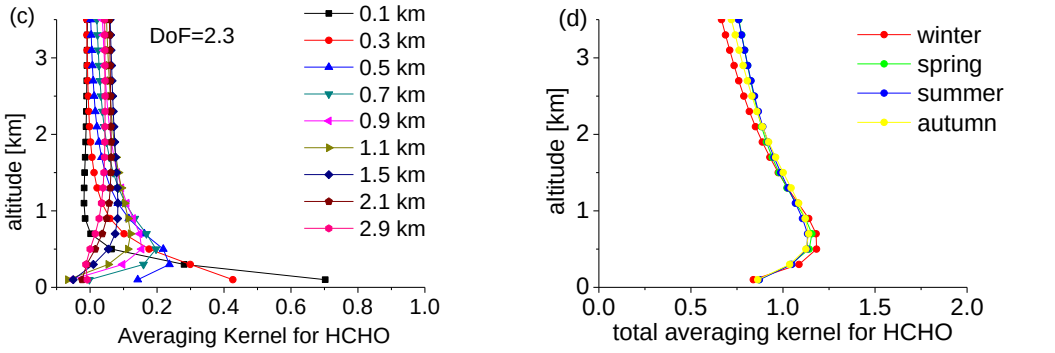

Figure S14: Same as Fig. S11, but for the HCHO retrieval.

(a) (b)

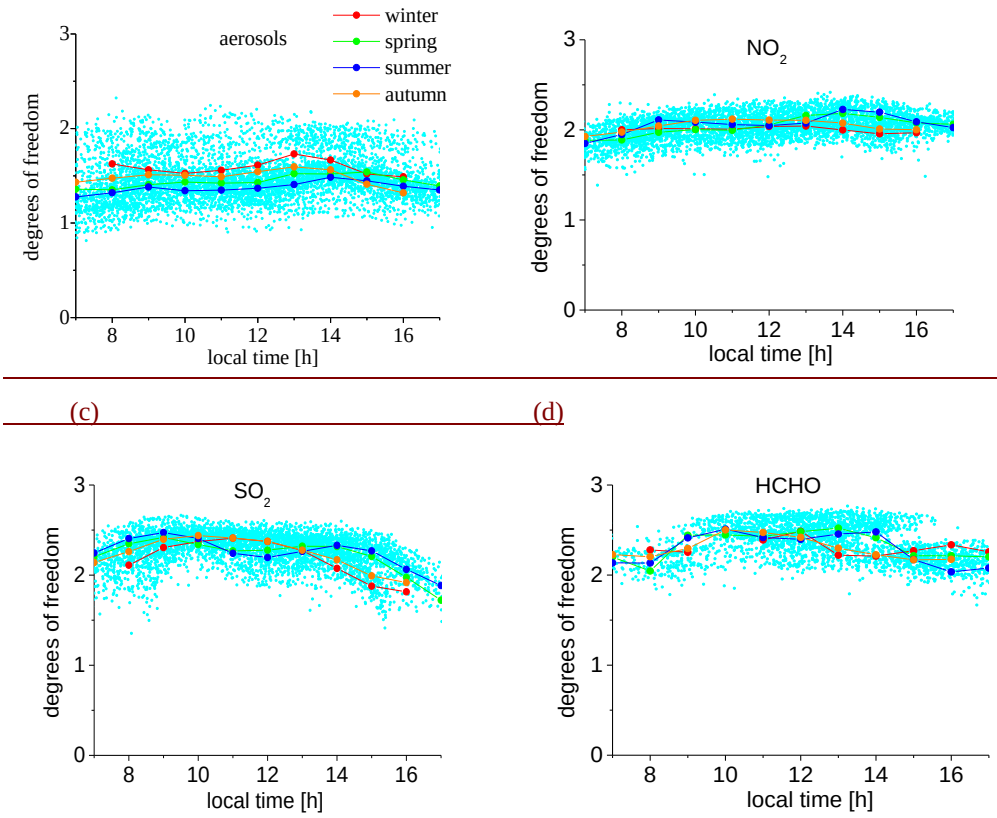

Figure S15: Seasonally averaged diurnal variations of the degrees of freedom (DoF) of the inversions for aerosols (a), NO_2 (b), SO_2 (c) and HCHO (d). For all four species, the DoF in the morning and afternoon ~~is~~are smaller than around noon mainly due to lower scattering probability in the boundary layer.

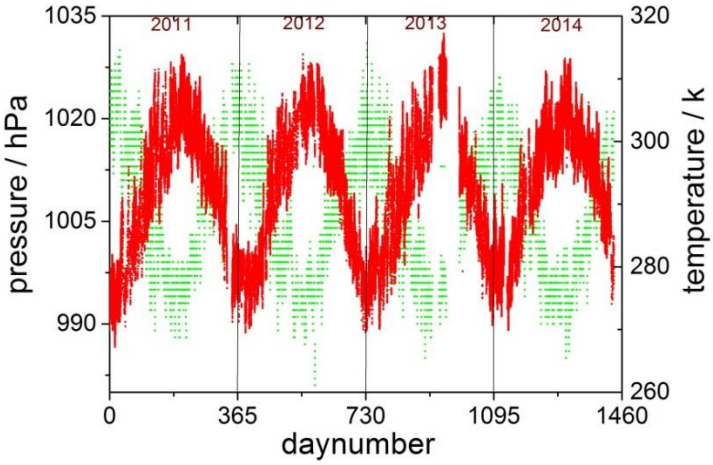

Figure S16: Time series of near-surface temperature and pressure obtained from the ground-based weather station near the MAX-DOAS instrument from 2011 to 2014.

(a) (b)

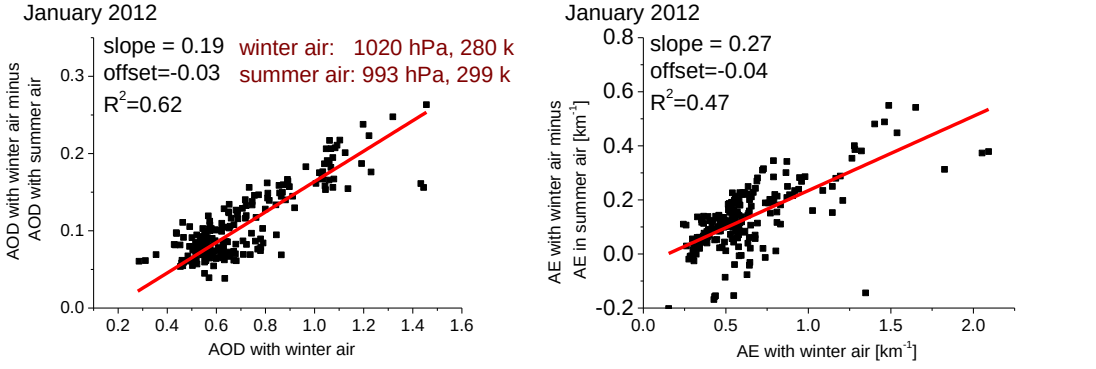

Figure S17: Dependence of the difference of the AOD (left) and AE (right) for January 2011 retrieved using TP profiles for either winter or summer versus the AOD and AE (retrieved using TP profiles for winter). TP profiles for winter are calculated assuming a surface pressure of 1020 hPa and surface temperature of 280 K; those for summer are calculated assuming a surface pressure of 993 hPa and surface temperature of 299 K. The retrievals based on the wrong (summer) TP profiles underestimate the AODs and near-surface AEs by about 20% and 27%, respectively.

(a) (b)

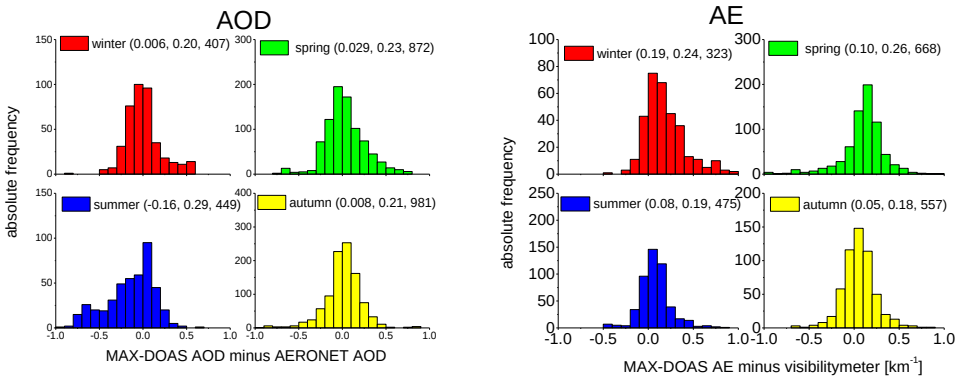

(c) (d)

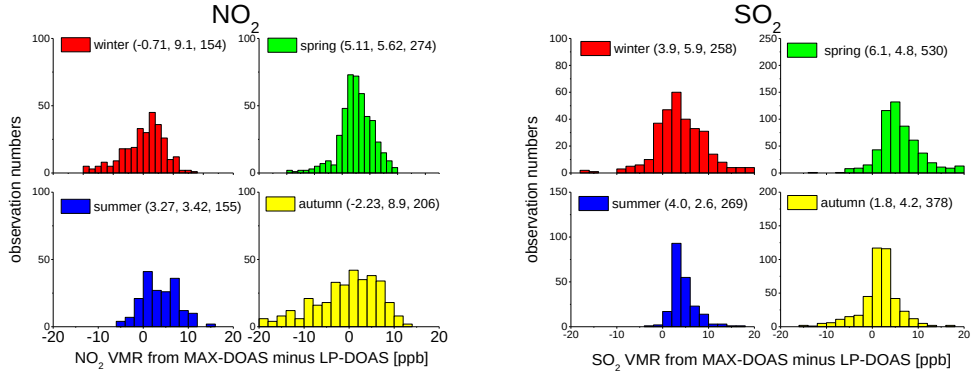

Figure S18: Histograms of the differences between MAX-DOAS results and independent techniques for different seasons for measurements under clear sky conditions with low aerosols. (a) difference of the MAX-DOAS AOD compared with the Taihu AERONET level 1.5 data, (b) difference of the MAX-DOAS AE compared with the results from the visibility meter; (c, d) VMRs of NO_2 and SO_2 derived from MAX-DOAS compared with the results of the nearby long path DOAS instrument. The mean differences, standard deviations and total numbers of observations are given in brackets for each season.

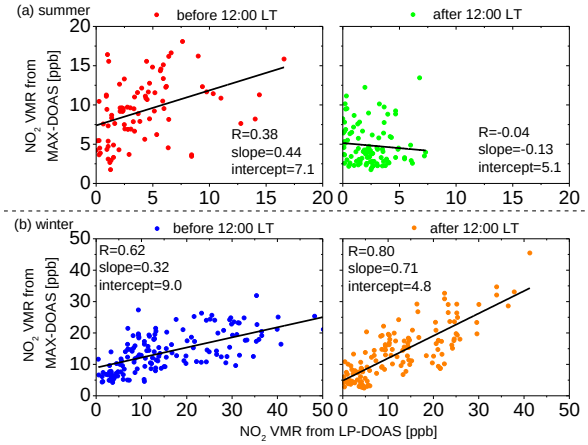

Figure S19: Scatter plots of the near-surface NO_2 VMR derived from MAX-DOAS versus those from LP-DOAS in summer (a) and winter (b) for clear sky conditions with low aerosols. The left and right subfigures show results for morning (before 12:00 local time (LT)) and afternoon (after 12:00 LT), respectively. Results of the linear regression are shown in the individual subfigures.

(a)

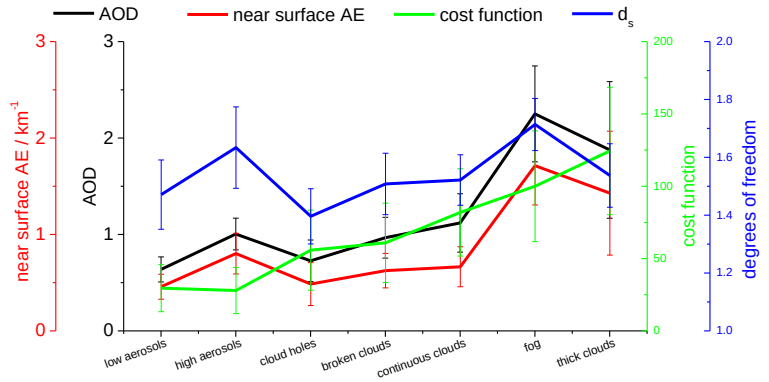

(b)

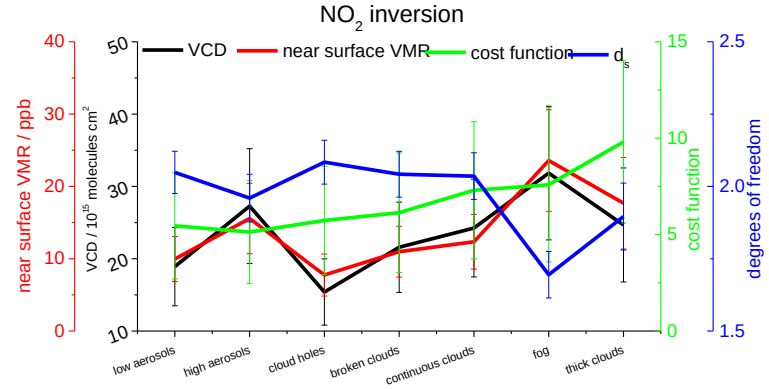

(c)

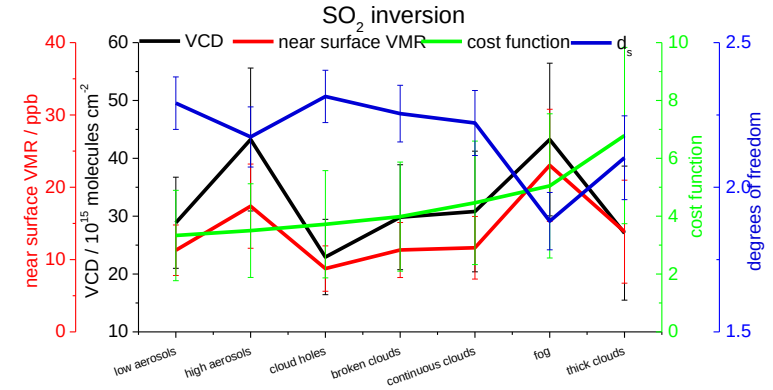

(d)

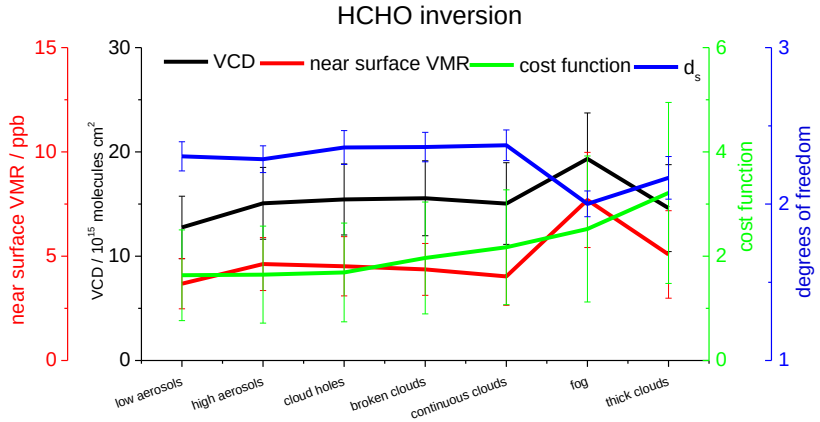

Figure S20: Mean results of all MAX-DOAS retrievals under different sky conditions. Besides the AOD and AE (a) and the trace gas mixing ratios and VCDs (b to d), also the cost functions and degrees of freedom are shown. The cost functions of all species are higher under cloudy conditions compared to clear sky conditions. The effect of clouds is stronger for aerosols compared to TGs. This is consistent with the larger discrepancy between modelled dSCDs and the measured dSCDs shown in Fig. 8 of the main manuscript. The reason is that clouds are not included in the forward model. The DoF of the inversions strongly depend on the cloud and aerosol load. A large aerosol load leads to an increase of the DoF of the aerosol inversion, but to a decrease of the DoF for the TG inversions. The column densities and near surface TG mixing ratios and AE are found to be quite different for the different sky conditions, probably due to cloud effects on the inversions and the different atmospheric chemistry conditions (photolysis) and dynamics for different cloud conditions.

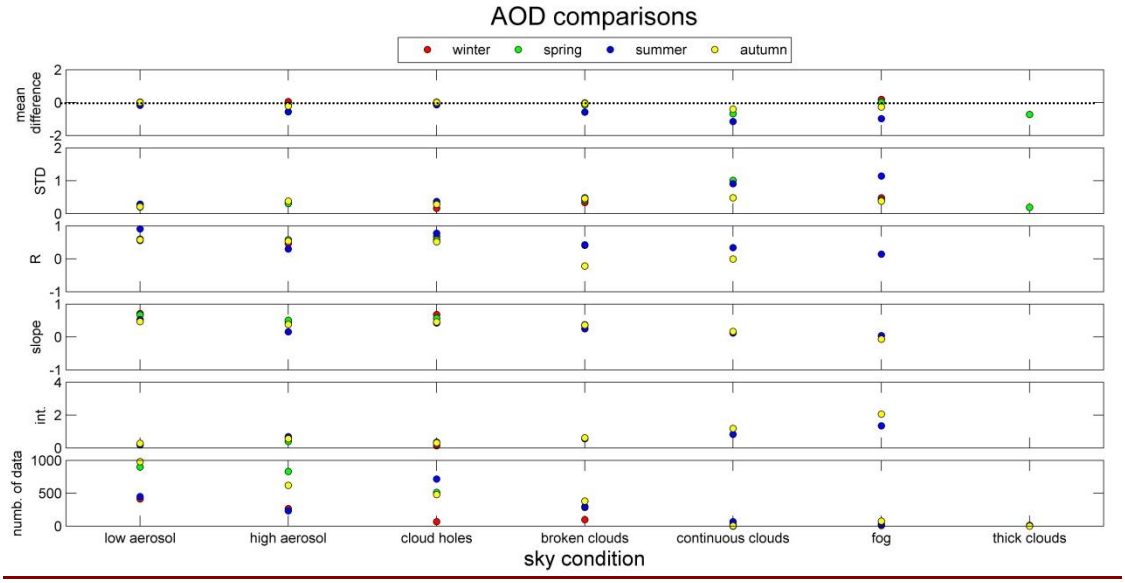

Figure S21: ~~m~~Mean absolute differences, standard deviations as well as correlation coefficients (R), slopes and intercepts derived from linear regressions ~~of the comparisons~~ of the AODs ~~between~~from MAX-DOAS and the Taihu AERONET level 1.5 data sets for different seasons (different colours) and ~~for different~~ sky conditions. Numbers of data in each comparison are shown in the bottom panel.

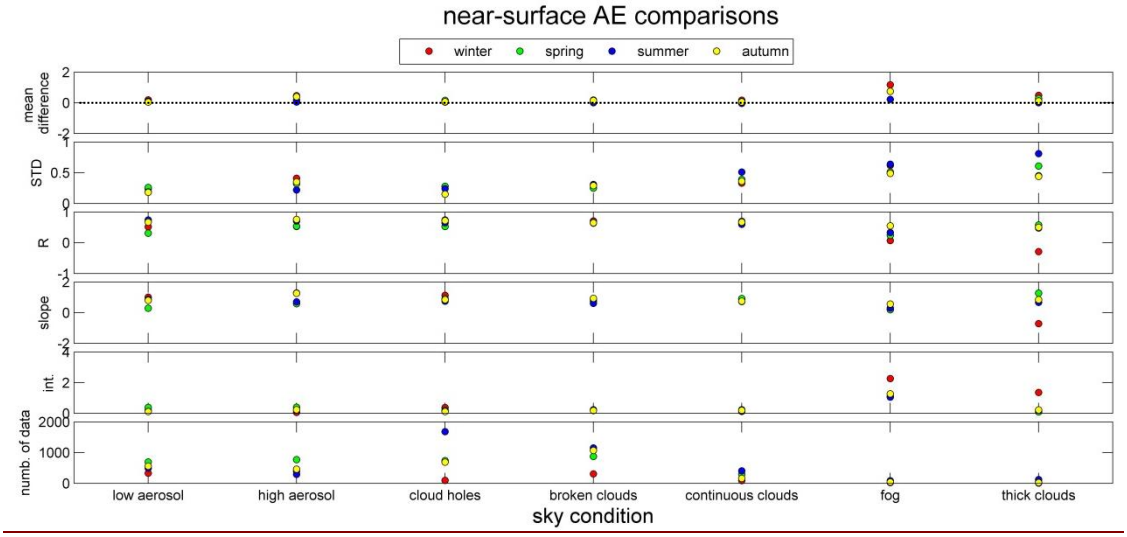

Figure S22: Same as Fig. S21 but for the near-surface AEs compared with the results from visibility meters.

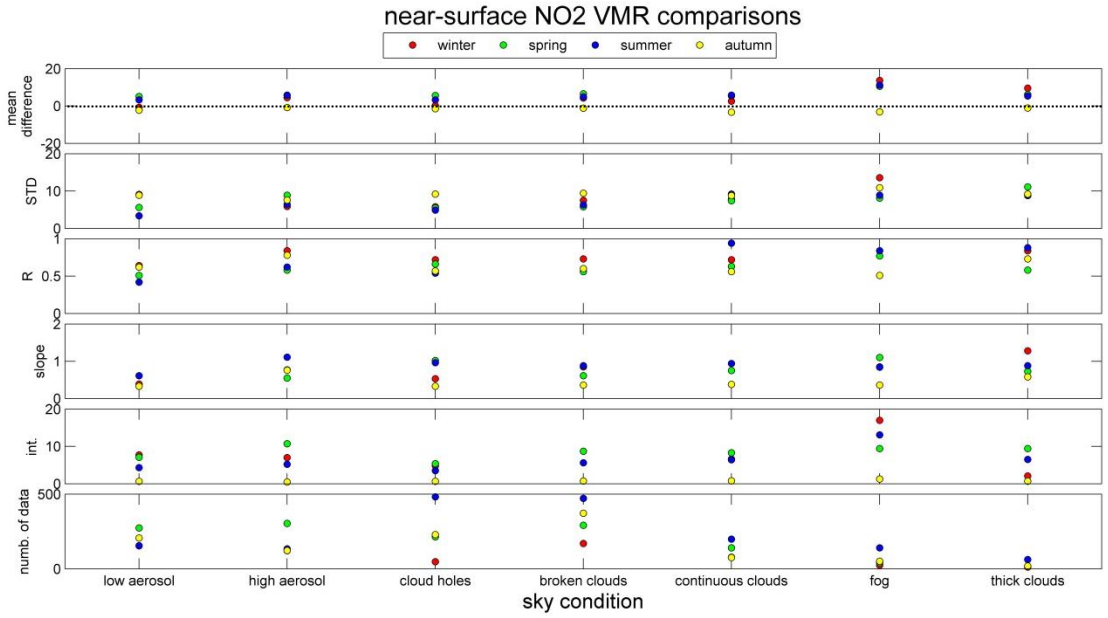

Figure S23: Same as Fig. S21 but for the near-surface NO_2 VMRs compared with the results from LP-DOAS.

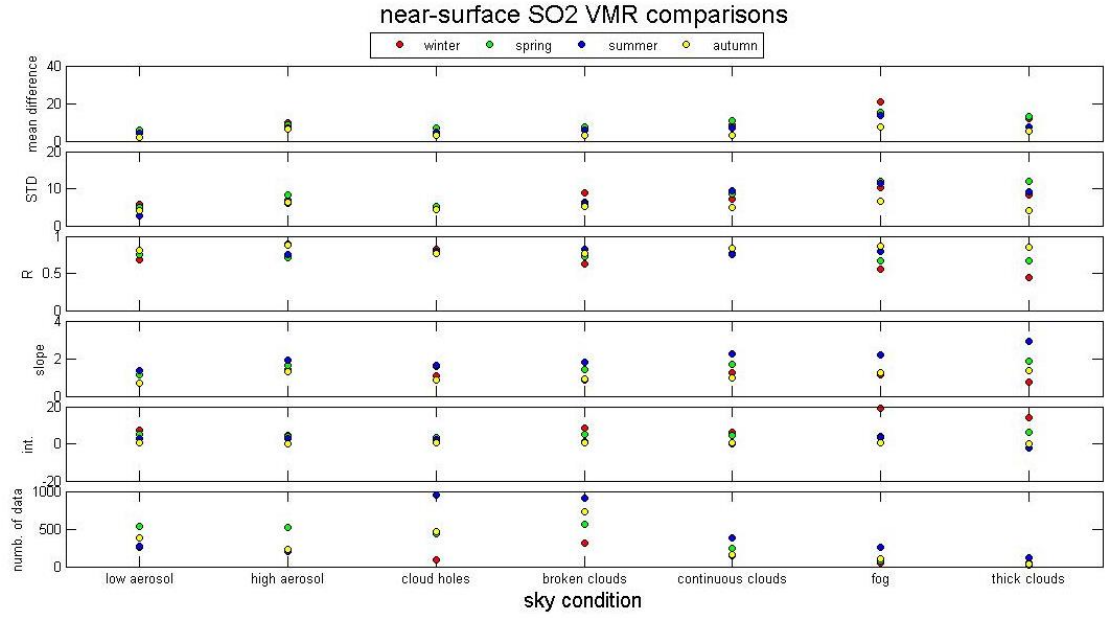

Figure S24: Same as Fig. S21 but for the near-surface SO_2 VMRs compared with the results from LP-DOAS.

(a)

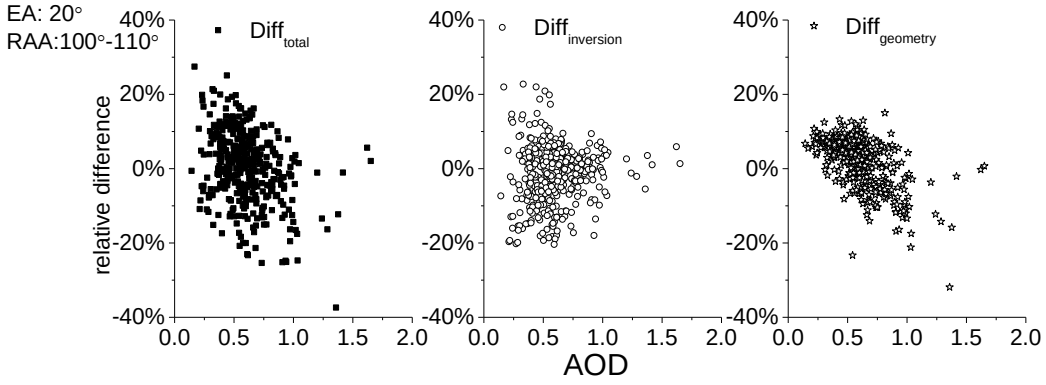
EA: 20°
RAA:100°-110°
Diff total
Diff inversion
Diff geometry
relative difference
AOD

(b)

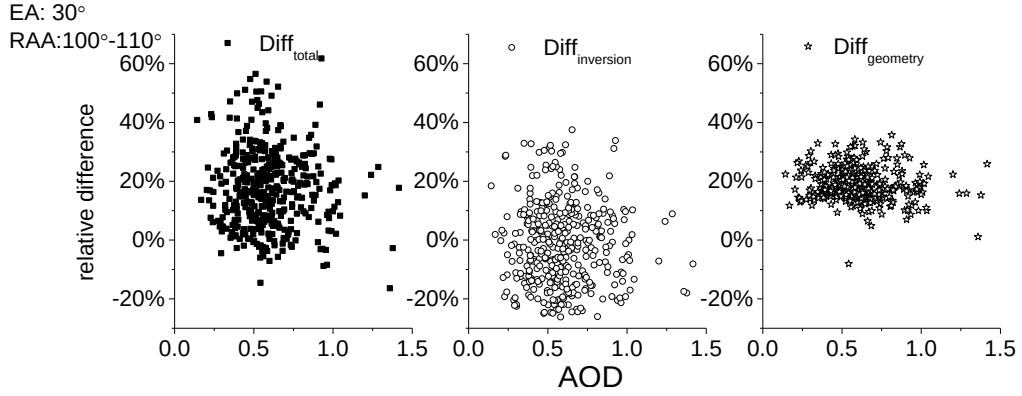
EA: 30°
RAA:100°-110°
Diff total
Diff inversion
Diff geometry
relative difference
AOD

(c)

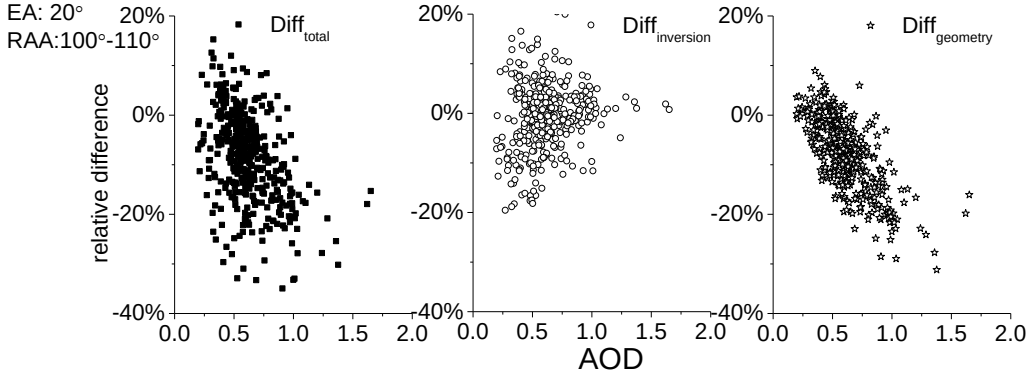
EA: 20°
RAA:100°-110°
Diff total
Diff inversion
Diff geometry
relative difference
AOD

(d)

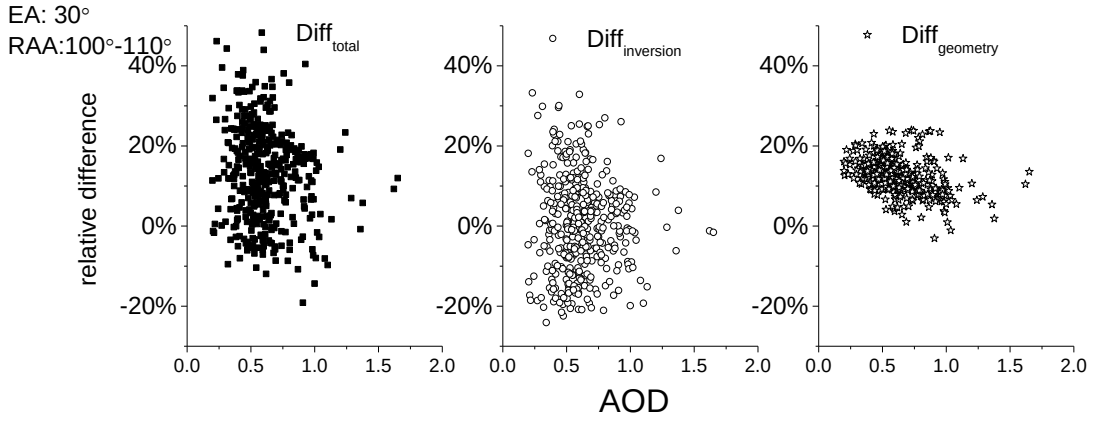

(e)

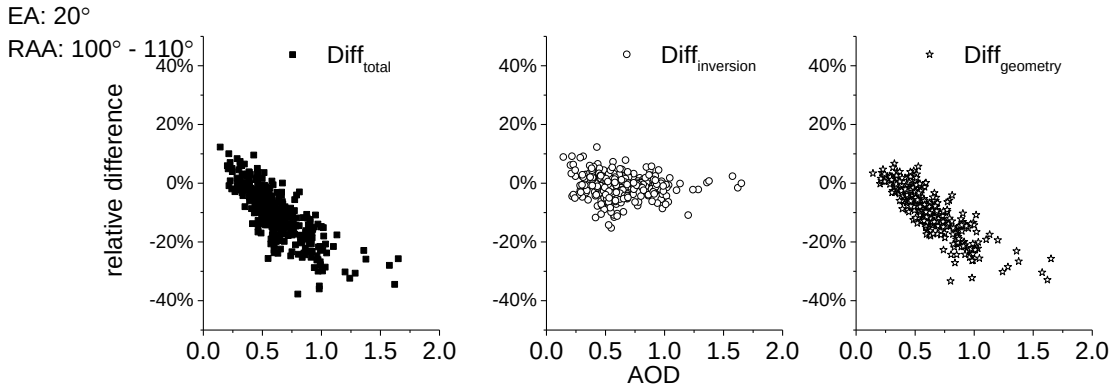

(f)

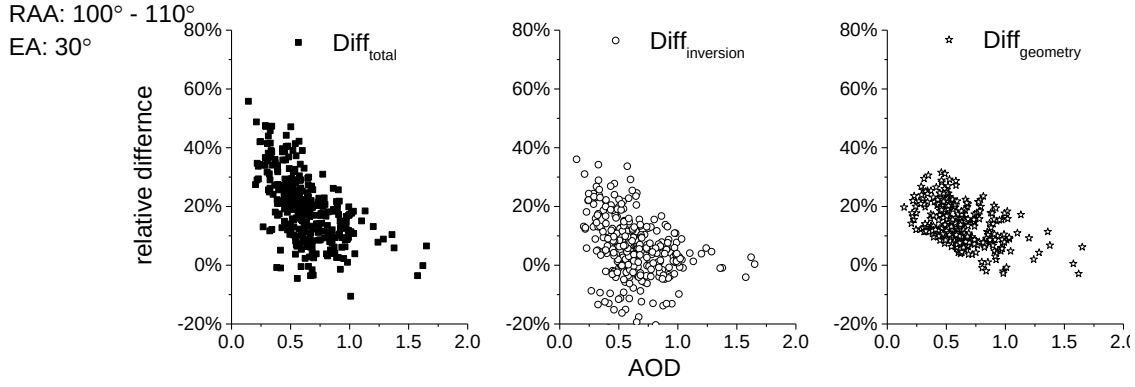

Figure ~~S9~~S25: $Diff_{total}$, $Diff_{inversion}$ and $Diff_{geometry}$ derived for MAX-DOAS observations under clear sky conditions at ~~RAA~~ SAA between 100 ° and 110 ° for NO_2 (a), SO_2 (c), HCHO (e) for elevation angle of 20 °; the corresponding results for an elevation angle of 30 ° are shown in sub-figures (b), (d), (f).

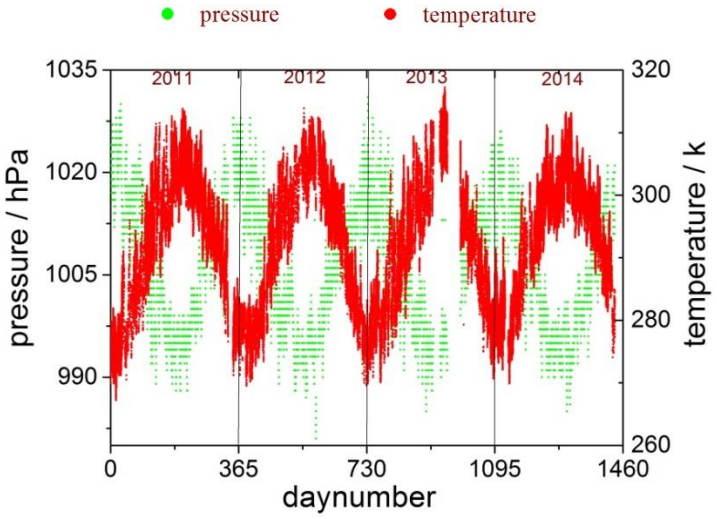

Figure S10: Time series of near-surface temperature and pressure obtained from the ground-based weather station near the MAX-DOAS instrument from 2011 to 2014.

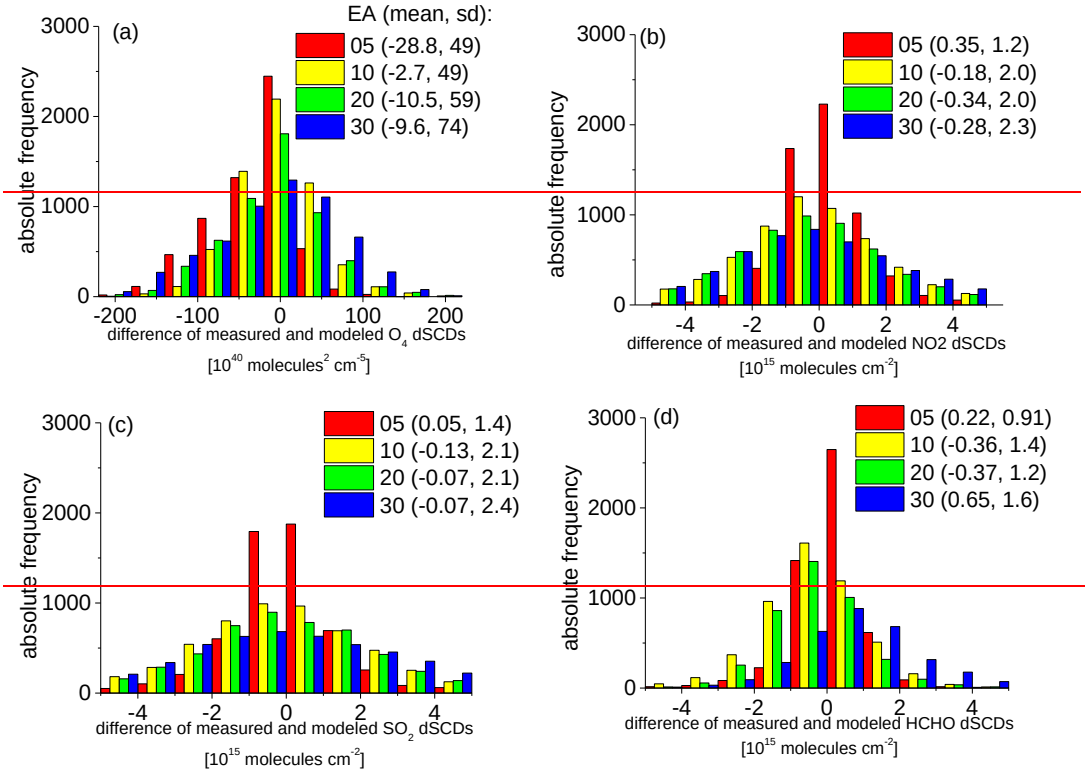

Figure S11: Frequency distributions of the differences between measured and modelled dSCDs for observations at clear sky with low aerosols: O_4 (a), NO_2 (b), SO_2 (c) and HCHO (d). The different elevation angles are indicated by the different colors. The mean values and standard deviations are given in brackets.

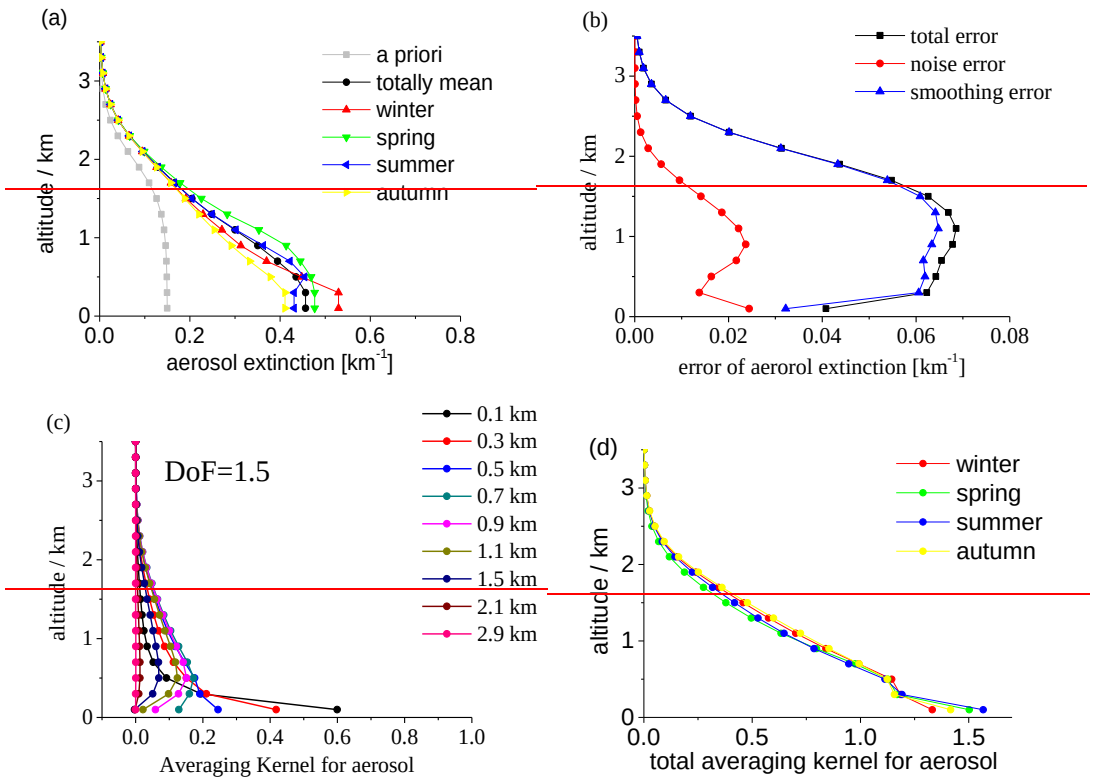

~~**Figure S12: (a) Mean AE profiles for the different seasons derived from observations under clear sky conditions with low aerosols. Also shown is the a-priori profile; (b) total, noise and smoothing errors of the averaged aerosol extinction profile; (c) the corresponding mean averaging kernels for the different height layers (DoF is the degree of freedom); (d) the total averaging kernel for the different seasons.**~~

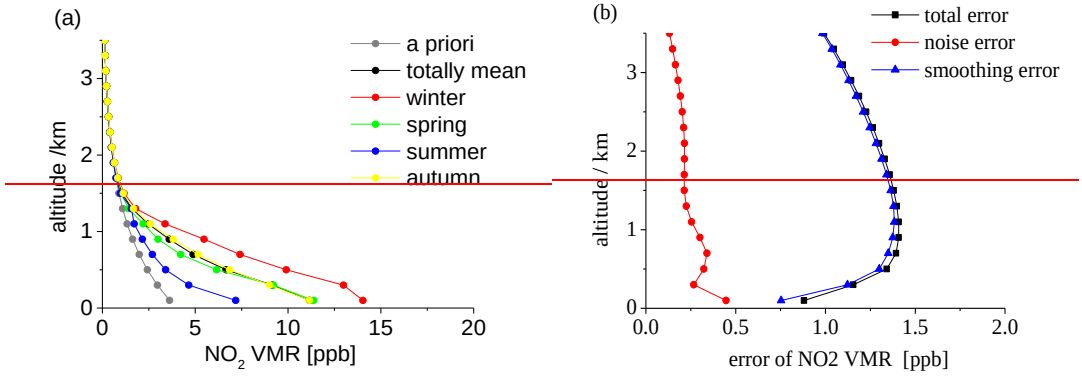

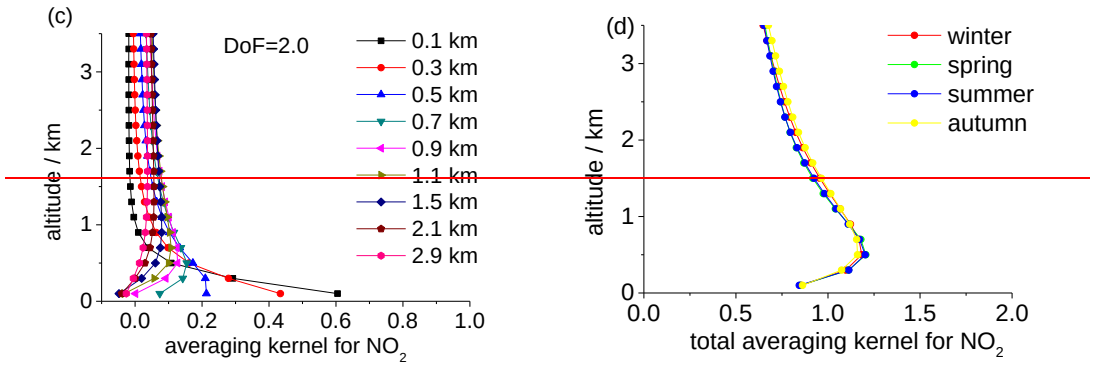

Figure S13: Same as Fig. S12, but for the NO_2 retrieval.

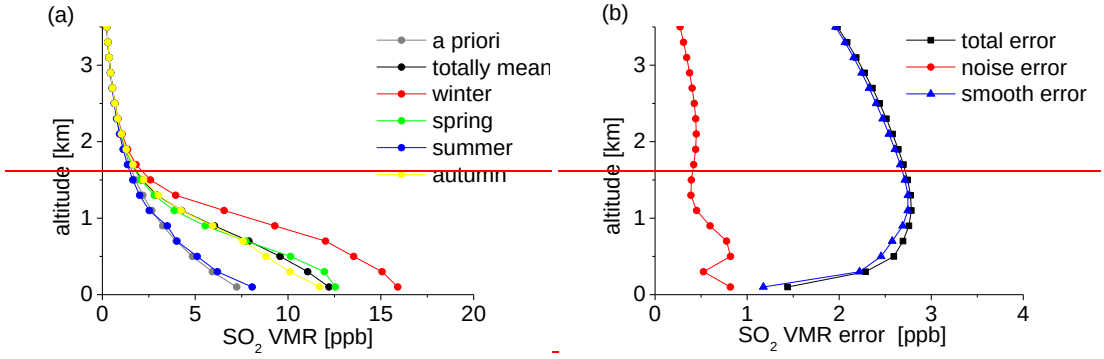

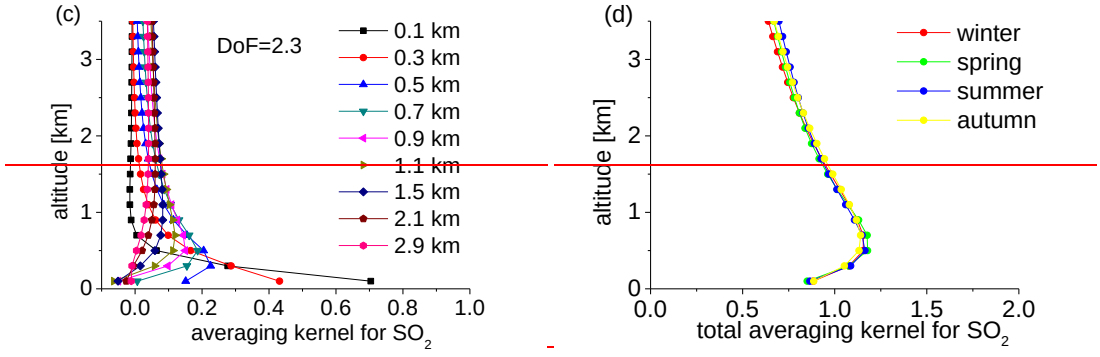

Figure S14: Same as Fig. S12, but for the SO_2 retrieval.

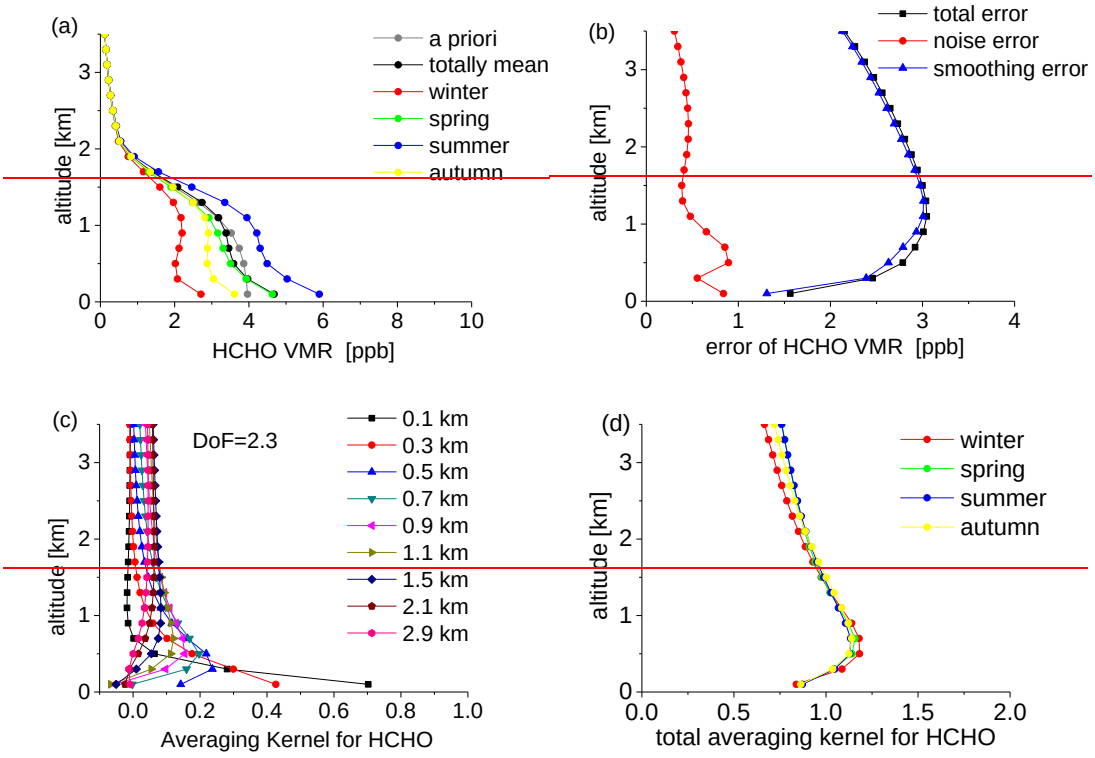

~~Figure S15: Same as Fig. S12, but for the HCHO retrieval.~~

~~(a)~~ ~~(b)~~

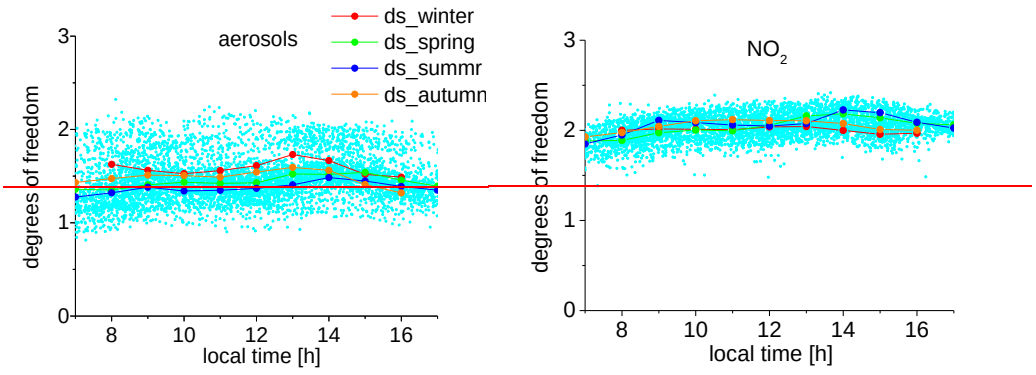

~~(c)~~ ~~(d)~~

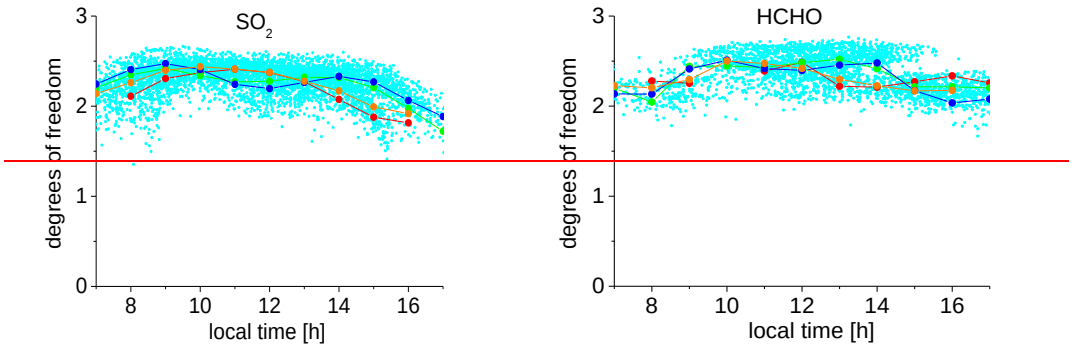

Figure S16: Seasonally averaged diurnal variation of the degree of freedom (ds) of the inversions for aerosols (a), NO_2 (b), SO_2 (c) and HCHO (d). For all four species, the ds in the morning and afternoon is smaller than around noon mainly due to lower scattering probability in the boundary layer.

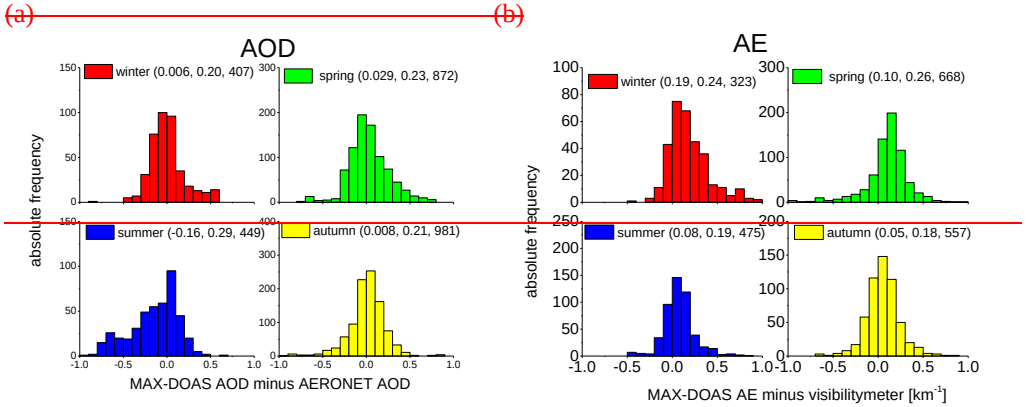

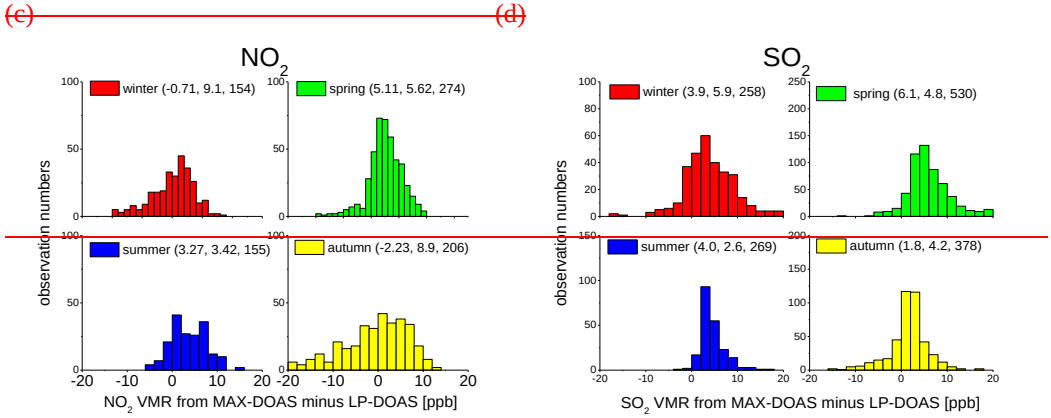

~~**Figure S17: Histograms of the differences between MAX-DOAS results and independent techniques for different seasons for measurements under clear sky conditions with low aerosols. (a) difference of the MAX-DOAS AOD compared with the Taihu AERONET level 1.5 data, (b) difference of the MAX-DOAS AE compared with the results from the visibility meter; (c, d) VMRs of NO_2 and SO_2 derived from MAX-DOAS compared with the results of the nearby long path DOAS instrument. The mean differences, standard deviations and total numbers of observations are given in brackets for each season.**~~

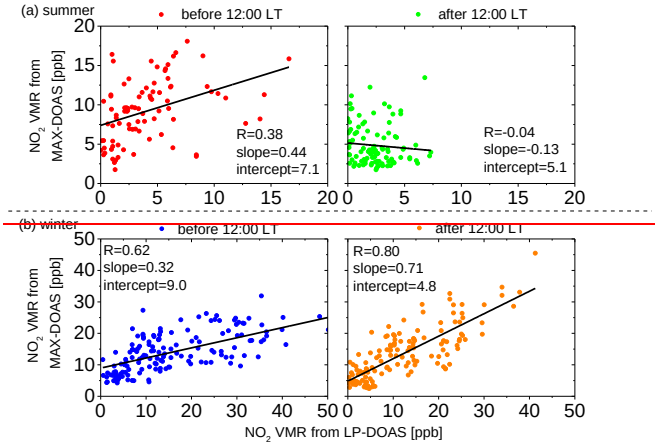

~~**Figure S18: Scatter plots of the near-surface NO_2 VMR derived from MAX-DOAS versus those from LP-DOAS in summer (a) and winter (b) for clear sky conditions with low aerosols. The left and right subfigures show results for morning (before 12:00 local time (LT)) and afternoon (after 12:00 LT), respectively. Results of the linear regression are shown in the individual subfigures.**~~

~~(a)~~

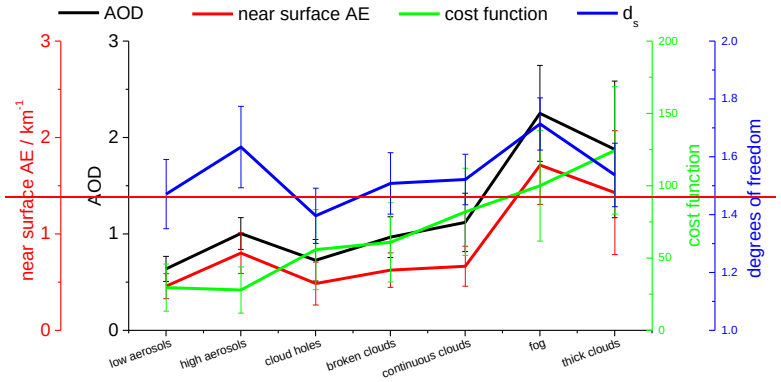

~~(b)~~

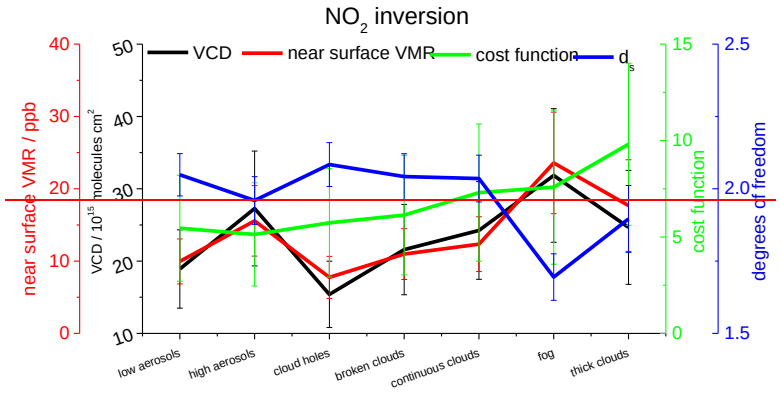

(c)

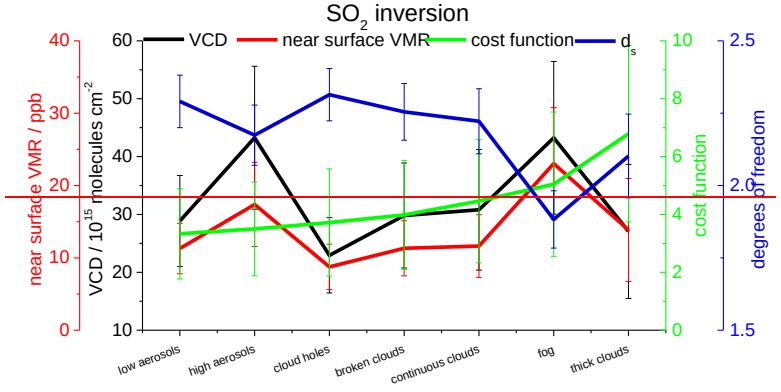

(d)

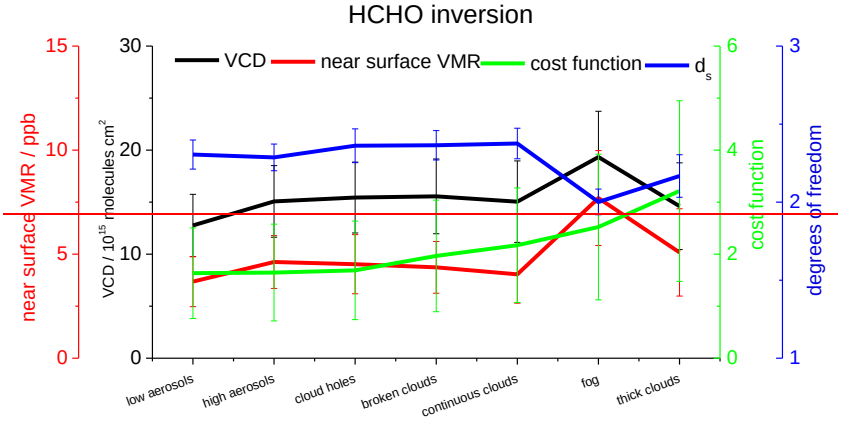

Figure S19: Mean results of all MAX-DOAS retrievals under different sky conditions. Besides the AOD and AE (a) and the trace gas mixing ratios and VCDs (b to d), also the cost functions and degrees of freedom are shown. The cost functions of all species are higher under cloudy conditions compared to clear sky conditions. The effect of clouds is stronger for aerosols compared to TGs. This is consistent with the larger discrepancy between modelled dSCDs and the measured dSCDs shown in Fig. 13 of the main

~~manuscript. The reason is that clouds are not included in the forward model. The DoF of the inversions strongly depend on the cloud and aerosol load. A large aerosol load leads to an increase of the DoF of the aerosol inversion, but to a decrease of the DoF for the TG inversions. The column densities and near surface TG mixing ratios and AE are found to be quite different for the different sky conditions, probably due to cloud effects on the inversions and the different atmospheric chemistry conditions (photolysis) and dynamics for different cloud conditions.~~

~~(a)~~

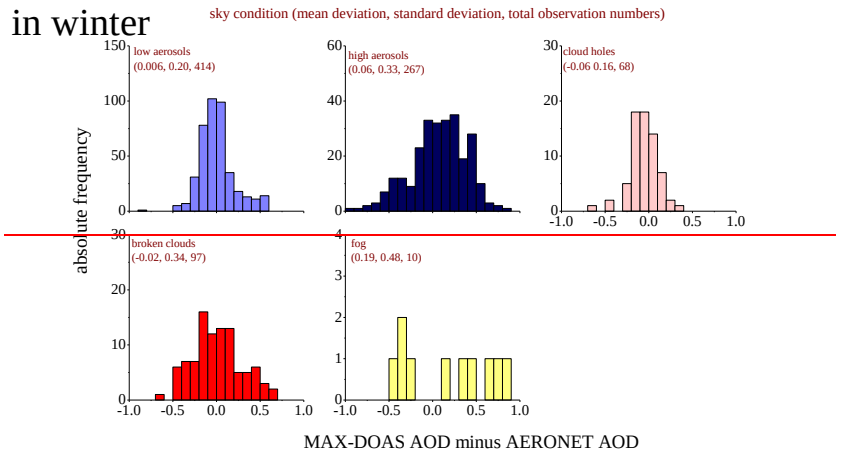

~~(b)~~

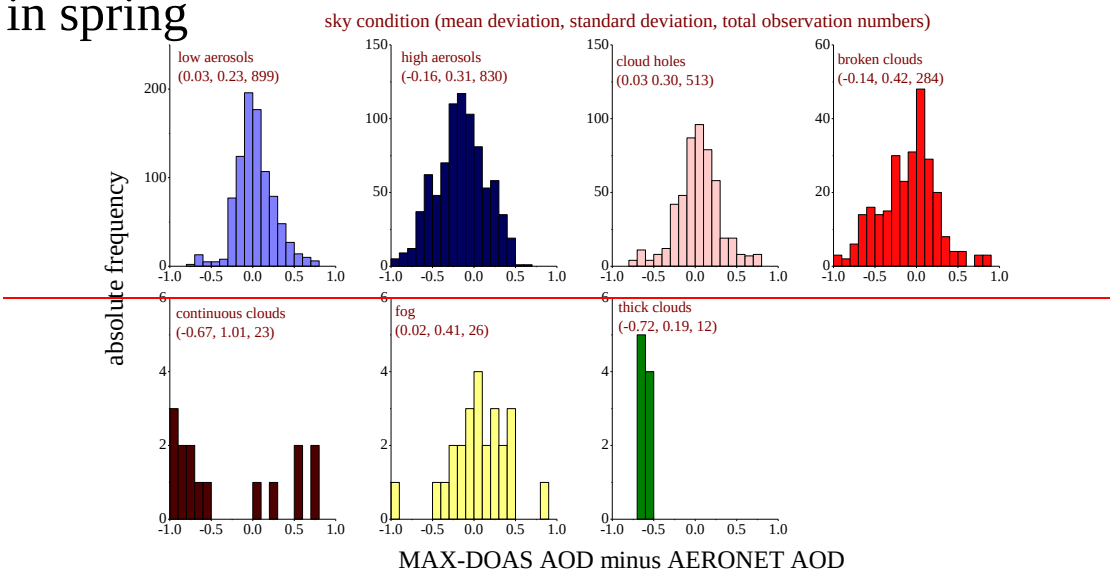

~~(c)~~

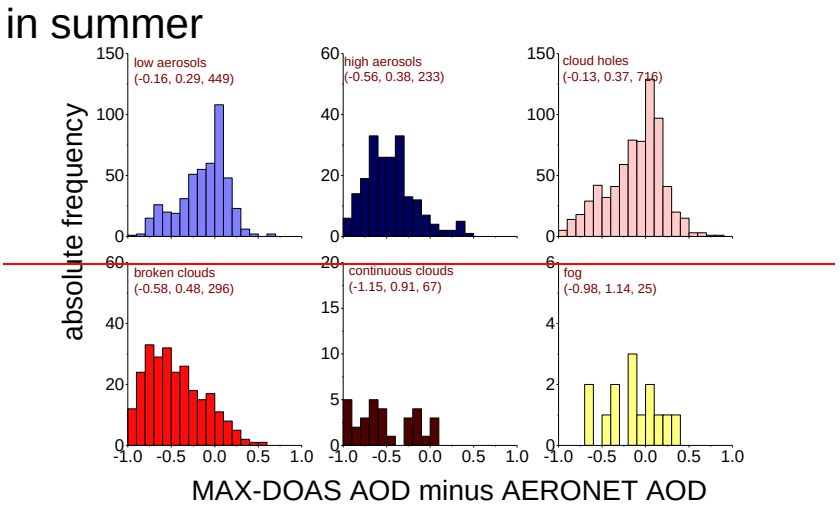
in summer
low aerosols
(-0.16, 0.29, 449)
high aerosols
(-0.56, 0.38, 233)
cloud holes
(-0.13, 0.37, 716)
broken clouds
(-0.58, 0.48, 296)
continuous clouds
(-1.15, 0.91, 67)
fog
(-0.98, 1.14, 25)
absolute frequency
MAX-DOAS AOD minus AERONET AOD

(d)

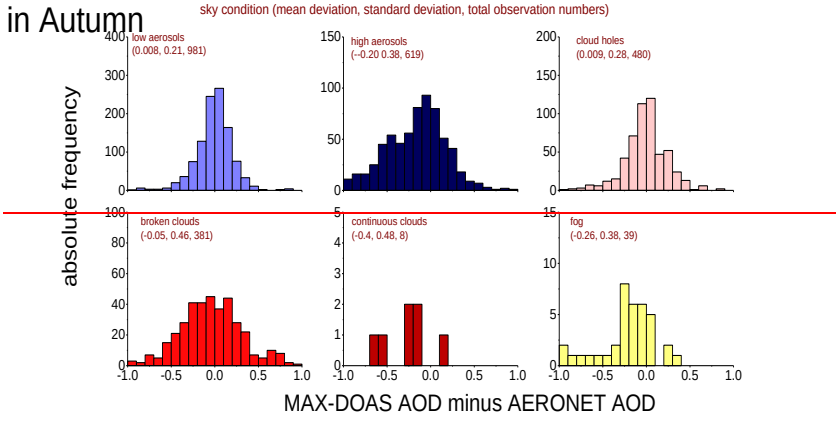
in Autumn
sky condition (mean deviation, standard deviation, total observation numbers)
low aerosols
(0.008, 0.21, 981)
high aerosols
(–0.20 0.38, 619)
cloud holes
(0.009, 0.28, 480)
broken clouds
(-0.05, 0.46, 381)
continuous clouds
(-0.4, 0.48, 8)
fog
(-0.26, 0.38, 39)
absolute frequency
MAX-DOAS AOD minus AERONET AOD

(e) (f)

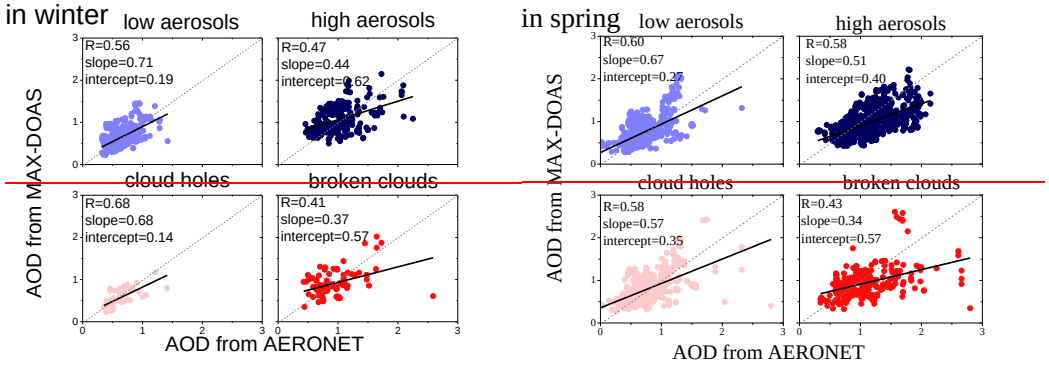
in winter
low aerosols
high aerosols
R=0.56
slope=0.71
intercept=0.19
R=0.47
slope=0.44
intercept=0.62
cloud holes
broken clouds
R=0.68
slope=0.68
intercept=0.14
R=0.41
slope=0.37
intercept=0.57
AOD from MAX-DOAS
AOD from AERONET
in spring
low aerosols
high aerosols
R=0.60
slope=0.67
intercept=0.27
R=0.58
slope=0.51
intercept=0.40
cloud holes
broken clouds
R=0.58
slope=0.57
intercept=0.35
R=0.43
slope=0.34
intercept=0.57
AOD from MAX-DOAS
AOD from AERONET

(g)

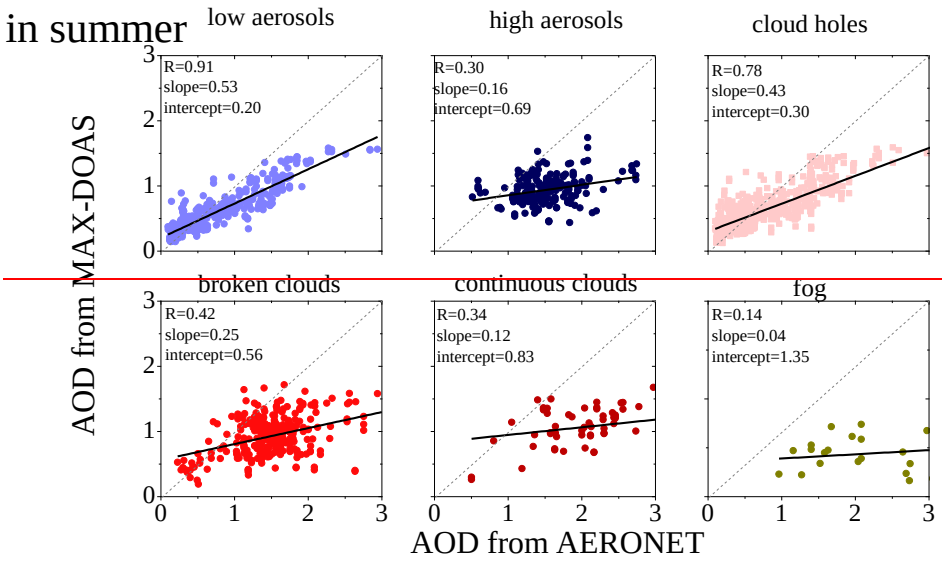

Figure S20: Histograms of the differences of the AOD between MAX-DOAS and the Taihu AERONET observations (level 1.5) under different sky conditions (as identified by the MAX-DOAS observations) in winter (a), spring (b) and summer (c) and autumn (d) for measurements from 2011 to 2013. The mean differences and standard deviations between the two techniques are shown in each subfigure; the AODs from MAX-DOAS are plotted against those from AERONET for different sky conditions; the linear regressions plots are shown in the individual subfigures for winter (e), spring (f) and summer (g). Note that the corresponding scatter plot for autumn is shown in Fig. 16 of the main manuscript.

(a)

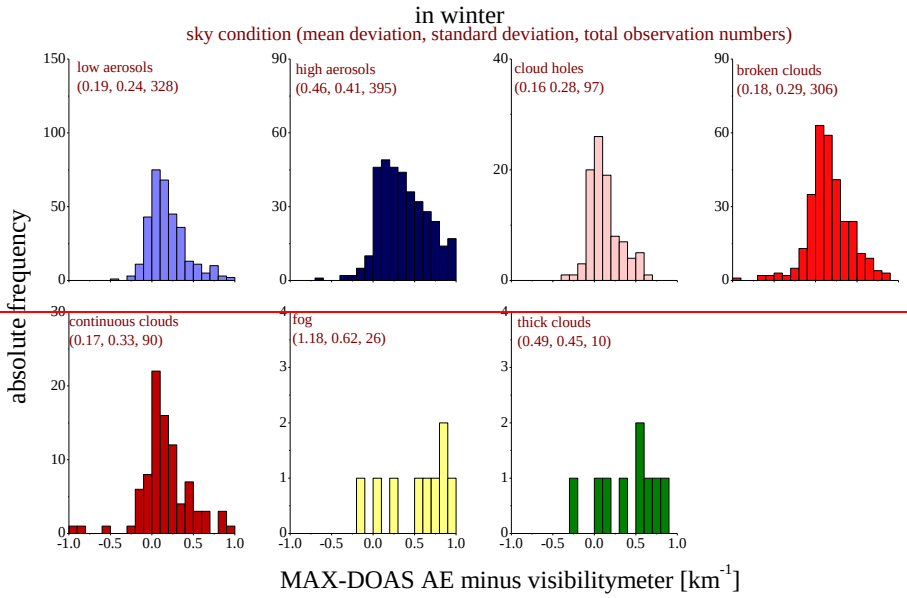

(b)

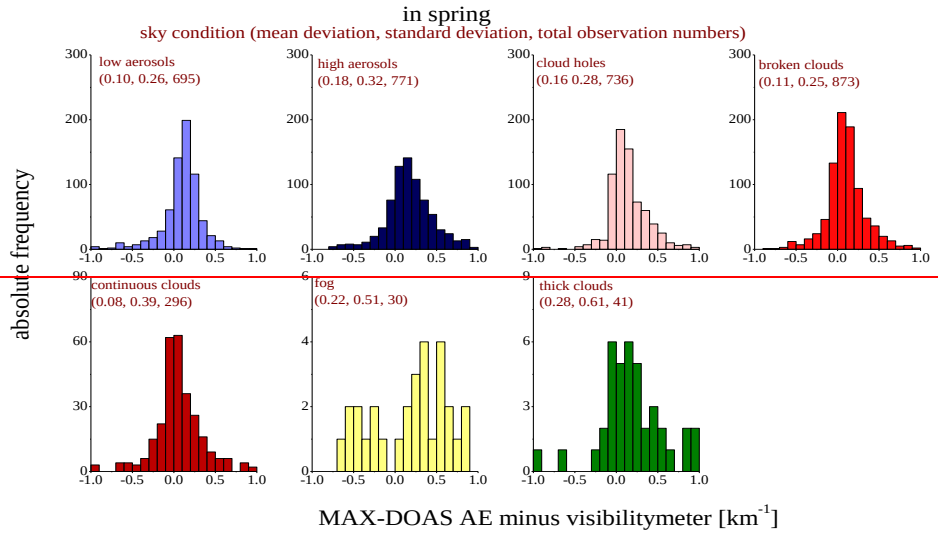
in spring
sky condition (mean deviation, standard deviation, total observation numbers)
low aerosols
(0.10, 0.26, 695)
high aerosols
(0.18, 0.32, 771)
cloud holes
(0.16 0.28, 736)
broken clouds
(0.11, 0.25, 873)
continuous clouds
(0.08, 0.39, 296)
fog
(0.22, 0.51, 30)
thick clouds
(0.28, 0.61, 41)
absolute frequency
MAX-DOAS AE minus visibilitymeter [km-1]

(c)

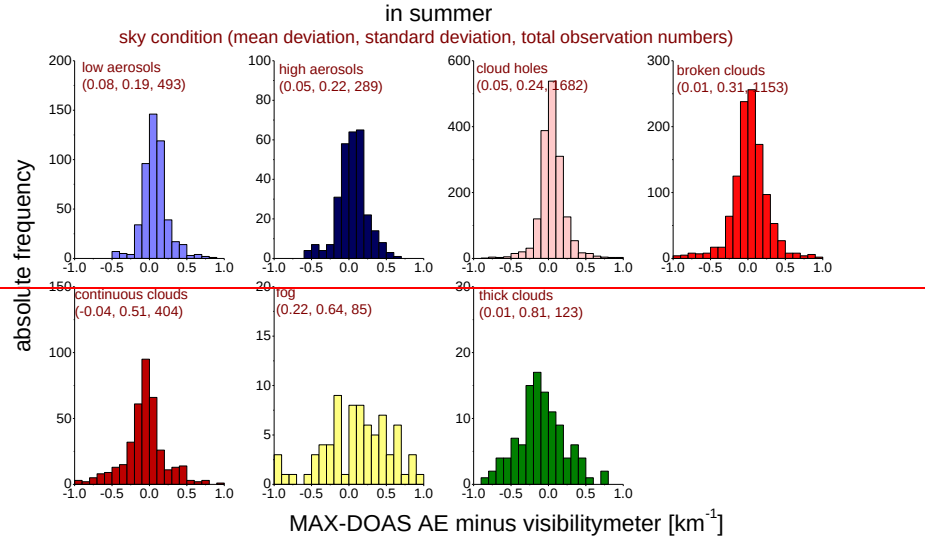
in summer
sky condition (mean deviation, standard deviation, total observation numbers)
low aerosols
(0.08, 0.19, 493)
high aerosols
(0.05, 0.22, 289)
cloud holes
(0.05, 0.24, 1682)
broken clouds
(0.01, 0.31, 1153)
continuous clouds
(-0.04, 0.51, 404)
fog
(0.22, 0.64, 85)
thick clouds
(0.01, 0.81, 123)
absolute frequency
MAX-DOAS AE minus visibilitymeter [km-1]

(d)

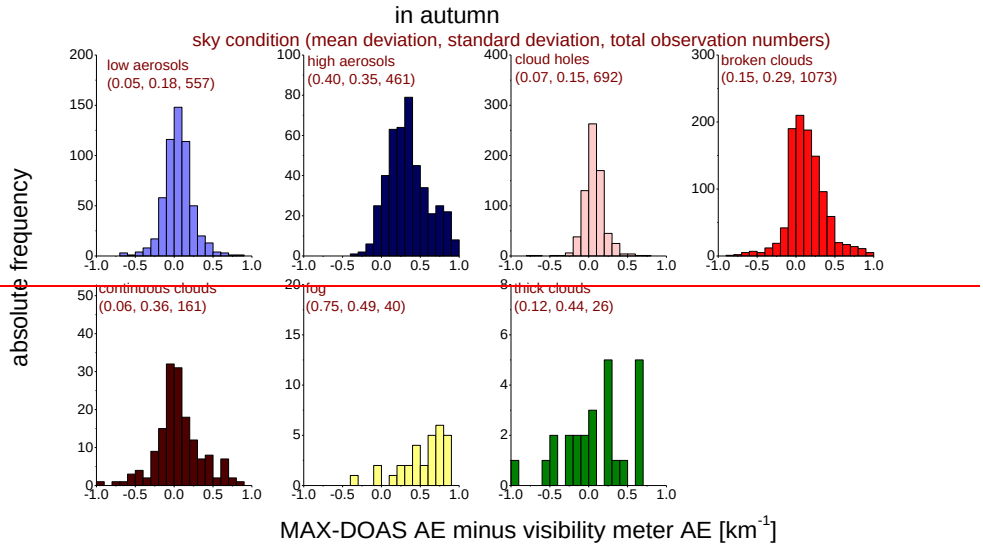
in autumn
sky condition (mean deviation, standard deviation, total observation numbers)
low aerosols
(0.05, 0.18, 557)
high aerosols
(0.40, 0.35, 461)
cloud holes
(0.07, 0.15, 692)
broken clouds
(0.15, 0.29, 1073)
continuous clouds
(0.06, 0.36, 161)
fog
(0.75, 0.49, 40)
thick clouds
(0.12, 0.44, 26)
absolute frequency
MAX-DOAS AE minus visibility meter AE [km-1]

(e)

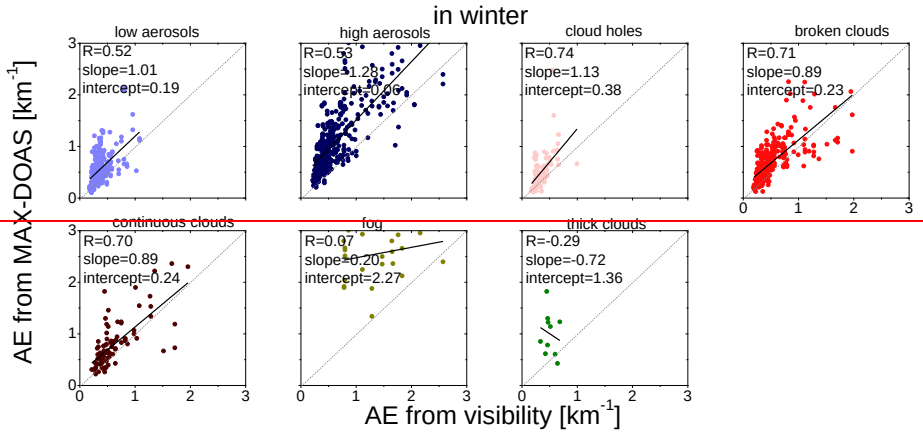
in winter
low aerosols
R=0.52
slope=1.01
intercept=0.19
high aerosols
R=0.53
slope=1.28
intercept=0.06
cloud holes
R=0.74
slope=1.13
intercept=0.38
broken clouds
R=0.71
slope=0.89
intercept=0.23
continuous clouds
R=0.70
slope=0.89
intercept=0.24
fog
R=0.07
slope=0.20
intercept=2.27
thick clouds
R=-0.29
slope=-0.72
intercept=1.36
AE from MAX-DOAS [km-1]
AE from visibility [km-1]

(f)

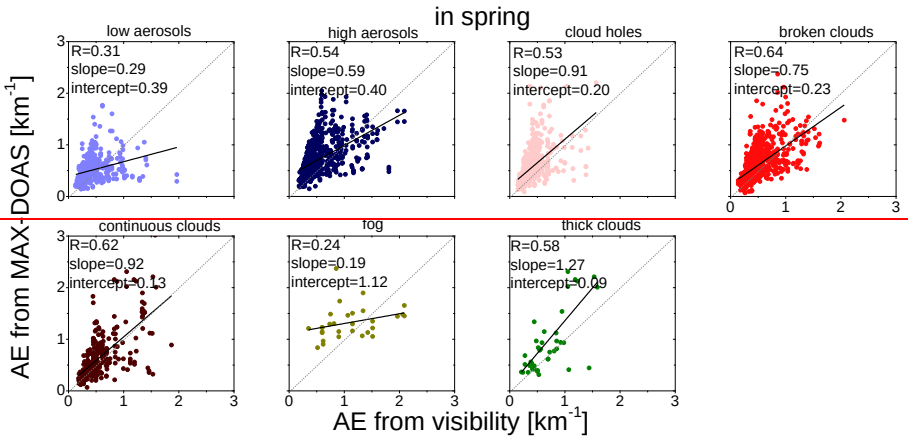

~~(g)~~

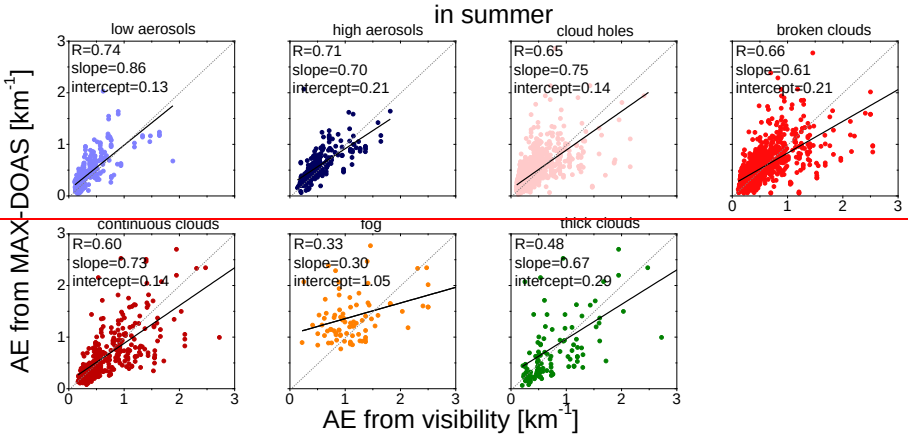

~~**Figure S21: Same as Fig. S20 but for the near-surface aerosol extinction compared with the results from the visibility meter. Note that the corresponding scatter plot for autumn is shown in Fig. 17 of the main manuscript.**~~

~~(a)~~

in winter

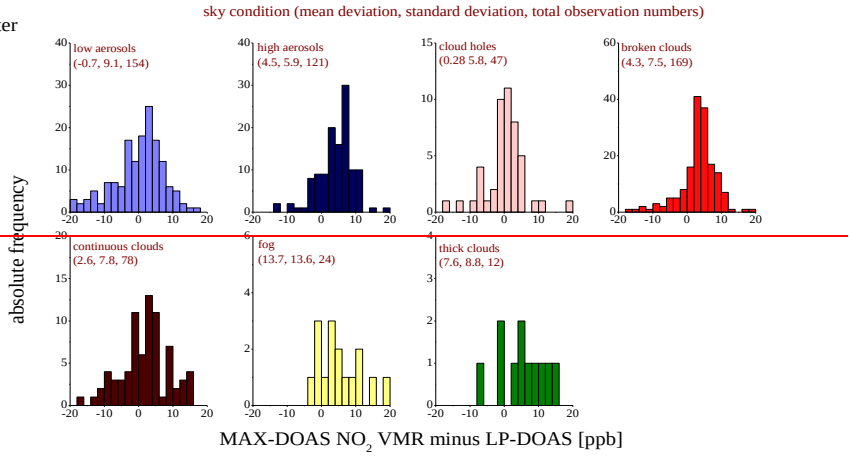

~~(b)~~

in spring

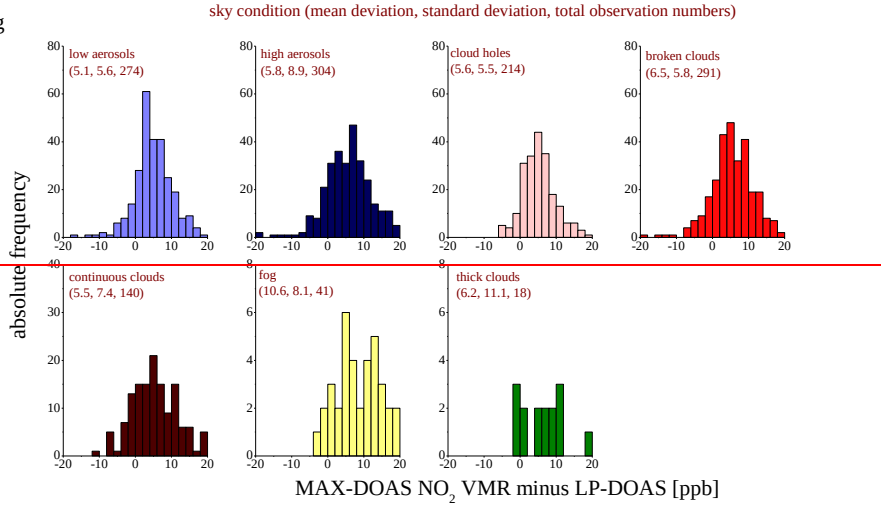

~~(c)~~

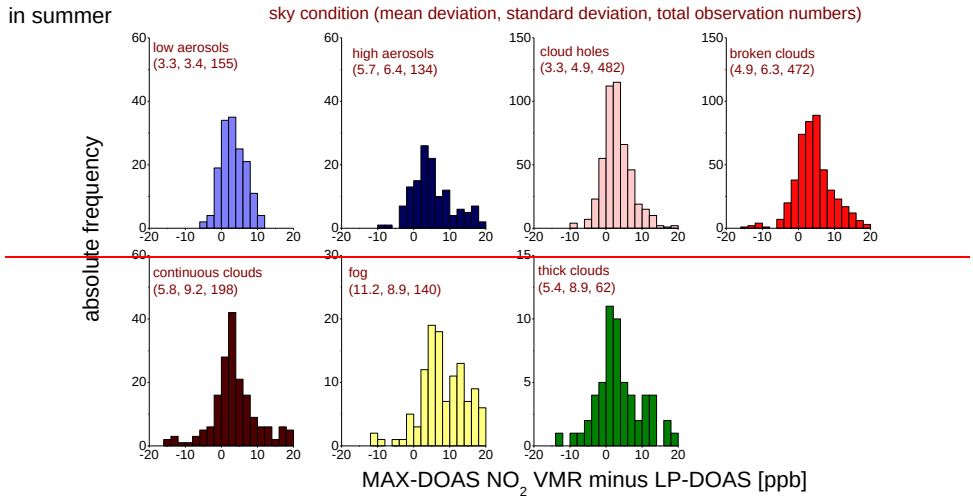
in summer
sky condition (mean deviation, standard deviation, total observation numbers)
low aerosols
(3.3, 3.4, 155)
high aerosols
(5.7, 6.4, 134)
cloud holes
(3.3, 4.9, 482)
broken clouds
(4.9, 6.3, 472)
continuous clouds
(5.8, 9.2, 198)
fog
(11.2, 8.9, 140)
thick clouds
(5.4, 8.9, 62)
absolute frequency
MAX-DOAS NO2 VMR minus LP-DOAS [ppb]

~~(d)~~

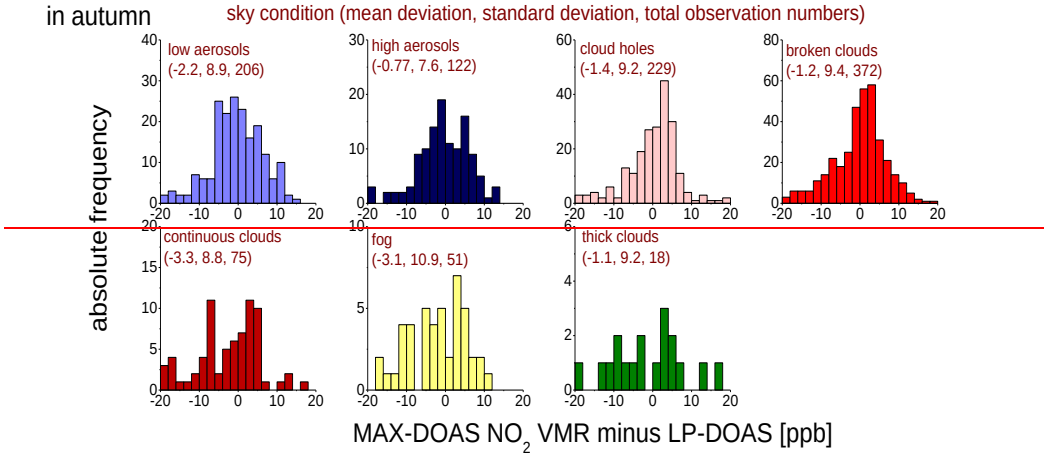
in autumn
sky condition (mean deviation, standard deviation, total observation numbers)
low aerosols
(-2.2, 8.9, 206)
high aerosols
(-0.77, 7.6, 122)
cloud holes
(-1.4, 9.2, 229)
broken clouds
(-1.2, 9.4, 372)
continuous clouds
(-3.3, 8.8, 75)
fog
(-3.1, 10.9, 51)
thick clouds
(-1.1, 9.2, 18)
absolute frequency
MAX-DOAS NO2 VMR minus LP-DOAS [ppb]

~~(e)~~

in winter

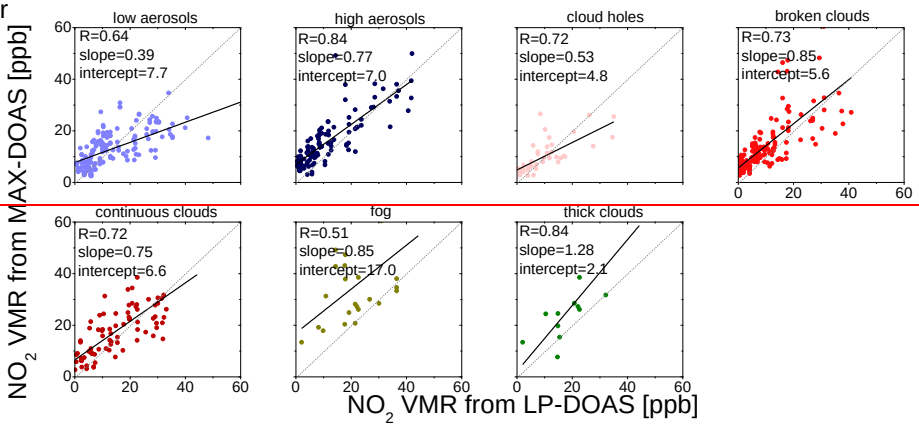

~~(f)~~

in spring

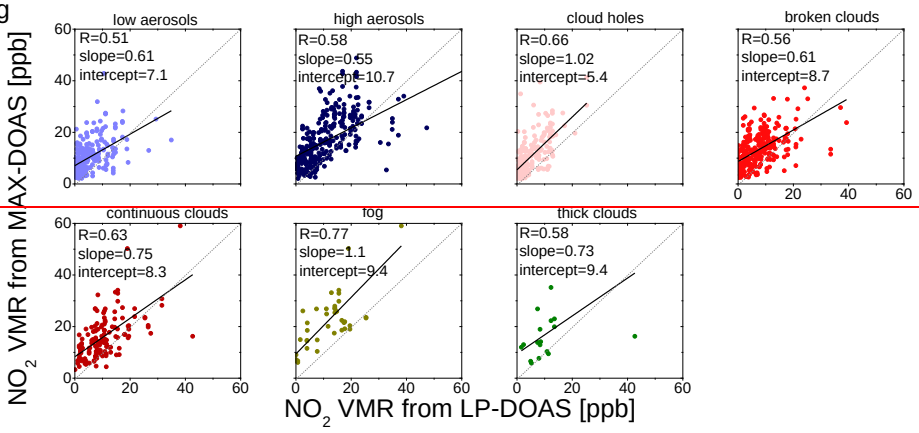

~~(g)~~

in summer

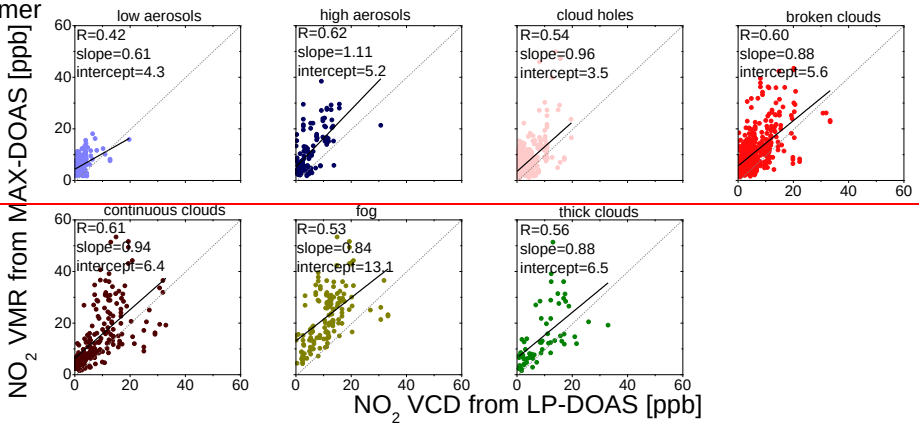

~~**Figure S22: Same as Fig. S20 but for the near-surface NO_2 VMRs compared with the results from LP-DOAS. Note that the corresponding scatter plot for autumn is shown in Fig. 18 of the main manuscript.**~~

~~(a)~~

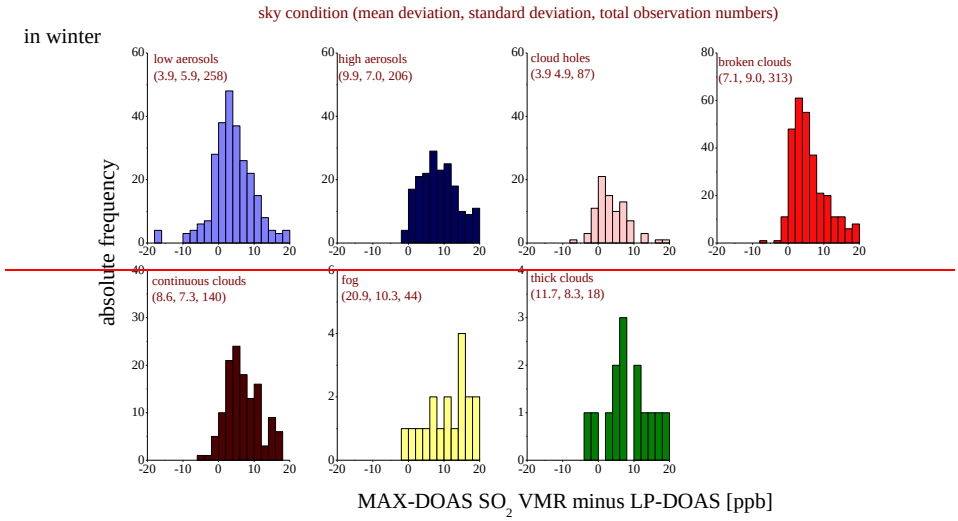

~~(b)~~

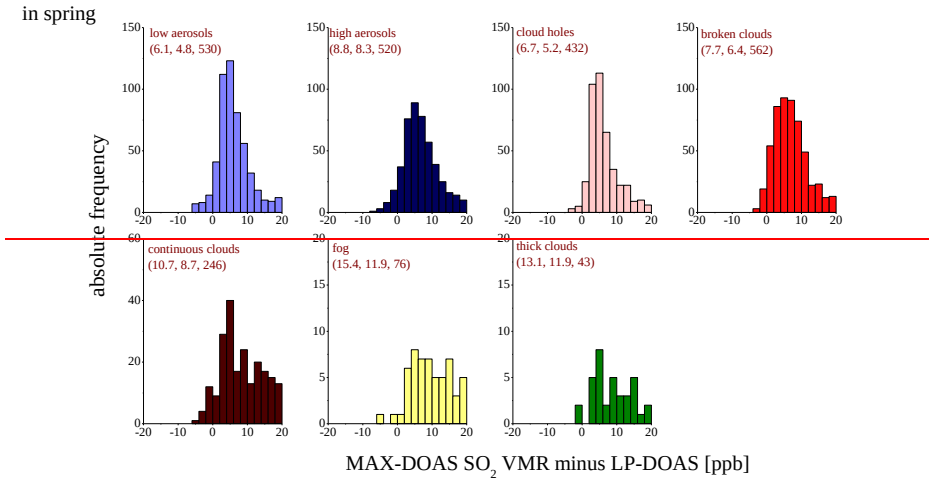

~~(c)~~

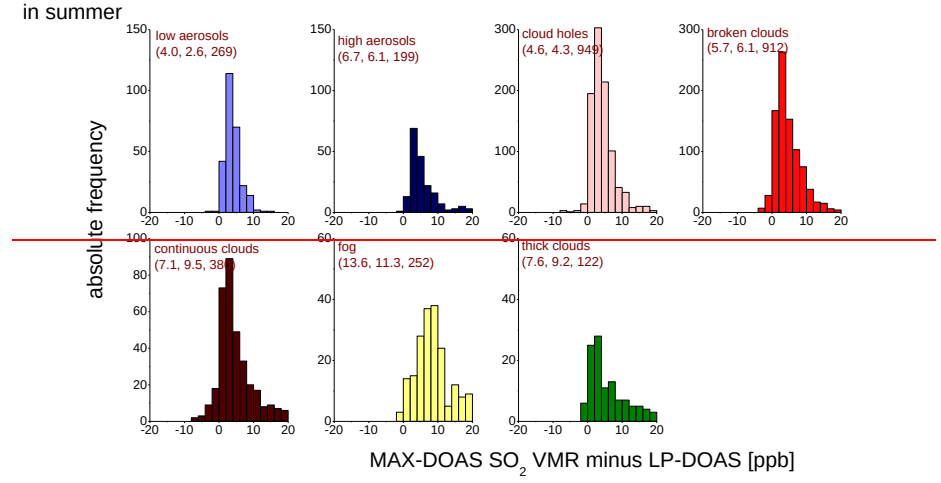
in summer
low aerosols
(4.0, 2.6, 269)
high aerosols
(6.7, 6.1, 199)
cloud holes
(4.6, 4.3, 949)
broken clouds
(5.7, 6.1, 912)
continuous clouds
(7.1, 9.5, 388)
fog
(13.6, 11.3, 252)
thick clouds
(7.6, 9.2, 122)
absolute frequency
MAX-DOAS SO2 VMR minus LP-DOAS [ppb]

(d)

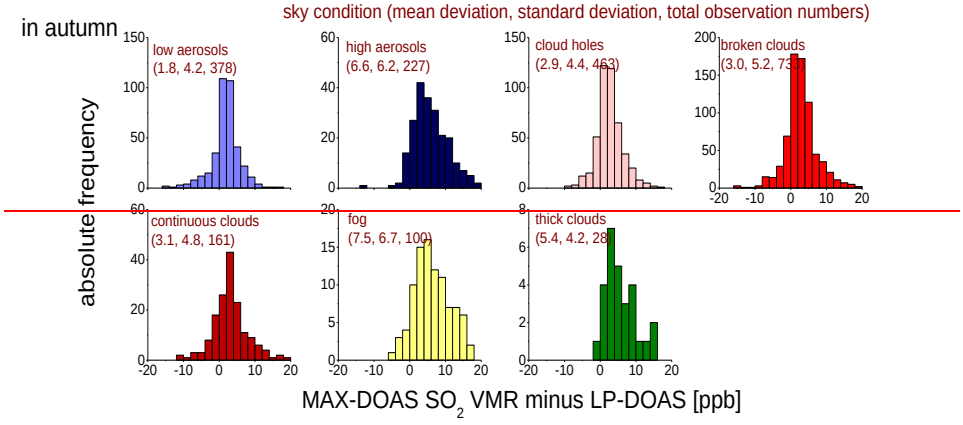
in autumn
sky condition (mean deviation, standard deviation, total observation numbers)
low aerosols
(1.8, 4.2, 378)
high aerosols
(6.6, 6.2, 227)
cloud holes
(2.9, 4.4, 463)
broken clouds
(3.0, 5.2, 73
continuous clouds
(3.1, 4.8, 161)
fog
(7.5, 6.7, 100)
thick clouds
(5.4, 4.2, 28
absolute frequency
MAX-DOAS SO2 VMR minus LP-DOAS [ppb]

(e)

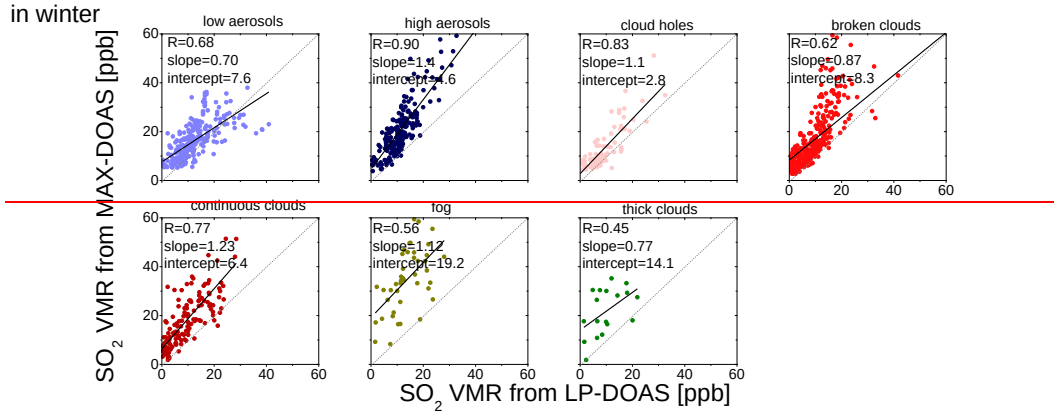
in winter
low aerosols
R=0.68
slope=0.70
intercept=7.6
high aerosols
R=0.90
slope=1.4
intercept=4.6
cloud holes
R=0.83
slope=1.1
intercept=2.8
broken clouds
R=0.62
slope=0.87
intercept=8.3
continuous clouds
R=0.77
slope=1.23
intercept=6.4
fog
R=0.56
slope=1.12
intercept=19.2
thick clouds
R=0.45
slope=0.77
intercept=14.1
SO2 VMR from MAX-DOAS [ppb]
SO2 VMR from LP-DOAS [ppb]

(f)

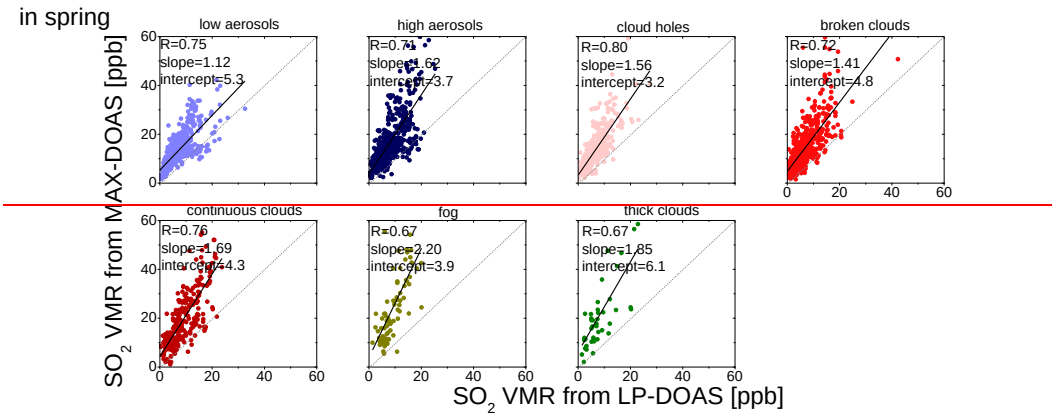

~~(g)~~

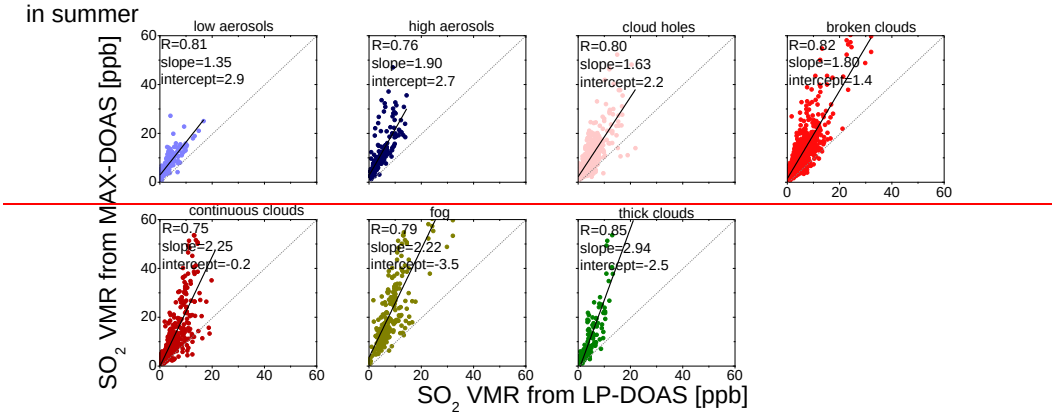

~~**Figure S23: Same as Fig. S20 but for the near-surface SO_2 VMRs compared with the results from LP-DOAS. Note that the corresponding scatter plot for autumn is shown in Fig. 19 of the main manuscript.**~~

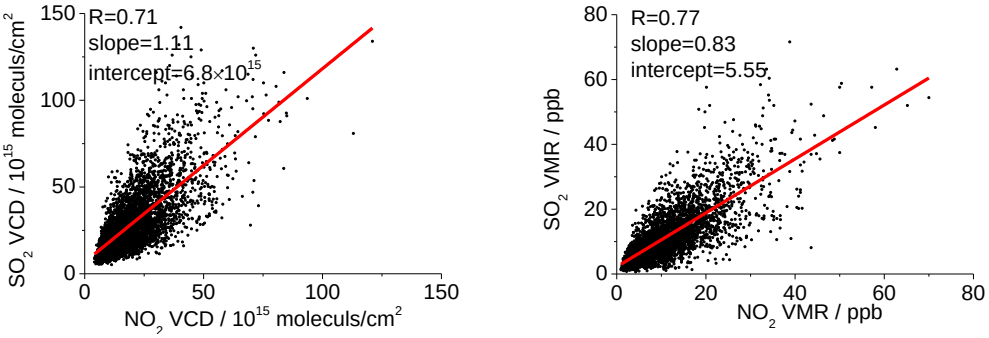

Figure ~~S24~~S26: SO_2 VCDs (a) and VMRs near surface (b) plotted against NO_2 VCDs and VMRs, respectively. The linear regressions are shown in each subfigure.

(a)

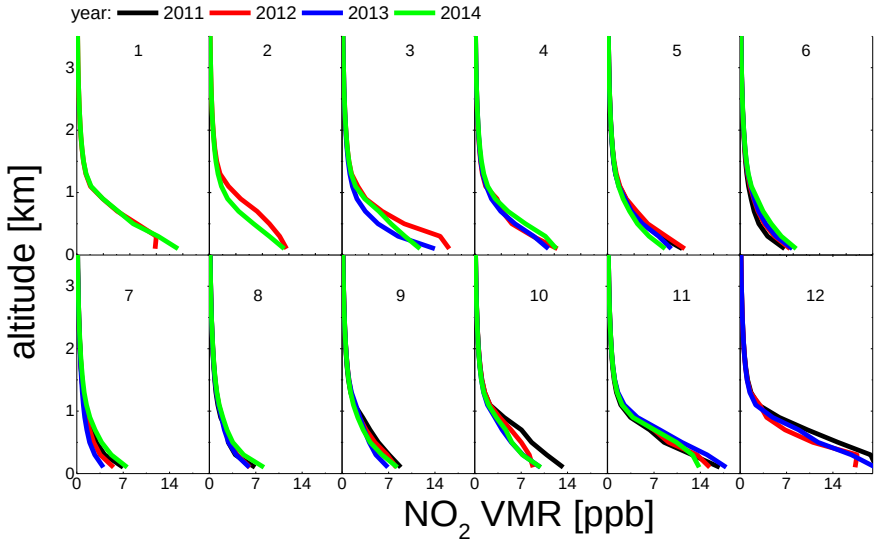
year: 2011 2012 2013 2014
1
2
3
4
5
6
7
8
9
10
11
12
altitude [km]
0
1
2
3
0
7
14
NO2 VMR [ppb]

(b)

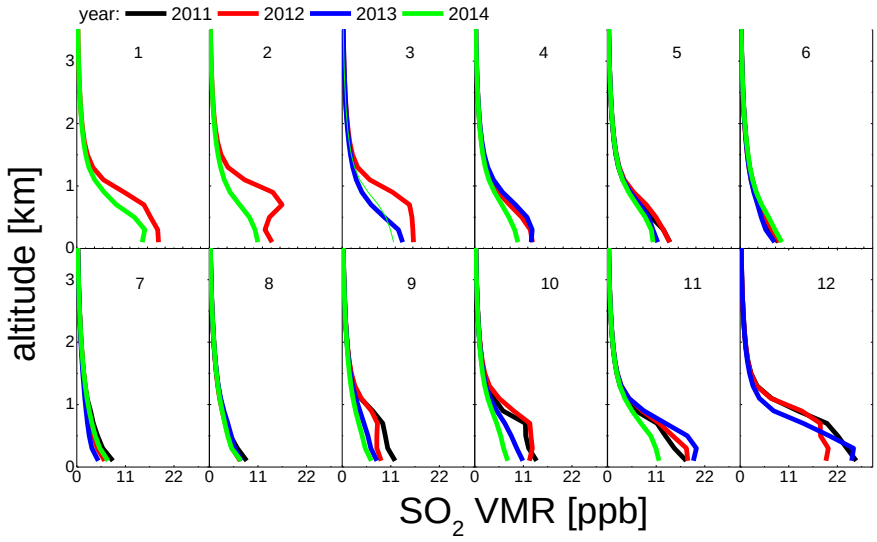

(c)

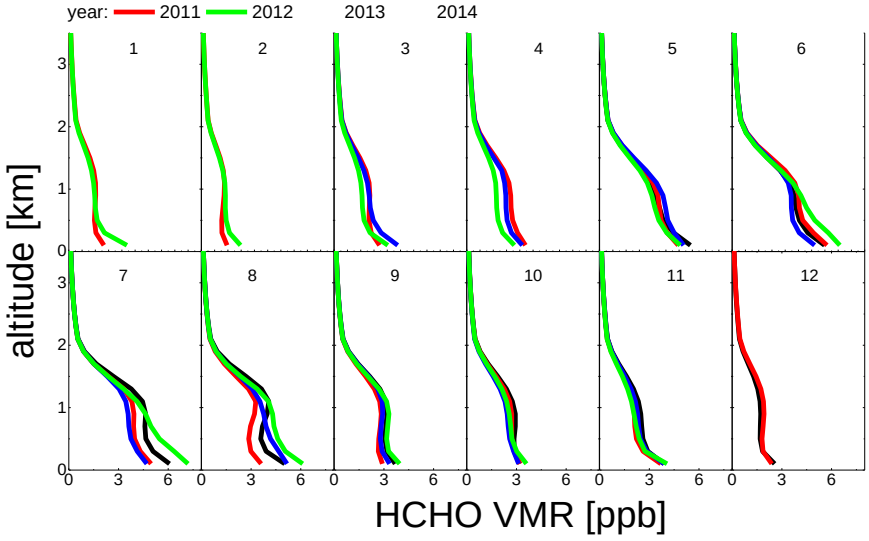

Figure ~~S25~~S27: Monthly mean profiles of NO_2 (a), SO_2 (b), HCHO (c) VMRs under clear sky conditions for May 2011 to November 2014.

(a) (b) (c)

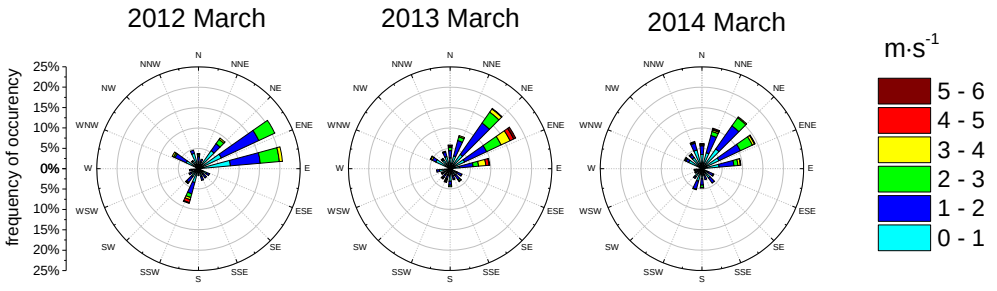

Figure S28: Wind roses for March 2012 (a), 2013 (b) and 2014(c).

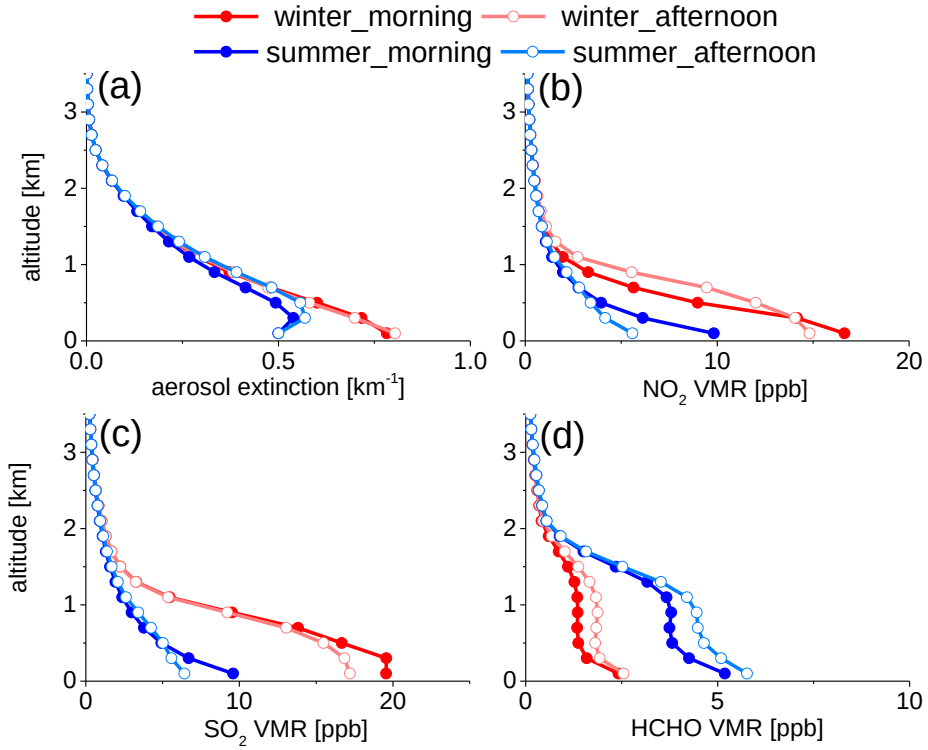

Figure S29: Average profiles of aerosol extinction (a), NO_2 VMR (b), SO_2 VMR (c) and HCHO VMR (d) in the morning and afternoon for winter and summer, respectively.

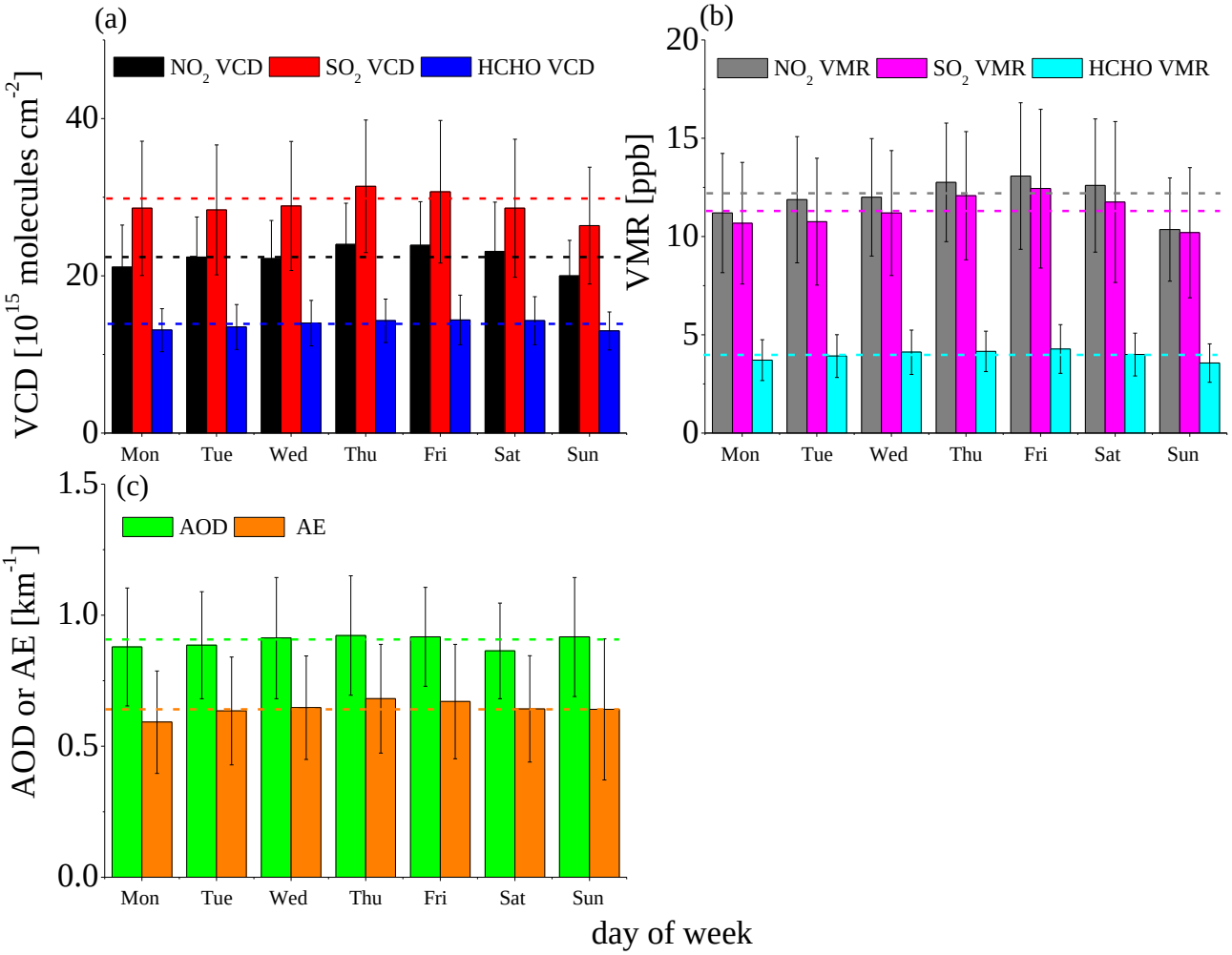

Figure S30: Mean weekly cycles of VCDs (a) and near-surface VMRs (b) of NO_2, SO_2 and HCHO as well as the AODs and near-surface AEs (c) for all MAX-DOAS observations from 2011 to 2014. The dashed lines denote the mean values during the working days from Monday to Friday (same colours as for the bars).

~~(a) (b) (c)~~

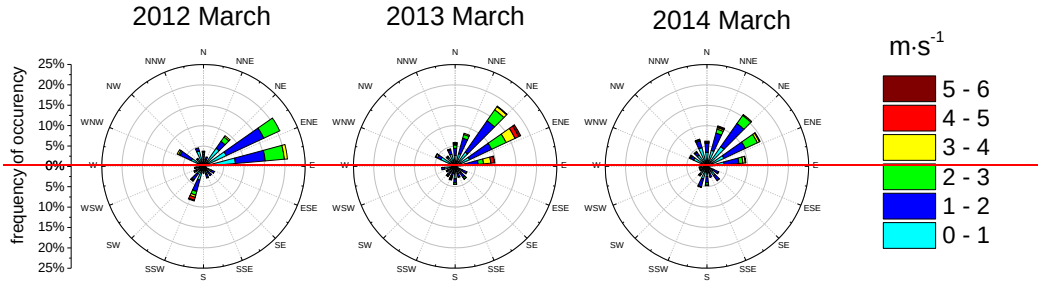

Figure S26: Wind roses for March 2012 (a), 2013 (b) and 2014(c).

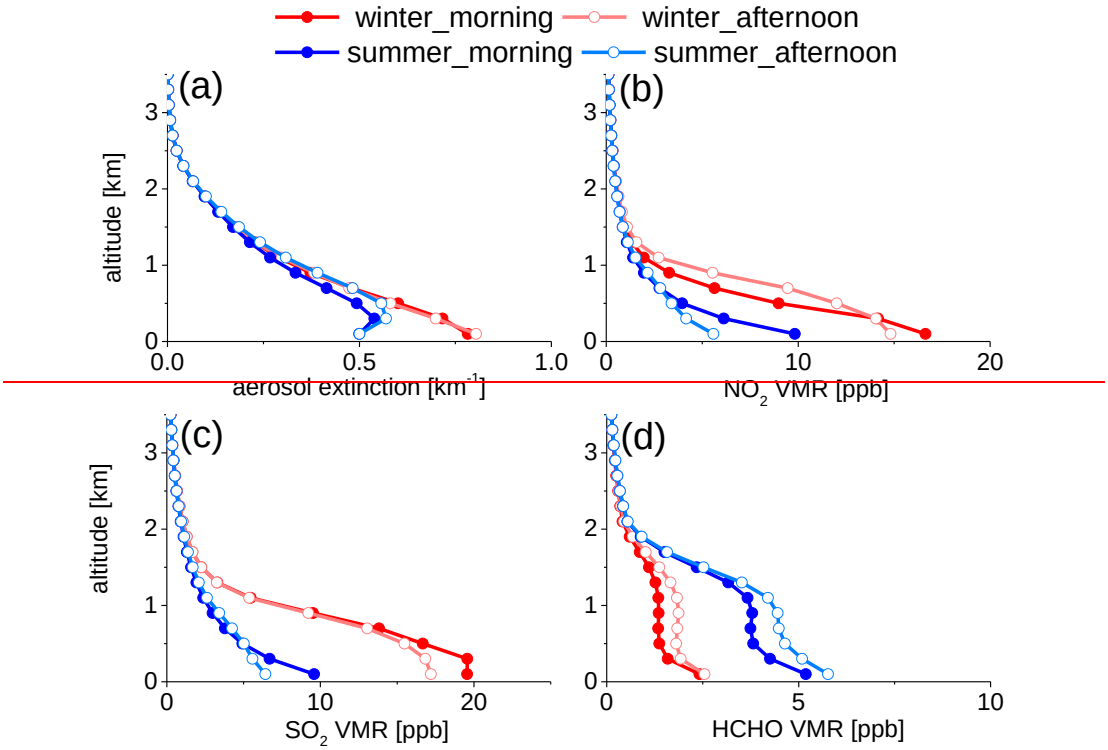

Figure S27: Average profiles of aerosol extinction (a), NO_2 VMR (b), SO_2 VMR (c) and HCHO VMR (d) in the morning and afternoon for winter and summer, respectively.

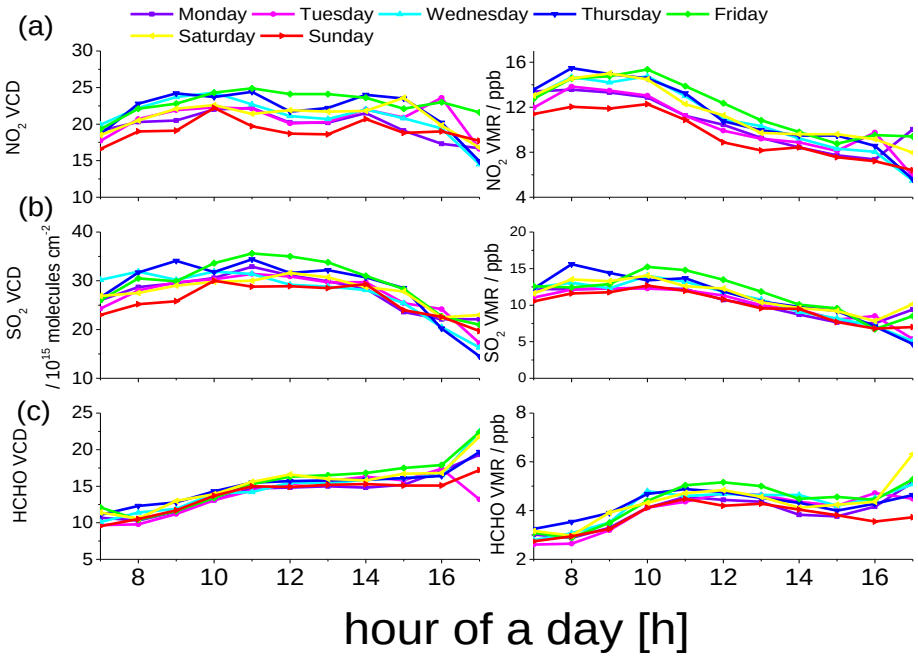

Figure ~~S28~~S31: Diurnal variations of VCDs (left) and surface VMR (right) of NO_2 (a), SO_2 (b) and HCHO (c) for different days of the week, averaged over the period of May 2011 to November 2014.

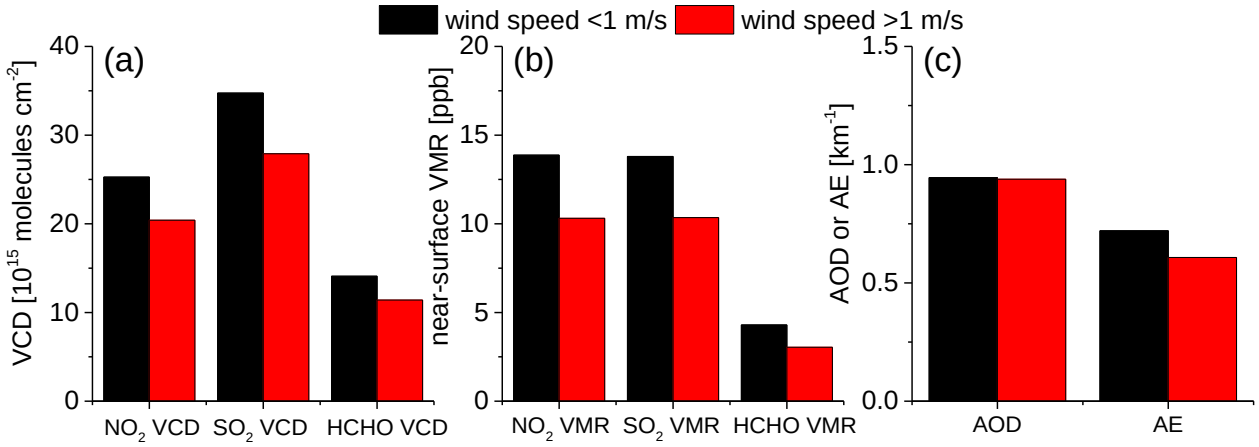

Figure S32: Comparisons of VCDs (a) and near-surface VMRs (b) of NO_2, SO_2 and HCHO, as well as AODs and near-surface AEs for different wind speeds (smaller than 1m/s or larger than 1m/s).

Table S1 Absolute and relative differences of the retrieved VCDs (and AOD) and near-surface VMRs (AEs) of NO_2, SO_2 and HCHO between either using the three test a-priori profiles or the standard a-priori profile (shown in Fig. S6)

species	a-priori profile	Absolute difference		Relative difference	
		VCD (10^{15} molecules cm^{-2}) or AOD	Near-surface VMR (ppb) or AE (km^{-1})	VCD or AOD	Near-surface VMR or AE
aerosols	Priori 1	-0.17	0.05	-24%	10%
	Priori 2	0.11	0.003	15%	0.6%
	Priori 3	-0.16	0.67	22%	136%
NO_2	Priori 1	-1.7	-0.29	-7%	2.2%
	Priori 2	2.4	0.18	10%	1.3%
	Priori 3	2.7	0.09	11%	0.7%
SO_2	Priori 1	-3.1	-0.21	-10%	-2%
	Priori 2	3.9	0.10	12%	1%
	Priori 3	2.3	-0.17	7%	-1%
HCHO	Priori 1	-0.22	-0.027	-1%	-0.5%
	Priori 2	0.85	0.049	5%	1%
	Priori 3	-1.1	-0.025	-7%	-0.5%

References

Bussemer, M.: Der Ring-Effekt: Ursachen und Einfluß auf die Messung stratosparischer Spurenstoffe, Diploma thesis, University of Heidelberg, 1993.

Chance, K. V. and Spurr, R. J. D.: Ring effect studies: Rayleigh scattering, including molecular parameters for rotational Raman scattering, and the Fraunhofer spectrum, Appl. Optics, 36, 5224–5230, 1997.

Coburn, S., Dix, B., Sinreich, R., and Volkamer, R.: The CU ground MAX-DOAS instrument: characterization of RMS noise limitations and first measurements near Pensacola, FL of BrO, IO, and CHOCHO, Atmos. Meas. Tech., 4, 2421-2439, doi:10.5194/amt-4-2421-2011, 2011.

Frieß, U., Monks, P. S., Remedios, J. J., Rozanov A., Sinreich R., Wagner T., and Platt, U.: MAX-DOAS O_4 measurements: A new technique to derive information on atmospheric aerosols: 2. Modeling studies, J. Geophys. Res., 111, D14203, 2006, doi:10.1029/2005JD006618.

Grainger J. F. and Ring, J.: Anomalous Fraunhofer line profiles, Nature, 193, 762, 1962.

Hendrick, F., Müller, J.-F., Clémer, K., Wang, P., De Mazière, M., Fayt, C., Gielen, C., Hermans, C., Ma, J. Z., Pinardi, G., Stavrakou, T., Vlemmix, T., and Van Roozendael, M.: Four years of ground-based MAX-DOAS observations of HONO and NO2 in the Beijing area, Atmos. Chem. Phys., 14, 765-781, doi:10.5194/acp-14-765-2014, 2014.

Holla, R., Schmitt, S., Friess, U., Pöhler, D., Zingler, J., Corsmeier, U., and Platt, U.: Vertical distribution of BrO in the boundary layer at the Dead Sea. Environmental Chemistry, 2015.

Hönninger, G., Friedeburg, C. von and Plat, U., Multi axis differential optical absorption spectroscopy (MAX-DOAS), Atmos. Chem. Phys., 4, 231–254, 2004

Junkermann, W.: On the distribution of formaldehyde in the western Po-Valley, Italy, during FORMAT 2002/2003, Atmos. Chem. Phys., 9, 9187–9196, doi:10.5194/acp-9-9187-2009, 2009.

Kraus, S.: DOASIS, A Framework Design for DOAS, PhD-thesis, University of lMannheim,http://hci.iwr.uni-heidelberg.de/publications/dip/2006/Kraus_PhD2006.pdf, 2006.

Pinardi, G., Van Roozendael, M., Abuhassan, N., Adams, C., Cede, A., Clémer, K., Fayt, C., Frieß, U., Gil, M., Herman, J., Hermans, C., Hendrick, F., Irie, H., Merlaud, A., Navarro Comas, M., Peters, E., Piters, A. J. M., Puentedura, O., Richter, A., Schönhardt, A., Shaiganfar, R., Spinei, E., Strong, K., Takashima, H., Vrekoussis, M., Wagner, T., Wittrock, F., and Yilmaz, S.: MAX-DOAS formaldehyde slant column measurements during CINDI: intercomparison and analysis improvement, Atmos. Meas. Tech., 6, 167-185, doi:10.5194/amt-6-167-2013, 2013.

Rodgers, C. D.: Inverse methods for atmospheric sounding, theory and practice, Series on Atmospheric, Oceanic and Planetary Physics, World Scientific, 2000.

Shefov, N. N.: Spectroscopic, photoelectric, and radar investigations of the aurora and the nightglow, Izd. Akad. Nauk., 1, 1959.

Solomon, S., Schmeltekopf, A. L. and Sanders, R. W.: On the interpretation of zenith sky absorption measurements, J. Geophys. Res., 92, 8311–8319, 1987.

Wagner, T., B. Dix, C. von Friedeburg, Frieß, U., Sanghavi, S., Sinreich, R. and Platt, U.: MAX-DOAS O_4 measurements: A new technique to derive information on atmospheric aerosols—Principles and information content, J. Geophys. Res., 109, D22205, 2004.

Wagner, T., Beirle, S., and Deutschmann, T.: Three-dimensional simulation of the Ring effect in observations of scattered sun light using Monte Carlo radiative transfer models, Atmos. Meas. Tech., 2, 113-124, 2009.

Wagner, T., Beirle, S., Brauers, T., Deutschmann, T., Frieß, U., Hak, C., Halla, J. D., Heue, K. P., Junkermann, W., Li, X., Platt, U. and Pundt-Gruber, I.: Inversion of tropospheric profiles of aerosol extinction and HCHO and NO_2 mixing ratios from MAX-DOAS observations in Milano during the summer of 2003 and comparison with independent data sets, Atmos. Meas. Tech. Discuss, 4, 3891–3964, 2011.

Wang, T., Hendrick, F., Wang, P., Tang, G., Clémer, K., Yu, H., Fayt, C., Hermans, C., Gielen, C., Müller, J.-F., Pinardi, G., Theys, N., Brenot, H., and Van Roozendael, M.: Evaluation of tropospheric SO_2 retrieved from MAX-DOAS measurements in Xianghe, China, Atmos. Chem. Phys., 14, 11149-11164, doi:10.5194/acp-14-11149-2014, 2014

Yilmaz, S.: Retrieval of Atmospheric Aerosol and Trace Gas Vertical Profiles using Multi-Axis Differential Optical Absorption Spectroscopy, Dissertation submitted to the Combined Faculties for the Natural Sciences and for Mathematics of the Ruperto-Carola University of Heidelberg, Germany for the degree of Doctor of Natural Sciences, 2012.